ANALYSIS AND EFFECTS OF FUSION RELEVANT DAMAGE IN TUNGSTEN

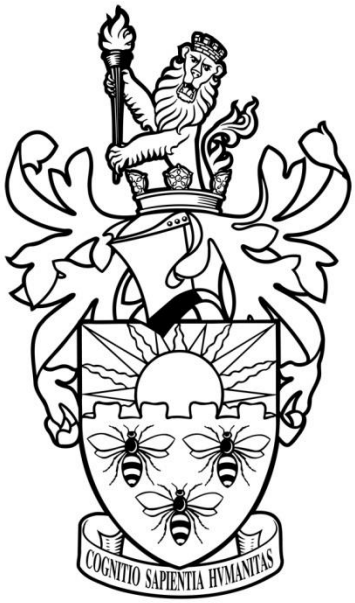

A thesis submitted to the University of Manchester for the degree of PhD in the Faculty of Science and Engineering

2017

Aneeqa Khan

School of Mechanical, Aerospace and Civil Engineering

Contents

Word Count: 87,370

List of Figures

Chapter 2

Chapter 3

Chapter 4

Chapter 5

Chapter 6

Chapter 7

Chapter 8

List of Tables

Chapter 2

Chapter 3

Chapter 4

Chapter 5

Chapter 6

Chapter 7

List of Abbreviations

AIST	National Institute of Advanced Industrial Science and Technology
ANU	Australian National University
appm	Atomic parts per million
ASDEX	Axially Symmetric Divertor Experiment
BCC	Body-Centred Cubic
BEPO	British Experimental Pile 0
BSE	Backscattered electron
CASINO	monte CArlo Simulation of electron trajectory in sOlids
CCFE	Culham Centre for Fusion Energy
CDT	Centre for Doctoral Training
CFC	Carbon fibre composite
CSM	Continuous Stiffness Measurement
CVD	Chemical Vapour Deposition
DD	Deuterium-Deuterium
DEMO	DEMOnstration Power Station
DFT	Density Functional Theory
DIFFER	Dutch Institute for Fundamental Energy Research
dpa	Displacements per atom
D-D	Deuterium-deuterium
D-T	Deuterium-tritium
EBSD	Electron Backscattered Diffraction
EDM	Electrical Discharge Machining
EDX	Energy-Dispersive X-ray spectroscopy
EELS	Electron Energy Loss Spectroscopy
EFDA	European Fusion Development Agreement
ELM	Edge Localised Mode
EPSRC	Engineering and Physical Sciences Research Council
FAFNIR	FAcility for Neutron Irradiation Research
FCC	Face-centred cubic
FEG	Field Emission Gun
FFTF	Fast Flux Test Facility
FFTF-MOTA	Fast Flux Test Facility-Materials Open Test Assembly
FIB	Focused Ion Beam
FOM	Foundation for Fundamental Research on Matter
FT	Frascati Tokamak
FTU	Frascati Tokamak Upgrade
FW	First Wall
HAADF	High Angle Annular Dark Field
HCP	Hexagonal Close Packed
HFIR	High-Flux Isotope Reactor
ICF	Inertial Confinement Fusion
IFMIF	International Fusion Materials Irradiation Facility

ISNAP	Institute for Structure and Nuclear Astrophysics
JAERI	Japan Atomic Energy Research Institute
JET	Joint European Torus
JMTR	Japan Materials Testing Reactor
LENNF	Leeds EPSRC Nanoscience and Nanotechnology Research Equipment Facility
LPD	Linear Plasma Device
MCF	Magnetic Confinement Fusion
MCNP	Monte Carlo N-Particle
MIRF	Multicharged Ion Research Facility
MIT	Massachusetts Institute of Technology
NBI	Neutral Beam Injection
NEC	National Electrostatics Corp.
NSL	Nuclear Science Laboratory
ODS	Oxide-Dispersion Strengthened
OECD	Organisation for Economic Cooperation and Development
ORNL	Oak Ridge National Laboratory
PFMC	Plasma-Facing Materials and Components
PKA	Primary knock-on atom
PPCS	Power Plant Conceptual Study
PSI	Plasma Surface Interactions
PWR	Pressurised Water Reactor
RAFM	Reduced activation ferritic martensitic
SADP	Selected Area electron Diffraction Patterns
SE	Secondary Electron
SEM	Scanning Electron Microscope
SIA	Self-interstitial atom
SNICS	Source of Negative Ions by Caesium Sputtering
SRIM	The Stopping and Range of Ions in Matter
STEM	Scanning Transmission Electron Microscope
TEM	Transmission Electron Microscope
UFG	Ultra fine grained
UHP	Ultra-high purity
UoL	University of Liverpool
USSR	Union of Soviet Socialist Republics
VDE	Vertical displacement event
VPS	Vacuum plasma sprayed
W-TENDL	Tungsten TALYS-based Evaluated Nuclear Data Library

Abstract

The University of Manchester, 2017
Aneeqa Khan, PhD in the Faculty of Science and Engineering
Analysis and Effects of Fusion Relevant Damage in Tungsten

Tungsten is a candidate material for plasma facing components in the experimental fusion reactor, ITER and the demonstration fusion reactor, DEMO. It has been chosen due to its high melting point, low sputtering yield and resistance to oxidation. However, there are still some issues that need addressing, such as its response to 14 MeV neutrons and helium production, products of the deuterium-tritium reaction that will be used to harness fusion energy. Additionally, the high temperatures of operation are another factor to consider. There is no dedicated materials testing device that can concurrently recreate all the conditions expected in ITER or DEMO.

Previous work has focussed on the use of ion beams and linear plasma devices to try and mimic the damage induced from the neutrons and helium. Following from this work, this thesis has focused on three methods in simulating the neutron and helium damage. The three methods used in this project are; helium plasma exposures at fusion relevant temperatures to tungsten and tungsten-rhenium alloys, where rhenium was used to mimic the transmutation induced by neutrons; heavy ion (tungsten and rhenium ions) irradiations in tungsten at 400 °C; and proton irradiations in tungsten at 400 °C and 800 °C. Analysis of the microstructural and micromechanical properties of the exposed samples has been carried out.

The effect of rhenium on the formation of a nanostructure (fuzz) in tungsten induced by helium plasma exposures was studied. Rhenium was shown to generally inhibit fuzz formation. Mechanisms by which inhibition could occur were discussed. The most recent literature had suggested that an incubation fluence was required before fuzz growth could occur, but the research in this thesis pointed more towards an alternative incubation time theory.

The simultaneous effects of transmutation and displacement cascade damage induced by neutrons were mimicked via irradiations with rhenium ions into tungsten, which were compared to tungsten ion irradiations. The effect on mechanical properties of tungsten was tested using nanoindentation. Up to levels of 40 dpa and 1600 appm, at temperatures of 400 °C, the difference in hardness increase between the two types of irradiations was negligible.

Proton irradiations at 400 °C and 800 °C, up to levels of ~2 dpa in the first 2 μm of the samples were explored. The hardness increase observed at 400 °C was much greater than that seen in the heavy ion irradiations, most likely due to the larger volume of irradiated material and the large Bragg peak in the proton irradiated samples.

In both the heavy ion and proton irradiated material, higher hardness increases were observed in annealed material, in comparison to an as-received material.

Impurity concentrations were observed to be an important issue when carrying out irradiation experiments, particularly at raised temperatures.

Declaration

No portion of the work referred to in the thesis has been submitted in support of an application for another degree or qualification of this or any other university or other institute of learning.

Copyright

Acknowledgements

For his supervision, I would like to thank Prof. Paul Mummery, who always gave me the freedom to do what I felt would be best.

I also want to thank Dr. Llion Evans who took on the role of my industrial supervisor at CCFE. His support helped me to improve and focus my work, especially when it came to writing publications. He also introduced me on several occasions to experts who I could discuss my work with and helped me to grow as a scientist.

A huge thanks to the Fusion CDT for their funding and support for this project. I would also like to thank the head of the CDT, Prof. Howard Wilson, specifically for providing me with the opportunity to present my work amongst world experts.

A huge thanks goes to Dr. Joven Lim, who was always around to help whenever there was a crisis. He helped me to grow, particularly in terms of my microscopy skills, as well as organising opportunities and meetings for me to present my work to experts in the field of fusion at CCFE and Oxford University.

Sincere thanks are given to all the people who collaborated and worked with me throughout this project, including all the staff and students at DIFFER, in particular Dr. Gregory De Temmerman and Dr. Thomas Morgan, Dr. Cormac Corr and Dr. Robert Elliman at Australian National University, Dr. Daniel Robertson at Notre Dame University and Dr. Michael Ward at LENNF, Leeds University. Without the in-kind contributions and support with my work, this project would have been impossible.

A massive thanks to all the staff at the University of Manchester who helped me throughout my PhD, including Andrew Forrest, Michael Faulkner, Dr. Christopher Wilkins, Xiangli Zhong, Andrew Wallwork, Dr. Marc Schmidt and Dr. John Lindsay. Your help and advice has been invaluable. Thanks to Prof. Tim Abram, who provided me with an SEM with EBSD when there were no others. Thanks also to Prof. Grace Burke for her feedback, help and advice throughout the PhD.

I would like to thank all the people who have helped and supported me throughout my PhD From endless hours polishing samples and forcing me to take lunch breaks (Karyn Cooper, May Chan and Julie Alias), to midnight SEM sessions (Jennifer Usiobo), and general help and solidarity from the beginning (Moritz Lessmann, Robert Worth), your support has been invaluable. For persuading me not to give up and their constant motivation, a huge thanks to Fatema Rajab, Rwayda Al Hamdi, Maria Yankova, Oluwatobi Afilaka and Cara Mulholland. I couldn't have done this without you! Thanks also to Dr. TJ Petty for his inspiration and help in all things fuzz. Additionally thanks to Dr Jose Arregui-Mena for all his help.

Lastly and most importantly I would like to thank my family and specifically my parents, who were there through everything and always encouraged me to chase my dreams, stay determined and persistent, and to not fear failure.

The Author

Aneeqa Khan graduated from the University of Manchester in 2012 with a BEng degree (1^{st}) in Mechanical Engineering. Her final year research project involved the experimental simulation of radiolytic oxidation of graphite.

After graduating, she embarked on a PhD, as part of the Fusion CDT, with a focus on using experimental techniques to mimic fusion relevant plasma and neutron irradiation damage in tungsten. The fusion CDT is funded by the Engineering and Physical Sciences Research Council and is a partnership between Durham, Liverpool, Manchester, Oxford and York universities, as well as research institutes such as ITER and CCFE. The CDT provided a solid foundation in the field of nuclear fusion. The research completed during the PhD involved the establishment of collaborations with several world leading facilities, including DIFFER, ANU, Notre Dame University and the LENNF facility at Leeds.

In 2016 Aneeqa was awarded the prestigious Monaco ITER Postdoctoral Fellowship, in order to study material migration and retention as part of the Science and Operation Department.

1 Outline and Programme of Work

1.1 Outline

Tungsten (W) is the candidate material for plasma facing components in future fusion reactors [1]. In this role it will be subject to a number of challenges, including high temperatures, damage from 14 MeV neutrons and bombardment from helium ions, amongst several others. The construction of ITER, an experimental reactor, is already underway. The role of ITER is to ensure that a net energy output is achieved and to prove the technology [2]. Although a tungsten divertor is in use in JET, the largest tokamak currently in operation, no tokamak of the scale of ITER has been built previously, where it is planned to have a plasma volume 8.4 times larger than JET [3]. Additionally, there is no large scale material testing facility in order to mimic damage specific to fusion. It is therefore of vital importance, that in conjunction with modelling and simulation, experimental techniques are investigated to mimic the effects of fusion relevant damage in tungsten. There is not one technique that perfectly mimics fusion, and so several methods are being pursued and investigated. Even within a single technique, there are so many variables and parameters that potentially may influence behaviour, it is difficult to determine what is truly representative of fusion damage. The aim of this work is to contribute to the work mimicking fusion relevant damage in tungsten resulting from the deuterium-tritium reaction that will be used in ITER and beyond in DEMO, a demonstration commercial fusion reactor. This work contributes to the understanding of what damage is expected in ITER or DEMO, which will help inform future materials testing experiments, and considerations for the designs of ITER and DEMO.

1.2 Programme of Work

This thesis is submitted in the University of Manchester's 'alternative format'. Unlike a traditional thesis, this format allows for sections of the thesis to be written in a format suitable for publication. Due to the fact that the work carried out for this thesis fell into four clear sections suitable for publication, it was decided to use this format.

This PhD was part of the materials strand of the Fusion Centre for Doctoral Training (CDT). The Fusion CDT is funded by the Engineering and Physical Sciences Research Council and is a partnership between Durham, Liverpool, Manchester, Oxford and York universities, as well as research institutes such as ITER and CCFE. As part of the CDT courses were undertaken, covering aspects across the whole field of fusion, including plasma physics, with a focus on materials aspects. During the first year, the completion of the literature review indicated that there was a need to look at ways of simulating the damage expected in tungsten within a fusion environment experimentally, such as ITER or DEMO. Initial training in experimental techniques was carried out, including SEM and nanoindentation. Suppliers were also identified and material was purchased for use in the project.

In the second year, the CDT allowed for a Collaboratory project, an opportunity to pursue a topic in collaboration with another institution, to be undertaken. A proposal was written to investigate the effect of transmutation products in tungsten on the formation of a nanostructure referred to as 'fuzz' and funding was obtained which allowed for a secondment to DIFFER and the use of the Magnum and Pilot- PSI devices. A successful application via peer-review was made to use the FIB and TEM at the LENNF facility at Leeds University. These collaborations, in addition to the SEM work by the author provided the results for the first publication (Chapter 4),

investigating the effect of rhenium (Re) addition on the ‘fuzz’ formation mechanism in tungsten exposed to helium plasmas. Following this links were fostered with Australian National University (ANU) and Notre Dame University in order to conduct heavy ion and proton irradiation experiments. In the third year of the PhD, nanoindentation and SEM, including EBSD and EDX were used to characterise the irradiated samples. The ANU experiments provided data comparing the effect of rhenium (a transmutation product expected under fusion conditions in tungsten) and tungsten ion irradiations in as received and annealed tungsten samples and formed the basis for Chapter 6. The Notre Dame experiments studied the effects of proton irradiations in as received and annealed tungsten samples at temperatures of 400 and 800 °C (within the operating window of tungsten components in ITER) and are presented in Chapter 7. This allowed comparison of heavy ion and proton irradiations as potential methods to simulate fusion relevant damage.

At the beginning of the fourth year, further samples of tungsten and tungsten-rhenium were sent to DIFFER to conduct more plasma experiments, which formed the basis of Chapter 5. Following exposure to plasma, these samples were analysed using SEM and FIB. The results from plasma damage experiments (Chapter 4 and 5), heavy ion irradiations (Chapter 6) and proton irradiations (Chapter 7) were submitted to the Journal of Nuclear Materials. At the time of writing, the results from Chapter 4 and 6 have been published and the results from Chapter 5 have been accepted.

1.3 Collaborator Contributions

1.3.1 Contributions to Chapter 4

Chapter 4 is the result of a CDT collaboratory project. The project was initially arranged with De Temmerman who helped to form the scope of the project. All

plasma exposures were carried out at DIFFER, which were either completed or overseen by Morgan. Ward was responsible for performing the FIB cross sections and the TEM work. The first author sourced and prepared the samples at DIFFER, was involved in the plasma exposures, and performed SEM analysis of all samples. The paper was produced by the first author with editorial contributions from all other authors. Comments from reviewers at the Journal of Nuclear Materials, as well as conversations with Petty, helped to further improve the work. This paper has been published in the Journal of Nuclear Materials.

1.3.2 Contributions to Chapter 5

Chapter 5 is the result of a second collaboration with DIFFER. The samples were prepared by the first author and Morgan at DIFFER. All plasma exposures were carried out by Morgan, using the Pilot-PSI device. Morgan also took mass measurements of samples before and after exposure. Ward was responsible for FIB cross sections in one of the samples. The author produced the remaining FIB cross sections and conducted the SEM analysis. Petty provided data of fuzz growth from various other devices, including his own work, and results from an extensive literature survey. The paper was produced by the first author with advice on content and editorial contributions from the other authors. At the time of writing, a version of this paper has been accepted by the Journal of Nuclear Materials.

1.3.3 Contributions to Chapter 6

Chapter 6 highlights the results from a collaboration with the Australian National University (ANU). Elliman and Corr were responsible for the ion irradiation work at ANU. Lim aided with the carrying out and analysis of the EBSD experiments. Forrest was responsible for the operation of the nanoindenter. Analysis of the nanoindentation results and the EBSD runs, SRIM and CASINO simulations were

carried out by the first author. The EBSD runs of the non irradiated material were carried out with the help of Schmidt. Wallwork helped with the heat treatments of the samples. Conversations with Faulkner helped with the EBSD analysis. The first author wrote the paper with editorial contributions from Elliman, Corr, Lim, Mummery and Evans. A version of this paper has been published in the Journal of Nuclear Materials.

1.3.4 Contributions to Chapter 7

Chapter 7 summarises work in collaboration with Notre Dame University. The proton irradiations and high temperature stage development were carried out by Robertson. Robertson also weighed the samples before and after the irradiations. Lim carried out the EDX analysis. Forrest was responsible for the operation of the nanoindenter. Wallwork helped with the heat treatments of the samples. The first author was responsible for writing the paper, with Robertson writing the section on the experimental set up related to the ion irradiations and the mass of the samples and Lim advising the content. Editorial contributions were provided by Robertson, Lim, Evans and Mummery. At the time of writing, this paper has been submitted to the Journal of Nuclear Materials.

2 Literature Survey and Work Required

2.1 Background

The world's energy demands will more than double by the year 2050 [4]. Currently 86% of energy comes from fossil fuel sources [5], contributing unsustainable amounts of greenhouse gases [4], although carbon capture technologies are under development [6], this is not enough. Carbon emissions are still growing and it is predicted that they will increase by 20% of the 2014 levels by 2035 (see Figure 2.1) [5]. Not only is this a significant contribution to global warming, but additionally sources of fossil fuels are limited. Therefore it is necessary to develop methods to supply high volumes of energy with a low environmental impact. There is no single solution to meet this demand. It is necessary to have a policy that addresses the 'Energy Trilemma' of security, equity, and environmental sustainability [7]. A combination of approaches must be pursued, including solar power, wind power, nuclear fission utilising both thorium and uranium breeders, and also nuclear fusion [8]. It is important to have a diverse approach so that the reliability and economics of all the energy sources is accounted for [9]. Fusion power and thorium fission are the only approaches that have not yet achieved technical and commercial viability. One of the key challenges for achieving commercial nuclear fusion power is the materials required to cope with the extremely demanding environment in the reactor. This thesis is focussed on the use of tungsten, one of the candidate materials, for fusion applications. The operating environment of a fusion reactor is very challenging and it is important to understand the suitability of tungsten to cope with such an environment.

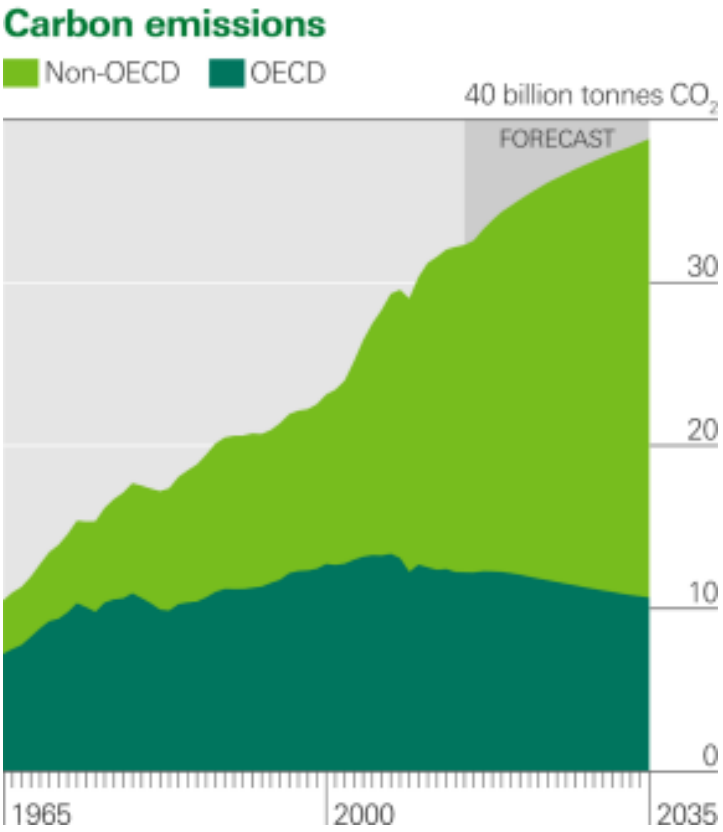

Figure 2.1: Predicted growth of carbon emissions, taken from [5]. OECD countries are members of the Organisation for Economic Cooperation and Development.

2.1.1 Why Fusion?

Fusion is an important candidate for a sustainable energy source due to four key aspects:

1. The supply of fuel is essentially unlimited – deuterium (D) and tritium (T) are the fuels required for achieving commercial nuclear fusion. Lithium (Li) is used to breed tritium and deuterium is sourced from water. There are enough lithium reserves to sustain fusion power for 250-600 years, with the possibility of extracting lithium from seawater in the future, which could essentially provide an unlimited supply [10]. The deuterium in half a bathtub full of water combined with the lithium found in a single laptop battery could provide the UK per capita electricity requirement for a time period of thirty years (~200 000 kWh) [11].

2. Intrinsically safe – Unlike in fission power, a runaway reaction could not occur in a fusion power plant. In the event of a loss of coolant accident, the temperatures reached would be considerably below the melting temperatures of the structure and the limited storage of radioactive isotopes means that even in the event of a worst case scenario, evacuation of surrounding areas would not be necessary [8].

3. Requires limited space – A fusion power plant would occupy an area of land comparable to that required for present day nuclear fission plants, however due to its intrinsic safety it could be situated closer to areas of population, as opposed to remote locations [8].

4. Limited impact on the environment and low levels of waste – A goal has been set that the components of a commercial fusion power plant that become active, will contain radioactive isotopes with half-lives of the order of 10 years, and hence recycling could occur in a time frame of only 100 years [8], compared to the hundreds of thousands of years required for components from a fission reactor. Additionally fusion will not result in fuel waste, as is the case for fission.

2.1.2 The Fusion Reaction

There is always a mass difference between the mass of all the component parts of an atom and the whole atom. This is referred to as a mass defect, and via Einstein's equation, $E = mc^2$, this mass defect corresponds to an energy [12]. This energy is known as the binding energy, which is the energy necessary to split an atom into all its component parts [12]. The binding energy varies with the mass of the atom, as shown in Figure 2.2. From the nuclear binding energy curve we can observe that if

atoms heavier than *Fe-56* (the atom with the highest binding energy, and hence the most stable) are split, energy will be released, as the resultant lighter atoms have a higher binding energy. Conversely if we look at atoms lighter than *Fe-56*, it can be seen that energy will only be released with fusion of the lighter elements. Nuclear fission is extensively used for electricity production and there are various different types of fission reactors, using isotopes such as *U-235* and *Pu-239*. However, more energy is released per nucleon during the fusion of the lightest elements, in comparison to fission of the heaviest.

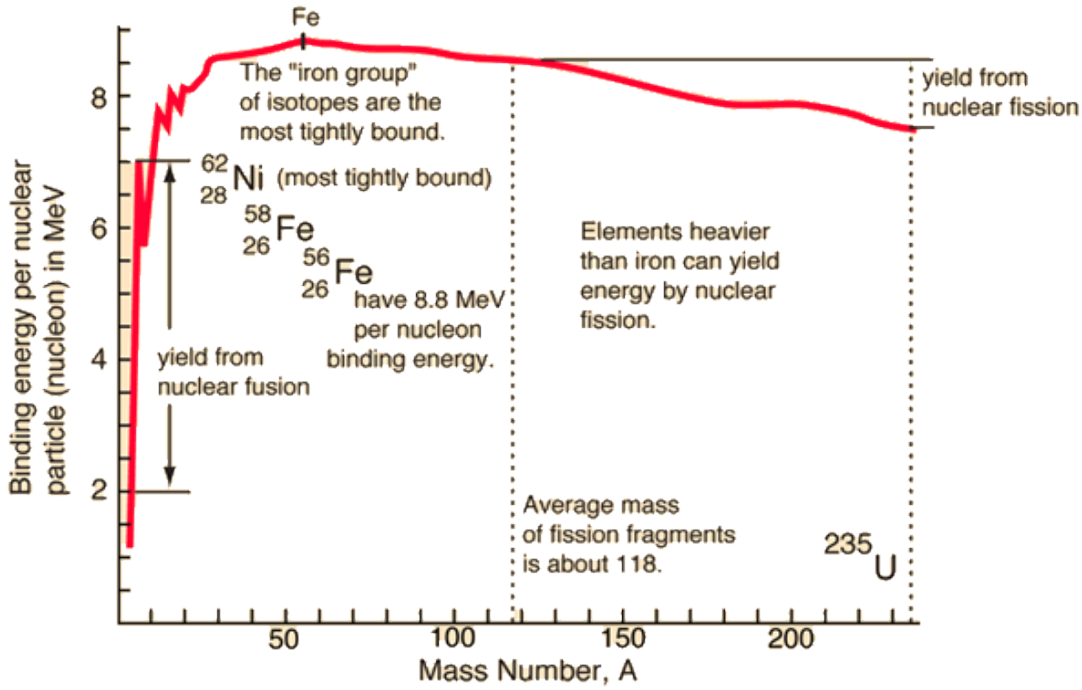

Figure 2.2: Nuclear binding energy curve, taken from [13].

Fusion is a process that naturally occurs in the Sun, where atoms of hydrogen (H) fuse together to form helium (He). However on Earth, this reaction is not so feasible due to the difference in gravitational forces [14]. On Earth, the most efficient fusion reaction for commercial energy production is the reaction between D and T (both isotopes of hydrogen). This is referred to as the 'D-T' reaction and is shown in

Equation 2.1[8]. This reaction has been chosen due to the energy required for the reaction and the high neutron cross section[1] (the cross section is ~100 times greater than other fusion reactions within a similar energy range [8]).

Achieving the D-T reaction requires the atoms to overcome the Coulomb barrier[2], so that the strong nuclear force is dominant. In order to achieve this, temperatures that are ten times greater than those reached during fusion of hydrogen in the sun, of the order of 150 000 000 °C are required for the atoms to have the necessary kinetic energy to fuse [8], [14]. At these temperatures, gases become ionised, and the electrons and nuclei making up atoms are separated. This ionised gas is referred to as plasma. The mass of the products of the reaction is less than that of the reagents, and via Einstein's equation, energy is released in the form of kinetic energy. The helium produced has a kinetic energy of 3.5 MeV and the neutron has 14.1 MeV [8].

Equation 2.1

$$^{2}_{1}D + ^{3}_{1}T \rightarrow ^{4}_{2}He + ^{1}_{0}n + energy\ (17.6MeV)$$

Tritium only has a half-life of 12 years and due to its instability, there is a low abundance and therefore it has to be bred via lithium. The neutron released from the D-T reaction can be used to breed tritium from lithium, allowing for more fuel to be produced during the process. This is done via Equation 2.2 and Equation 2.3. No fusion reactor has yet been operated with a test blanket. The first fusion reactor to investigate the breeding of tritium via test blanket modules containing lithium will be ITER [8], [15].

Equation 2.2

$$^{6}_{3}Li + ^{1}_{0}n \rightarrow ^{3}_{1}T + ^{4}_{2}He + (4.8\ MeV)$$

[1] The likelihood of a reaction taking place
[2] The energy barrier that has to be overcome for two nuclei to get close enough to react

Equation 2.3

$$^{7}_{3}Li + ^{1}_{0}n \rightarrow ^{3}_{1}T + ^{4}_{2}He + ^{1}_{0}n + (-2.47\ MeV)$$

2.1.3 Path to commercial fusion power

The two main methods that can be used to achieve nuclear fusion are Magnetic Confinement Fusion (MCF) and Inertial Confinement Fusion (ICF). The European route to achieving commercial fusion power is shown in Figure 2.3 and will utilise MCF in the form of a toroidal shaped device, referred to as a tokamak [11]. A comparison of the tokamaks shown in Figure 2.3, the major radii of JET, ITER and the PPCS (Power Plant Conceptual Study) A design for DEMO are 3, 6.2 and 9.55 m respectively [16]–[18].

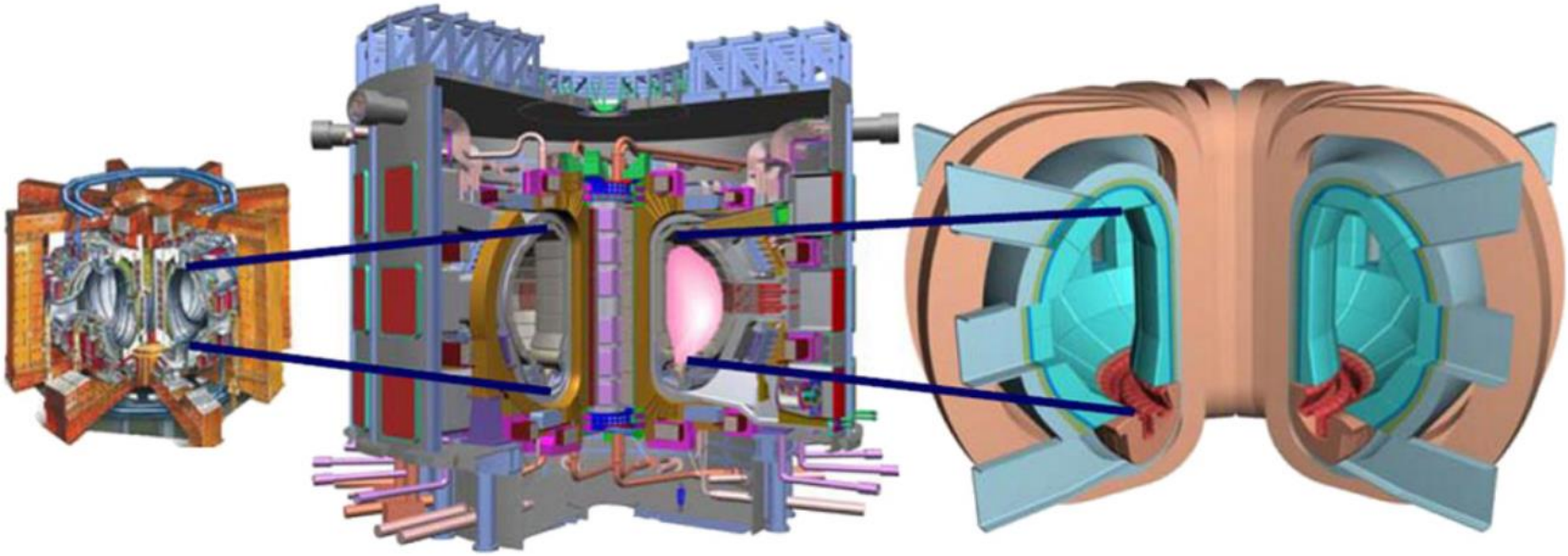

Figure 2.3: Path to commercial fusion power. The blue person at the bottom right of ITER gives an indication of scale [11].

The path to commercial fusion, involves confining D-T plasma within a tokamak. Since the first tokamak, TMP (USSR), was built in 1954, at least 200 further tokamaks have been built worldwide [19]. Currently the largest and most powerful tokamak in operation is JET, located at the Culham Centre for Fusion Energy, UK [20]. Construction has begun on ITER in the south of France, a pilot reactor, where experiments will be conducted in order to solve key issues. The results from ITER will aid the building of DEMO, a demonstration commercial reactor, by the year 2050 [4]. The aim of ITER is to output ten times more energy than is input, i.e. achieve $Q \geq 10$, and be the first fusion device in history to obtain a net energy output, for pulses between 400 and 600 s in length [2]. Additionally ITER will be required to prove tritium breeding is feasible via lithium blanket technology, produce a D-T plasma that is sustained via internal heating, and demonstrate the technology and safety of a fusion device [2].

A schematic of ITER is given in Figure 2.4, with the key components highlighted. The cryostat will surround the superconducting magnets and the vacuum vessel, maintaining a super-cool vacuum. It is planned that it will be made from 3800 tonnes of stainless steel with a volume of 16 000 m^3, it will be the biggest high-vacuum pressure chamber ever constructed of stainless steel [21]. The superconducting magnets will be manufactured from niobium-tin or niobium-titanium. They will be cooled to temperatures of -269 °C using supercritical helium. They will be responsible for producing the high strength magnetic fields to control the plasma in ITER [22]. The vacuum vessel will also be made of stainless steel and will be able to contain a plasma volume of 840 m^3, which is 8.4 times greater than JET [3], [23]. Additionally it will give support to the parts of the reactor within the vessel and will be the main radioactivity confinement barrier [23]. The blanket will comprise of 440

modules, each measuring 1×1.5 m and will provide shielding to the external vessel components from high neutron and heat loads. Each module will have a first wall, that can be detached and will remove heating from the plasma and additionally a neutron shielding block [24].

ITER will be the first device to investigate the concept of tritium breeding and therefore specific modules will be replaced during operation in order to test materials and prove this concept [8], [15], [24]. The first wall of the blanket will be covered with beryllium (Be) [24]. The divertor will be responsible for extracting helium from the D-T reaction and other impurities [25], [26]. The fuel and impurity densities will be regulated via the interception of the magnetic fields in the scrape-off layer that is outside the last closed flux surface of the plasma. The plasma ions will then travel through the scrape-off layer region to the divertor, where they will be neutralised, forming a gas, which can then be exhausted via the vacuum system [27]. The divertor will be exposed to the greatest surface heat loads in ITER and remove up to 15% of the total fusion power, with thermal loads of 10 MWm^{-2} expected during steady state and 20 MWm^{-2} during transient events [26], [28]. The ITER divertor will comprise of 54 individual cassettes that will be constructed from a stainless steel support, an inner and outer vertical target and a dome (plasma facing components). Active water cooling will be utilised in order to extract heat induced by high energy particle bombardment of the inner and outer targets [26]. A schematic of the cassette assembly is shown in Figure 2.5 [27].

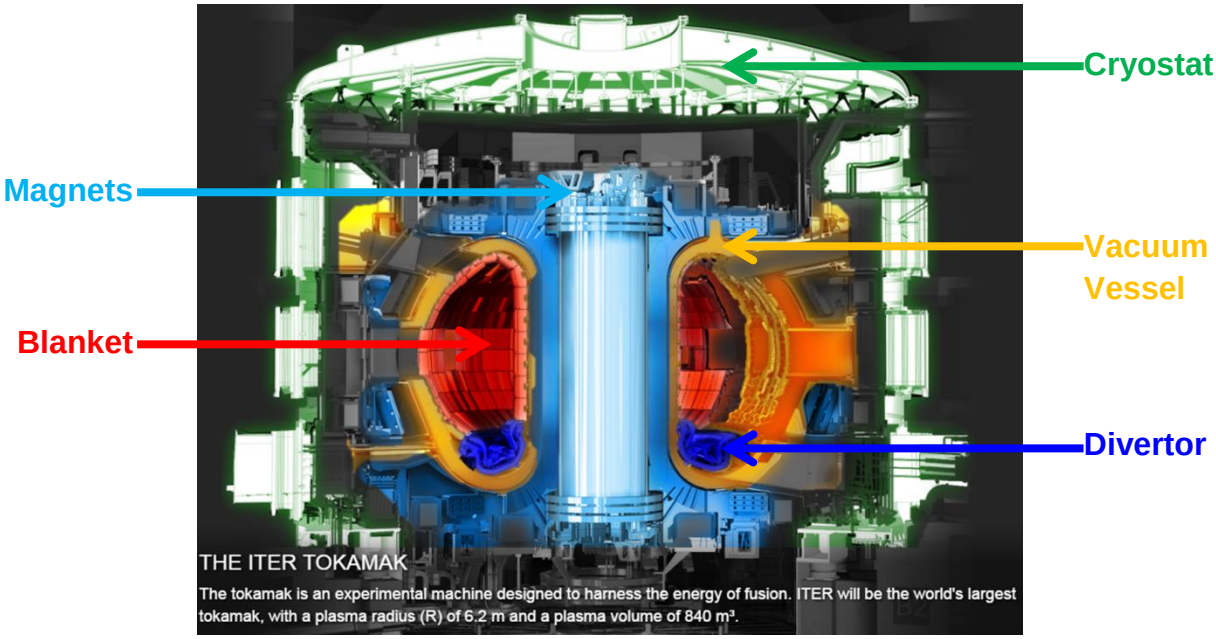

Figure 2.4: Schematic of ITER adapted from [29].

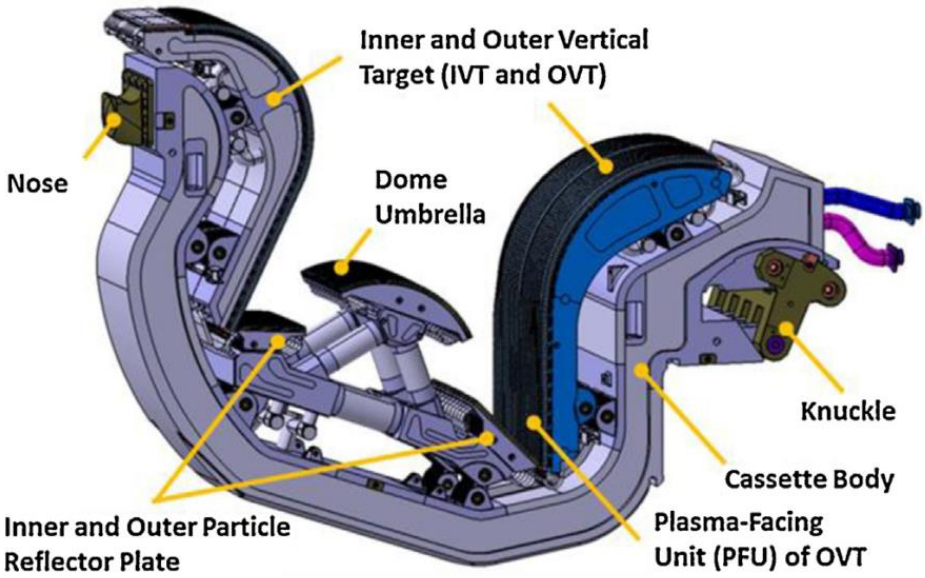

Figure 2.5: ITER divertor cassette assembly, taken from [27].

2.2 Materials for Fusion Reactors

The operating conditions within a commercial fusion reactor are extremely challenging and indeed the development of suitable materials for fusion has been referred to as the "greatest structural materials development challenge in history" [30]. There is a complex set of demands for materials that need to be addressed,

which vary depending on the part of the reactor they will be used for. Blanket materials will be required to shield the vacuum vessel and the superconducting magnets from neutrons and heat loads, as well as facilitate the breeding of tritium [31], [32]. The plasma facing divertor materials will also be required to withstand the high neutron and heat loads [33], [34]. In addition to the structural and loading requirements that limit the materials choice for a fusion reactor, the desire to only use materials with reduced activation properties has significantly reduced the options in terms of conventional materials that have been used in previous fusion and fission reactors. This has restricted the main choice of alloying materials to iron (Fe), chromium (Cr), titanium (Ti), vanadium (V), tungsten (W), silicon (Si) and carbon (C) [31]. Tungsten has been chosen for plasma facing materials in ITER and DEMO and depending on the design of DEMO, could also be used for certain structural components. Heat sink materials will contain the coolant in fusion reactors and will have to be bonded to plasma facing materials [35]. For heat sinks copper alloys are the main candidate materials[36].

2.2.1 Materials for Structural Components

As a structural component there is a requirement for a material to be ductile, strong and stable at high temperatures, and have a high temperature of recrystallization [37]. There are four main candidates for this role: vanadium alloys, SiC/SiC composites, reduced activation ferritic martensitic (RAFM) steels and tungsten alloys.

Vanadium alloys are one of the advanced options for structural components in future fusion reactors, with particular emphasis on the V-4Cr-4Ti alloy [38]. V alloys have high temperature strength, and have low activation properties [39]. A reactor using a V based alloy for a structural material in the blanket, would utilise liquid Li as a

coolant as well as a breeder for T [40]. This would avoid the use of beryllium, which would remove the handling and safety issues surrounding its use [38]. However, the use of such a coolant could result in a reduction in pressure due to magneto-hydrodynamic forces [38]. It has been suggested that V alloys can operate at temperatures up to ~750 °C [41]. Thermal creep requires further investigation as this is a factor limiting the maximum operation temperature [38]. V alloys are also prone to He embrittlement, which is another factor that restricts the maximum operating temperature [41].

Temperature has been observed to not have a significant impact on the ultimate tensile strength of V-4Cr-4Ti at temperatures between 300-800 °C [41]. V-4Cr-4Ti has been observed to have significant tensile ductility, with area reduction in tensile tests at temperatures between 300-800 °C being greater than 70% [41].

The yield strength of V-(4-5%)Cr-(4-5%)Ti has been observed to increase with neutron irradiation doses from 0.1-6 dpa. At 4-6 dpa the yield strength is ~2.4 times that of the non-irradiated material [42]. Irradiation hardening is said to saturate above doses of ~5 dpa [42]. Irradiation embrittlement is the key factor that limits the lower bound of operating temperature for V alloys to ~400-450 °C [38]. Additionally at temperatures greater than 550 °C, embrittlement could occur due to the introduction of interstitial impurities, such as O, C or N [43].

SiC or SiC composites are another option for structural materials in a fusion reactor. It is often said that SiC is the “most promising, but least developed candidate structural material” for fusion applications [44]. SiC has a melting point of 2730 °C, and a thermal conductivity of 490 W/mK [44], [45]. SiC or SiC composites could operate at temperatures above 1000 °C [46]. SiC has creep resistance, with an

activation energy for creep observed to have a value of ~1.81 eV/atom [47]. SiC has been observed to have low activation properties [45]. This is due to the low neutron cross section, however ultimately this results in a higher volume of material that is active due to increased neutron penetration, in comparison to a material with a larger neutron cross section [48]. If SiC or SiC composites were to be used as a structural material, the thermodynamic efficiency of the reactor would be increased, as higher temperature coolants could be used for the blanket and first wall [44]. There are still issues in manufacture of SiC or SiC composites as some of the additives that are used in manufacture could result in increased activation [44]. It is critical to produce a material with a limited porosity to inhibit degradation from He [44]. He has been shown to result in a 20% reduction in strength of a SiC composite irradiated with He ions to fluences of 150-170 appm [49]. It is also important to ensure that the tensile stress, modulus and through-thickness thermal conductivity at 1000 °C are greater than 300 MPa, 200-300 GPa and 30 W/mK, respectively [44]. Achieving a material with a thermal conductivity that reaches the high temperature targets following irradiation is a significant obstacle before SiC/SiC composites can be used as a structural material. Neutron irradiation results in swelling of SiC/SiC composites which consequently results in a significant reduction in thermal conductivity [44].

Reduced activation ferritic martensitic (RAFM) steels are the most technologically advanced candidate structural material and are taken to be the reference material for structural components in the first wall and blanket for ITER and beyond [43], [50]. The composition of the reference RAFM steels is Fe-0.1C-9Cr-2W-0.25V-0.07Ta [50]. This is different from conventional steels, where typical alloying elements include Mo, Nb and Ni. The replacement of these alloying elements with W and Ta results in the reduced activation of RAFM steels, which can reach ‘low level waste’

classification in 80-100 years, in comparison to the 200 000 years for conventional steels [31]. RAFM steels are also more resistant to swelling due to irradiation and embrittlement from He [50]. Additionally they are compatible with several different coolant options, making them a highly versatile material for future fusion reactor designs [50]. However, there are issues in regards to irradiation induced embrittlement at temperatures below ~400 °C with RAFM steels [50]. He produced via transmutation in a fusion reactor will form bubbles within steels which also results in embrittlement [51]. Non-irradiated ferritic martensitic steels typically have a ductile to brittle transition temperature (DBTT)[3] of ~ -100 °C, however, irradiation to doses above 30 dpa would result in the DBTT increasing to above room temperature [31]. Currently the upper operating temperature of ferritic martensitic steels is ~550 °C, however, the use of oxide-dispersion strengthened (ODS) steels could allow for a maximum temperature greater than 700 °C [52], [53].

Tungsten is certain to be used as an armour material for the divertor in ITER and DEMO as discussed in section 2.2.2. However there is a possibility that W could also be used as a structural material in fusion devices post-ITER [37].

Tungsten is a body-centred cubic (BCC) metal with a melting point of 3420 °C [54] and a Young's modulus of 390-410 GPa [55]. Tungsten is typically produced via the powder metallurgy route, following which it is processed (via swaging or rolling for example), resulting in a microstructure which is anisotropic and contains subgrains [55], [56]. The strength and ductility of W has been observed to increase with increased deformation induced by rolling at temperatures below recrystallization temperature [57]. Studies have shown primary recrystallization in W to start at 1150 °C for long (43 hour) annealing times, and for shorter annealing times (an

[3] The DBTT is the temperature above which a material will behave in a ductile manner.

hour), at 1250 °C. Complete recrystallization was observed following a one hour heat treatment at 1300 °C. After annealing at 1300 °C for an hour, a grain size of 17 μm was obtained. For a one hour treatment at 2000 °C, a grain size of 27 μm was seen [58]. Secondary recrystallization was seen at 2000 °C [58]. Reiser *et al.* [59] conducted annealing studies in a tungsten foil with elongated grains in the rolling direction. Small amounts of grain growth were observed following annealing treatments for an hour at 1300 °C and 2000 °C, however no recrystallization was seen (i.e. the texture remained the same). An annealing treatment at 1400 °C for 20 hours resulted in large grains without any dislocations observed [59].

The difficulty with using W as a structural component is primarily due to the low fracture toughness, which across all temperatures is below 100 MPa $m^{0.5}$, and at temperatures of 1000 °C, is ~ 30 MPa $m^{0.5}$ [60]. These values are comparable to the lowest values of fracture toughness following irradiation in vanadium alloys and ferritic-martensitic steels [60]. Alloying of tungsten using lanthana or yttria as dispersed oxides results in an increase in the temperature of recrystallization and the creep strength , however such alloying can also result in an increased likelihood of intercrystalline fracture [37]. Furthermore, irradiation is shown to increase the DBTT of W. The DBTT of W has been observed to generally lie between 120-400 °C, and is predicted to increase with neutron irradiation up to 800-1000 °C [61]–[66], which results in difficulty for using W as a structural material [60]. There is a range of DBTT values due to anisotropy in the microstructure, the strain rates utilised and other variations in testing methods.

In order to improve the ductility of W, three main methods are being investigated including the production of alloys, composite materials and nanostructuring [37]. Rhenium (Re) is the only alloying element in solid solution that has been shown to

improve the ductility of W. However, this has only been observed to hold true in non-irradiated material, and in W-(3-5%)Re alloys that have been irradiated to doses greater than 0.4 dpa, the hardness increase observed is greater than that in pure W [25], [67], [68]. Furthermore, following a dose of ~0.4 dpa, a sharper DBTT increase is seen in W-10%Re in comparison to pure W [69]. Therefore although Re may ductilise W in non-irradiated material, it is not feasible for fusion applications where the Re will actually cause increased embrittlement following irradiation. All other alloying solid solution elements (Ta, V, Mo) have shown to increase the brittle behaviour of W, with the exception of Ti which has not been studied and requires further investigation [37].

The microstructure of W heavily influences its performance. Typically smaller grain sizes correlate to an increased strength [70]. Nanostructuring of W has been investigated in pure W, as well as other alloys; including W-Ti, W-V and W-Ta. Dispersed particle (TiC, La_2O_3, Y_2O_3) reinforced materials have also been investigated [37], [71]. Many of these nanostructured materials show increased brittle behaviour in comparison to pure W due to impurities and the manufacturing techniques employed [37]. However, the W-2%Y_2O_3 nanostructured material produced by PLANSEE has shown to behave in a ductile manner at temperatures between 400-1000 °C [72]. Chemical powder metallurgy methods of manufacturing nanostructured W alloys has also been shown to be promising [73].

In terms of composites, fibre reinforced composites and tungsten laminates have been investigated [74]–[76]. Such techniques have a lot of potential in improving the ductility of W. The response of such materials to neutron irradiation and He embrittlement is something that requires further research. Material properties at increased temperatures and the effect of recrystallization are being investigated.

2.2.2 Materials for Plasma Facing Components

Plasma facing components, such as the inner and outer vertical targets and dome of the divertor will have to cope with the damage induced by 14.1 MeV neutrons, extremely high heat fluxes of 10 MWm^{-2} during steady state and up to 20 MWm^{-2} during slow transients in ITER [77], plasma damage, and additionally cyclic stresses (due to Lorentz forces) [31]. In certain DEMO concepts, the lowest armour temperatures will be greater than the temperature of the coolant at ~800 °C, and exceed 1700 °C at the surface of the divertor [28]. Additionally due to goals set on activation limits, they will have to be low activation materials. There is also a 700 g safety limit of potential mobilised tritium in ITER that has been set by French authorities, to mitigate the impact of any tritium that could be released into the atmosphere in the case of a loss-of-vacuum accident [78], [79]. In addition to the safety reasons for reduced tritium retention, consequently, if a lot of tritium is retained in plasma facing components, this would limit the amount of fuel that could be used, and this would mean the fuel cycle would no longer be efficient and economically viable [80].

The ideal plasma facing material would therefore have a low activation energy, have high strength at low and high temperatures, be ductile, have a high resistance to thermal shock and fatigue and have high thermal conductivity. However, there is no perfect material that can completely meet these criteria and indeed some of the desirable characteristics cannot always be achieved simultaneously, such as strength and ductility [31]. Additionally not only does the effect of the damage induced on the material need to be addressed, but the effect of any degradation or erosion of materials and their effect on the plasma purity is vital, as one of the goals of ITER is to achieve a ‘burning plasma’, where the D-T reaction is self-sustained via internal

heating [2], [81]. High atomic number (Z) materials are good radiators and will cool the plasma, increasing the difficulty of achieving fusion that is self-sustaining [82]. Low Z materials are not efficient radiators if they are present in the plasma core and therefore will not have as negative an impact on plasma performance [79].

There are a few choices for materials that could be used for plasma facing components, including tungsten and other refractory metals such as molybdenum (Mo), carbon and carbon fibre composites (CFCs) and beryllium (Be) [31], [83]. Another option for plasma facing materials, although not in ITER but in a future fusion reactor, could be flowing liquid metals, such as lithium, gallium, tin, or a tin-lithium mixture. Flowing liquids could cope with heat loads of up to 50 MWm^{-2}, and would allow for the extraction of heat and particles simultaneously. However this type of technology is not proven and requires significant research, particularly with regards to the effect of magnetic properties of the plasma on liquid metals, issues of interaction with other materials, how particles would be exhausted and how to physically implement it in a reactor [84]. Additionally copper and stainless steel alloys have been considered as substrates [83].

The majority of tokamaks with moderate plasma densities and magnetic fields in previous years have used carbon based materials for plasma facing components, due to the fact that it had been observed that plasma operation had been poor in older tokamaks when high Z materials had been used [66], [85]–[88]. However, in tokamaks operating with magnetic fields ranging from 6-10 T with higher plasma densities, including the tokamaks FT and FTU (Frascati tokamak and Frascati tokamak upgrade), Alcator A and C, high Z materials, molybdenum and tungsten have been used successfully in plasma facing components [66], [89], [90]. Most recently JET has moved from carbon to an ITER-like Wall, with a tungsten divertor

and a beryllium first wall, in order to give performance predictions for the materials of choice for ITER [91]. ASDEX (Axially Symmetric Divertor Experiment) upgrade is currently the only tokamak to operate with all tungsten plasma facing components [92].

Originally CFCs were considered for the divertor strike point[4] with rest of the plasma facing part of the divertor being made of tungsten during the initial non-nuclear phase of operation of ITER [81], [93]. CFCs are considered advantageous due to the fact they will not melt even at the high heat fluxes (10 MW m^{-2} in steady state) expected [81]. Furthermore the plasma can tolerate higher quantities of low Z materials, in comparison to high Z materials in the instance of any erosion [64], as the radiative effects of low Z materials are not as significant as high Z materials. There is also a wealth of experience with CFCs, which have been used in tokamaks all around the world [94]. Therefore, in order to reduce uncertainties during commissioning and non-nuclear operations of ITER, where development of heating, plasma control and ELM mitigation systems will be a priority, CFCs were a suitable choice [1].

However, predictions of fuel retention from reference plasma scenarios and data from the PISCES linear plasma device (LPD) suggest that the 700 g tritium limit could be attained within ~40 pulses (neglecting any active cleaning and long term outgassing) during D-T operation in ITER if carbon was used for the divertor and first wall [78]. Clearly this is a highly conservative estimate, as CFCs are only considered for certain points of the divertor. However, other estimates, assuming a CFC and W divertor and a Be first wall still predict the 700 g limit being achieved within 250-750, 400 s pulses, with the CFCs contributing most significantly [95].

[4] The point where the plasma boundary strikes the vessel wall.

With at least 10 pulses expected a day, this is highly unsustainable [79]. This long-term retention in low Z materials is mainly due to co-deposition, where material is eroded, migrates and is then re-deposited, resulting in the formation of layers that contain deuterium and tritium [95]. Despite this, CFCs would still be a good candidate for non-nuclear operation of ITER, however during D-T operation they would be unsuitable. Therefore it was originally planned that CFCs would be used for the divertor in the non-nuclear campaign, before being replaced by an alternative during D-T operations. However due to budget restrictions it became clear that it was not possible to have two different divertors, and therefore it was decided that operations should start with a full tungsten divertor [1].

Refractory metals are considered as they are more resistant to sputtering than other materials [96], however, high Z materials can negatively impact the plasma.

Molybdenum has been used as a plasma facing material in both the TEXTOR and Alcator C-Mod tokamaks [90], [97]. Molybedum has a melting point of 2620 °C [98]. The sputtering threshold of Mo by He can be calculated using Equation 2.4 [99].

Equation 2.4

$$E_{th} = \frac{(M_i + M_t)^2}{4M_i M_t} E_s$$

E_{th} is the threshold sputtering energy, M_i is the mass of the incident ion, M_t is the mass of the target and E_s is the surface binding energy, which for Mo is taken as 6.89 eV [100]. This results in a sputtering threshold of ~45 eV which is much higher than the ~10 eV calculated for C (assuming a surface binding energy of 7.42 eV [100]). Despite the relatively high melting point and sputtering threshold, as well as

proven suitability as a plasma facing material, Mo has to be discounted for ITER and beyond. This is because the radiation products that would be produced following irradiation by the 14 MeV neutrons would be active beyond the 100 year limit by which time waste should be suitable for recycling or fit for 'clearance' as suggested for ITER [64], [101]. For Mo irradiated over 2.5 years at a flux of 5 MWm^{-2}, the decay time to achieve a surface dose rate of 10^{-2} Sv would be 2×10^{5} years [64].

Out of the refractory metals, W is currently the favoured option for the divertor. Mo has been used as a plasma facing material in the TEXTOR and Alcator C-Mod tokamaks [90], [97]. However, due to the activation limits W is preferred over Mo [64]. V does not have the activation problems of Mo and its alloys have a much lower DBTT than W. For example non-irradiated V-5Cr-5Ti has a DBTT of ~ -193 °C [84] in comparison to W where the DBTT generally ranges from 120-400 °C [61]–[63], [66]. However, V has a much lower melting point in comparison to W, and therefore although it may be suitable for the first wall, in the divertor region, where temperatures could reach up to 1100 °C, and even higher during disruptions, W is preferred [1].

W was chosen to replace CFCs primarily because it has highly improved T retention properties in comparison to CFCs. W is more resistant to sputtering than CFCs (The sputtering threshold, E_{th}, of tungsten is ~200 eV for deuterium [62], compared to 27 eV for carbon [102]) and is less susceptible to erosion at high temperature [64]. Using a full W divertor with a Be first wall, it is predicted that the 700 g T limit will only be reached after 1500-5000 pulses [95]. In this case the co-deposition of the low-Z Be is contributing the most to the retention. If a full W first wall and divertor were to be utilised, neglecting for neutron damage effects, it is predicted that the T inventory will remain below 700 g even after 18 000 pulses [95]. Neutron damage

effects however could result in increased retention, and reduce the number of pulses to 5000 [95]. Although in DEMO or other future fusion reactors Be would be unsuitable as it has a high erosion yield (although still better than CFCs). For ITER, Be will be used for the first wall in order to reduce the risk of cooling the plasma that may occur from erosion if tungsten was used for the first wall, and allow more flexibility during operation [91], [103].

There is also experience using Be in the JET ITER-like wall [104]. JET has moved from a carbon to an ITER-like wall, using W and W-coated CFC tiles and Be limiters, where it has been observed that the mean erosion rate of the inner wall has been reduced 4-5 times in comparison to the carbon wall [105], [106]. This provides reassurance for the choices of W and Be for ITER. It is predicted that a full tungsten wall and divertor could be used for DEMO or other future fusion reactors [66], [91]. In certain divertor concepts for future fusion reactors W could be used for structural components [28].

In addition to the primary reason of reduced T retention, W has been chosen for the divertor due to the fact that it has the highest melting point of any metal at 3420 °C and good thermal conductivity properties [54], [60]. Solid W has a thermal conductivity that ranges from ~170 W/mK at room temperature to ~105 W/mK at 1300 °C [107]. Additionally it also has good high temperature strength, with stress-relieved tungsten having a yield strength of ~604 MPa at a temperature of 800 °C [108]. Furthermore Troev *et al.* suggested that out of all the candidate first wall materials, W has the highest irradiation resistance, which has been suggested to be possibly due to the crystal lattice bonding energy of W being large (7.9-10.09 eV/atom) [55], [109]–[111].

However, there is no perfect divertor material and W certainly has its issues. It has a low fracture toughness, for example for longitudinal three point bend tests in polycrystalline tungsten from rolled rods, K_Q has values of 5.4 -9.1 $MPam^{0.5}$ [108]. It also has poor resistance to oxidation at high temperatures. Pure tungsten has an oxidation rate of 1.4×10^{-2} $mgcm^{-2}s^{-1}$ at 1000 °C [112]. It's DBTT generally ranges from 120-400 °C, and is predicted to increase with neutron irradiation up to 800-1000 °C [61]–[66]. The DBTT is highly dependent on strain rate. It has been shown that the DBTT in tungsten is related to the movement of screw dislocations via a kink pair mechanism and depends on the glide of dislocations from sources, rather than nucleation of dislocations [61], [113] and Gibson *et al.* have suggested that an increase in nanoindentation hardness following W and He irradiations indicates that dislocation glide is being inhibited [114].

The high DBTT provides three main challenges; firstly manufacturing components with such a high DBTT is challenging. Secondly, although it is expected that the parts of the divertor with the highest heat loads will operate above the DBTT [1], there are still likely to be regions operating in the brittle regime, particularly in the non-nuclear phases of operation of ITER where the peak temperatures on the divertor surface are not likely to be greater than ~700 °C [1]. Finally W will be joined to a structural heat sink material, that will most likely contain copper and therefore the joined part should operate at lower temperatures, so as to not cause damage to the copper [25], [115]. It is for this reason that ductilising techniques are being pursued in W. Three main methods of ductilization have been pursued as part of the EFDA[5] programme, including alloying, nanostructuring and the production of composites (see section 2.2.1). The only element that has been seen to improve

[5] European Fusion Development Agreement

ductility of W via solid solution is Re [28], [116]. DFT (density functional theory) calculations have shown that this is due to the fact that addition of Re results in a reduction in the Peierls stress, σ_P, a change in the core symmetry and additionally the number of slip planes increases [117]–[119]. However, this increase in ductility only holds true if the W is non-irradiated or has been damaged to low levels below 0.4 dpa. As can be seen in Figure 2.6, even after damage of only 0.4 dpa, it has been observed that the hardness increase in neutron irradiated W-3-5%Re is greater than in pure W [25], [67], [68]. Additionally Re addition has been shown to result in a greater increase in the DBTT in comparison to W at doses of ~0.4 dpa, as observed in Figure 2.7 [69].

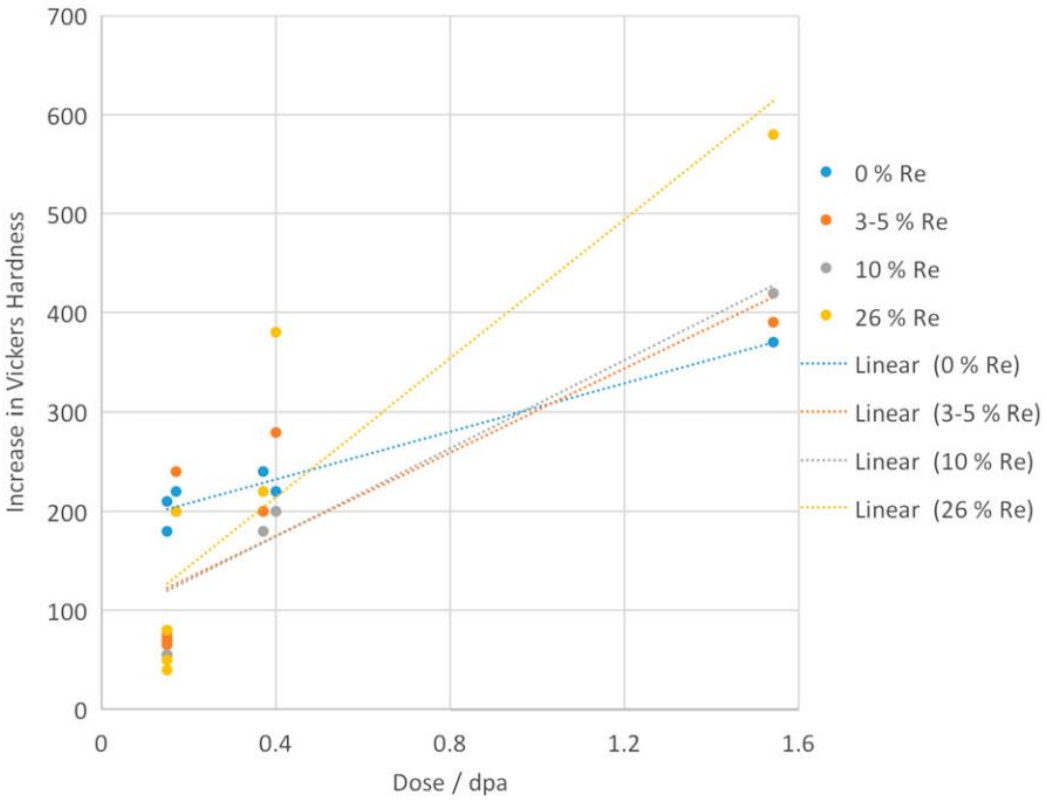

Figure 2.6: Vickers hardness increase of W-xRe with neutron dose at different temperature ranges, taken from [25], using data from [67], [68].

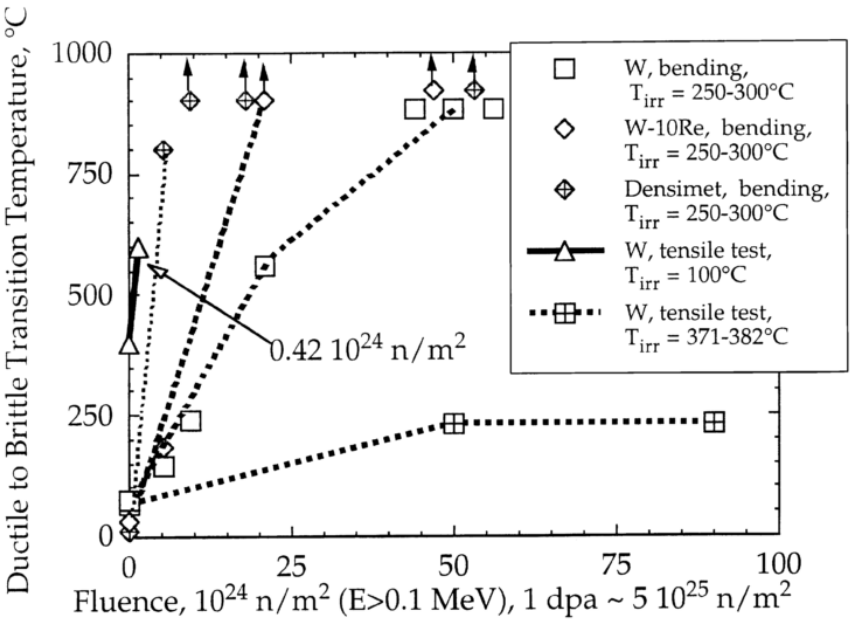

Figure 2.7: Effect of neutron irradiation on DBTT of W, W3.4Nil.6Fe (Densimet) and W-10%Re taken from Barabash *et al.* [69].

2.3 Irradiation Damage

As has been shown in Equation 2.1, one of the products of the D-T reaction is a 14 MeV neutron. As neutrons have no charge, they are not confined by the magnetic field that confines the plasma in the tokamak, meaning they will bombard and penetrate the walls of the reactor. The 14 MeV neutrons will result in significant damage to materials, mainly cascade damage as well as transmutation. These result in changes to microstructural properties and consequently material properties, which is of critical importance for a nuclear fusion reactor. The time and length scale of the 14 MeV neutron damage process is summarised in Figure 2.8 [31]. The initial damage occurs at very short time and length scales, and then accumulates over time resulting in larger defects that influence material properties at longer time scales. Therefore a variety of techniques are required in order to understand the mechanism of damage. At the smaller length and time scales, modelling is used extensively in order to try and elucidate the damage mechanisms. This includes density functional theory (DFT) at the smallest length and time scales [120], producing results that feed

into molecular dynamics simulations, which are used to simulate collision cascades, and operate on the nanometre length and picosecond time scales [111]. At higher time and length scales, Monte Carlo methods are employed. SRIM (Stopping and Range of Ions in Matter) is a Monte Carlo code that is extensively used to model ion irradiation experiments and compute displacements per atom[121]. There are 27 000 experimental data points and more than 500 plots that indicate the accuracy of SRIM [122]. At the micro- to millisecond time and micrometre length scales, rate/field theory models or dislocation dynamics are used, followed by continuum and fracture mechanics and thermodynamics in the milli- to kilosecond time and micro- to millimetre length scales. Finally for macroscopic modelling, finite element analysis is utilised [31].

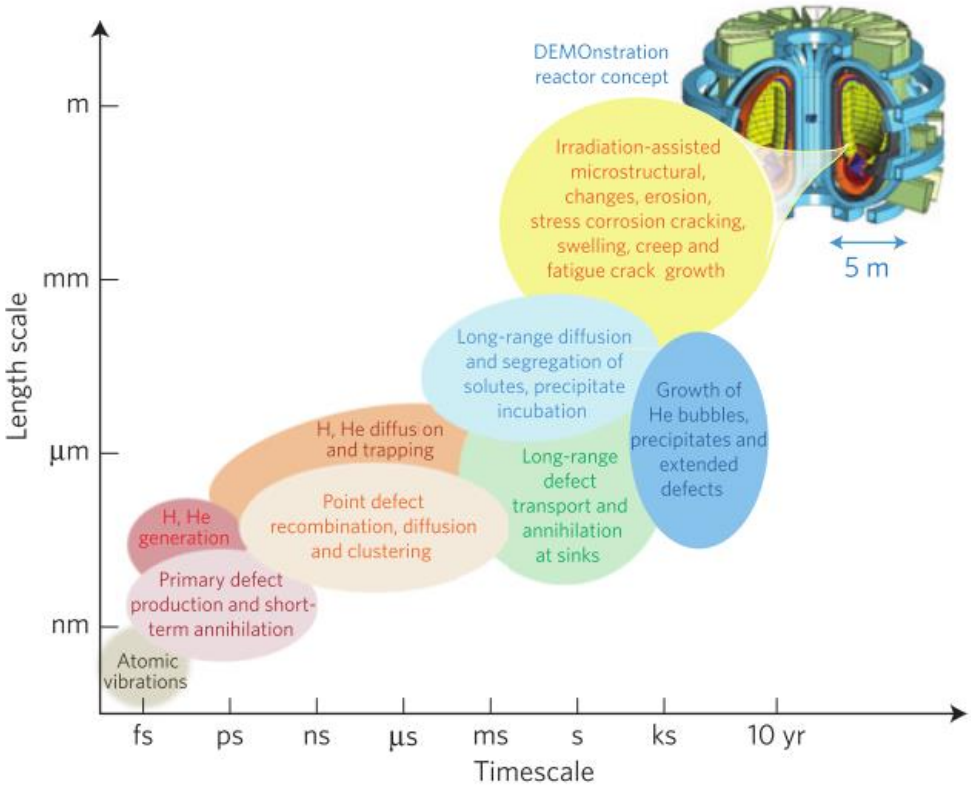

Figure 2.8: Time and length scale dependence of the 14 MeV neutron radiation induced damage processes in PFMCs in a fusion reactor that effect microstructural and material properties, taken from Knaster *et al.* [31].

2.3.1 Cascade Damage

When a neutron (or an ion) first collides with an atom within a material, at energy greater than the displacement threshold energy of the material, an atom, known as the primary knock-on atom (PKA) is displaced from its lattice site, resulting in a vacancy. The PKA generation, tends to occur in less than a fs (10^{-15} s) [31], [123]. The displacement threshold varies for different materials [124]. This collision can be either elastic or inelastic [31], [125]. A schematic of the irradiation process is shown in Figure 2.9 [31].

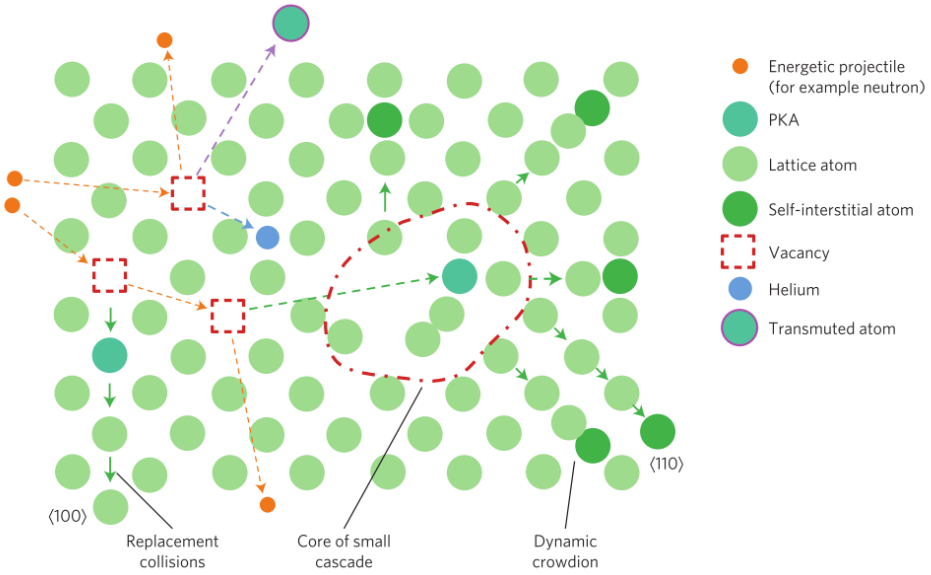

Figure 2.9: A schematic of irradiation damage taken from Knaster *et al.* [31].

After an initial elastic interaction the PKA can dissipate energy in a quasi elastic manner. The energy of the PKA is lost through excitation of electrons within the medium, however, this is a small amount. The majority of the energy is dissipated through nearly elastic collisions with nearby atoms within the material [31], [123]. In the quasi-elastic collisions, the energy is nearly conserved and the kinetic energy of the incident PKA is almost equal to the kinetic energy of the target atom and projectile atom post collision [123]. While the PKA has an energy greater than the

threshold displacement energy of the material it can continue to displace further secondary atoms, and additionally while the secondary atoms have a high enough energy, they can also cause further displacements within the lattice. This results in a tree-like damage cascade. These displacements will continue, until the energy of the PKA and secondary atoms fall below the displacement threshold, where they will then remain as interstitials (this occurs within ~100 fs) [31], [123]. Following this, migration and recombination of some of the interstitials, vacancies will occur, with some point defects also remaining. Some of the defects will also cluster, which results in microstructural features that affect the physical properties of the material, such as dislocation loops and voids [123]. This occurs in the ps to s or greater timescale [31], [123]. The type of defect created is dependent on the material, the irradiation particle type, the dose, dose rate and temperature.

In the inelastic collisions, the target nucleus remains in an excited state [126], resulting in the incident neutron and the PKA having a greatly reduced kinetic energy [31]. Inelastic collisions can result in the transmutation of material and this is an extremely important factor to consider when selecting fusion materials. Typically transmutation can occur via (n,γ), (n,p), (n,np) and (n,α) reactions (i.e. reactions where an incident neutron results in the emission of a γ ray, a proton, a neutron and a proton, and an α respectively) [31]. Due to transmutation, phase changes may occur. Additionally, He particles can build up and cause embrittlement [127].

Neutron Fluences in ITER

Zinkle and Snead calculated expected fast neutron fluences for components in ITER and DEMO, using data from Sawan [83]. These are shown in Table 2.1. It can be seen that the fluences are highest in the blanket and divertor regions in both ITER and DEMO, and that the expected fluences will be higher in DEMO than ITER for

all components. There will also be variations in fluence across the same component, for example the divertor, as the geometry is quite complex (Figure 2.10).

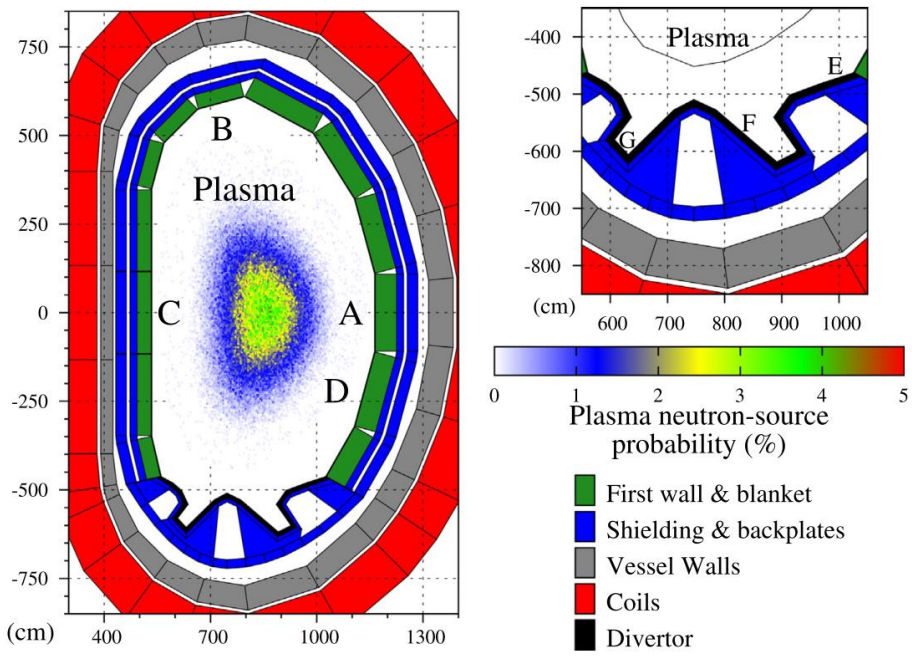

Figure 2.10: Homogeneous DEMO model used for MCNP (Monte Carlo N-Particle) simulations to obtain neutron fluxes and spectra [33].

Table 2.1: Calculated fast neutron fluences for components in ITER and DEMO based on input from Sawan, taken from [83].

Component	**ITER: lifetime fast neutron fluence (n/m^2; E>0.1 MeV)**	**DEMO fusion power reactor: annual fast neutron fluence (n/m^2; E>0.1 MeV)**
Blanket	3.7×10^{21}	5×10^{22}
Magnet	5.1×10^{14}	7×10^{15}
Divertor	1.9×10^{21}	2.6×10^{22}
Vacuum Vessel	1.1×10^{19}	1.5×10^{20}
Cryostat	3.4×10^{11}	4.5×10^{12}

Quantifying Cascade Damage

In order to correlate the dose a material is exposed to following irradiation by different particles, the unit of displacements per atom or dpa was developed. Initially Kinchin and Pease suggested that following fast neutron irradiation, secondary collisions between interstitial atoms that were moving and stationary atoms within the lattice of a material would result in the formation of a vacancy and interstitial

[128]. Permanent displacement of atoms could only occur if the energy imparted on the displaced atom exceeded the threshold displacement energy. The displacement energy varies with material, direction of displacement and temperature [129]. The number of displacements generated by PKAs with energy, T, was defined (Equation 2.5, Figure 2.11).

Equation 2.5

$$\nu(T) = \begin{cases} 0 \; for \; T < E_d \\ 1 \;\; for \; E_d < T < 2E_d \\ \dfrac{T}{2E_d} \; for \; 2E_d < T < E_c \\ \dfrac{E_c}{2E_d} \; for \;\; T \geq E_c \end{cases}$$

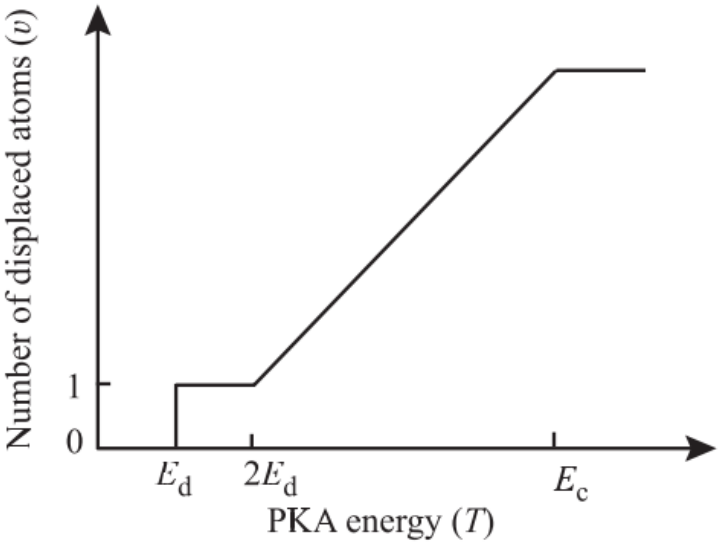

Figure 2.11: Kinchin Pease model, showing number of displacements vs PKA energy, taken from [130].

E_d is the displacement threshold energy and between this energy and $2E_d$ there is a probability that one atom will be displaced, at energies between $2E_d$ and the cut-off energy, E_c, $\frac{T}{2E_d}$ atoms will be displaced and at energies greater than E_c (where energy

loss from electronic stopping occurs) the number of displacements remains constant, at $\frac{E_c}{2E_d}$ [128], [130].

Norgett, Robinson and Torrens (NRT) then expanded the Kinchin Pease model [131]. They defined the number of Frenkel pairs, $\nu(T)$ induced by a PKA, with initial energy, *T* as illustrated in Equation 2.6.

Equation 2.6

$$\nu(T) = \frac{0.8\hat{E}}{2E_d}$$

$\hat{E}$ is the available energy for the generation of atomic displacements via collisions that are elastic and E_d is the threshold displacement energy. In order to obtain the NRT dpa, the number of Frenkel pairs is divided by the number of atoms in a certain volume. Currently the standard measure of irradiation damage is dpa, however care must be taken when using it due to the fact it doesn't not take into account migration, coalescence and recombination of defects [31].

A more complete picture of damage that takes into account other influences can also be developed (Equation 2.7) [130]. If we divide *R* by *N* we get dpa/s.

Equation 2.7

$$R = N \int_{\check{E}}^{\hat{E}} \int_{\check{T}}^{\hat{T}} \varphi(E_i)\sigma(E_i, T)\nu(T) dT dE_i$$

R is the number of displacements/cm^{3}s. *N* is the atom number density, $\hat{E}$ and $\check{E}$ are the maximum and minimum energies of the incoming particles respectively, $\varphi(E_i)$ is the energy dependant particle flux, $\hat{T}$ and $\check{T}$ are the maximum and minimum energies transferred in a collision with a particle with energy, E_i and an atom in the lattice,

$\sigma(E_i, T)$ is the cross section for the collision of a particle with energy E_i that causes an energy transfer, T to the target atom, and $\nu(T)$ is the number of displacements resulting from a primary knock-on [130].

2.3.2 Transmutation

Neutron capture reactions result in transmutation of the target material to different elements [126]. The transmutation typically occurs through *(n,γ), (n,p), (n,np)* and *(n,α)* reactions [31]. The typical pathways specifically for Re and Os generation in W are given in Equation 2.8.

Equation 2.8: Main pathways for Re and Os generation [132]

$$^{186}W(n,\gamma)^{187}W \rightarrow (\beta-)^{187}Re \begin{cases} (n,\gamma)^{188m}Re \rightarrow (\gamma)^{188}Re \rightarrow (\beta)^{188}Os \\ (n,2n)^{186}Re \rightarrow (\beta-)^{186}Os \end{cases}$$

$$^{184}W(n,\gamma)^{185}W \rightarrow (\beta-)^{185}Re(n,\gamma)^{186}Re \rightarrow (\beta-)^{186}Os$$

For W, Gilbert and Sublet have calculated the expected transmutation in DEMO after 5 full power years using the FISPACT inventory code. This has predicted the transmutation of pure W to W-3.8%Re-1.4%Os, as well as 34 atomic parts per million (appm) He and 76 appm H [133]. However the concentration varies with the position in the divertor, and more significantly between the divertor and the first wall (Figure 2.10, Figure 2.12) [33]. A concentration of 2% (atomic) Re predicted after three years in region A of the first wall (FW) armour, and less than 1% after the same amount of time in region E of the divertor [33]. If we consider that in region A the dose is expected to reach 14.5 dpa/fpy (full power year), the appm/dpa ratio of Re comes out to ~460 appm/dpa [100]. In ITER the transmutation rates expected are much lower, and after 2 D-D (fusion of deuterium atoms) and 12 D-T (fusion of deuterium and tritium atoms) years of operation, W is expected to transmute to W-0.18%Re, with the additional formation of 1 appm of He and 2 appm of H [133].

From the phase diagram shown in Figure 2.13, the addition of Re should only result in the formation of the brittle σ or χ phases at concentrations above 30%, but as will be subsequently discussed (section 2.3.3.3) these phases have been observed at much lower concentrations following neutron irradiation [134].

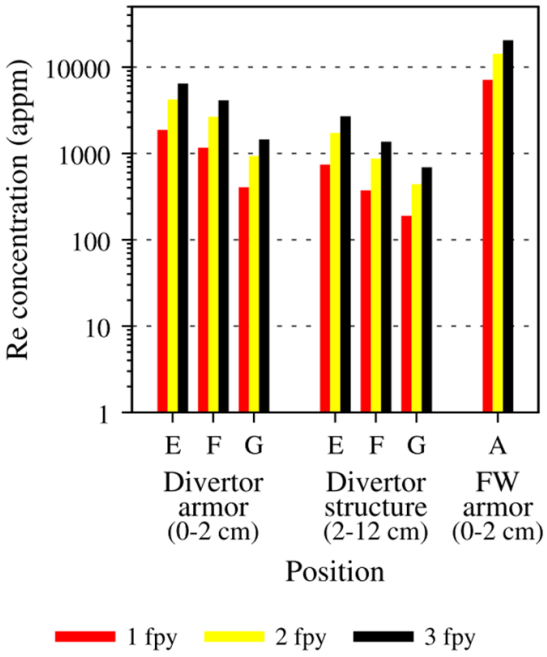

Figure 2.12: Variation of transmutation to Re in different positions in the DEMO reactor [33]. For locations of letters, refer to Figure 2.10.

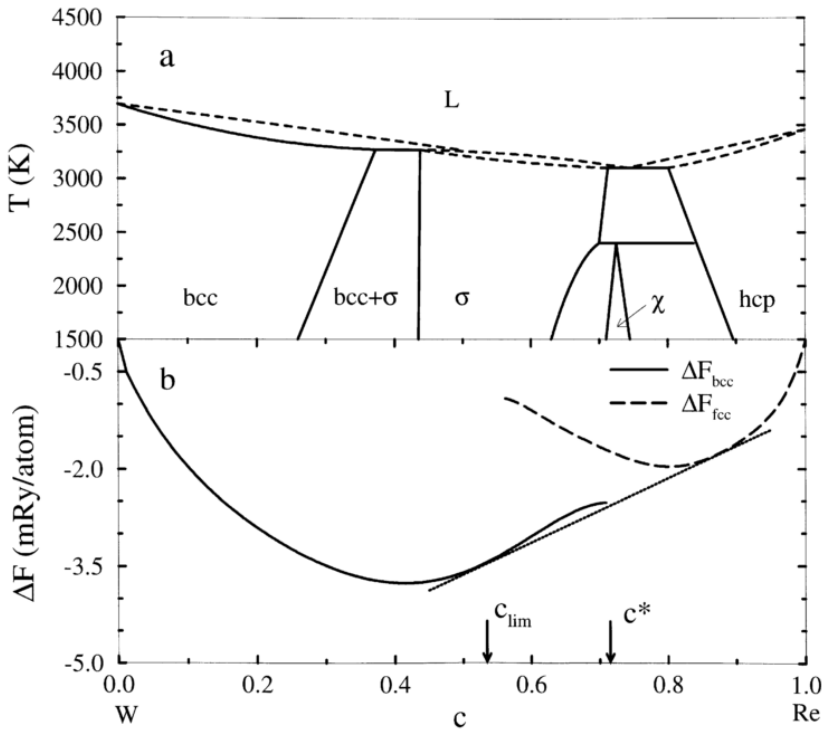

Figure 2.13: Experimentally determined phase diagram and Helmholtz energy curves derived from ab initio electron calculations for W-Re, taken from [135]

2.3.3 Irradiation Damage in Tungsten and Tungsten Alloys

2.3.3.1 Fusion Materials Testing Device

For decades there have been plans for building a dedicated fusion materials testing facility, producing 14 MeV neutrons via the use of an accelerator. Initially a design for the facility, IFMIF (International Fusion Materials Irradiation Facility), was proposed [136]. Following a re-evaluation of the regulatory approach required for the demonstration fusion device, DEMO, it was determined that a lower specification, lower risk neutron source, referred to as FAFNIR (FAcility For Neutron Irradiation Research) would be able to generate data on materials required for DEMO [137]. However, presently it is not clear when or if either of these facilities will be built, and it is for this reason that several alternative, methods to simulate fusion damage are being pursued.

2.3.3.2 Particles Used to Simulate Fusion Damage

Typically four different types of particle are used to induce irradiation damage in materials in order to study irradiation damage mechanism and effects for fusion applications, and these are electrons, protons, heavy ions and neutrons. Relevant to this thesis are protons, heavy ions and neutrons. A brief overview will now be given of issues in comparing different types of irradiation experiments with these three methods, followed by the history of these approaches in more detail as related to tungsten specifically . A basic comparison of the damage profiles of the three particle types in stainless steel are shown in Figure 2.14.

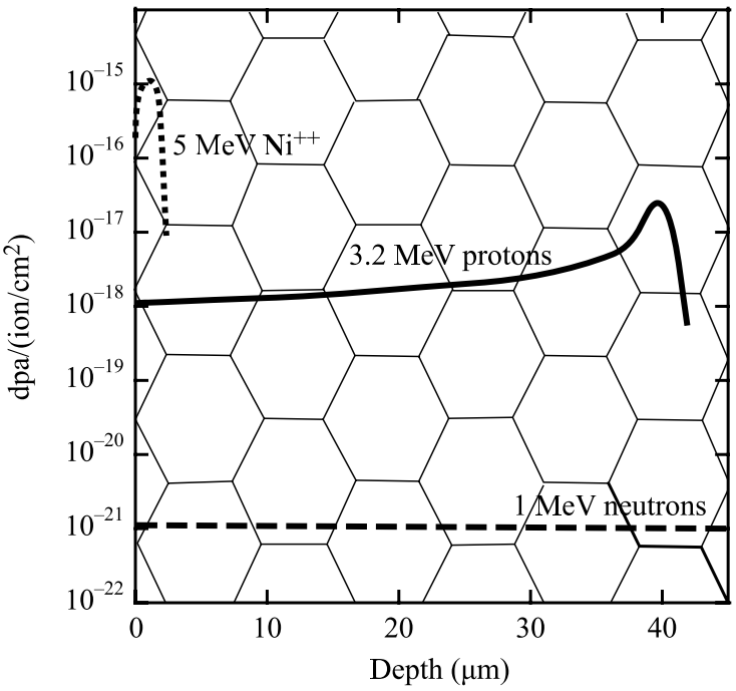

Figure 2.14: The damage profile created by 5 MeV Ni^{++} ions, 3.2 MeV protons and 1 MeV neutrons in stainless steel, taken from [138].

Neutron irradiations result in damage that can penetrate 10s of centimetres into W [33], and the damage profile is fairly flat across the micrometre length scale (Figure 2.14) [125], however over the range of centimetres, the damage is highest close to the surface and then decreases as the neutron travels through the material, losing energy with increased depth (Figure 2.15) [33]. The cascades produced by neutron

irradiation are dense [125]. Neutron irradiation experiments are costly and require time scales of the order of years to achieve high dose levels. Additionally current fission neutron sources do not have the same spectrum as that expected in a fusion reactor (Figure 2.16), resulting in differences in the damage processes observed [33]. The displacement cross section for 14 MeV fusion neutrons is ~4 times greater than that of 1 MeV fission neutrons [129]. Furthermore due to activation of material, analysis often requires small specimens and special 'hot' facilities. The PKAs generated by 14 MeV neutrons could achieve energies up to 1 MeV [139] and an average value of 150 keV in W [140]. However, in typical fission reactors, the energy of only 2% of the PKAs is >200 keV [141]. The energy losses for the 1 MeV PKAs are approximately equally due to nuclear and electronic scattering [139]. A comparison of a recoil cascade from a 20 keV fission neutron and 200 keV fusion neutron in iron is shown in Figure 2.17. As a result of the dense damage cascades, there is extensive recombination of defects in the cooling phase of irradiation [130].

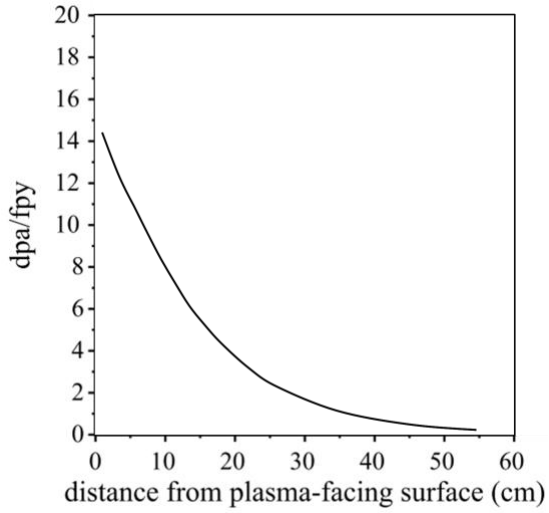

Figure 2.15: dpa/fpy values vs distance from plasma facing surface into the outboard equatorial first wall for pure W (labelled A in Figure 2.10), calculated using the W-TENDL 2011 nuclear data library. Redrawn from [33].

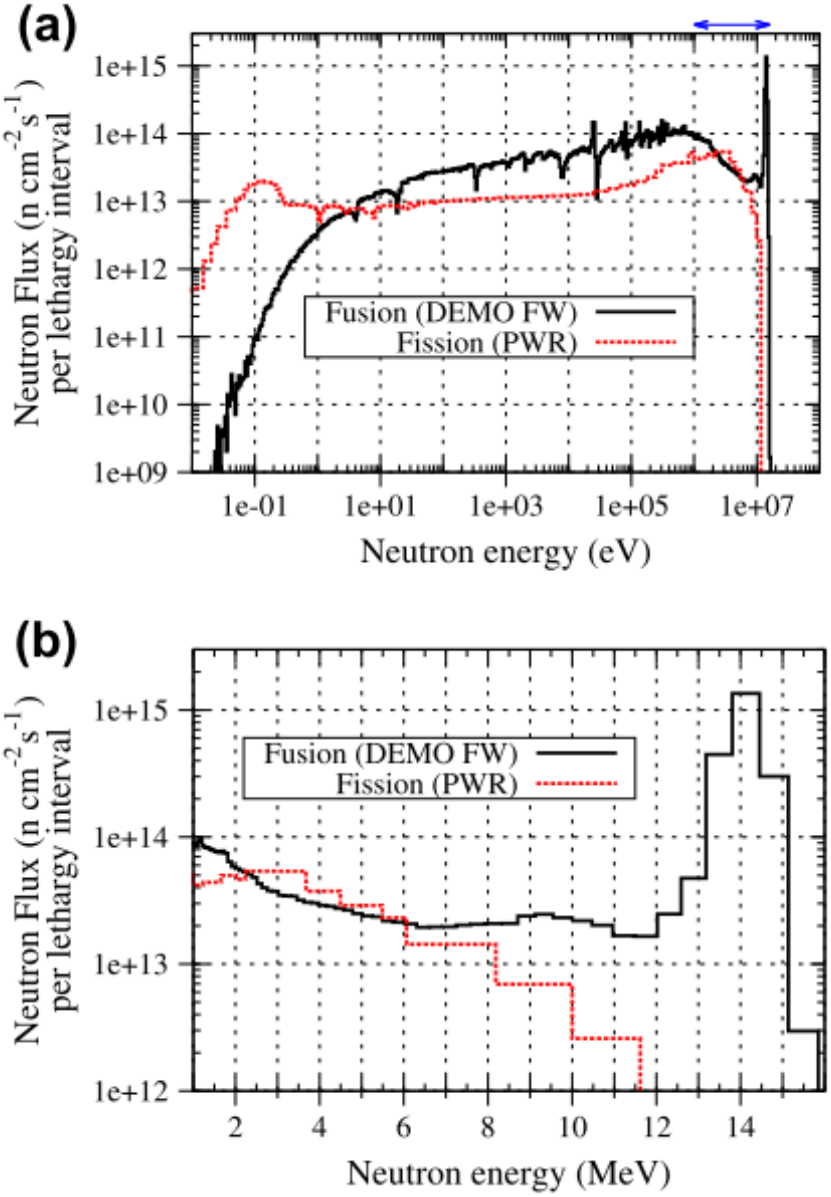

Figure 2.16: Neutron flux spectra for future fusion reactor (DEMO) and PWR fission reactors, taken from Gilbert *et al.* [33]. The full range is shown in a), and b) shows the range defined by the blue arrow in a).

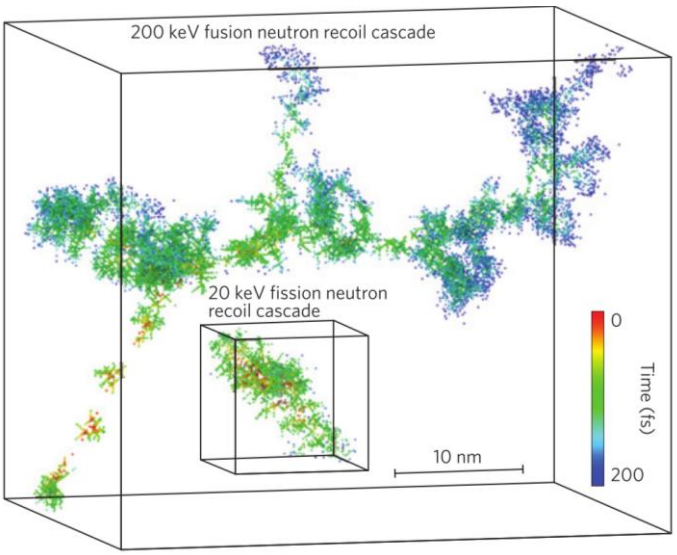

Figure 2.17: A comparison of a 20 keV fission neutron cascade and a 200 keV fusion cascade in pure iron calculated using molecular dynamics by Sand and Nordlund, taken from [31]. The colours of the atoms represent the times when the kinetic energy of the atoms exceeds 5 eV. The fusion damage cascade occurs within ~200 fs, compared to 100 fs for the fission cascade.

Molecular dynamics has been used to study cascade damage in W (Table 2.2, Figure 2.18) [142] up to PKA energies of 150 keV [111], [140]. The simulations indicated that at 150 keV the cascades would not break up into sub cascades [140]. The variation of defects with increased PKA energy is shown in Table 2.2. Large dislocation loops and complex clusters are formed after 300 fs. In the most compact regions of the cascade the largest self-interstitial atom (SIA) and vacancy type clusters are formed. SIA and vacancy type dislocation loops with Burgers vectors of $\boldsymbol{b} = \langle 100 \rangle$ and $\boldsymbol{b} = 1/2\langle 111 \rangle$ are formed in the debris of the cascade, which is in agreement with experiments by Yi *et al.*, where both $\boldsymbol{b} = \langle 100 \rangle$ and $\boldsymbol{b} = 1/2\langle 111 \rangle$ loops were observed [143].

Table 2.2: Number of Frenkel pairs (N_{FP}), size of largest vacancy ($\boldsymbol{Cl_{max}^{vac}}$), size of largest SIA cluster ($\boldsymbol{Cl_{max}^{SIA}}$), fraction of vacancies (F_{vac}) *and SIAs* (F_{SIA}) in clusters bigger than 4 and the total energy lost to electronic stopping (E_{ES}) [140].

T_c (eV)	N_{FP}	Cl_{max}^{vac}	Cl_{max}^{SIA}	F_{vac}	F_{SIA}	E_{ES} (keV)
1	122.2±2.9	5	54	0.00	0.47±0.03	82.5±1.2
5	182.8±27.9	118	164	0.21±0.07	0.71±0.07	47.6±0.65
10	179±21.0	96	175	0.19±0.06	0.72±0.06	42.9±0.6
20	183±18.1	72	94	0.16±.06	0.81±0.01	39.1±0.227
100	257±49.7	177	224	0.28±0.10	0.81±0.05	34.6±1.55

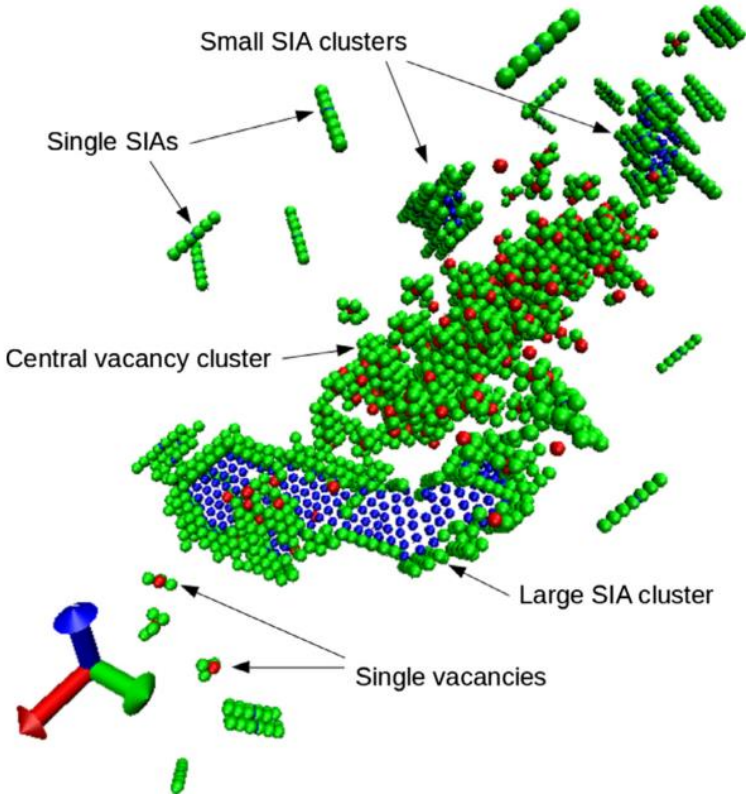

Figure 2.18: Spatial distribution of defects resulting from 150 keV PKA that extends ~35 Å in the ⟨**111**⟩ direction. Green spheres are W atoms with a potential energy that is >0.3 eV greater than the cohesive energy. Red spheres are vacancies and blue spheres are interstitials [140].

Heavy ion irradiations can be used to simulate the PKA and subsequent elastic collisions that occur during neutron irradiation and also result in dense damage

cascades [125], [129]. For bulk irradiations, typically energies greater than 1 MeV are used to mimic the PKAs generated by fusion neutrons most closely [144]. There is significant recombination of these dense cascades in the cooling phase of the irradiation. The heavy ions can only penetrate distances of the order of nanometres and microns into the surface (Figure 2.14). This is because heavy ion irradiations have an elastic scattering cross section that can be more than 6 orders of magnitude greater than the 10^{-24} cm^2 cross section typical for fast neutrons. This results in the mean free path between collisions in fast neutrons (order of centimetres) to be much greater than that for heavy ions (depending on energy and material, could be as low as 100 Å) [144].

Unlike neutrons, heavy ions are charged so they will interact more with the other atoms. The damage profile always has a peak and the damage is non-uniform, as the nuclear and electronic losses occur at varying amounts as the ions penetrate the sample [125]. The advantage of heavy ion irradiations is that there is no sample activation, allowing for analysis straight after the exposures. However, heavy ion irradiation does not result in transmutation as has been observed in neutron irradiations, and therefore either alloys containing the expected transmutation products are irradiated, or sequential or dual beam irradiations are required to recreate these effects [145], [146]. Due to the small samples involved, microscopy studies are commonly used to analyse the irradiation damage. In order to determine material properties, specialised techniques are required to analyse such small samples. Heavy ion irradiations can achieve high doses in time scales of the order of hours. The disadvantage of such a high dose rate is that a temperature shift (i.e. the higher the dose rate you are using, the higher the temperature increase required to achieve the same defects as achieved using a lower dose rate) is normally required in

order to induce the same defects as a neutron experiment [147]. However this shift is often dependent on the type of microstructural defect (swelling, loops, voids, RIS etc) you are looking to reproduce in the ion irradiation experiment. Additionally, there may be some variations in damage induced at different temperatures, which may make it difficult to compare heavy ion experiments to neutron ones [130].

Protons are much lighter than heavy ions. The damage cascades thus produced are very different to those generated by heavy ions. The recoil energy is lower and the damage cascades are smaller and more spaced out (i.e. small clusters) [125]. Isolated Frenkel pairs are also produced [125]. Therefore during the cooling phase there is less recombination of defects following proton irradiations in comparison to heavy ion irradiation [130]. The issue of temperature shifts still remains for proton irradiations, as the dose rates are still higher than those used in neutron irradiations [125]. The depth of damage is greater than that of heavy ions, but still of the order of microns and 10s of microns. The damage profile varies fairly slowly with depth into the sample at shallow depths and is then characterised by a large Bragg peak close to the final depth of penetration of the protons (Figure 2.14). The disadvantage of proton irradiation is that sample activation can occur, as the Coulomb barrier can be overcome at a few MeV for light ions [125].

2.3.3.3 Neutron Damage

Variation in Spectra

The neutron flux spectra for the fuel assembly of a 3.8 GW PWR (Pressurised Water Reactor) fission reactor and in the first wall of the 3 GW concept DEMO fusion reactor are shown in Figure 2.16 [33]. As can be seen the fluxes are much higher in the fusion spectrum at high energies in comparison to the fission spectrum, and additionally there is a peak at 14 MeV which is not observed in the fission spectrum.

This results in an increase in the dose in terms of dpa as well as a greater probability of threshold nuclear reactions [33]. At present there is no dedicated 14 MeV neutron source, so the only neutron damage experiments that have been conducted to date have utilised fission neutrons. As may be observed in Figure 2.19 [130], within different fission reactors there is also a significant difference in the neutron flux spectra, with the HFIR (High-Flux Isotope Reactor) mixed spectrum reactor and the FFTF (Fast Flux Test Facility) fast reactor, two of the reactors that have been used to conduct neutron irradiation experiments in tungsten having very different spectra to each other, as well as the ITER first wall.

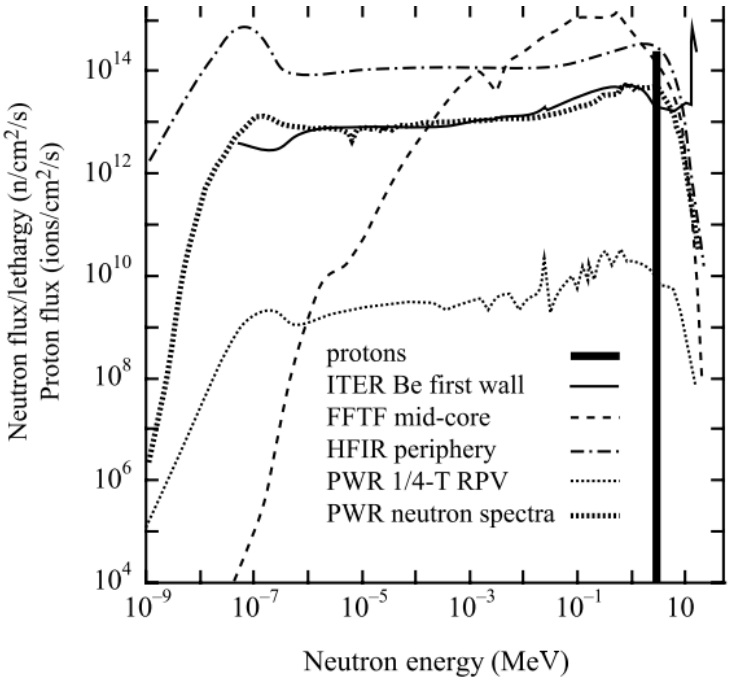

Figure 2.19: Energy spectra for neutrons for different reactors, as well as from protons from an ion beam, taken from [130].

2.3.3.3.1 Neutron Damage in W and W Alloys Using Fission Sources

Pre Fusion Studies

Although not for fusion applications, neutron irradiation experiments in tungsten were initially carried out in the 1950s-1970s. Thompson carried out neutron irradiations at the BEPO (British Experimental Pile 0) reactor at Harwell, a mixed

spectrum reactor (10^{12} $cm^{-2}s^{-1}$ thermal neutron flux and 0.3-1.2×10^{11} $cm^{-2}s^{-1}$ fast (i.e. neutrons with an energy of 1 MeV or above) neutron flux), at temperatures of -269 °C and -196 °C [148]. Via resistivity measurements, four stages of recovery were observed at -170 °C, between -170-350 °C, between 350-450 °C and above 450 °C. It was suggested that the migration of vacancies for W occurs at 400 °C and that the recovery process above -170 °C was due to the release of interstitials from traps around dislocation lines and impurities [148].

Resistivity measurements were also carried out by Keys and Moteff, which were used to identify the stages of recovery for W following neutron irradiation [149] [150]. The neutron irradiation experiments were carried out using fast neutrons, at temperatures of ~70 °C, at fluences from 8.5×10^{17} -1.5×10^{21} cm^{-2}. Three major stages of recovery were identified, at 0.15 (suggested this was due to the migration of self-interstitials), 0.22 (postulated that this stage was either due to migration of impurities and/or divacancies and/or the escape of interstitials from shallow traps) and 0.31 (suggested that this was due to migration of vacancies) of the melting point of tungsten in K. Additionally in these studies the transmutation of W to Re was also observed [149], [150].

The first studies on the effect of neutron irradiation on mechanical properties of W were also carried out in the 1970s. Steichen carried out the irradiation of W in the EBR-II reactor at Idaho National Engineering Laboratory, a fast reactor [151]. The W was irradiated to fluences between 0.4-0.9×10^{22} cm^{-2}, with neutron energies greater than 0.1 MeV, at temperatures of ~385 °C. Within this study the DBTT of W was observed to increase by 150 °C. Tensile tests were carried out at varying strain rates and temperatures post irradiation and it was observed that the yield strength of W increased with increased fluence, increased strain rate, and decreased

temperatures. Regardless of the test strain rate or temperature, the ductility decreased with increased fluence [151].

Irradiations in W-10%Re and W-25%Re in the same reactor carried out in the 1980s by Herschitz and Seidman up to a fluence of ~4×10^{22} cm^{-2} (an average of 8.6 dpa over 2 years) at temperatures between 575 °C and 675 °C showed the formation of WRe (σ) and WRe_3 (χ) phase precipitates via field ion microscope atom probe measurements in the W-10%Re and W-25%Re alloys respectively [152], [153]. In the case of the W-10%Re, it was also observed that Re addition supressed the formation of voids during irradiation of W with neutrons. It was suggested that this was due to a mechanism where by the recombination of vacancies and interstitials was the dominant process, as opposed to point defect destruction at dislocations (a biased sink). The recombination mechanism results in a reduced number of vacancies, leading to a suppression of voids, and additionally provides an explanation for the homogeneous nucleation of WRe precipitates observed via field ion microscope atom probe [152] . A mechanism was also suggested for the formation of the WRe_3 precipitate in W-25%Re whereby self-interstitials at the edge of displacement cascades react with Re atoms in order to produce a mobile mixed dumbbell. Two of the dumbbells can then react together, resulting in a di-Re cluster that is immobile, which will then itself react with a further dumbbell, producing a Re_3 which then reacts with a W self-interstitial, resulting in a WRe_3. It was postulated that these clusters will form precipitates via an irreversible vacancy:self-interstitial atom annihilation mechanism that had been previously suggested by Cauvin and Marvin [153], [154]. Although in previous experiments, voids had not been observed in W-25%Re irradiation experiments, in this experiment, 90 Å diameter voids were observed [153].

In summary:

- The recovery stages of W were identified. Keys and Moteff identified these as 0.15, 0.22 and 0.31 of the melting point of tungsten in K [149], [150]
- Tensile tests were carried out in neutron irradiated W (at ~385 °C and fluences of 0.4 and 0.9 $\times 10^{22}$ cm^{-2}), showing a decreased ductility with irradiation [151]. For example, following tensile tests at ~ 500 °C and a strain rate of 3×10^{-4} s^{-1}, a 7.2% elongation was observed in W irradiated to 0.9 $\times 10^{22}$ n/cm^2, in comparison to 10% for the non-irradiated material. The yield strength of W irradiated to 0.9 $\times 10^{22}$ n/cm^2 was observed to be ~950 MPa in comparison to 600 MPa for non-irradiated W [151].
- The DBTT was observed to increase post irradiation by 150 °C [151].
- Transmutation of W to Re was observed [149], [150].
- Following irradiation of W-Re alloys, WRe (σ) and WRe_3 (χ) phase precipitates were observed [152], [153]. After irradiation of W-10%Re up to fluences of ~4×10^{22} cm^{-2}, ~57 Å, disc shaped, σ phase precipitates were observed at a density of ~10^{16} cm^{-3} [152]. Following irradiation of W-25%Re up to the same fluence , ~40 Å diameter χ phase precipitates were observed with a number density of ~10^{17} cm^{-3} [153].
- In the case of the W-10%Re, it was observed that Re addition supressed the formation of voids during neutron irradiation (no vids were observed via field ion microscopy post irradiation) [152].

Investigating W for Future Fusion Devices

In the mid-1990s it was proposed that tungsten should be considered for the divertor in ITER [155]–[157], which resulted in further neutron irradiation experiments. These were carried out in both mixed spectrum and fast neutron reactors (JOYO fast

test reactor, mixed spectrum JMTR (Japan Material Testing Reactor) reactor, HFIR mixed spectrum reactor and the FFTF fast reactor) using W, W-Re and W-Re-Os alloys. The irradiations were carried out at temperatures between 373-800 °C and at doses between 0.15-11 dpa. These studies analysed the neutron implanted samples via the use of microscopy, resistivity tests and micro-hardness tests [67], [68], [119], [134], [158]–[164]. The dpa levels reached in these experiments are relevant to the 0.7 dpa expected at the end of operation of ITER [165]. However, from Monte Carlo simulations conducted by Gilbert *et al.* the dpa levels in DEMO are expected to be much higher (Figure 2.15) and could be ~14.5 dpa/fpy at the plasma facing surface of the equatorial first wall [33].

Hardening Studies

He *et al.* investigated hardening processes in pure W and W-Re alloys ranging in composition from W-3%Re up to W-26% Re in the JMTR mixed spectrum test reactor [68].The samples were irradiated up to levels of 0.15 dpa at temperatures between 600-1000 °C. The Re addition was seen to reduce the hardness increase, with the concentration of Re having little impact (Figure 2.20) [68].

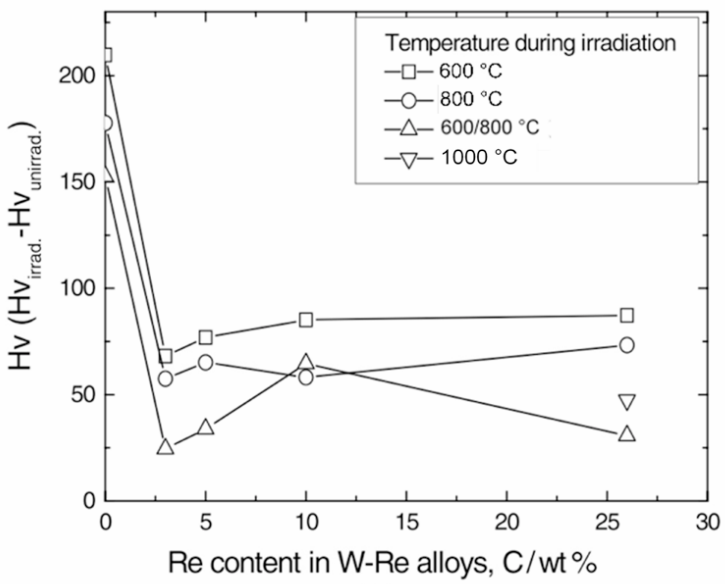

Figure 2.20: Vickers hardness increase of W and W-Re alloys irradiated to 0.15 dpa at temperatures between 600-1000 °C as a function of Re content. Taken from [68]

It was observed that the number density of dislocations, dislocation loops and voids was lower in the W-Re samples in comparison to pure W (Table 2.3). It was suggested that solute Re atoms resisted vacancy and interstitial migration, resulting in a reduction in the number of voids and dislocation loops. For the W-26%Re no voids or dislocation loops were observed at all, however some form of precipitates were observed at grain boundaries at 800 °C, suggesting that the neutron irradiation induced Re segregation. The precipitates observed however, were not the σ and χ phase that had been observed previously during irradiations at much higher dpa levels of ~8.6 dpa and 11 dpa [152], [153], [164].

Table 2.3: Radiation Damage in W and W-3Re irradiated at different temperatures, taken from [68].

Materials (Temperature during Irradiation)	**Voids**		**Swelling**	**Loops**		**Dislocations**
	Density 10^{22} m^{-3}	Radius nm	%	Density 10^{21} m^{-3}	Radius nm	Density 10^{14} m^{-3}
W (600 °C)	6.4	1.3	0.09	4.6	7.9	4.0
W (600-800 °C)	3.4	1.4	0.06	0.7	7.4	4.5
W(800 °C)	4.2	1.9	0.18	1.1	8.5	2.6
W-3Re (600 °C)	3.4	1.1	0.03	1.4	3.6	-
W-3Re (600-800 °C)	2.0	1.1	0.02	-	-	-
W-3Re (800 °C)	0.9	1.3	0.01	1.1	2.8	-

Additionally the hardness increase in the W-26%Re irradiated at 800 °C to 0.15 dpa was seen to be ~1/10 of that seen by Nemoto *et al.* at 11 dpa in the FFTF reactor at the same temperature, most likely due to increased transmutation and precipitate formation at higher doses [68], [164]. Although it should be noted that the FFTF is a fast reactor and the JMTR reactor is a mixed spectrum reactor, and there is variation in the flux spectra [166], therefore direct comparison may not be accurate.

Following this low dose investigation, Tanno *et al.* conducted a campaign in the JOYO fast reactor at dpa levels between 0.17-1.54 dpa and at temperatures between 400 and 750 °C [67], [134], [162]. Pure W as well as alloys of W-Re (5-26%), W-Os (3 and 5%), and W-Re-Os (5-25%Re, all with 3% Os, and 5%Re with 5%Os) were investigated in order to investigate the effect of transmutation products on mechanical property development during neutron irradiation [67], [134]. The initial Vickers hardness of the materials used is shown in Figure 2.21 [167]. Only the annealed materials were used for the irradiation experiments. The fluence of neutrons with energies above 0.1 MeV ranged between 1.3-12×10^{25} m^{-2}. Tanno *et al.* stated that even after 1.54 dpa the transmutation in W would be negligible, due to

the small transmutation cross section in JOYO [67], [134]. However, Abernethy suggested that this may not be a suitable assumption [25]. This is due to the fact it has been reported by Greenwood and Garner that within the Fast Flux Test Facility-Materials Open Test Assembly (FFTF-MOTA) that the transmutation rate/dpa is highly variable depending on the position within the reactor [168], [169]. Additionally transmutation had been observed previously within the EBR-II fast reactor, which could suggest that neglecting transmutation may not be accurate [170].

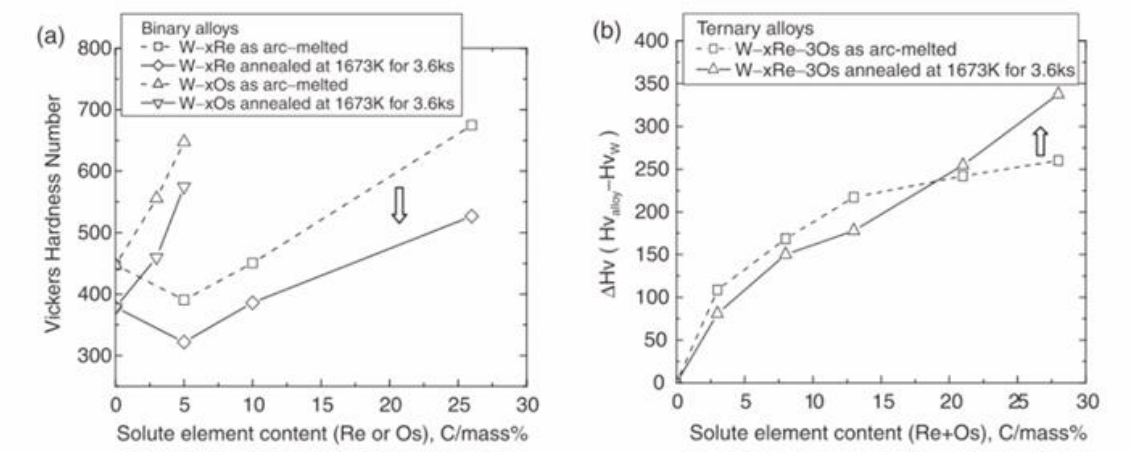

Figure 2.21: a) Vickers hardness of W-Re and W-Os alloys before and after annealing at1673 K for 3.6 ks. The arrow indicates annealing induced softening. b) Vickers hardness change of W-Re-Os alloys in comparison to pure W after annealing. The arrow indicates precipitate induced hardening. The alloys used in the irradiation experiments were all annealed material. Taken from [167].

Initially the W and W-Re alloys from the JOYO reactor are considered [67], [162]. At dpa levels of 0.17, 0.37 and 0.4 dpa, the Re addition has a negligible effect on the hardness increase. An exception is for the case of the W-26%Re irradiated to 0.4 dpa at 740 °C, which showed an increase in hardnessof~400 H_V in comparison to ~200 H_V in the pure W case [67]. This is unlike observations by He *et al.* at 0.15 dpa in JMTR, where it was observed that hardening decreased with the addition of Re, regardless of the Re concentration [68]. A comparison is conducted with an air of

caution due to the differences in the neutron flux spectrums in the JOYO fast reactor and the JMTR mixed spectrum reactor. This again highlights the strong effect neutron flux spectrum has on the observed changes. The W-26%Re irradiated to 0.17 dpa at 400 °C in JOYO showed a hardness increase of ~200 H_v [67] compared to an increase of ~100 H_v of the W-26%Re irradiated in the JMTR up to 0.15 dpa at 600 °C [68]. This fits in with the trend observed by He. *et al.* of increased hardening at reduced temperatures [68], however again the variation in neutron flux spectrum also needs to be considered.

At the higher dpa levels between 0.4 and 1.54 dpa, the change in hardness increases with increased initial concentration of Re [67], [162]. The increase in hardness between 0.4 and 1.54 dpa was slower at the higher temperature of 750 °C, in comparison to the hardness increase between 0.4 and 1 dpa at ~500 °C. For example the increase in W hardness for pure W at ~500 and 750 °C is ~350 and 320 H_V respectively, in comparison to the hardness increase for W-26%Re of ~850 and 600 H_V at ~500 and 750 °C respectively [162]. A summary of the pure W and W-Re hardness data is given in Figure 2.22.

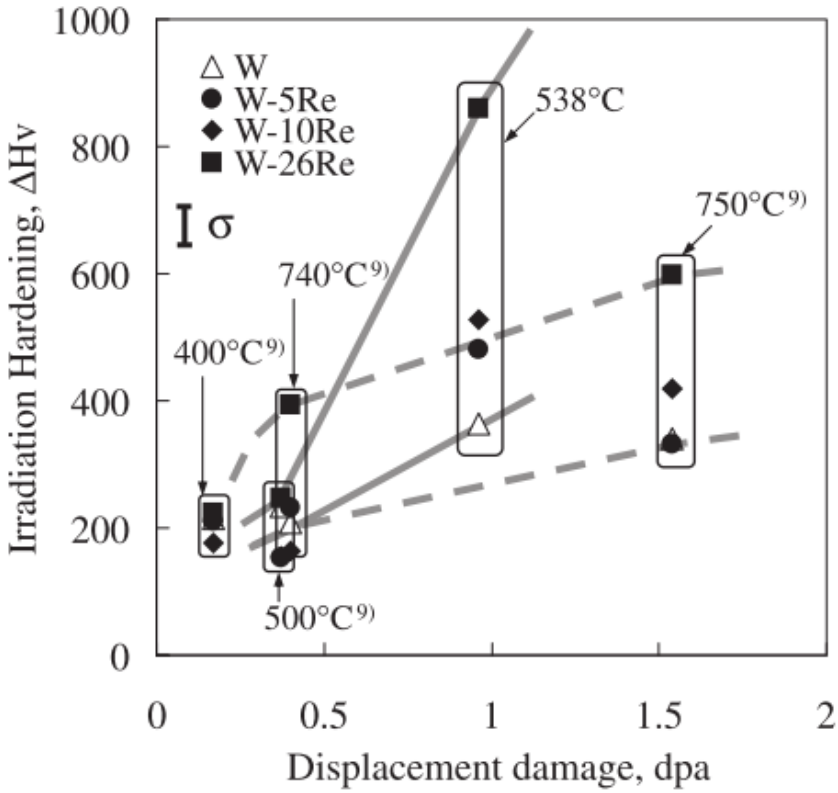

Figure 2.22: Summary of irradiation hardness data for W and W-Re alloys in JOYO reactor. The solid lines indicate the increase in irradiation hardening with dpa at ~500 °C and the dashed lines at 750 °C, taken from [162].

A summary for the hardness increase observed following irradiation for the W-xOs, W-xRe-3Os and W-5Re-xOs alloys is shown in Figure 2.23[67]. At dpa levels between 0.17 and 0.4 dpa, for the W-5%Os alloys, the hardness increase was ~3 times greater than that observed in the W-5%Re. The W-3%Os alloys showed similar levels of hardness increase to the W-5%Os alloys (~600 H_V increase). At 1.54 dpa, the hardness increase followed a similar trend with increasing Os content; however it was shifted up by ~150 H_v. In the case of the W-xRe-3Os alloys, for the lower temperature and dpa irradiations (up to 0.37 dpa, at temperatures between 400-500 °C), there appeared to be a decrease in hardness with increased Re concentration. For the 0.17 dpa irradiation, the hardness increase observed in the W-25Re-3Os alloy was ~0.6 of that seen in the pure W, and for 0.37 dpa irradiation it was about 0.8 of the pure W [67]. However, at 0.4 dpa and 1.54 dpa at temperature

of 740 and 750 °C, respectively, there was no clear trend on the influence of Re on the hardness change. The W-5Re-xOs alloys showed a similar trend of hardness increase at 0.37 and 0.4 dpa and temperature of 500 and 740 °C to the binary W-Os alloys, in that there was an increase in hardness with the addition of Os, but little variation between the hardness increase at 3 and 5%Os. For the irradiations at 0.17 dpa and 1.54 dpa, at temperatures of 400 and 750 °C, respectively, there appeared to be a more linear increase of hardness with Os concentration. The hardness increases in the W-5Re-xOs alloys was much greater than the W-5%Re alloy, for example the hardness increase of W-5Re-5Os following irradiation to 1.54 dpa is almost double that observed for W-5Re.

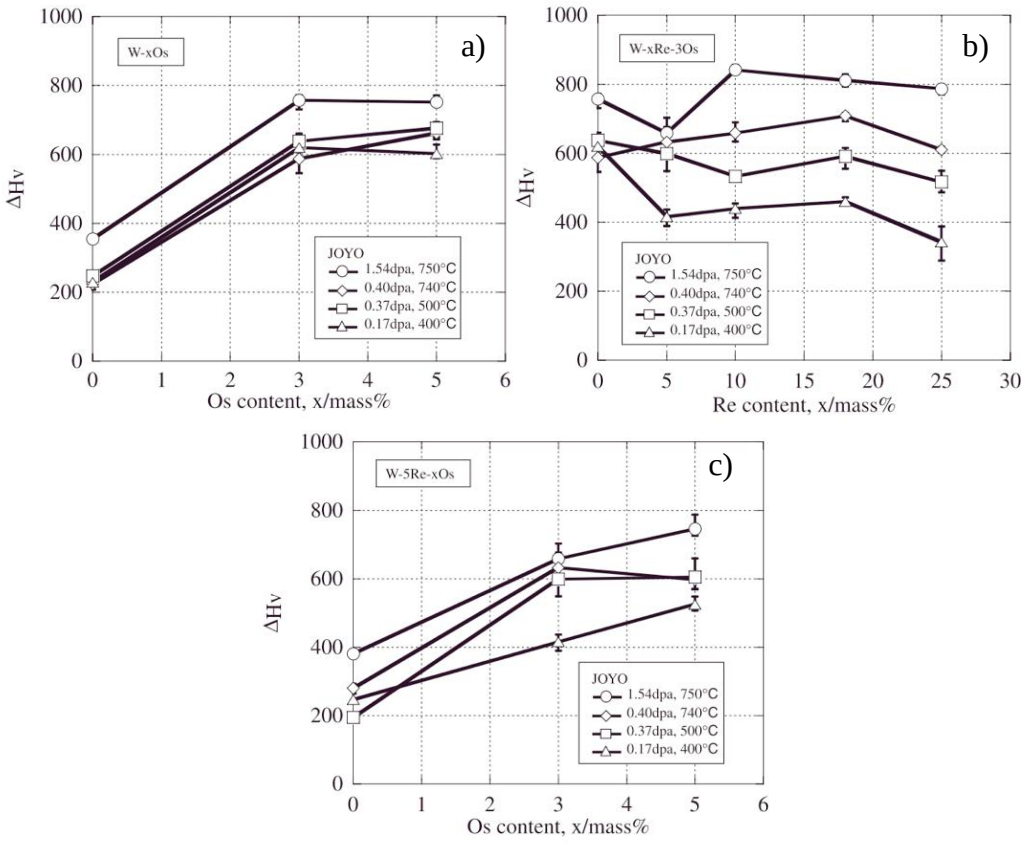

Figure 2.23: Change in hardness for a)W-xOs samples as a function of Os content, b) W-xRe-3Os samples as a function of Re content and c) W-5Re-xOs samples as a function of Os content irradiated between 0.17-1.54 dpa at temperatures between 400-750 °C in the JOYO reactor [67].

The hardening observed in the pure W was much lower than the alloys and there was not a massive increase in hardness with increased dpa [162], which correlates to the void formation mechanism observed via TEM (Figure 2.24, Figure 2.25). There is little difference between the hardness increase at 0.96 dpa and 1.54 dpa. After 0.96 dpa at 538 °C, out of all the irradiated samples, this sample had the greatest void number density (Table 2.4) [162].

Table 2.4: The number density and size of irradiation induced defect clusters in W and W-10%Re following irradiation in the JOYO reactor. ΔH_V (Calc.) and (Meas.) are the change in Vickers hardness post irradiation obtained via calculations based on microstructure and by measurement respectively [162].

			N (10^{22}m^{-3})	d (nm)	$(Nd)^{1/2}$ (10^{6}m^{-1})	ΔH_V (Calc.)	ΔH_V (Meas.)
1.54 dpa 750 °C	W	Void	12.0	4.7	23.8	355	341
	W-10Re	Void	3.1	1.6	7.0	104	419
		Prec.	41.7	9.5	62.9	422	
0.96 dpa 538 °C	W	Void	48.7	2.1	32.1	478	363
		Loop	4.7	4.7	14.9	74	
	W-10Re	Loop	<0.2	~5	<2	<10	528
		Prec.	83.7	6.8	75.6	507	

Additionally after 1.54 dpa at 750 °C, a void lattice was observed in the pure W, indicating that there can be a saturation in damage due to void formation in pure W [67]. Voids that were less than 2 nm in diameter were observed to not contribute to irradiation hardening [162]. The observation of a void lattice is also consistent with observations by Sikka and Moteff in 1972, who irradiated W in the EBR-II fast reactor at a temperature of ~550 °C, to a fast neutron fluence of 1×10^{22} cm^{-2} [171]. Additionally it may be observed from Figure 2.22, that the effect of temperature on the irradiation hardness behaviour was not as severe as that observed for W-Re alloys [162].

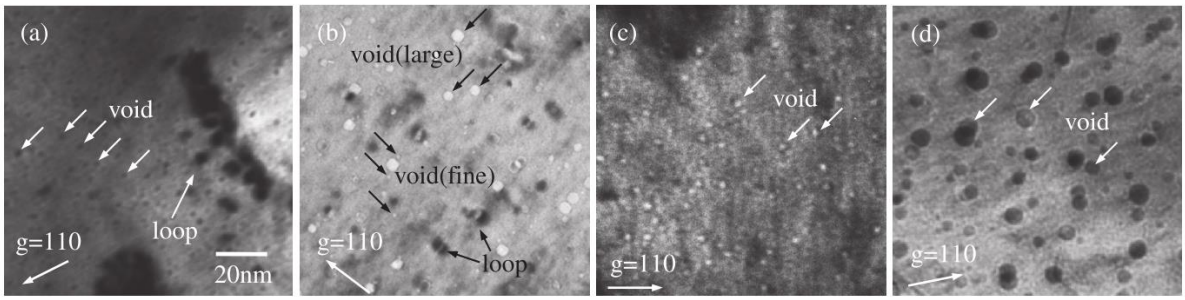

Figure 2.24: Voids observed via TEM in pure W irradiated to a) 0.17 dpa at 400 °C, b) 0.96 dpa at 538 °C, c) 0.4 dpa at 740 °C and d) 1.54 dpa at 750 °C. Images a) and d) are taken in over focused condition. Images taken by Tanno *et al.*[162].

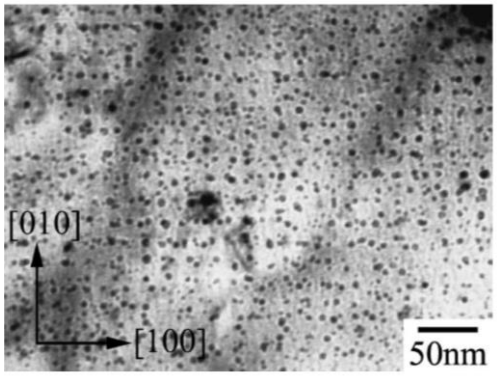

Figure 2.25: Void lattice observed via TEM in irradiated W after 1.54 dpa at 750 °C, taken by Tanno *et al.* from [67]**.**

Microscopy Studies

Nemoto *et al.* carried out neutron irradiation experiments on W-26%Re alloys in the FFTF fast reactor. Although this Re percentage is much higher than would be expected in ITER or even a DEMO fusion reactor, at this time W-Re alloys were also being considered as divertor materials, due to the increased ductility of non-irradiated W-Re over pure W [164], [172]. The irradiations were carried out at fluences of up to ~1×10^{27} m^{-2}, where the neutrons had energies greater than 0.1 MeV in a He atmosphere. The range of dpa achieved was between 2 and 11 dpa and the temperatures at which irradiation occurred were between 373 and 800 °C. It was interesting that although voids had been previously observed in W-25%Re irradiated up to levels of ~8.6 dpa by Herschitz and Seidman [153], Nemoto *et al.* did not observe voids, and additionally did not observe dislocations or dislocation loops.

Both platelet type, χ (Re_3W), and equiaxed type, σ (ReW), precipitates were observed. The size of the precipitates was observed to increase with irradiation temperature. The χ phase precipitates were observed to increase from 10-35 nm from 373-800 °C, and the σ phase precipitates increased from 5-15 nm [164]. It was suggested that irradiation hardening and embrittlement could be due to the formation of the σ and χ phases. Due to the brittle nature of the precipitates, cracking could be instigated, and weakening of grain boundaries could occur if the precipitates were to form at grain boundaries. Additionally, matrix hardening could occur, particularly in the case of the χ phase precipitate. The χ phase was observed on the (011) plane and therefore would inhibit dislocation glide in the (110) plane, and as inhibition of dislocation glide has been shown to effect the DBTT [113], [114], this provides a mechanism by which embrittlement could occur [164].

He *et al.* subsequently did a study in pure W and W-Re alloys ranging in composition from W-3%Re up to W-26% Re in the JMTR mixed spectrum test reactor [68].The samples were irradiated up to levels of 0.15 dpa at temperatures between 600-1000 °C. The fast neutron fluences achieved were between 3.7-3.8×10^{24} m^{-2}. Additionally some samples were irradiated at periodically varying temperatures of 600 and 800 °C. The samples were irradiated within a He-filled capsule. Dislocations, dislocation loops and voids were observed in neutron irradiated W and W-3%Re and the size and number density of the defects was seen to influence the irradiation hardening. Irradiation hardening was observed to decrease with increased temperature, with the number density of dislocation loops and voids also decreasing with increased temperature (Table 2.3), suggesting that at higher temperatures there is increased recombination of vacancies and interstitials that are created due to the irradiation [68].

The W samples irradiated at the periodically varying temperature had a much lower density of dislocation loops, compared to the single temperature irradiations at 600 °C and 800 °C, again suggesting increased vacancy/interstitial recombination [68]. This could be interesting for a future fusion reactor like ITER or DEMO, where there would be significant variations in temperature, either as a result of ELMS or the cooling down between pulses [68].

Void growth within pure W was also observed to be highly dependent on temperature, and was seen to occur when the irradiation temperature was approximately $3/10^{th}$ of the melting point of tungsten [68].

Microscopy analysis was carried out in the W, W, 5%Re, W-10%Re and W-3%Os samples irradiated to 1.54 dpa at 750 °C, as well as W-5%Re and W-10%Re irradiated to 0.96 dpa at 538 °C in JOYO [67], [134]. The density of voids was significantly lower in the W-Re and W-Os alloys, in comparison to pure W and in addition thin needle like precipitates were observed in both alloy cases [67], [162]. In the W-Os alloys, it was suggested that these were WOs, σ precipitates (Figure 2.26), and they aligned along the {110} plane [160]. In the W-Re alloys these were identified as χ phase precipitates [162]. The number density of χ phase precipitates was less in the 1.54 dpa, 750 °C irradiated sample in comparison to the 0.96 dpa, 538 °C sample, and they were coarser in nature (Table 2.4). This is mostly likely due to the increased vacancy and interstitial mobility at raised temperatures [162]. Furthermore, Herschitz *et al.* had previously observed Re depletion zones around precipitates in irradiated W-25%Re at temperatures between 575-675 °C [153]. At higher temperatures Re could move to the depletion zone from the matrix, resulting in the formation of large and coarse precipitates. It was suggested that this corresponds to the 750 °C irradiations in the Tanno experiment [162]. At lower

temperatures, the Re would not be able to migrate to the depletion zone, limiting precipitation growth. There would be nucleation of fine, dense precipitates [153]. This was said to correspond to the results from the 538 °C Tanno experiment [162]. The denser χ phase precipitates observed at 0.96 dpa, 538 °C, corresponded to higher hardness increases, in comparison to the 1.54 dpa, 750 °C sample [162].

Again it was suggested that Re supressed void formation due to reduced SIA mobility and increased vacancy/interstitial recombination [162]. The χ phase precipitates were observed on the {110} planes. The small number of precipitates observed in the W-Os alloys did not explain the much larger hardness increase observed in the W-Os alloys, in comparison to pure W or W-Re and additionally as only a few voids were observed in the W-Os, it was suggested that perhaps another mechanism may affect irradiation hardening in W-Os alloys [160]. Equiaxed, σ phase precipitates were also observed in the W-10%Re, and W-5%Re irradiated to 1.54 dpa at 750 °C [162]. TEM images of the precipitates in irradiated W-Re are shown in Figure 2.27.

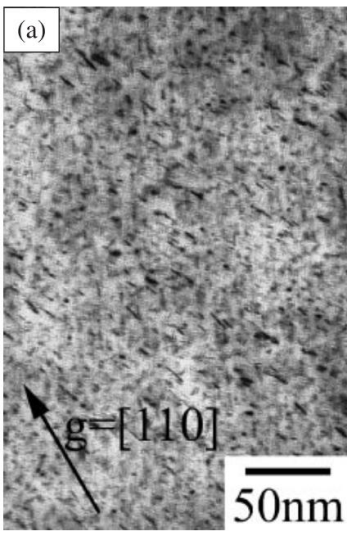

Figure 2.26: TEM of thin, needle-like precipitates observed in W-3Os irradiated to 1.54 dpa at 750 °C, taken by Tanno *et al.* [67]

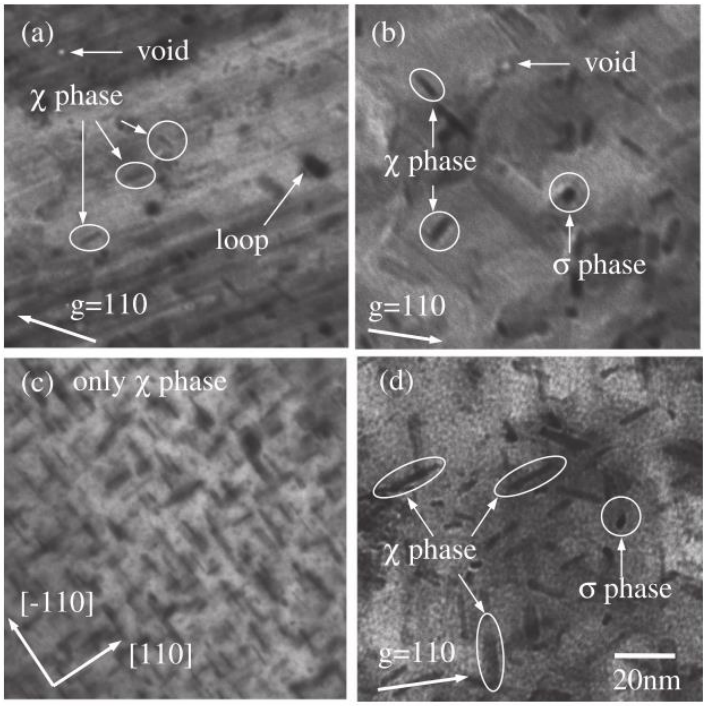

Figure 2.27: TEM image of σ and χ phase precipitates, and a small number of voids in ‘a) and b)’ W-5%Re and ‘c) and d)’ W-10%Re irradiated to ‘a) and c)’ 0.96 dpa at 538 °C and ‘b) and d)’ 1.54 dpa at 750 °C, taken by Tanno *et al.*[162].

Fukuda carried out irradiations at temperatures of 500 °C and 800 °C up to doses of ~1 dpa in the HFIR mixed spectrum reactor in W and W(3-26%)Re alloys [173]. For the first time the percentage of expected transmutation products were calculated for the samples post-irradiation, although not experimentally verified. The predicted transmutation levels were much higher than those expected in ITER or DEMO, with the pure W said to transmutate to W-9.22%Re-5.02%Os following irradiation. In the originally pure W sample, σ and χ precipitates were observed post-irradiation. A summary of precipitate size and density is shown in Figure 2.28. The precipitates were larger and had a lower number density in comparison to the samples alloyed with Re prior to irradiation, where the precipitates were fine and densely populated. The size of the precipitates was seen to increase at higher temperatures. Again Re addition as an alloying element appeared to suppress void and dislocation formation in W. The hardness increases in HFIR were significantly greater than those seen

previously at similar doses in JOYO [158], [159]. For pure W, the hardness increase was ~1.5-2 times greater than that observed in the JOYO fast reactor by Tanno *et al.* [159], [162]. It was suggested that this was because unlike in JOYO where no precipitates were observed in the pure W, in HFIR, dense precipitates were observed (Figure 2.29) [159]. The hardness increase was observed to increase with Re concentration at both temperatures [159].

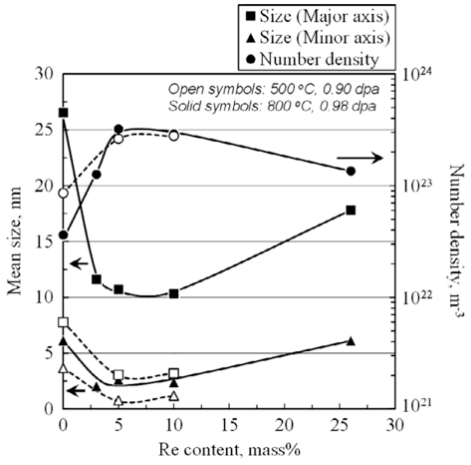

Figure 2.28: Number density and size of precipitates in pure W and W-Re following neutron irradiation to 0.9dpa at 500 °C and 0.98 dpa at 800 °C in HFIR. Taken from [173].

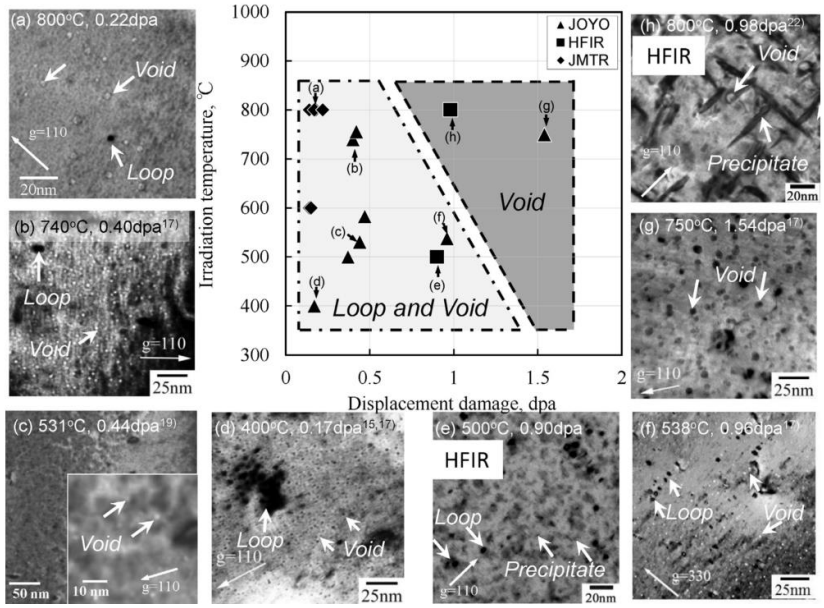

Figure 2.29: Irradiation conditions and microstructures observed in pure W post-irradiation in JOYO, HFIR and JMTR reactors. Taken from [159].

Summary of Neutron Irradiations

Due to the variation in flux spectra of the different fission reactors, there has been some variation in the results. In the case of pure W irradiations, the damage mechanism has typically involved loops and voids at doses less than 1 dpa, with only voids observed at higher doses (Figure 2.29). No precipitates were observed in the JOYO fast reactor, even at high doses, in contrast to the observations in the mixed spectrum HFIR (Figure 2.29 e), h)). In the mixed spectrum JMTR only voids and loops were observed (Figure 2.29 a)). The variation of hardness with dose for the JOYO fast test reactor, JMTR mixed spectrum reactor and HFIR mixed spectrum reactor are shown in Figure 2.30. The data from JOYO appears to show some level of saturation by 1 dpa, however this is not the case in HFIR.

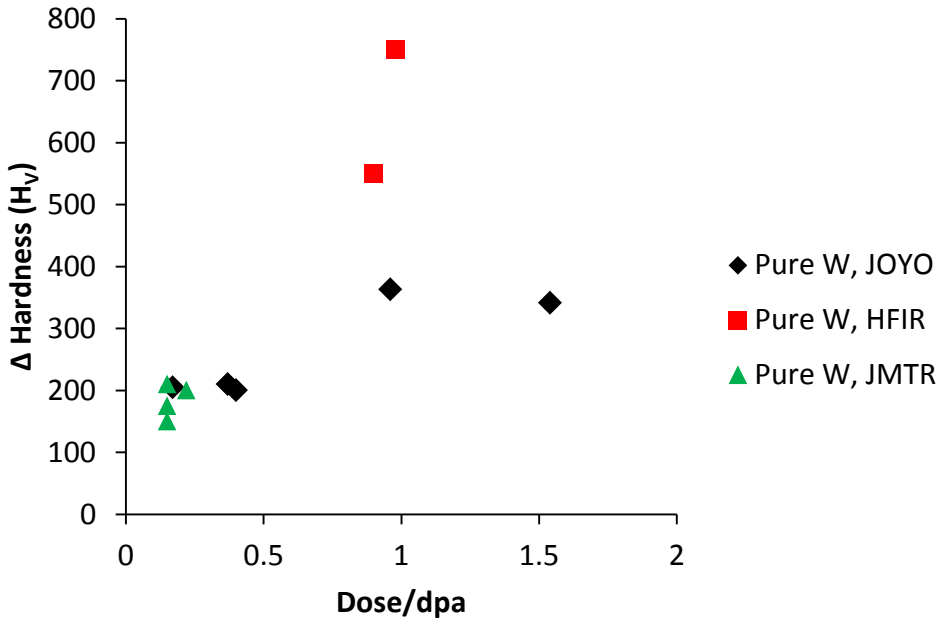

Figure 2.30: Variation of irradiation hardening with dose in pure W, at temperatures between 400-800 °C, using data from [68], [159], [162].

In the JOYO fast reactor there is clearly a different mechanism of damage, dependant on whether Re is in an alloying element in the initial material subject to neutron irradiation or if it is introduced through transmutation during the neutron

irradiation process. When Re is an initial alloying element, void formation is supressed and the main mechanism driving hardness increase is through the formation and growth of precipitates. Whereas, if the initial material is pure W, a void formation mechanism will be dominant [67], [134], [162].

The void formation mechanism appears to result in a saturation of hardness increase, in the case of Tanno *et al.*, with irradiations carried out in the JOYO reactor, at ~1 dpa, whereas the precipitation mechanism does not appear to saturate, and increased hardness with increased dose is observed for W-Re alloys. At dpa levels between 0.4-1 dpa it appears there is a damage threshold that is dependent on the concentration of Re. At 0.4 dpa or less the effect of Re on irradiation hardening is negligible (with the exception of W-26%Re, where there is a higher hardness increase), however above this threshold, the concentration of Re has a strong impact, and much greater hardness increases are observed in comparison to pure W. Furthermore there is a greater hardness increase at 0.96 dpa at 538 °C as opposed to 1.54 dpa at 750 °C. This could be due to the fact at lower temperatures there is nucleation of precipitates, resulting in dense and fine precipitates, whereas at higher temperatures the mechanism is dominated by the growth of precipitates [162].

The results from the mixed spectrum reactor, HFIR vary from those observed in JOYO or JMTR. The hardness increases observed at ~1 dpa in pure W in the HFIR mixed spectrum reactor are ~1.5-2 times greater [158], [159] than those observed in the JOYO fast reactor by Tanno *et al.* at a similar dose [162]. It is suggested that this is because the HFIR reactor is a mixed spectrum reactor, and the rate of transmutation to Re and Os is greater, as there is a greater flux of thermal neutrons [158] (and indeed the predicted rate of transmutation is greater than that expected in ITER or DEMO). Unlike JOYO, where no precipitates were observed in pure W

after 1 dpa, precipitates were observed in HFIR. However, it is not clear why the irradiation hardening is so much greater at 800 °C, in comparison to 500 °C. At 500 °C, the majority of precipitates observed were χ phase, whereas both σ and χ were observed at 800 °C, This implies that in this reactor, the precipitation mechanism of damage is also affecting irradiation hardening in pure W, rather than just void formation as observed in JOYO, and this correlates with the precipitates that were observed in TEM images of the HFIR samples by Hasegawa *et al.* [159] (Figure 2.29).

It is proposed that the hardening mechanism in W-Os alloys is different from the void formation or precipitation mechanism in pure W and W-Re alloys [160]. Recently Xu *et al.*[146] carried out an atom probe study in W ion irradiated W-2at.%Re and W-1at%Re -1at%Re , which suggested that the presence of Os suppressed Re cluster formation, which was thought to be due to Os atoms being more strongly bound to vacancies than Re atoms, resulting in the formation of Os clusters, also corresponding to increased hardening in the ternary alloy in comparison to the binary alloy [146].

Combining the microstructural observation in JOYO, HFIR and JMTR, Hasegawa *et al.* have predicted that within a future fusion reactor, the microstructure at ~1 dpa (relevant to ITER) will comprise mostly of voids in a lattice structure, with some loops and above 10 dpa (relevant to DEMO), there will still be voids, but they will be less ordered and precipitates will also be present [159].

In terms of mechanical properties the only data currently available from the fusion specific experiments are hardness measurements of neutron irradiated tungsten based upon small sample sizes. In terms of engineering design of a large reactor like ITER

or DEMO, these are insufficient and fracture properties of tungsten post irradiation are in great demand.

2.3.3.4 Ion Irradiations

Ion Irradiations in W Prior to Fusion Use

Ion irradiation experiments have been carried out since the 1970s in different metals in order to simulate neutron damage [144]. Again like the neutron irradiations studies in W the W ion irradiation studies in the 1970s were not for fusion applications.

Buswell carried out a study comparing heavy ion irradiations with fast neutron irradiation, using electron and field ion microscopy in order to compare the vacancy damage induced by both irradiation types [174]. The ions in this study were Zn, Hg and W at energies of 100 or 150 keV. The irradiations were carried out at ambient temperatures. From the field ion microscopy it was observed that heavy ion irradiation at low energies resulted in small vacancy clusters with less than 10 vacancies per cluster observed in 80% of cases. Voids that contained up to 300 vacancies as well as dislocation loops were observed via field ion microscopy. The dislocation loops were $\mathbf{b} = \frac{1}{2}\langle 111\rangle$ or $\frac{1}{3}\langle 112\rangle$. Dislocation loops with Burgers vectors $\frac{1}{2}\langle 111\rangle$ were also observed by Häussermann *et al.* during a TEM study of W foils irradiated with 20-70 keV Au ions up to levels of ~0.44 dpa [175], [176]. Electron microscopy was only capable of resolving the dislocation loops, which only made up 10% of the total radiation induced damage. The neutron and ion irradiations induced similar types of damage, although a dose variation was required in order to get similar densities of damage [174]. Jäger and Wilkins subsequently carried out TEM of W irradiated with 60 keV Au ions [177] which confirmed that the model

suggested by Eyre and Bullough for the formation of dislocation loops with Burgers vectors $\frac{1}{2}\langle 111\rangle$ in BCC metals [178].

Ion Irradiations for Fusion Applications

Armstrong *et al.* carried out an extensive investigation into W ion irradiation of W, W-Re and W-Ta for nuclear fusion applications [145], [179]. A 2 MeV W^+ ion beam was used to achieve doses of 0.07, 0.4, 1.2, 13 and 33 dpa and a damage layer of ~300 nm in thickness at temperatures of ~300 °C. A summary of the hardness increase with respect to dose is given in Figure 2.31.

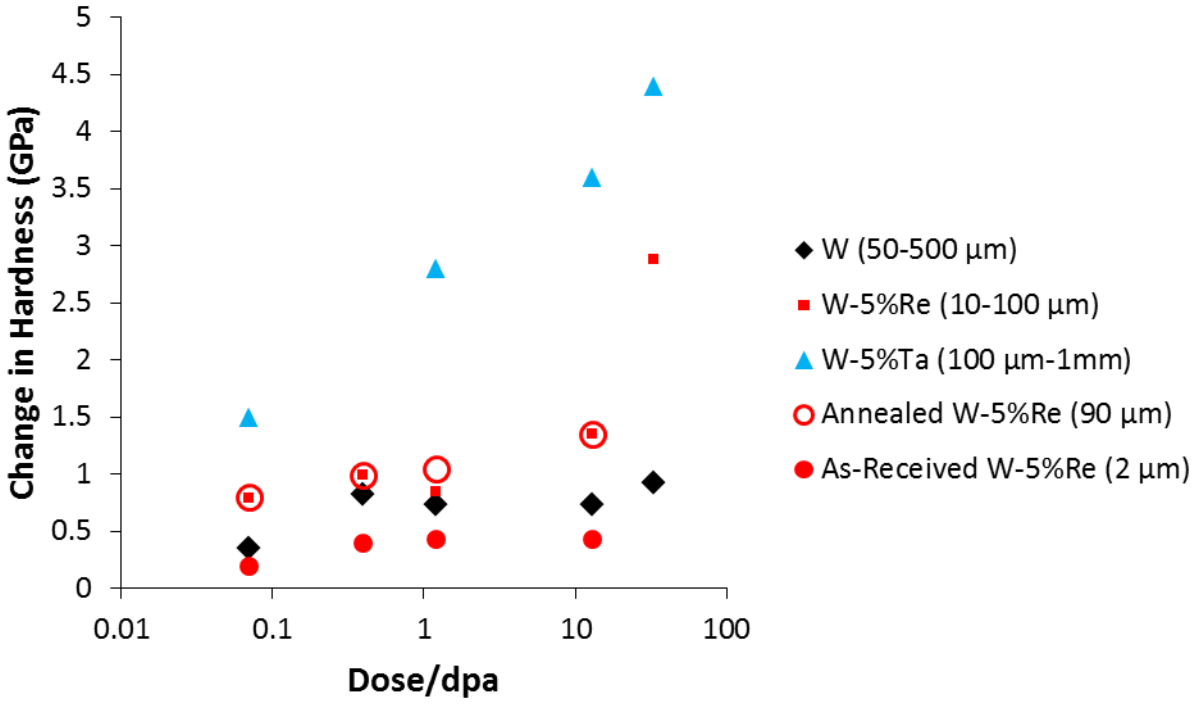

Figure 2.31: Irradiation hardening in W, W-Re and W-Ta following W ion irradiation using data from [145], [179], [180]. All irradiations were using W ions at 300 °C. The change in hardness was taken at a depth of 125 nm for the pure W and W-5%Re, between 50-250 nm for the W-5%Ta and at a depth of 125 nm for the annealed and as received W-5%Re samples. The grain size is provided in brackets.

For pure W, the hardness increase is observed to saturate at a value of ~0.8 GPa at ~0.4 dpa, and this has been correlated to TEM observations which show similar dislocation loop densities at 0.4 and 1 dpa, and a small increase at 33 dpa. The W-

5%Re alloy shows similar hardness increase to W up to 1.2 dpa, however at 13 and 33 dpa the hardness increase is much greater. This is correlated to the observation of nanometre size clusters of Re in concentration observed via atom probe tomography at 13 and 33 dpa. The concentration of Re within the clusters is observed to increase with dose, and concentrations of 20-26% Re are observed at 33 dpa. It is postulated that this could be a precursor to the σ phase precipitates observed following neutron irradiation [145].

Yi *et al.* [143] also carried out an in-situ self-ion irradiation study in W and W-5%Re at 500 °C, at doses between 10^{16}-10^{18} m^{-2}, equivalent to ~1 dpa. The observations revealed that cascade collapse resulted in vacancy loop formation and interstitial loops were formed via interstitial migration at a slower rate. For the largest fluences, it was observed that there was a greater number density, and a reduced average loop size in the W-5%Re, in comparison to the pure W. This indicated that the addition of Re was supressing loop mobility and growth. An annealing experiment at 500 °C also revealed that the motion of the $\mathbf{b}=\frac{1}{2}\langle 111\rangle$ loops were retarded by Re, which may give an indication as to why Re supresses void formation in neutron irradiation experiments [25], [143].

Armstrong and Britton also investigated the effect of initial microstructure on the hardening mechanism in W-Re alloys [180], again conducting 2MeV W^{+} ion irradiations at doses between 0.07-13 dpa in an as-received W-5wt%Re material with ~200 nm thick pancake shaped grains (average ~2 μm rolled plane grain diameter) and a high dislocation density, as well as an annealed material with a low dislocation density and an equiaxed grain structure with a ~90 μm average grain size. What was interesting is that the hardening increase in the as-received sample

seemed to saturate by 0.4 dpa, whereas the hardness increased with dpa for the annealed sample, and was consistently greater than in the as-received material (~3 times greater at 13 dpa). It was suggested that areas of high dislocation densities, such as the walls of the sub grains in the as-received sample act as sinks, allowing for point-defect recombination, and fewer new dislocation loops being formed, resulting in a saturation in the hardening, and also a much lower rate of hardening increase in comparison to the annealed sample [180]. This showed that microstructure has a strong effect on irradiation damage mechanisms, and additionally that within a fusion reactor it would be beneficial to use a nanostructured W sheet for structural components within a future fusion reactor [180].

The hardness increase observed in W-5%Ta is consistently higher than both the pure W and the W-5%Re, however no TEM or atom probe was carried out in order to provide a possible mechanism for this increase [179]. It should be noted that the grain sizes of this material were of the range of 100 μm-1mm. This is significantly higher than the 50-500 μm of the pure W and 10-100 μm of the W-Re in the initial study. Considering the results of Armstrong and Britton [180], it is possible that there were fewer sinks for point defects, and therefore a much greater increase in hardness. From Figure 2.31 it can be seen that both initial microstructure as well as the starting alloy composition has a significant impact on the irradiation hardening mechanism. In general it can be observed that with increasing grain size, and reduced initial dislocation density, there is an increase in irradiation hardening, with the exception of pure W where, despite the larger grain size in comparison to the two annealed W-5%Re cases, the hardness increase is less (specifically at higher doses) . It is postulated that this is due to the fact that the clustering of Re atoms results in

higher hardness values, in comparison to the point defect and dislocation loop generation alone in the case of the pure W.

Ciupiński *et al.* carried out 20 MeV W^{6+} ion irradiations, using a 3 MV tandem accelerator, in polycrystalline ITER grade tungsten up to levels of 0.01, 0.1 and 0.89 dpa at temperatures of ~17 °C. Active cooling was utilised to maintain the temperature and the vacuum pressure in the chamber was reported as better than 10^{-5} Pa [181]. The Monte Carlo code, SRIM was used to predict the peak damage at 1.35 µm and a maximum depth of penetration of ~2.35 µm. Focused ion beam (FIB) was used to produce TEM lamella which were analysed in order to observe irradiation induced defects. At 0.01 dpa, 5nm size, evenly distributed dislocation loops were observed. With increased dose, there is entanglement of the defects. At 0.89 dpa, close to the surface, there is a 400 nm layer of high density, entangled dislocations, followed by a region with a coarser dislocation network, and a lower density of defects up to 1.9 µm, and then finally at ~2 µm, small, evenly distributed loops were observed at high densities. The depth of the damage observed in the TEM agreed well with the SRIM calculations; however the intensity varied, with the lowest areal density of defects observed at 1.35 µm in the 0.89 dpa case. It was suggested that this was due to recombination and rearrangement of defects, but the migration of tungsten at temperatures of ~17 °C is too low, and therefore it was proposed that there was also localised heating caused by the irradiation that for MeV ions, that could be of the order of 10 000 °C, referred to as a thermal spike that would dissipate over the 1-100 ps range [181].

A recent study by Xu *et al.* [146] in W^{+} ion irradiated W-2at.%Re and W-1at.%Re-1at.%Os at temperatures of 300 °C and 500 °C up to a dose of 33 dpa. At 300 °C, the increase in hardness observed was similar in both alloys; however at the higher

temperatures of 500 °C, the hardness in the ternary alloy was ~1.4 times greater than that observed in the W-2%Re. The fact that the presence of Os results in an increased hardness in comparison to a W-Re binary alloy corresponds to neutron irradiation experiments up to 1.54 dpa at temperatures between 400-750 °C conducted by Tanno *et al.* [67]. Although the same alloy compositions and doses are not available for comparison, if the lowest concentration alloys of W-5%Re and W-5%Re-3%Os from the neutron irradiation experiment are considered, also at 500 °C, but at doses of 0.37 dpa, there is ~3 times greater hardness increase in the ternary alloy, compared to the binary W-Re alloy [67].

Comparing Heavy Ion Irradiation Experiments to Neutron Irradiation Experiments

Abernethy has conducted a review comparing recent heavy ion and neutron irradiation experiments in W and W-5%Re [25]. Interestingly the neutron irradiation experiments are showing a higher degree of hardening in comparison to the ion irradiation experiments to the same doses, which considering the higher does rate used in heavy ion experiments (higher dose rate means less time for annealing of defects and therefore should theoretically result in higher hardness increases) is quite surprising. Abernethy suggested that this could be due to the fact that transmutation effects from the neutron irradiations have not been taken into account, giving a possible explanation for the greater discrepancy observed between ion and neutron irradiated W (Figure 2.32) in comparison to W-5%Re (Figure 2.33) [25], [67], [68] [145].

Another suggestion was that at the lower dose rates employed during neutron irradiation, there could be increased segregation, and this could help to explain why precipitates were observed in W-5%Re neutron irradiated to only 0.96 dpa [162],

whereas Re dense clusters were only observed at 13 and 33 dpa following ion irradiation [145]. Studies in Fe-Cr alloys, implanted with heavy ions showed increased hardening at lower doses, which was linked to the segregation of Cr, which provides some credence to this theory [182]. Additionally the hardness of the neutron irradiated samples was typically given via Vickers hardness testing, and the ion irradiation results from nanoindentation data. On conversion to GPa, the 'raw' Vickers hardness data in the non-irradiated material are ~0.5 times the value of the raw nanoindentation measurements of non-irradiated material, and therefore this could also affect the changes in hardness measured. Without the use of the same technique to measure hardness in both materials, it is difficult to accurately correlate the two damage techniques [25]

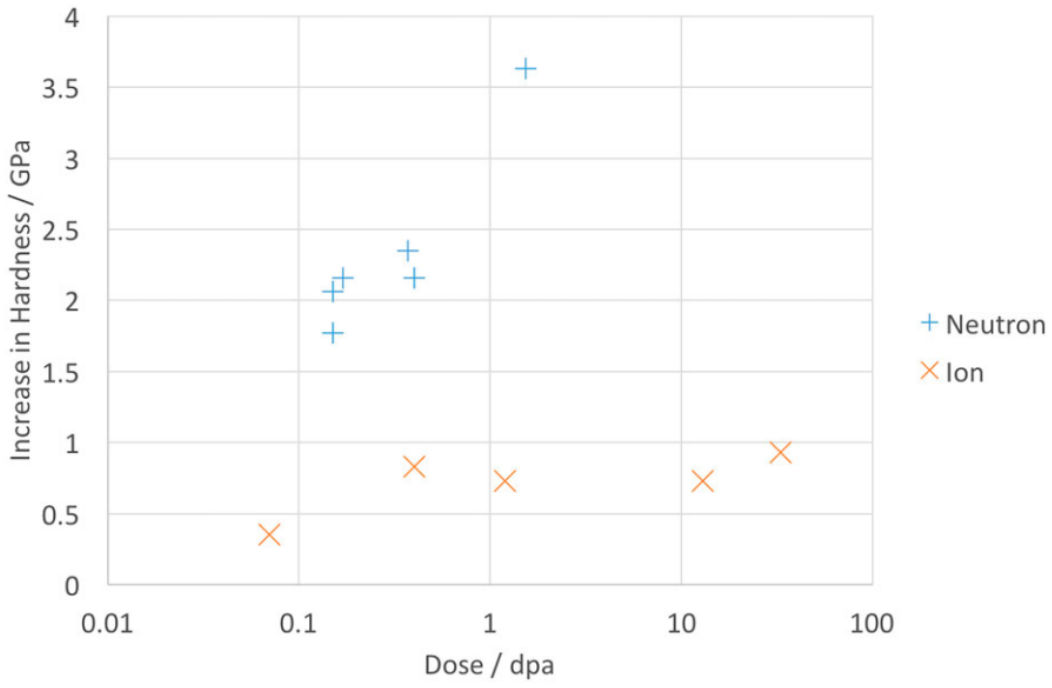

Figure 2.32: Comparison of hardness increase observed in neutron and ion irradiation experiments in pure W, taken from [25], using data from [67], [68], [145].

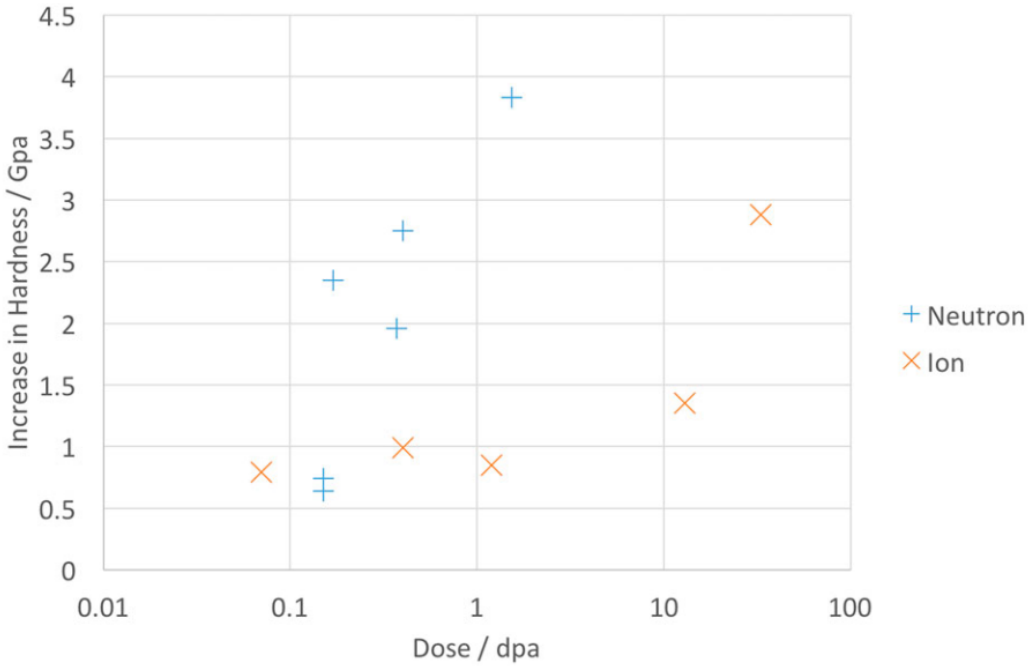

Figure 2.33: Comparison of hardness increase observed in neutron and ion irradiation experiments in W-5%Re, taken from [25], using data from [67], [68], [145].

Summary of Heavy Ion Irradiations

- Self-ion irradiations have been carried out in W, W-Re, W-Ta and W-Re-Os alloys and microstructural and nano-hardness testing has been carried out [143], [145], [146], [179]–[181].
- There is a saturation in hardness increase with dose for pure W and W-Re with high dislocation density. Saturation in hardness increase is not seen in the other alloys, including W-Re with a low dislocation density[145], [179], [180].
- In W-Re, up to doses of 13 dpa the irradiation hardening is due to formation of point defects and dislocation loops. Above 13 dpa clustering of Re has been observed [145].
- Re has been observed to retard the mobility of $b=\frac{1}{2}\langle 111\rangle$ loops [143].
- Initial microstructure was found to significantly impact irradiation hardening. Areas of high dislocation densities can act as sinks, allowing for

point-defect recombination, and fewer new dislocation loops being formed, resulting in a saturation in the hardening, and also a much lower rate of hardening [180].

- Hardness increases in W and W-5%Re following W ion irradiation has been found to lie below hardness measurements following neutron irradiation experiments [25], [67], [68], [145].

2.3.3.5 Proton Irradiations

Maloy *et al.* carried out an investigation into the effect on mechanical properties from 800 MeV, 1 mA proton irradiations, with the aim of investigating its use as a spallation neutron source [183]. Unlike other ion irradiation studies this was a long term irradiation over a period of 6 months, up to a maximum dose of 23.3 dpa, at temperatures between 50-270 °C. The investigation was carried out on 99.95 % purity wrought W rod material, with grain sizes between 20-40 μm. During the irradiation the samples were clad with either 304 L stainless steel or annealed Alloy 718 and back filled with He. Compression and hardness testing was carried out in order to analyse mechanical property changes. It was observed that there was little change in yield stress (1200-1400 MPa in non-irradiated state, ~1600 MPa in irradiated) up to irradiation levels of ~4 dpa, with little variation with dose. Whereas between 4-23 dpa, there was a large increase in yield stress with dose, with yield stress values ranging from 1600 MPa up to 2200 MPa. It was suggested that until doses of 4 dpa, it is the stress needed for dislocations to break free from pinning sites that affects the yield strength. Above this threshold value, there is an increased density of interstitial clusters with dose, and the stress required for dislocations to move through the interstitial clusters is what influences the yield stress. After the compression tests, cracking was seen at the sides of the samples, which suggested

that irradiation resulted in decreased tensile ductility. The hardness testing showed an increase in hardness up to doses of 0.8 dpa, followed by a slightly lower hardness increase at 4 dpa, after which the hardness increase again increased with dose up to 23 dpa [183]. This is very interesting, as previous neutron irradiation (Tanno *et al.*) and heavy ion irradiation (Armstrong *et al.*) experiments suggested a saturation in hardness increase at 1 dpa [162] and 0.4 dpa [145], respectively.

Sakamoto *et al.*[184] carried out in-situ TEM proton irradiations in single crystal 99.99% purity W and polycrystalline 99.9% purity W at energies between 0.5-8 keV at temperatures of 20-800 °C. In the single crystal W, dislocation loops were seen at temperatures of 500 °C or less. Dislocation networks were produced at temperatures below 100 °C. However, due to the free surface, which is a problem during in-situ TEM ion irradiations, at temperatures greater than 200 °C, dislocation networks were not formed. At temperatures between 600-800 °C, hydrogen bubbles were observed. The areal density of the dislocation loops increased with fluence before saturation. Increased fluences were required at higher temperatures for formation of the dislocation loops. The final areal density of the dislocation loops was seen to decrease with temperature. This temperature dependence was more apparent in the single crystal W, in comparison to the polycrystalline. Unlike the single crystal material, at temperatures greater than 600 °C, bubbles, and also dislocation loops were seen in the polycrystalline material [184].

The incoming ion energy also influenced the damage induced. In the single crystal W, no defects were observed at energies below 2 keV. Clusters of hydrogen were observed at 3 keV, followed by dislocation loops at energies greater than 4 keV. With increased ion energy, there was a reduction in the fluence required for defect formation, as well as the final density of the defects[184].

An annealing study up to temperatures of 700 °C, post irradiation revealed a higher remaining density of loops in the polycrystalline W in comparison to the single crystal, which may indicate a higher rate of hydrogen retention [184].

He *et al.* carried out a study comparing proton irradiation effects and neutron irradiation effects on W, W-Re, W-Os and W-Re-Os alloys [185]. The proton irradiations were carried out at energies of 1 MeV, temperatures of 500 and 600 °C, at a dose rate of 2.1×10^{-5} dpa s^{-1}, resulting in dpa ranging from ~0.1 dpa at the surface to 1.2 dpa at the peak of the damage profile, which extended up to ~6 μm into the sample [185]. The vacuum used during irradiation was less than 3.7×10^{-4} Pa. Twin JET electro-polishing was used to produce TEM samples from around 2 μm into the damage region. The neutron irradiations were carried out at 600 °C in the JMTR mixed spectrum reactor up to levels of 0.15 dpa, as described in [68]. It was observed that during proton irradiation the number density and size of dislocation loops induced was smaller than those seen in neutron irradiation. Additionally there were a greater number of voids observed in the case of the proton irradiation in comparison to neutron irradiation (Figure 2.34, Figure 2.35), and specifically in the case of pure W, the void density measured was double that of the neutron irradiated case. However, in the neutron irradiated specimens it is not specified from where exactly the TEM samples were obtained. Again it was shown that the presence of Re and Os inhibited void and dislocation loop formation in W, which is similar to the observations in neutron irradiations by Tanno *et al.* [67], [162]. From Figure 2.36 it can be seen at doses of 0.15 dpa, the hardness increase is ~10% higher in the neutron irradiated W, in comparison to proton irradiated W. In the case of the W-3%Re, the opposite is seen, with the hardness increase in the neutron irradiated material only ~70% of that seen in the proton irradiated W-3%Re.

The hardness increases were seen to correlate with the size and density of irradiation induced voids and dislocation loops [185].

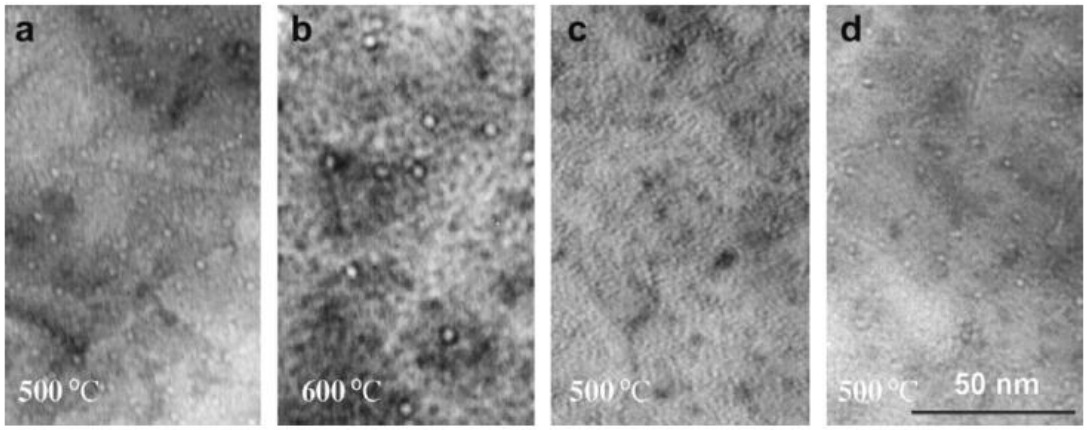

Figure 2.34: TEM micrographs showing voids after 0.15 dpa in 1 MeV proton irradiated a)W, b)W-3Re, c)W-3Os and d) W-5Re-3Os, from [185].

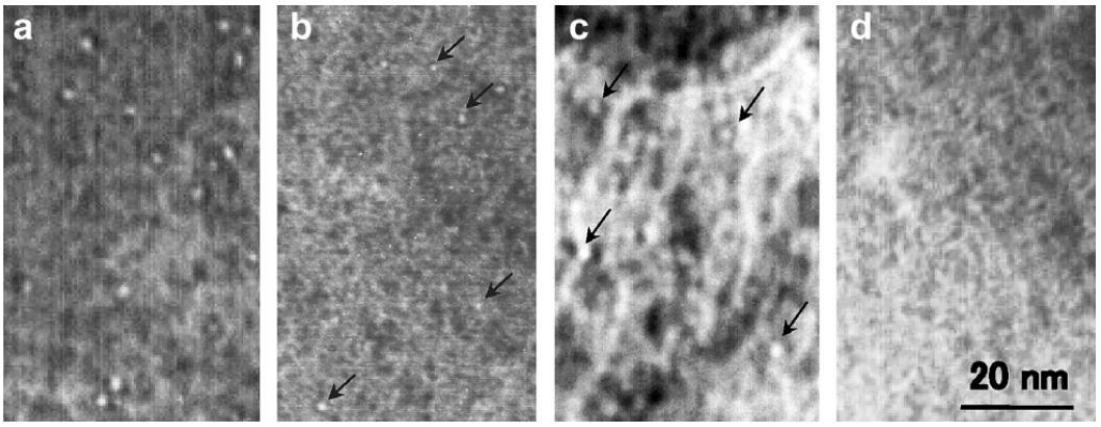

Figure 2.35: TEM micrographs showing voids in 0.15 dpa fast (>1 MeV) neutron irradiated a)W, b)W-3Re, c)W-5Re and d)W-26Re. The irradiations were carried out at 600 °C. The arrows highlight voids. Images are from [185].

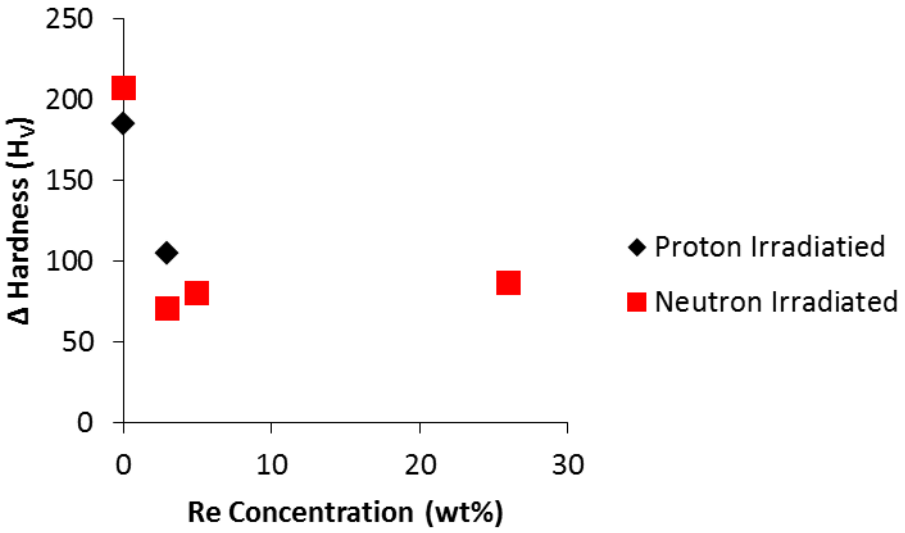

Figure 2.36: Comparison of change in Vickers Hardness for proton irradiated and neutron irradiated W and W-Re alloys up to 0.15 dpa, at 600 °C, with exception of the proton irradiated W, which was irradiated at 500 °C, using data from [185].

Summary of Proton Irradiations

Proton irradiations in W up to a dose of 23 dpa do not show a saturation in hardness increase, in contrast to previous neutron and heavy ion irradiation studies[145], [162], [183]. The number density and size of dislocation loops induced in proton irradiations was smaller than those seen in neutron irradiations [185]. More voids were observed in proton irradiation experiments in comparison to neutron irradiation ones[185]. The hardness increase observed following proton irradiation in pure W is similar to that following neutron irradiations at the same dose. There was slightly more variation between the hardness increase observed following proton or neutron irradiation in W-3%Re [185].

2.3.3.6 Correlating neutron and ion irradiation damage

Abromeit [186] stated that the main parameters that require consideration when comparing different irradiation experiments, are a) the energy and species of the irradiating particle, b) the dose and c) the dose rate. Additionally of importance is the composition of the material under investigation, and any transmutation that may

occur as a result of irradiation, the microstructure of the material prior to irradiation and the sample geometry (for example a bulk sample vs a TEM sample with a free surface) [186]. The differences in the species of the irradiating particle have been discussed at the beginning of the section, the effect of starting material and transmutation has also been addressed during this section. A quick discussion on the effect of dose, dose rate and consequently the required temperature shift is now given.

2.3.3.6.1 Dose and Dose Rate

In pure W there is generally an increase in neutron irradiation hardening with dose, which in some experiments then appears to saturate after ~1 dpa [67]. For ion irradiation hardening there is an increase in hardening with dose until ~0.4 dpa, after which there is no significant increase [145]. On the other hand the damage mechanism is different in irradiated W-Re alloys, where in neutron irradiated material hardness appears to increase with dose, without any signs of saturation [67], [68]. Also in ion irradiated W-5%Re, the hardness increases with dose without any signs of saturation [145].

Recent irradiation experiments have not specifically addressed the dose rate issue in W, and no systematic study has been carried out to look at the effect of dose rate in W systems. As discussed in section 2.3.3.3, depending on the reactor used there is a difference in dose rate, and between different particle irradiations the difference is even more significant. The dose rate clearly has an impact on the mechanism of damage, as can be seen by the review of literature neutron irradiation experiments by Armstrong *et al.* [145]. The review shows there is a general increase in hardness with dose in both W and W-5%Re. There is a lot of scatter, which could partially be due to difference in the starting material and impurities. However, dose rate is likely to

be a significant issue, especially when considering both fast and mixed spectrum reactors were used, all with widely different neutron flux spectra [145]. Dose rate affects the density of the defects produced in a unit volume per unit time, with a higher density generated in a unit volume per unit time in a high dose rate ion irradiation experiment, in comparison to a low dose rate neutron irradiation experiment. Within moving particles, the frequency by which interaction events occur is proportional to the square of the density of the particles [187]. Therefore, in high dose rate experiments there will be an increased number of interactions between defects induced by irradiation [187]. Point defect annihilation can occur via three different mechanisms, i) loss at surfaces, grain boundaries or other extended sinks, ii) capture of vacancies or interstitials, leading to defect growth or shrinkage, and iii) nucleation of the same type of defects and recombination of interstitials with vacancies. With increased dose rate or a decreased temperature, the recombination mechanism is more likely to occur, whereas at low dose rates or high temperatures, the sink mechanism is more dominant [186].

2.3.3.6.2 Temperature Shift

When using different dose rates (as is the case when using ions to simulate neutrons), there is a difference in the damage created, and generally for an increased dose rate an increased temperature is required to get the same types of damage. Mansur developed equations in order to deduce the increase in temperature required [147], [188]. However, this temperature shift is very much dependant on the type of microstructural defect that is under analysis, therefore there is not a single temperature shift that will recreate all the same damages expected from a neutron irradiation at a certain temperature, to a higher dose ion irradiation. It should be noted that at increased temperatures there is increased mobility of defects, and

therefore increased defect losses at sinks, which could mean less damage [186]. However, if there is an increased dose rate for the same dose, the irradiation time is shorter, leading to less time for annealing of defects, and therefore increased damage. The temperature shift looks to balance out this effect. There has been little research into the effect of dose rates and the required temperature shift in tungsten, mostly due to the limited amount of neutron irradiated material to compare to ion irradiated samples, and the inconsistency of the neutron reactors used, providing variation in damage as well.

2.4 Helium Damage in Tungsten

Gilbert and Sublet have predicted that after five years operation in a DEMO reactor that there will be 34 appm of He and 76 appm of H due to neutron transmutation effects in W [133]. In ITER, following 2 D-D and 12 D-T years of operation, there is even less transmutation, with only 1 appm of He and 2 appm of H expected [133]. However, in both cases of ITER and DEMO there will be significant He and H introduced from the plasma itself, and the effect these elements will have on tungsten will vary with the temperature of the exposure.

Both H isotopes and He result in the degradation of mechanical and thermal properties via the solution of these atoms within thin layers of tungsten and the subsequent formation of nano-scale bubbles [165]. The temperature windows for He/H damage in relation to the temperature profile across the outer target of the ITER divertor are shown in Figure 2.37. At low temperatures (<~600 °C), H has been observed to induce blistering. However, due to the engineering surfaces that will be used in a future fusion reactor like ITER or DEMO, and additionally due to the presence of other impurities present within the plasma, including He and Be, this is not likely to be an issue [165], [189]–[191]. For example, the presence of He in D

plasmas has been observed to supress blister formation [192]–[194]. If Be is in the plasma as an impurity, mixed Be and W layers may form, which also can supress blister formation [195], [196]. On engineering surfaces it has been experimentally observed that blistering due to H is not a significant issue. It is suggested that this is because H gas is released from nano-bubbles before any blisters can form and relaxation of internal stress [197]. In W, He-He clusters have strong bonds, in contrast to H-H clusters [198].

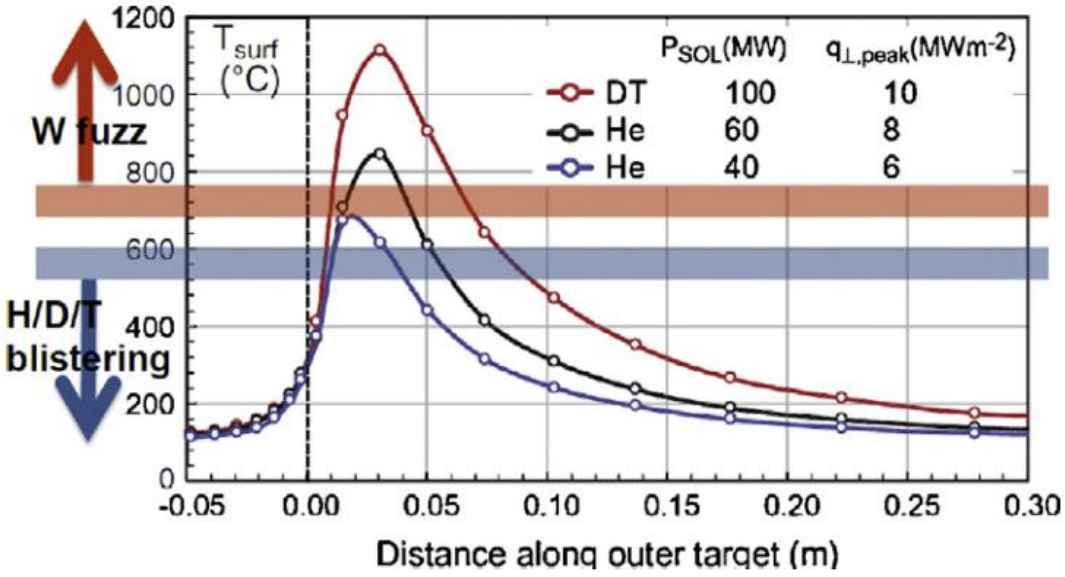

Figure 2.37: Temperature profile across ITER divertor outer target and the temperature windows for H/D/T blistering and W fuzz formation, from [165], using data from [1].

Implanted He atoms in tungsten become trapped at vacancies, voids, dislocations and grain boundaries, which causes embrittlement [199]–[201]. With increased fluence, He becomes trapped at He vacancy complexes, which eventually results in the formation of nanometric He bubbles, which will link together to form pores connecting to the surface, at temperatures <~600 °C [165], [202]. At temperatures >~600 °C there is increased mobility of the He vacancy complexes and larger (> than several nanometres) bubbles are formed [165].

A nano-structural modification of tungsten, referred to as fuzz, due to He bombardment, has been observed at temperatures greater than ~700 °C and at energies typically above 20 eV [165], [203]. It should be noted that this modification is only known to be caused by He. At higher temperatures, He has been observed to induce the formation of micron sized holes within tungsten [165], such as those observed by Nishijima *et al.* in the NAGDIS-II LPD at temperatures above ~1327 °C and with He ion energies greater than 5 eV [204]. Due to the surface barrier potential energy of W for He, 5 eV is the minimum energy required for He to enter the bulk of the W. The higher temperatures produce thermal vacancies, which could be potential trap sites for He atoms, and allows for increased migration of He, resulting in vacancies and bubbles coalescing and growing. At temperatures above the W recrystallization temperature, this process occurs more rapidly [204].

Investigations into the effect of He on the properties of tungsten at temperatures up to 800 °C, have been carried out using high energy (of the order of MeV) He ion implantations in W, through the use of ion beam accelerators [114], [205], [206]. Experiments exposing W to lower energy (of the order of eV) He ions at a range of temperatures, even exceeding 1700 °C have also been conducted using LPDs, tokamaks, and magnetrons among other devices [207], [208]. The high energy investigations have typically focused on hardness changes and embrittlement post irradiation, and additionally some microstructural observations, while the lower energy investigations typically look at microstructural modifications.

The high energy implantations result in small levels of lattice damage, and the penetration depth of the He ions is of the order of microns, whereas at lower energies, like in a tokamak or a LPD, there is no lattice damage and the He ions are stopped within 100 Å from the surface [198]. Additionally at energies greater than

1 keV the growth process of He bubbles is driven by penetration of the He, unlike with lower energy He ions at energies <100 eV, where the energies are too low for vacancy formation [209]. Typically the fluxes used in high energy bombardment are lower than those used in the lower energy bombardments [114], [207], [210]. In the low flux, high energy experiments, the He ions create vacancies, and He gets trapped at vacancies, resulting in small He clusters [205], [210]. There is no saturation of the vacancies. Whereas, in the higher flux, low energy experiments, mobile He will be trapped mostly by self-trapping at He clusters. These clusters can then grow via a loop-punching mechanism, as more He is absorbed resulting in the formation of bubbles [209].

2.4.1 He Ion Irradiations

The interaction of point defects in tungsten induced by neutron damage with the high concentration of He that will be present in the plasma will have an effect on microstructural and mechanical property development of tungsten within a fusion reactor [211], and therefore studying the impact of He ion bombardment on the mechanical properties of W is important.

Armstrong *et al.* carried out an investigation into sequential implantation of W^+ and He^+ ions into W, in order to simultaneously mimic neutron damage and the damage expected from He ions present in the plasma from the D-T reaction [205]. The irradiations were carried out at temperatures of 300 °C. For the W ions, 2 MeV W^+ ions were implanted at fluences of either 3.5×10^{13} cm^{-2} (corresponding to 0.4 dpa), or 1.05×10^{15} cm^{-2} (corresponding to 13 dpa). The dpa was calculated using SRIM, using the full cascade damage model and a 68 eV displacement threshold energy for W. On the same samples, He^+ irradiations were carried out at multiple energies between 0.05-1.8 MeV in order to get a uniform implantation profile, up to either

300 appm or 3000 appm concentrations. Nanoindentation was utilised to obtain hardness data from the samples (Figure 2.38). It was suggested that dislocation loops and helium vacancy complexes were responsible for the hardness increase observed after sequential implantation. Helium vacancy complexes resulted in the highest hardness increases, observed in the case of pure He irradiation. When the W ion irradiation was carried out prior to He ion irradiation, it was proposed that the dislocation loops formed during the heavy ion irradiation acted as trap sites for He, leading to a reduction in the amount of He trapped at vacancies [205].

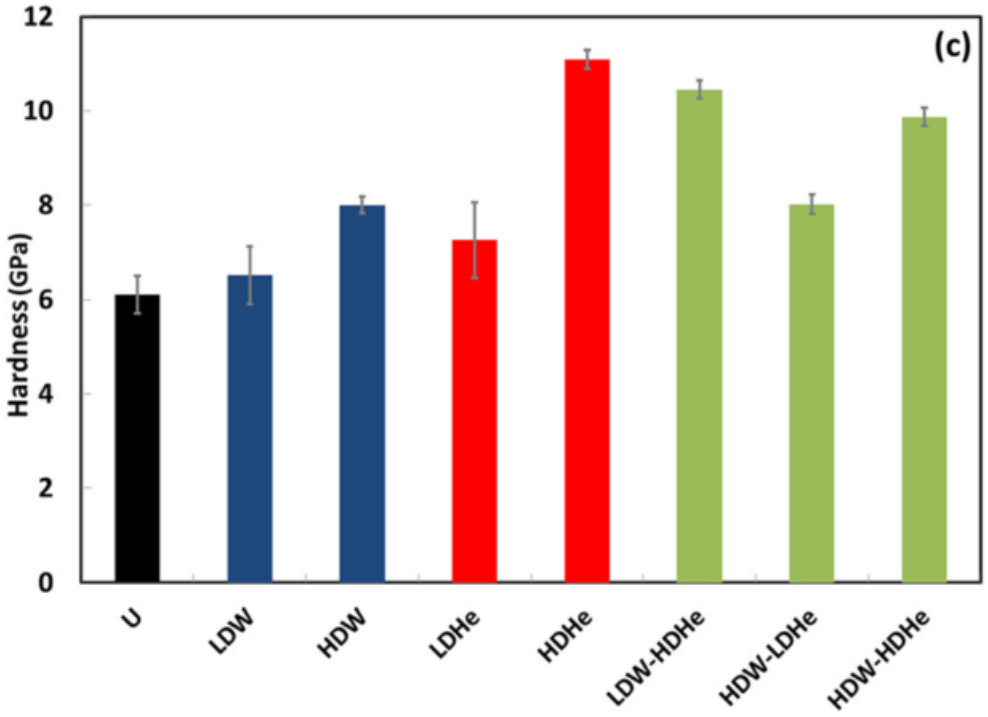

Figure 2.38: Nanoindentation hardness measurements in tungsten irradiated with W ions to either 0.4 dpa (LDW) or 13 dpa (HDW) and He ions to 300 appm (LDHe) or 3000 appm (HDHe), taken from [205].

Gibson *et al.* also subsequently investigated W^{12+} and He^{+} ion irradiations [114], this time also investigating simultaneous W and He ion irradiation, as opposed to just sequential irradiation conducted by Armstrong *et al.* [205]. The irradiations were carried out at temperatures of 800 °C. For the W ion irradiations the fluence was

5×10^{14} cm^{-2} at a damage rate of 5.2×10^{-5} dpa s^{-1} and for the He^{+} irradiations, the fluence was 1.22×10^{16} cm^{-2} at a damage rate of 5.2×10^{-8} dpa s^{-1}. SRIM was used, assuming a 68 eV displacement energy, in order to calculate the peak dpa induced by the heavy ion irradiations to be ~2 dpa, at a depth of 1.25 µm, and a damage profile that extended across 3 µm. The depth of damage also extended across 3 µm in the He ion irradiations, with an average implantation of ~600 appm across the damage profile. The implanted material has an average grain size of ~2 µm. Micro-cantilevers were used to obtain modulus and yield strength values. Nanoindentation was again used to measure changes in hardness. The yield stress was observed to increase with irradiation, with a slightly greater increase in the simultaneous W and He irradiated sample. Yield stress is a more 'useful' parameter in engineering design, so it was significant that it could be obtained from such small samples. However, as with many tests at this scale a size effect was observed, with greater yield stress values observed, compared to bulk measurements. This size effect is due the generation of high density geometrically necessary dislocations in order to support the plastic strain gradients within the cantilever beam [114], [212]. Post-irradiation, the yield stress measurements were fairly similar, but a hardness increase was observed using nanoindentation, which was said to be due to the fact that the two techniques were measuring different plasticity stages. Gibson suggested that the irradiation did not have an impact on dislocation sources, but resulted in inhibition of dislocation glide [114]. Furthermore it was observed that there was a slightly greater hardness increase in the simultaneously W and He irradiated sample, in comparison to the W irradiated tungsten. It was postulated that this was due to a mechanism whereby the high binding energy between He ions and vacancies within the W lattice, results in the formation of He filled vacancies, leading to a higher hardness

increase in comparison to the dislocation and vacancy loops generated by W ion irradiation alone [211].

Further simultaneous implantations of W and He were carried out at the same conditions as the study by Gibson *et al.* [114], by Armstrong *et al.* [213], both in a ultra-high purity (UHP) W, annealed for 24 h at 1400 °C in order to achieve a grain size of ~100 μm, and in a polycrystalline W with a grain size of 2 μm, as previously used by Gibson *et al.*. Berkovich nanoindentation in the UHP W revealed a 2 GPa increase in hardness in the W ion implanted W and a 4 Gpa increase in the simultaneously W and He ion implanted W. Spherical indentation using a partial load unload method was also utilised in order to determine yield stress (via the method of Bushby *et al.* [214]) and a spherical indentation work hardening coefficient. The yield stress was observed to increase by ~1.8 GPa for the W ion implanted material, and by 2.5 GPa for the W and He ion implanted material, correlating well with the hardness increases observed with the Berkovich indentation. The work hardening coefficient decreased from 0.33 in the non-irradiated material to 0.20 in the W ion irradiated material, but was observed to increase to 0.41 in the W and He ion implanted material. It was suggested that the difference in response in this case was due to differences in the damage mechanism. It was postulated that dislocation loop formation was dominant in the self-ion implanted material, as opposed to the formation of He vacancy complexes being more prevalent in the dual ion irradiated material [213].

Notched pentagonal micro-cantilevers were made in the samples, using the method of Di Miao and Roberts [215] in order to determine fracture toughness. No fracture was observed in the non-irradiated material or the W ion irradiated material, however, the load at which the yield of the cantilever occurred was taken as a failure

load which gave a lower band for fracture toughens. This gave fracture toughness values of >10.1 MPa$\sqrt{m}$ for the non-irradiated W, and > 6.0 MPa$\sqrt{m}$ for the self-ion irradiated W. Out of 14 cantilever tests on the dual ion irradiated material, 2 cantilevers were observed to fracture and a fracture toughness of 4.8 MPa$\sqrt{m}$ was determined [213].

All nanoindentation measurements up to this point had been done at room temperature, post-irradiation. However, during D-T operation of ITER, temperatures of up to 1100 °C could be reached on the surface of the divertor (Figure 2.37) [1]. Additionally, at temperatures above 530 °C, Tanno *et al.* reported mobility of vacancies within tungsten to increase [162], and therefore the hardness properties will vary at raised temperatures [206]. Gibson *et al.* carried out high temperature microindentation and nanoindnetation testing in He ion irradiated W, to an average level of 600 appm across a 3 μm damage profile (again calculated using SRIM with a 68 eV displacement energy, this time using the Kinchin-Pease damage model) [206]. The irradiation was carried out at 800 °C and the high temperature nanoindentation was carried out under a vacuum of less than 10^{-5} mbar at temperatures up to 750 °C. The hardness increase observed post irradiation at 50 °C was ~0.9 GPa, however, above temperatures of 450 °C, this hardness increase was negligible. It was suggested that this was because of an increase in mobility of dislocations, via either cross slip or climb past He vacancy complexes at the raised temperatures. Hardness measurements on cooling gave similar measurements to that before heating, indicating the He remained trapped within the samples, even at temperatures up to 750 °C. This was in agreement with thermal desorption spectrocscopy measurements carried out in 60 keV ^{3}He implanted W by Lhuillier *et al.* where it was found that up to temperatures between 1200-1300 °C He remained

trapped in mono-vacancies and helium vacancy complexes [216]. This also agrees with TEM observations by Armstrong *et al.*[205], where no He bubbles were observed following implantation of He to 3000 appm in W, suggesting He retention must occur in the length scale below the limit of resolution of the TEM [206].

In order to consider the impact of transmutation products on the response of W to He ion irradiations, Beck *et al.* carried out a study into the hardness response of W-Re and W-Ta alloys [210]. 1 and 5% Re and Ta alloys without significant texture and with grain sizes between 50-500 μm were irradiated with He ions at 300 °C, using multiple energies between 0.05-1.8 MeV, at fluences of the order of $1\text{-}6\times10^{15}$ ions cm^{-2} in order to get a fairly uniform dose profile across ~2.5 μm, corresponding to 3000 appm and 0.2 dpa, as calculated using SRIM, with a displacement energy of 68 eV. Prior to irradiation the only material to have a significantly higher hardness in comparison to pure W was W-5%Ta. Post irradiation it was seen that there was greater absolute irradiation hardening in the W-Ta alloys in comparison to the W-Re alloys. Additionally the hardness increase was seen to decrease with Ta concentration, but increase with Re concentration, proportionally the hardness increase was higher in the pure W samples in comparison to the alloyed material. The proportional increase was similar for both 1 and 5% Re concentrations, but was observed to decrease with increased tantalum concentration. The modulus was also observed to increase in all samples following He irradiation. The modulus increase was higher in the W-Ta alloys in comparison to the W-Re alloys, and in both cases there was a reduction in modulus increase with alloy concentration. The W-1%Re alloy was the only material with a slightly lower absolute modulus value in comparison to pure W. Again, in agreement with previous work [205], no He bubbles were observed in TEM micrographs, indicating that the He existed as small

He-vacancy clusters. It was suggested that He-vacancy pinning of mobile dislocations could be responsible for the hardness increases observed [210].

2.4.2 Plasma Damage and the Formation of 'Fuzz'

Fuzz is a nanostructural modification that is observed on exposure to He plasmas. As discussed at the beginning of Section 2.4 and shown in Figure 2.37, fuzz growth is observed at temperatures greater than 700 °C and energies higher than 20 eV [165]. This modification has been seen in several materials, but has only been observed on materials exposed to plasmas containing He. It is suggested that this is due to the fact the penetration depth of He at energies less than sputtering threshold is greater than other noble gases [217]. Fuzz is made of tendrils that are typically tens of nanometres in thickness, and which via TEM observations have been seen to contain He bubbles (Figure 2.39, Figure 2.40). Diffraction patterns of the fuzz have revealed it to have a crystalline structure, that is similar to that of α-tungsten [218], in contrast to previous suggestions by Baldwin *et al.* that the fuzz was amorphous [219].

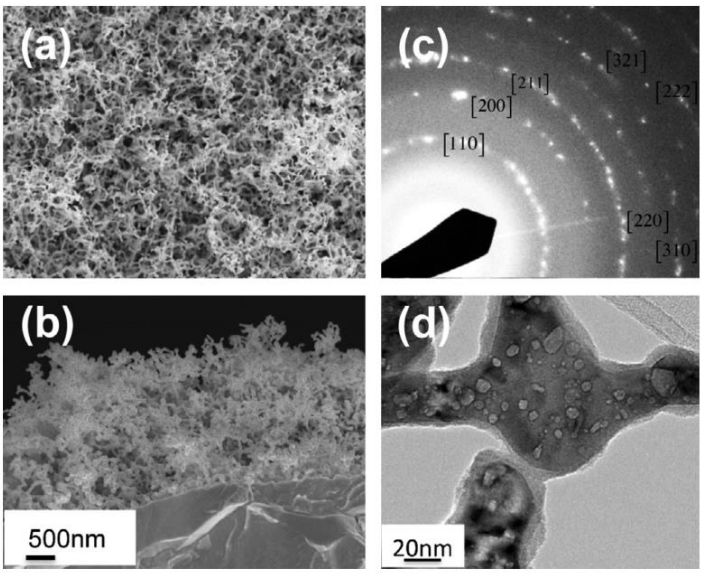

Figure 2.39: SEM of a) top surface and b) cross section of fuzz formed in tungsten following 50 eV He ion irradiation at 1000 °C for 500 s and c) diffraction pattern of tungsten filament and d) TEM image of tungsten filament, taken from [218] .

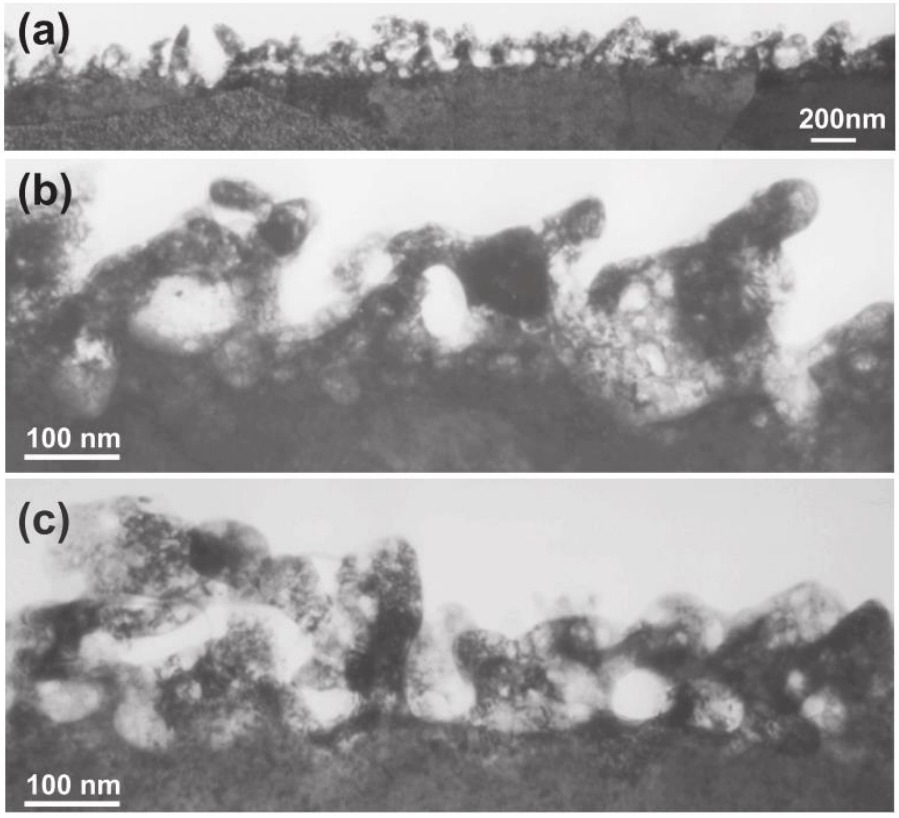

Figure 2.40: TEM images of fuzz grown in He irradiated tungsten up to fluences of 1.1×10^{25} m^{-2}, taken from [220].

EDX analysis (Figure 2.41) of fuzz growth have also confirmed that the layer is tungsten, rather than the deposition of another material [219]. The C and Mo observed in low amounts are said to be due to the presence of impurities during the plasma exposure and the O observed was said to be due to surface oxide passivation when the samples were removed from the vacuum chamber [219].

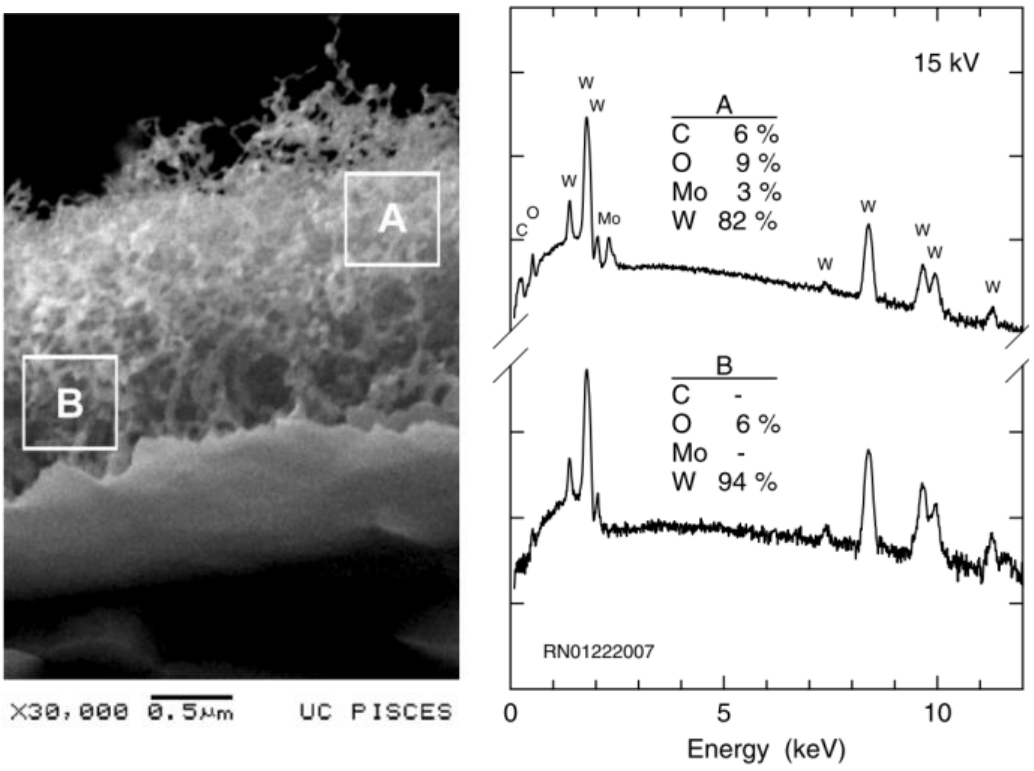

Figure 2.41: Fuzz growth in W in PISCES-B and corresponding EDX spectra taken from the regions A and B on the SEM image, taken from [219].

Fuzz formation is of concern for ITER due to the fact it can easily be removed from the surface of bulk tungsten, and it has been noted in the literature that fuzz can be removed via a scratch with tweezers [221], [222], exposing the bulk W in the process. This is not only worrying as the removed W would lead to cooling of the plasma due to the radiation increase in the core of the plasma [223], but additionally the re-exposure of the bulk following removal, could mean the process may be repeated, rendering the plasma inefficient. Furthermore there are concerns over the thermal response of fuzz to Edge Localised Modes (ELMs), a disruption, and potential melting, vaporisation and arcing, which could again result in erosion of the fuzz [224], [225]. Therefore it is of vital importance that the mechanisms and effects of fuzz formation are well understood.

Instances of fuzz formation are believed to have been formed, but not categorically observed via microscopy since the 2000s. The first case where it is thought fuzz was

formed, but not confirmed was by Ye *et al.* [226], where W was exposed to He plasma in the NAGDIS-I LPD. The ion energy was 50 eV, the fluences varied between ~10^{25}-10^{26} ions m^{-2}, and the temperatures varied between 750-1500 °C; all parameters within the typical formation conditions required for fuzz in a LPD. A decrease in reflectivity was also measured, another indication that there could have been fuzz growth [226]. Tokunaga *et al.* observed microstructural modifications in W exposed in the PISCES-B device to He plasma at a fluence of 6×10^{25} m^{-2} at 600 °C, and again observed that the sample turned black, which indicates that fuzz could have grown [227]. Fuzz was first categorically observed by Takamura *et al.* in the NAGDIS-II linear plasma device, on graphite coated with tungsten exposed to He plasmas, with a fluence of 3.5×10^{27} m^{-2}, at temperatures of 1000 °C and 1300 °C and a 12 eV incident ion energy [228]. Helium bubbles, that were nanometre sized, were observed in the tendrils of fuzz via TEM analysis by Kajita *et al.* [229]. Baldwin *et al.* then investigated the formation mechanism of fuzz in the PISCES-B linear plasma device, carrying out He plasma exposures for durations between 300-2.2×10^{4} s and at two different temperatures; 1120 K and 1320 K. It was observed that fuzz growth followed Fick's law, with the thickness of the fuzz layer (d) being proportional to the square root of the exposure time (t), and a diffusion coefficient (D) that was dependant on the exposure temperature. They developed Equation 2.9 [219]. At the temperatures investigated, two diffusion coefficients; $D_{1120\ K}=6.6\pm0.4\times10^{-12}$ cm^2 s^{-1} and $D_{1320\ K}=2.0\pm0.5\times10^{-11}$ cm^2 s^{-1} with a thermal activation energy of 0.71 eV were provided [219]. It was suggested that a He atom diffusion mechanism alone would be too fast to explain the fuzz growth rate, and therefore thermal vacancy availability and diffusion of He at a slower speed through the fuzz as it was forming were also suggested to have an impact[219].

Equation 2.9

$$d = (2Dt)^{1/2}$$

Equation 2.10

$$C = 2D/\Gamma$$

Equation 2.11

$$x(\Phi) = (C(\Phi - \Phi_0))^{\alpha}$$

Kajita *et al.* saw a square root dependence between the thickness of a fuzz layer and the helium fluence, with an incubation fluence of ~4×10^{24} m^{-2}. Petty *et al.* then further investigated the fuzz growth equation, conducting exposures using the PISCES A and B linear plasma devices, the PISCES E helicon plasma source and the University of Liverpool Magnetron device. They normalised the diffusion coefficient, D used in Equation 2.9, via Equation 2.10, to the He ion flux, Γ in order to obtain the growth constant, *C*. The thickness of the fuzz growth layer was then related to fluence, Φ, via Equation 2.11, where Φ_0 is the incubation fluence and $\alpha = \frac{1}{2}$ [207]. The incubation fluence was stated as 2.5×10^{24} m^{-2}. The time dependence that was initially observed in Equation 2.9 was simply a special case of Equation 2.11 as can be seen in Figure 2.42. This research suggested that there was an incubation fluence before which fuzz would not grow possibly due to the formation of a field of He nanobubbles close to the surface of the sample [207].

These equations were developed for fluxes between 0.01-11×10^{22}ions m^{-2}, so it is not certain if they would apply at lower and higher fluxes. Additionally these equations do not take into account annealing of fuzz that may occur at raised temperatures. Annealing out of the fuzz has been observed on samples that have already had fuzz grown on them previously (i.e. without any helium ions incident at

the same time) at temperatures of 1200 °C and 1600 °C by Baldwin *et al.* [221]. These temperatures also lie within the temperature range of growth of fuzz, and therefore Kajita *et al.* suggested that there was a threshold flux, where there was a growth/annealing equilibrium of fuzz [230]. Kajita *et al.* carried out experiments varying the helium flux and temperature of the sample surface, in order to investigate this threshold flux and the growth/annealing equilibrium, as shown in Figure 2.43. They determined that annealing occurred between ~1000-1200 °C, at fluxes between 10^{21} -10^{22} $m^{-2}s^{-1}$. On annealing, the fuzz would reintegrate into the surface of the sample. When annealing dominates over growth, the appearance of the surface changes from being covered with a fine tendril-like nanostructure to coarser strands and eventually small bumps that are widely spaced out, with the smooth bulk visible underneath [230].

At high temperatures above the recrystallization temperature of tungsten (~1350 °C) [54]), it is also important to consider the effect of recrystallization on fuzz growth [231].

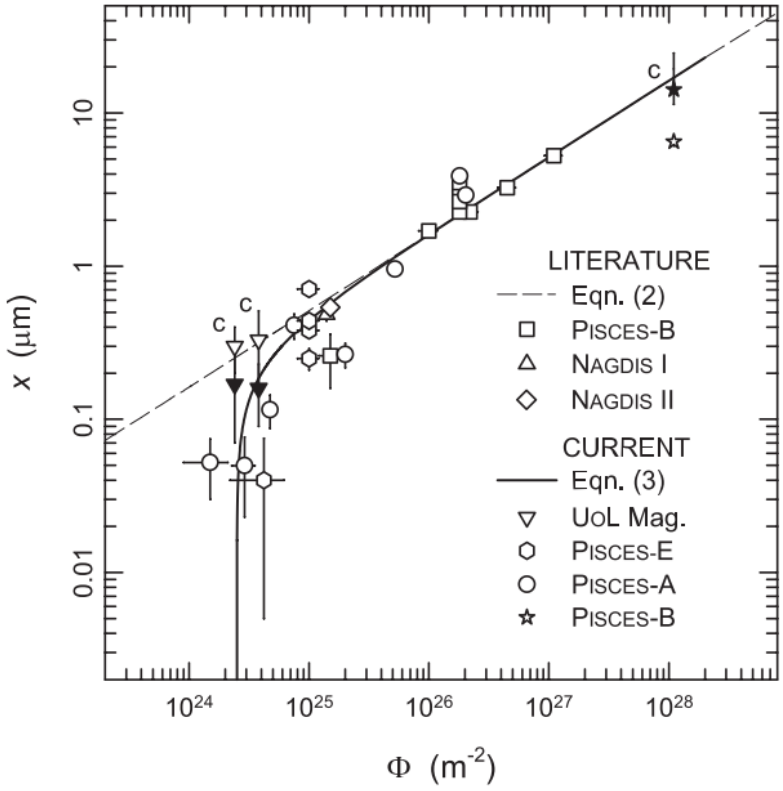

Figure 2.42: Fuzz layer thickness vs fluence from [207], also using data from [219], [221], [232], [233]. The 'c' labelled points are corrected values. The dashed line is obtained from Equation 2.9 and has been extrapolated over the full data set. The full line is obtained using Equation 2.11, using an incubation fluence, Φ_0=2.5×10^{24} m^{-2}.

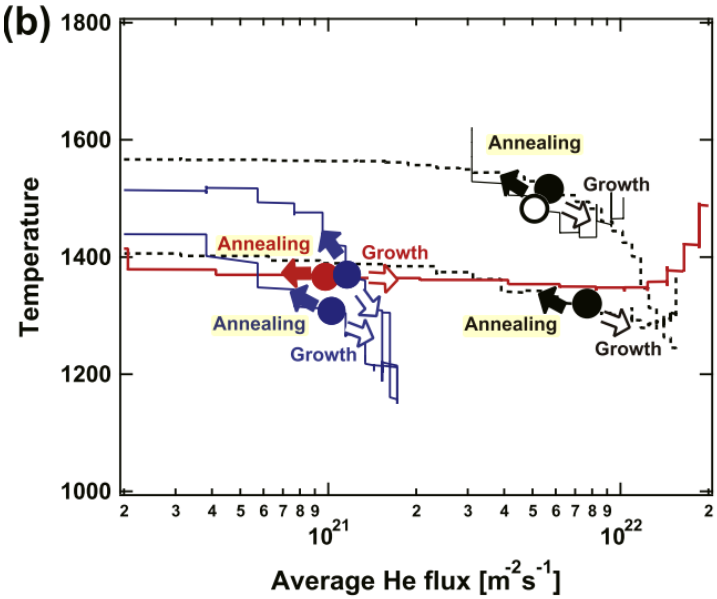

Figure 2.43: Surface temperature vs time averaged He flux. The circles represent the boundary between growth and annealing of fuzz [230]. The red line corresponds to a He flux of 2×10^{22} m^{-2}s^{-1}, the blue line to 1.6×10^{21} m^{-2}s^{-1}, the solid black line to 1×10^{22} m^{-2}s^{-1} and the dashed black line to 1.6×10^{22} m^{-2}s^{-1}.

In addition to an annealing/growth equilibrium, there is also an erosion/growth equilibrium. The effects of erosion on fuzz growth were investigated by Doerner *et al.* at incident ion energies above the sputtering threshold and Equation 2.9 was differentiated to get Equation 2.12 (where x is the fuzz thickness), and then the effect of erosion in predicting fuzz growth was included by adding the sputtering yield term, E (Equation 2.13) [234]. This equation however is not without issues as it predicts that as the length of exposure, t goes towards infinity, the growth term will tend towards 0, and as the sputtering yield remains constant, the fuzz should be eroded away. However this does not agree with experimental observations, where there is a critical exposure time, at which erosion and growth will balance, and the fuzz remains at a constant equilibrium thickness [222].

Following this, Noiri *et al.* developed Equation 2.14, where E is the rate of erosion (again due to sputtering) in ms^{-1}. Using Equation 2.9, t was eliminated from Equation 2.13 in order to account for the effect of the fuzz thickness on the rate of growth. Equation 2.14 solves the problem of Equation 2.13, where the fuzz is predicted to be eroded away. In Equation 2.14 as t goes toward infinity, and the critical exposure time is exceeded, x will simply equal the equilibrium thickness, and therefore the growth and erosion terms will be equal in value, resulting in the fuzz layer thickness remaining constant [235] . The numerical solution of Equation 2.14 agreed well with experimentally observed data in erosive plasmas.

Equation 2.12

$$\frac{dx}{dt} = \left(\frac{D}{2t}\right)^{1/2}$$

Equation 2.13

$$\frac{dx}{dt} = \left(\frac{D}{2t}\right)^{1/2} - E$$

Equation 2.14

$$\frac{dx}{dt} = \left(\frac{D}{x}\right) - E$$

Petty *et al.* proposed a growth/erosion equation, however, this time in terms of fluence as opposed to duration of exposure. Equation 2.14 was re-written in terms of fluence and the growth constant, C from Equation 2.10, in order to give Equation 2.15 [207], [222]. ϵ_{fuzz} was the erosion term and was redefined, as $\epsilon_{fuzz} = \frac{E}{\Gamma}$. Equation 2.15 was then solved mathematically to give Equation 2.16, where the W function is the Lambert W function [207], [236]. As the fluence tends to ∞, the exponential term also tends to 0. $W[0] = 0$, so therefore as the fluence tends to ∞, the fuzz thickness tends to $\frac{C}{2\epsilon_{fuzz}}$. This equation only produces real solutions, when the fluence is greater than the incubation fluence, and as ϵ_{fuzz} tends towards 0, then Equation 2.16 converges to Equation 2.11 [207] .

Equation 2.15

$$\frac{dx}{d\Phi} = \left(\frac{C}{2x}\right) - \epsilon_{fuzz}$$

Equation 2.16

$$x(\Phi) = \frac{C}{2\epsilon_{fuzz}}\left(W\left[-exp\left(-\frac{2\epsilon^2{}_{fuzz}}{C}(\Phi - \Phi_0) - 1\right) + 1\right]\right)$$

Meyer *et al.* have suggested that the incubation fluence is dependent on the incident energy of the He ions and have also suggested that there is a flux threshold before fuzz can grow [237]. They also have observed fuzz growth at energies of up to

8.5 keV using an ion beam [237], which is much greater than the sputtering threshold of tungsten exposed to helium, of 109 eV [99].

2.4.2.1 Conditions for Fuzz Growth

The D-T fusion reaction results in the production of He ions. It is important to understand if the presence of these He ions within fusion plasma will result in damage to the tungsten used for plasma facing components and the divertor. In order to predict this we need to know under what range of conditions fuzz will grow. The main parameters responsible for fuzz growth are temperature, ion energy, flux, length of exposure and therefore fluence. Additionally the physical properties of the material under exposure is of vital importance, and not all materials will be susceptible to fuzz growth. There are six different types of devices in which fuzz has been observed to date: linear plasma devices (NAGDIS-I,II [203], [228], PISCES-A,B [207], [221] (LaB_6 cathode), Magnum,Pilot-PSI [238], [239] (cascaded arc sources)), expanding thermal plasma devices (Nano-PSI [240]), inductively coupled plasma devices (PISCES-E [207]), magnetrons (UoL magnetron [241]) and ion beams (MIRF(Multicharged Ion Research Facility) [237], [242], JAERI (Japan Atomic Energy Research Institute) Particle Beam Engineering Facility (quasi-steady ion beams, 1.5 MW for 1000 s and 9.6 MW for exposures $\leq$ 10 s [243]–[245], NBI (neutral beam injection) system at AIST (National Institute of Advanced Industrial Science and Technology) [246]), and tokamaks (Alcator C-Mod [208]). However, theoretically any device that is capable of generating He ions, and fulfilling the formation conditions required for fuzz could be used to generate fuzz.

Linear plasma devices have been used most extensively to mimic divertor conditions by bombarding samples with He and D plasmas. This mimics the D and He ion bombardment expected from the D-T reaction. There are several divertor simulators

internationally, including the Pilot and Magnum-PSI devices at DIFFER, NAGDIS I and NAGDIS II at Nagoya University and PISCES A and PISCES B at the University of San Diego. The fluxes that are achievable in each of the devices vary, but typically they reach fluxes between 10^{22}-10^{24} $m^{-2}s^{-1}$ [222]. This is clearly of the same order with the >10^{23} $m^{-2}s^{-1}$ expected in ITER and 10^{23}-10^{24} $m^{-2}s^{-1}$ envisaged in DEMO [222]. The devices at DIFFER are also capable of simulating ELM like events, utilising a pulsed plasma in conjunction with a high flux continuous plasma[247], [248]. Magnum-PSI is being developed in order for it to operate at steady state. It is important to utilise linear plasma devices when investigating fusion damage due to the fact they are capable of producing fluxes relevant to ITER and DEMO and they are also capable of functioning at temperatures within the operating range of the tungsten divertor, which also happens to coincide with the temperature required for the formation of fuzz (700-1700 °C) [1]. LPDs generally produce ions at a much lower energy than tandem accelerators. It is important to try to design experiments that utilise linear plasma devices, while also considering the neutron damage expected within ITER and DEMO and how to simultaneously mimic this as well as the plasma damage expected.

There is a general consensus within numerous linear plasma accelerators, when tungsten is exposed to helium plasmas between temperatures of 700 and 1700 °C, at energies greater than or equal to 20 eV, nanostructure modifications form [203], [219], [221], [231]. Figure 2.44 provides graphical representation of these fuzz formation conditions in NAGDIS-II and PISCES-B, two linear plasma devices[203]. Fuzz has been observed at fluences between 2.4×10^{24} -1.1×10^{28} ions m^{-2} in linear plasma devices and magnetrons [207], [241]. Additionally in 3200 s exposures at 847 °C in the PISCES-B LPD, to either He or D_2-He plasmas, the thickness of fuzz

layers has been observed to increase with He flux, until levels of ~10^{22} $m^{-2}s^{-1}$, after which the flux no longer has an impact [249]. Although this may be related to the incubation fluence theory suggested by Petty *et al.* [207], as with the lower fluxes the incubation fluence would not be reached in the fixed time exposure. The fact the thickness of the fuzz layer is similar at higher fluxes could potentially be due to erosion effects. The width of the tendrils of fuzz has been observed to be heavily influenced by the temperature of exposure. The higher the temperature, the larger the size of the helium bubbles and consequently the greater the widths of the tendrils [203], [239], [250].

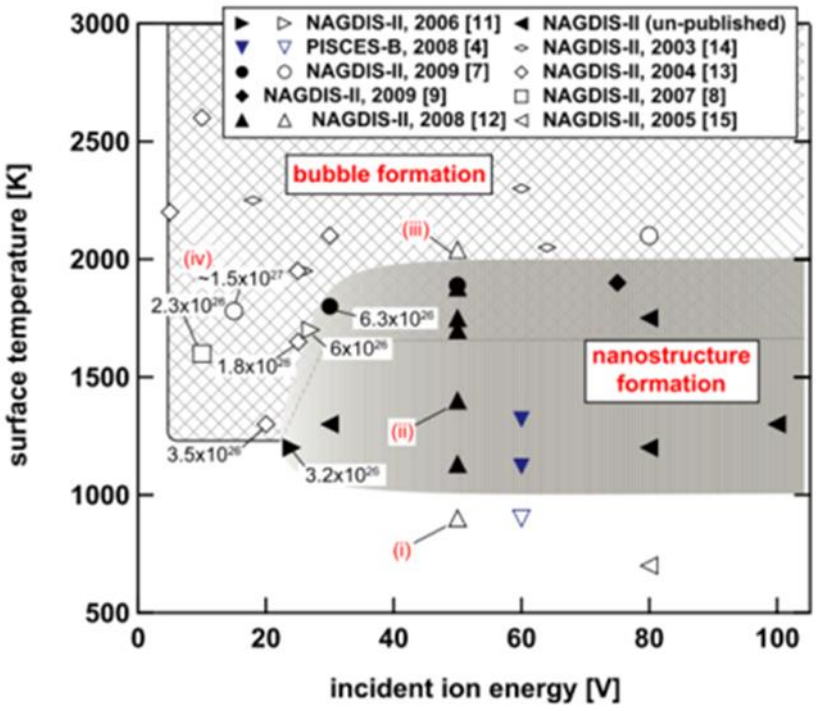

Figure 2.44: Surface temperature against incident ion energy for helium plasma experiments carried out in NAGDIS-II and PISCES-B. Fuzz formation was observed in the filled-in shapes and not in the open shapes [203].

However, there is variation between devices in terms of the energies and temperatures at which fuzz formation has been observed. For example in NAGDIS-II fuzz has been observed at energies as low as 12 eV [228] (below the typically quoted

threshold of 20 eV) and in one study in an inductively coupled plasma reactor, Baldwin *et al.* did not observe fuzz growth even at energies of 27 eV (above the threshold energy) [251]. Typically fuzz had been investigated at energies below the sputtering threshold of tungsten (109 eV for W exposed to He [99]), however there have also been nanostructural modifications observed at energies much higher than this. A type of fuzz growth has been observed at energies of 19 keV by Tokunaga *et al.* at temperatures of 2600 °C in the JAERI ion beam.[243]. However the fuzz observed had much wider tendrils, in comparison to that observed in linear plasma devices. Fuzz has been observed by Meyer *et al.* at energies between 218 eV and 8.5 keV at temperatures of 1027 °C at the ORNL MIRF (Oak Ridge National Laboratory multicharged ion research facility) [237]. Tokitani *et al.* have also observed a kind of nanostructure growth using the NBI system at AIST at energies of 25 keV and fluences of 4×10^{22} m^{-2} at temperatures of ~1500 °C [246]. It is debatable whether the same mechanism is at play in all these devices, especially at the higher energies above the sputtering threshold of W.

If we consider fuzz growth outside the currently accepted temperature range (700-1700 °C); Nishijima *et al.* have observed fuzz growth at temperatures up to 2000 °C in the NAGDIS-II LPD at energies of 60 eV [252]. Additionally as will be discussed in section 2.4.2.2, fuzz has also been observed in a tokamak at temperatures above 1700 °C [208].

2.4.2.1.1 Pulsed vs Continuous Exposures

Several studies into fuzz growth, especially to achieve long fluences have used pulsed exposures [207]. Petty *et al.* have also investigated the differences between discrete and continuous exposures to plasma in a Magnetron sputtering device [253], where a sample was exposed to a He plasma for 8 hour continuously, while another

was exposed for 4 hours, after which the plasma and heating was turned off, and the sample was left within the vacuum chamber, and then the next day the sample was again exposed to plasma for another 4 hours. In the resulting samples, the thickness of the layer of fuzz growth was fairly similar; however the reflectivity and roughness measurements suggested that the sample exposed to the pulsed plasma was slightly less developed. Three possible reasons for this were proposed, including the escape of He ions, either overnight or during the heating of the sample prior to the second plasma exposure, reintegration of the fuzz into the bulk prior to the second exposure, annealing of the fuzz during the heating period prior to the initiation of the second plasma exposure [253]. Therefore it may be important to consider whether samples are exposed to continuous or pulsed plasmas when investigating fuzz growth. However generally in LPDs, the time between pulses is of the order of minutes rather than hours, so it could be that the effect is not as important on such timescales.

2.4.2.1.2 Suggestion of Incubation Fluence Variation with Ion Energy

It has been suggested that there is an incubation fluence for fuzz growth by Petty *et al.*[207]. Meyer *et al.* suggested that there is also an incubation flux before fuzz can form, which varies depending on the incident energies of the He ions [237]. The reasoning provided for an incubation flux is that on a sample exposed to a He ion beam with a variable flux profile, with the flux highest in the middle and less at the edges, fuzz should be found on the whole sample after a certain length of time. Meyer *et al.*, using an ion beam, observed a fairly constant incubation fluence of ~(2-4)×$10^{22}$$m^{-2}$ at energies between 480 eV-8.5 keV and ~(2-4)×$10^{23}$$m^{-2}$ at lower energies of 218 eV [237]. These energies are much higher than the typical energies required for fuzz formation in a linear plasma device, which are typically between 20 and 100 eV [203], [207]. Therefore there could indeed be an incubation flux, but it is

also possible that the incubation fluence was not obtained at the edges of the beam profile.

The various incubation fluences from the literature have been plotted against incident ion energy in Figure 2.45. The fluence for the LPDs and PISCES-E were taken from Petty *et al.* [207], and those from the ion beam were also given by Meyer *et al.* [237]. The incubation fluence for AIST was not given in the paper, therefore it was estimated as the fluence where fuzz features became visible in SEM images within the publication [246]. The data are not extensive and there is temperature variation between exposures, which may also impact the data, but there is a suggestion that with a reduction in energy there is an increase in incubation fluence, which appears to imply that fuzz formation depends on the rate of energy deposition into a surface, although a dedicated study is required in order to confirm this. It should also be noted that the higher energies are above the sputtering threshold for W, so the modifications may occur via a different mechanism than those below the sputtering threshold. There is a prediction that surface damage on samples will reduce the flux required for fuzz formation[237], this could be important in ITER where not only will the surfaces of components be engineering surfaces, but neutron damage on tungsten components may affect the fuzz formation mechanism.

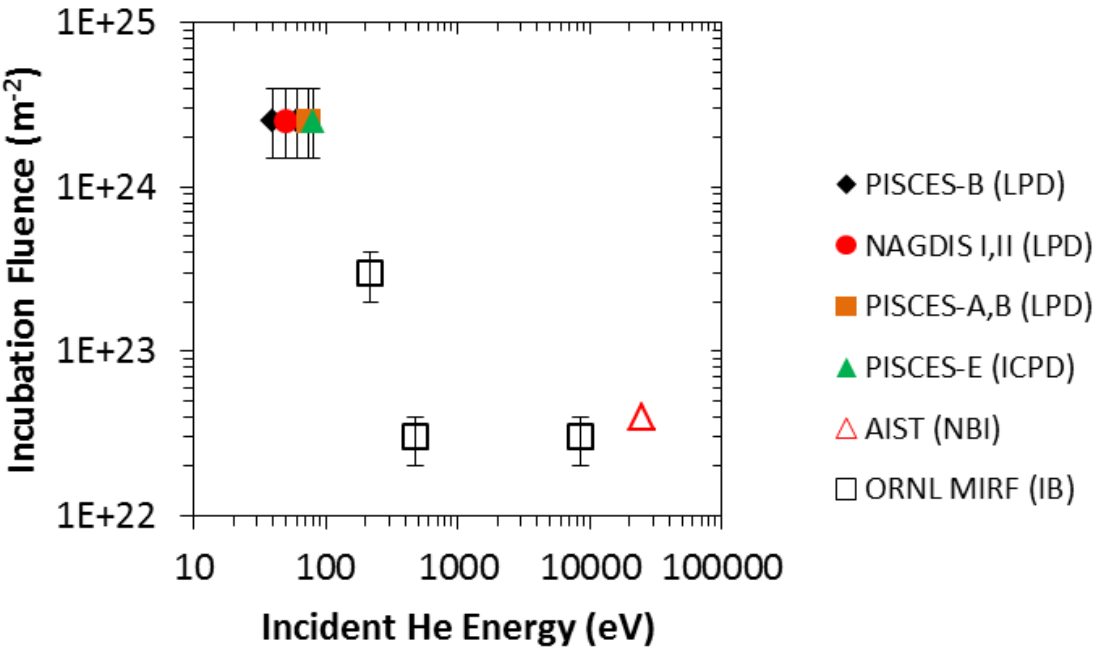

Figure 2.45: Variation of Incubation Fluence with Incident He Energy, using data from Linear Plasma Devices (LPDs) and Inductively Coupled Plasma Devices (ICPDs) [207], Neutral Beam Injection Facility (NBI) at AIST [246] and the Ion Beam (IB) at ORNL MIRF [237]. Temperatures of exposure vary from ~800-1527 °C.

2.4.2.2 Fuzz Growth in Existing Tokamaks

It should be noted that plasmas in linear plasma devices and tokamaks are different. In a LPD, the ions will be normal on the surface of a sample, whereas in a tokamak they would be grazing. Additionally in a tokamak there would be a higher parallel heat flux in comparison to a LPD [208]. Fuzz has been observed within the Alcator C-Mod tokamak (at the Plasma Science and Fusion Center, MIT, USA), where it grew and remained even after being exposed to high heat fluxes of up to ~40 MWm^{-2} [1], [208]. Under normal operations the divertor surface typically would not reach the temperatures required for fuzz formation in a LPD, however there are some Mo tiles of the divertor tilted ~2° into the toroidal B field, on which W Langmuir probes are embedded and tilted at 11° into the B field lines, where temperatures greater than the 700 °C required for fuzz formation in LPDs could be achieved [208]. The peak

temperatures were ~1900 °C and the energy of the ions was between 50 and 250 eV, with a fluence of ~9×10^{25} m^{-2} reached. Within a 12.7 s (achieved via 14 consecutive pulses)exposure time, a fuzz layer of thickness 600±150 nm was produced [208]. It is interesting that such a significant fuzz layer was achieved in just 12.7 s, which is significantly lower than typical LPD exposures. In this experiment it was attempted to recreate the conditions for fuzz growth observed in LPDs, however the conditions were not exactly like the conditions that would be expected in ITER or DEMO, for example there was no active cooling, ELMS or a D-T plasma, so the fact that fuzz was observed in this instance does not confirm that fuzz could form in ITER or DEMO [208]. An experiment was then carried out in the Pilot-PSI LPD, attempting to recreate the experiment in the Alcator C-Mod tokamak. Despite the differences in the plasmas in the two devices, what is significant is that the fuzz formed in the LPD was extremely similar in terms of appearance and thickness to that seen in the tokamak [254]. This provides support for using LPDs as a good simulator for a realistic tokamak environment.

Additionally fuzz formed in the NAGDIS LPD was exposed to edge He/D or pure D plasmas in the TEXTOR tokamak at temperatures of 300 and 800 °C [232] . Either complete erosion of the fuzz was observed, or else a deposition of C on top of the fuzz (C is present from erosion of the graphite limiter [255]). It was observed that C deposition was greater on fuzzy surfaces in comparison to pristine surfaces [232]. The complete erosion of the fuzz is in contrast to recent findings in the DIII-D tokamak [256]. Fuzz was grown on samples in the PISCES-A device and then was placed in the lower divertor region of the DIII-D tokamak and were exposed to D plasmas. The samples were either exposed to 2 discharges (3.5 s each) or three

discharges that ended with a vertical displacement event (VDE)[6]. For a duration of 4 ms, in the current quench phase of the disruptions, a heat flux of 20 MW m^{-2} was reached. Some samples were also exposed to He plasmas (3 s in one discharge, 11 s in four discharges and 13.5 s in four discharges). In all the experiments the fuzz remained undamaged, except in some areas where unipolar arcing had occurred. Rudakov *et al.* suggested the fact that the fuzz remained undamaged meant that it may be less susceptible to erosion, however, it was also observed that arcing was more likely to occur on fuzzy surfaces as opposed to pristine ones (also in agreement with Kajita *et al.* [257]). The removal of fuzz via arcing could still result in dust production, which again would be detrimental to plasma performance [256].

2.4.2.3 Fuzz Growth in Future Tokamaks

If we consider the conditions expected in ITER, as to whether the parameters for fuzz growth could be achieved, in terms of temperature, it is observed from Figure 2.37, that for D-T operation, on the outer target of the divertor, the 700 °C minimum temperature is exceeded across ~6 cm of the outer target on one cassette. As there are 54 cassettes making up the divertor, this is a considerable area where the temperature required for fuzz growth is reached.

Considering energy requirements for fuzz formation; a key parameter of ion energy expected within ITER will be dependent on whether the plasma in ITER is attached or detached. In order to limit the heat flux during nuclear operation of ITER, detached plasmas will be used. The ion energies in the detached plasma are not likely to exceed 8 eV, which is achieved via the injection of gas into the divertor [165], [222], [258], [259]. Within the attached regime, incident ion energies close to

[6] A large (can be up to several tonnes) upward force on the vessel generated due to the interaction between the poloidal magnetic field and the magnetic field of the current induced in the vessel as a result of escaped magnetic energy from the plasma, during a disruption or instability [312].

the divertor are expected to be greater than 30 eV [79]. Therefore if we take the currently accepted minimum energy of 20 eV, during the detached regime it is unlikely fuzz will form. However, as mentioned in Section 2.4.2.1, fuzz has been observed at energies as low as 12 eV [228] and therefore it cannot categorically be stated that fuzz will not form in ITER or DEMO.

The fluences required for fuzz formation are also considered. The incubation fluence for fuzz growth is assumed to lie between 2.5-4×10^{24} m^{-2}, as suggested by Kajita and Petty. The particle flux at the outer strike point in ITER is estimated to be ~10^{24} $m^{-2}s^{-1}$ [93], and considering that the He concentration in burning plasmas is expected to be ~5-10% of the incident flux [250], the He flux to the divertor could reach up to ~10^{23} $m^{-2}s^{-1}$, which across a 400 s pulse would correspond to a fluence of 4×10^{25} s^{-1}, which is well above the current incubation fluence values.

Furthermore, the engineering surfaces or the neutron damage could reduce the flux required for fuzz formation, and this is something that needs investigation. Another aspect to consider is the Be or C impurities which are likely to be present in ITER could mitigate fuzz growth, and result in the formation of C or Be-W layers, as has been observed in experiments where Be and C were injected into D_2-He plasmas by Baldwin *et al.* [249].

Several of the leading researchers in fuzz have said that it is a possibility that fuzz will grow within future tokamaks [254].

2.4.2.4 Fuzz Growth Mechanisms

2.4.2.4.1 Experimentally Observed Mechanisms

There have been many equations developed that predict the growth of fuzz, including those suggested by Baldwin *et al.* and Petty *et al.* [207], [219]. However,

such equations did not address the basic physics over why fuzz is formed. SEM and TEM observations of fuzz growth have been used to try and understand the formation mechanism of fuzz, and there have also been attempts to look at the basic physics of fuzz formation, which shall be discussed. Several theories exist in regards to the mechanism for fuzz growth. All of them require the formation of He nanobubbles and high temperatures, however, they look at various different thermally activated process that could be responsible for the mechanism of fuzz growth. This includes bubble clustering and migration, transport of vacancies, mobility of W and adatom[7] diffusion [203], [220], [221], [260]–[263]. These possible mechanisms are discussed in detail in this section.

Initially Kajita *et al.* studied the fuzz formation mechanism, using SEM to investigate the morphological changes of samples exposed to He plasmas in the NAGDIS-I LPD for different durations, so as to try and elucidate a formation mechanism [203]. A schematic of the proposed mechanism is shown in Figure 2.46 [203]. It was proposed that initially He bubbles form below the surface, coalesce and then burst, resulting in the formation of pinholes (Figure 2.46 a). This requires a minimum temperature of 700 °C, and Monte Carlo simulations by Sharafat *et al.* indicate that with increased temperature the pinhole size increases [264]. The pinholes and the bubbles surrounding them then coalesce, causing the holes to become deeper (Figure 2.46 b), (Figure 2.46 c). Following this, the bubbles inside the nanostructure swell and coalesce, resulting in a rod-like formation (Figure 2.46 d). This is a very simplistic explanation, and only considers early stages of formation.

[7]Adatoms are atoms that lie on the surface of a crystal lattice

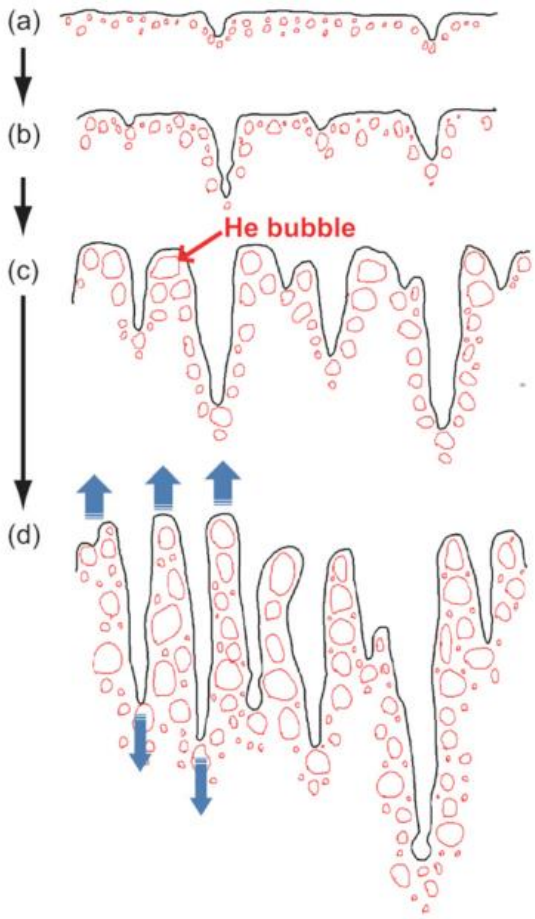

Figure 2.46: Initial proposed mechanism for fuzz formation by Kajita *et al.* Image taken from [203].

TEM analysis of fuzz formed in NAGDIS-I and II LPDs was then used to predict a more detailed fuzz growth mechanism by Kajita *et al.*[220]. A schematic of the proposed mechanism is given in Figure 2.47. Kajita *et al.* proposed that helium bubbles form close to the material surface following exposure to He plasmas at temperatures >700 °C (Figure 2.47 a). The bubbles will then thermally migrate and coalesce, resulting in bubble growth. These large bubbles then push up on the surface, resulting in blister formation (Figure 2.47 b). At this stage, ion energy and temperature are key factors that dictate vacancy formation and consequently bubble formation in the material. As the helium fluence increases, some of the blisters burst, resulting in the formation of pinholes and protrusions (this visibly resembles early

stage fuzz) (Figure 2.47 c). Bubbles in the base of the protrusions migrate and grow and also burst, resulting in elongated and thinner structures (Figure 2.47 d).

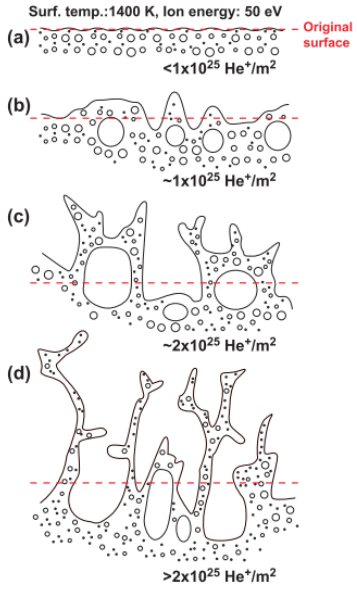

Figure 2.47: Fuzz growth mechanism proposed by Kajita *et al.* Image taken from [220]

The most recently observed mechanism by Takamura *et al.* is shown in Figure 2.48. Surfaces were partially covered, so as to observe fuzz growth at different time stages of growth in just one shot, essentially relying on the flux gradient of the plasma beam. This model suggests that initially pitting occurs on the surface of the bulk metal (see Figure 2.48 (1)). This is followed by helium bubbles from within the sample thermally migrating to the surface of the sample, where they burst, resulting in He gas being released (2). As the holes grow in size, due to the increased fluence of He ions impinging on the surface (3-4), 'nano-walls' (thin regions of W in between holes) are formed (5). There are also helium bubbles within the nano-walls, which results in the formation of holes in the centre of the nano-walls (6). This leads to a loop structure (7). As the He ion fluence continues to increase, the loops increase in size due to the nano bubbles inside the loops exerting increasing surface

tension (8). When the loops fracture and branch, fuzz is formed (9) [263]. Takamura *et al.* also suggested that the shear modulus (describes shear motion), a parameter that varies with He content as well as temperature could provide an indication as to whether fuzz was likely to grow on the surface of a material. They suggested within a critical range of shear modulus values, if the temperature band for fuzz growth is wide enough, and is within the range where He mobility in the bulk material is ensured, then fuzz will grow (see Figure 2.49 (a)). They postulated that within this critical modulus range, if the temperature band for fuzz growth is too narrow, and/or within this band there is no mobility of He, fuzz will not form (see Figure 2.49(b)). However in these cases it is still possible that at higher temperatures holes and bubbles are still able to form [263].

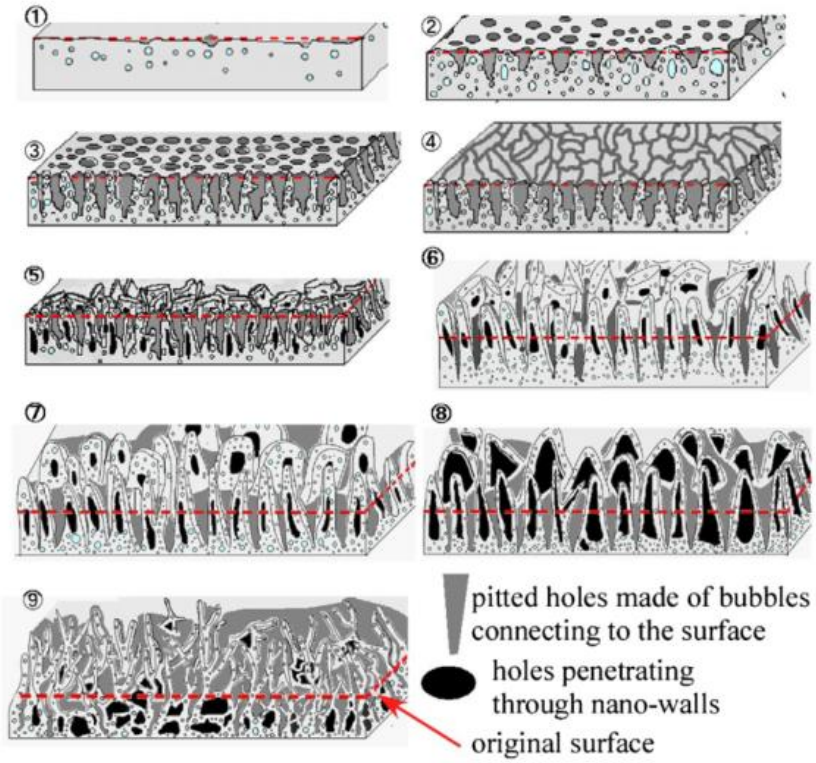

Figure 2.48: Experimentally observed fuzz formation mechanism [263]

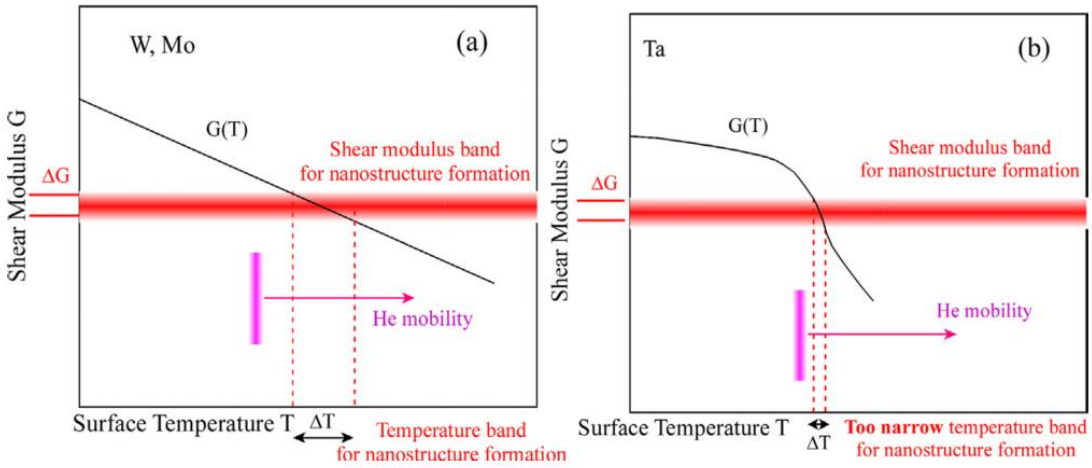

Figure 2.49: Schematic showing the relationship between the shear modulus and surface temperature of metals and the likelihood of fuzz formation. ΔG is the shear modulus range in which fuzz growth can occur, ΔT is the temperature range in which fuzz growth can occur. The vertical bar is the lowest temperature above which He mobility can occur. Fuzz formation is feasible in W and Mo, but in Ta the narrow temperature band at which fuzz can grow, makes it difficult to form. Taken from [263]

All three models shown in Figure 2.46, Figure 2.47 and Figure 2.48 reinforce the prerequisite for helium bubble formation and bursting for fuzz formation to occur.

2.4.2.4.2 Physics Based and Computer Models

Krasheninnikov then used a physics based approach in order to develop a model for fuzz growth, which was centred around viscoelastic behaviour of tungsten at high temperature, exposed to He irradiation [260]. A schematic of the model is shown in Figure 2.50. On irradiation, He bubbles of the order of 10s of nanometres in diameter form below the surface of the sample. There is an asymmetrical force on the surface atoms due to one side being the bulk and the other the edge. This results in the bubbles being pushed up towards the surface. As the fluence increases, new bubbles can form above the original bubbles that had pushed up on the surface (Figure 2.50 a). This results in further stress in the W, and due to the fact the viscosity of W decreases with temperature, creep becomes of importance, W then begins to move up around the bubbles, and the fuzz is formed (Figure 2.50 b). Krasheninnikov

predicted that high pressure helium bubbles are created, resulting in a large force being exerted on the W, and this results in the viscose flow of W around the bubbles and towards the tip (Figure 2.50 c) [260]. This model resulted in equations being developed that predicted the $t^{1/2}$ growth rate predicted by Baldwin *et al.* in Equation 2.9 [219] and therefore consequently will also agree with Petty's $\Phi^{1/2}$equation (Equation 2.11) [207] at exposures above the incubation fluence, if considering a constant flux, as often is the case in experiments. The Krasheninnikov model predicted the temperature dependence of the rate of fuzz growth observed experimentally, and also that the fuzz growth would saturate after fluxes of 10^{22} m^{-2} s^{-1}, another experimental observation by Baldwin *et al.* in [249]. The model also predicted that fuzz growth would stop at temperatures greater than 1700 °C, which fits with the majority of experimental observations in linear plasma devices in Section 2.4.2.1. However, fuzz has been observed at higher temperatures in the literature, for example in the Alcator C-Mod tokamak (~1900 °C [208]) and in the JAERI ion beam (2600 °C [243]). However, it is not clear in these cases whether the fuzz still grows at these temperatures above 1700 °C or if it grew before these temperatures were reached and then was not removed or annealed at the higher temperatures. Therefore this model may not be suitable for the growth observed in the Alcator C-Mod tokamak or JAERI ion beam if it occurred above 1700 °C. The model does not address the competition of annealing versus growth.

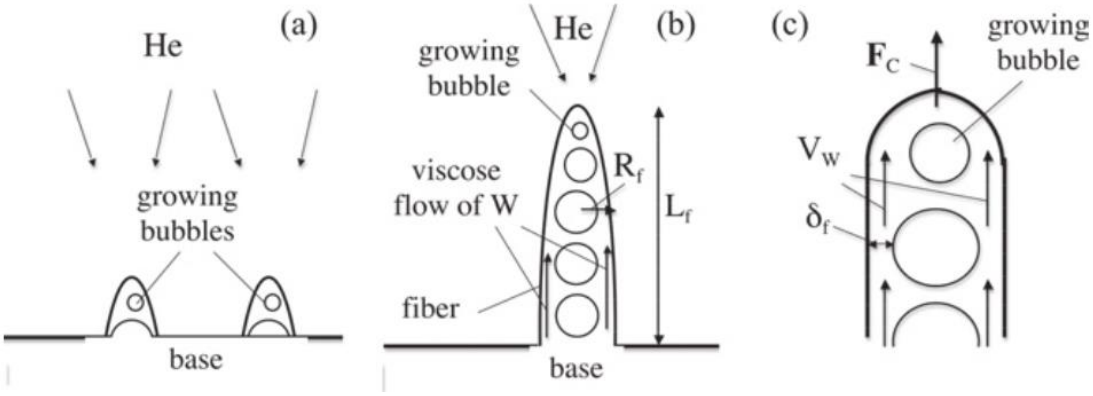

Figure 2.50: Proposed model for fuzz growth by Krasheninnikov, reproduced from [260].

Another model proposed by Martynenko and Nagel suggested that helium ion irradiation results in adatoms appearing on the surface [261]. The threshold energy for adatoms to be knocked out from the surface layer is a third of the sputtering threshold, which corresponds with the 20-30 eV typically quoted in the literature necessary for fuzz formation (although as has been mentioned in Section 2.4, fuzz has been observed at lower energies of 12 eV). Clusters of adatoms are formed and fibre growth occurs in two main areas; over the surface of high pressure helium bubbles and at the edges of open He bubbles. There are many traps for adatoms at the tips of the fibres and diffusion of the adatoms over the fibre occurs, resulting in fuzz growth. The model also agrees with the $t^{1/2}$ growth rate predicted by Baldwin *et al.* in Equation 2.9 and with Petty's Equation 2.11, given the appropriate caveats listed above [207], [219]. Recent tests however have suggested that the formation mechanism does not depend on adatom diffusion, but rather purely He ion bombardment[265].

Another proposed mechanism for fuzz was developed via molecular dynamics and kinetic Monte Carlo methods by Lasa *et al.*[262]. Again, like all previous models the mechanism starts with the trapping of helium, resulting in the formation of bubbles.

The bubbles result in growth of the surface, which is achieved via a loop punching mechanism. The bubbles close to the surface burst. These two parts of the growth mechanism balance, resulting in increased roughness of the surface. As the surface roughness increases, there is an increased surface area for bubbles to burst, which leads to a reduction in the retention rate of helium and consequently the rate of growth of fuzz. This again corresponds to a $t^{1/2}$ dependence of fuzz growth. This model does not take into account the observed temperature window of 700-1700 °C observed in LPDs [262].

Sefta *et al.* [266] also conducted molecular dynamic simulations investigating the early stages of the fuzz growth mechanism. They predicted that when the He atoms are implanted in the W, they form clusters and are mobile up to the point at which the size of the cluster is bigger than 7 or 8 atoms, following which a trap-mutation process, resulting in a vacancy and W self-interstitial atom (SIA), reduces mobility of the cluster. The SIA will then either move to the free surface or stay bound loosely to the He cluster. At a He cluster, there is an increase in density of the SIAs, which eventually form prismatic dislocation loops, which can glide in the ⟨111⟩ direction towards the surface of the W, resulting in adatom 'island' formation. This results in the growth of He bubbles, and the surface above the bubbles becomes thinner and eventually ruptures, resulting in the surface roughness that precedes fully formed fuzz. The model also revealed the influence of grain boundaries on fuzz formation. The grain boundaries act as a sub-surface sink, resulting in a high density of small clusters, in contrast to larger clusters observed within single crystal models. The presence of grain boundaries increases the total helium retention. The retention of He in a (100) surface was seen to decrease with temperature, whereas for a (100)

surface with a grain boundary, the temperature had a limited impact on retention [266].

Smirnov *et al.* have developed a molecular dynamics model in order to describe the growth and coalescence of He bubbles in W [267], following which Krasheninnikov and Smirnov developed another theoretical model in order to describe He cluster dynamics in W [268]. The molecular dynamics model revealed that dislocations and vacancies form close to nano-bubbles. The dislocations and vacancies act as traps for He, leading to further nano-bubbles to nucleate, which is something that can occur in bulk samples, as well as within the fuzz tendrils. This process results in a snowball effect, which it was suggested meant that the starting density of defects only weakly influences the final stages of evolution of nano-bubbles. The He bubbles were polyhedron in shape and the bubble faces were seen to be parallel with the slip planes. The edges of the bubble were observed to be in line with the ⟨111⟩ slip directions. The shear strength of the crystal responsible for the generation of dislocations, rather than surface tension was seen to be more influential on the pressure within He bubbles. Regions of tension formed around the face of the bubbles and compression at the vertexes of the bubbles, meaning that the induced stress field around bubbles was anisotropic. It was suggested that the main mode of He transport in the stress field is via drift from the area of compression to tension and this results in the migration of He to the vertexes of the bubble along the dislocation lines. The bubbles were seen to coalesce via lateral growth of adjacent bubbles [267], [268]. The Krasheninnikov model predicted that surface modification will not occur until the fluence exceeds ~2-3×10^{24} m^{-2} (in agreement with incubation fluence suggested by Petty *et al.* [207]), regardless of the flux used. The model predicts that a 30 nm thick layer of He bubbles that are ~2 nm in size will form prior

to the growth of fuzz. As in Smirnov *et al.*'s article, the strain around bubbles as they grow results in the generation of traps, which act as nucleation sites for further bubbles, providing an explanation for the bubbles observed within tendrils experimentally [268].

Many of the models to explain fuzz growth have just focused on the very early stages and used molecular dynamics with focus on the formation and dynamics of He nano-clusters. The fluxes used in such simulations (~10^{27} m^{-2} s^{-1} , e.g. [262], [266]) are generally higher than those typically used experimentally (10^{22}-10^{24} m^{-2} s^{-1}[207]).

Ito *et al.* [209] suggested that rather than using a single modelling approach, as most previous attempts to model fuzz have done, to use different modelling approaches for each stage of fuzz growth, splitting it into four parts. The first three parts were classified as penetration, diffusion and agglomeration, and helium bubble growth, which could be analysed via binary collision approximation, density functional theory and molecular dynamics. The fourth step was the formation of the fuzz nanostructure itself and was modelled using a hybrid molecular dynamics and Monte Carlo simulation. In the first stage of the model, the lower bound for incident energy for He to penetrate into tungsten was calculated as 6.29 eV, in good agreement with experimentally observed value of 6 eV [204], [252] and the upper bound was set as the sputtering threshold for He incident on W of 100 eV. In the diffusion and agglomerations step, density functional theory was used and showed that He diffused faster than H, the agglomeration of He was found to be unlimited and additionally the agglomeration of He at interstitials was seen. In the growth stage, again loop-punching was observed, and strain is observed in the W lattice around He bubbles, which is released via dislocation loop formation. It was observed that bubble growth

could occur via agglomeration of He at both vacancy and interstitial sites. The fuzz growth step used Monte Carlo methods in order to model He diffusion and injection, whereas molecular dynamics was used to model the tungsten deformation. It was seen that with increased fluence, bubbles grew, and those close to the surface would push up the atoms of W at the surface, resulting in the formation of an arch. He bubbles would burst below arches, resulting in the breaking of the arch at the support points, causing the turning up of the arch. The surface of the sample is then observed to have concave and convex regions, with preferential He bubble growth in the concave regions. The bursting of the He bubbles in the concave regions, results in deepening of those regions, as well as strengthening and growth of the convex regions. This model was the first computational model to cover multiple scales and seemed to show the initial stages of fuzz growth. The fluences used in this model are of the order of 10^{21} m^{-2}, which is still ~3 orders of magnitude less than the typical 10^{24} m^{-2} used in experiments [209].

To conclude, modelling work has used several different types of simulation methods including kinetic Monte-Carlo [198], molecular dynamics [262], [266], [267], binary collision approximation [217] and density functional theory [211]. The models have indicated that He clusters at W vacancies, forming bubbles, with the indication of larger bubbles at higher temperatures [269] (something that has also been observed experimentally, resulting in wider tendrils at higher temperatures [203], [239], [250]).

There are several fuzz growth mechanisms that have been proposed, both from experimental observations using SEM and TEM, physics approaches and modelling methods. The majority of the proposed mechanisms are based around the formation of nanobubbles at elevated temperatures, and other thermally activated mechanisms.

The majority tend to agree with Baldwin's $t^{1/2}$ growth rate. However, as has been proposed by Petty *et al.*; this is simply a special case of a fluence dependence [207], where there is also an incubation fluence, so it is not clear if these models would hold at fluences close to the incubation fluence, where the $t^{1/2}$ growth rate is not observed. Additionally these models do not take into account orientation dependence of fuzz growth.

2.4.2.4.3 Orientation Dependence of Fuzz Growth

In the literature it has been observed that there is an orientation dependence of fuzz growth [270], [271], specifically during early stages of development [239]. Once the fuzz has fully developed, this orientation dependence has been observed to disappear [239]. As the tendrils become longer and bend, the original orientation is no longer observable.

Yamagiwa *et al.* suggested that the initial orientation dependence was to do with the variation of diffusion of He in the different grains [270]. Yamagiwa *et al.* suggested that the early stage growth of nano-bubbles may be slower on the (110) tungsten face.

Ohno *et al.* then conducted an investigation of the orientation dependence of helium plasma damage on W in the NAGDIS-I LPD [271]. Samples were exposed to a He plasma at temperatures of 1427 °C, energies of 25 eV, up to a fluence of 5.6×10^{26} m^{-2}, for an exposure time of 10 800 s. A wavy structure, indicative of early stage fuzz growth was observed in the {001}, {112}, {101} and {111} grains, while any modifications in the {103}, {102}, {407} and {203} grains was limited, as may be observed in Figure 2.51. It was suggested that the angle between the {101} slip face (the face with the greatest areal density) and the surface of the grain under bombardment influenced the wavy structure formation (Figure 2.52 b)). On exposure

to He plasma, He atoms become trapped within thermal vacancies, resulting in the formation of He bubbles as shown in Figure 2.52c). As the fluence increases, the bubbles grow, resulting in increased pressure within the bubbles, causing them to exert a force on the W lattice (Figure 2.52 d)). As He bubble formation is related to interaction between He atoms and thermal vacancies, areal density impacts He bubble growth. The {101} slip face areal density is higher than other faces and the binding energy of W in the {101} face is stronger than in the other faces. Therefore pressure in the He bubbles in this face becomes larger than the others. The high pressure He bubbles can then push the W lattice along the {101} face, resulting in a wavy structure (Figure 2.52 e). They propose that how regular the wavy structure is depends on the angle between the {101} slip face and the plane of the grain under exposure. The larger the angle, the increased likelihood of wave structure formation, with more regular structures at larger angles. For example, there is a large angle between the {001} orientation and the {101} face and therefore the wave structure forms easily in the {001} grains. However, there is a much smaller angle between the {103} orientation and {101}, resulting in a much reduced wave structure growth, as is observed in Figure 2.51 e) and Figure 2.52 b) and f) [271].

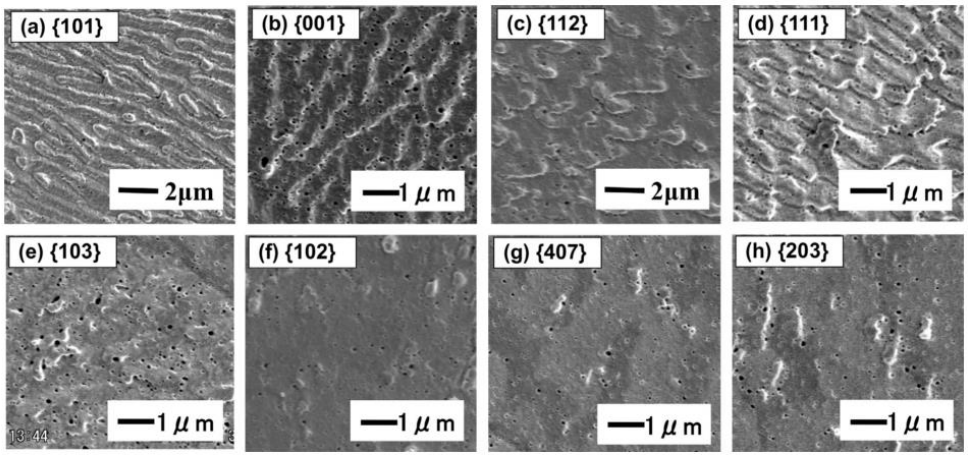

Figure 2.51: He plasma damage in a) {101}, b) {001}. c) {112}, d) {111}, e) {103}, f) {102}, g) {407} and h) {203} orientations of W at temperature of 1427 °C, energy of 25 eV, and fluence of 5.6×10^{26} m^{-2}, for an exposure time of 10 800 s [271].

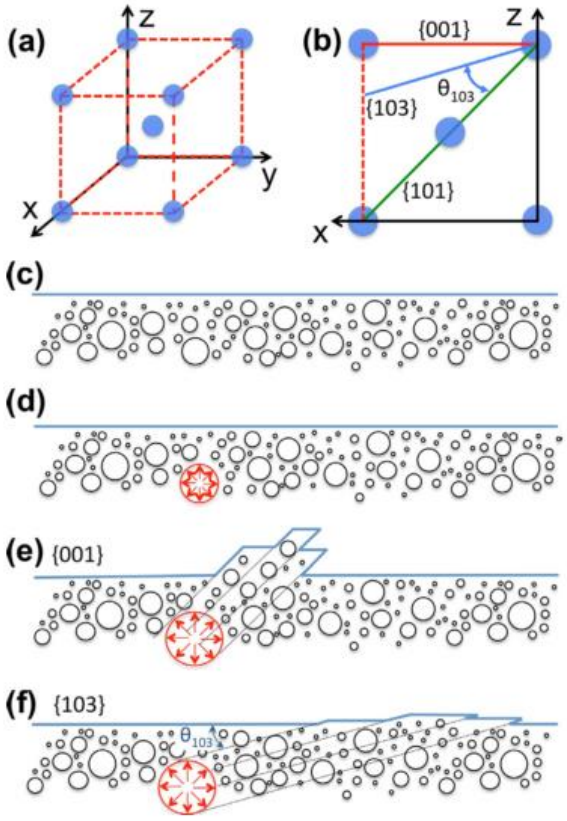

Figure 2.52: Potential mechanism for wavy structure: a) BCC structure schematic, b) faces of the crystal orientation of {101}, {103} and {001}, and (c-f) formation mechanism of wavy structure in grains with different surface crystal orientation [271].

Martynenko and Nagel suggested that helium ion irradiation results in adatoms appearing on the surface [261]. Hammond and Wirth conducted an investigation via

molecular dynamics simulations into the effect of orientation on the depth distribution of He atoms and surface modifications (including adatoms) at 100 eV [272]. The model shows that retention of He is not only highly dependent on the flux of the incoming He atoms**,** but additionally again an orientation dependence is predicted. The mean depth to which He will penetrate, as well as the reflection and initial retention of He is found to vary with orientation (in agreement with Yamagiwa *et al.* [270]). They observed that the formation of a single He substitutional atom below a {111} or {211} orientation results in the release of energy, and as only one interstitial He atom is required in order to produce an adatom/substitutional pair, these orientations have a higher retention of He during initial plasma exposure and a concentrated band of small He clusters is seen near the surface. On the other hand energy is required to produce a single He substitutional atom below {011} surfaces. They also observed that in order to induce adatom formation in the {001} and {011} surfaces, at least two He atoms in a cluster were required. The {011} surfaces therefore will have lower He retention rates, and as more He atoms are required to produce adatoms, larger bubbles, at higher depths into the surface will be required before any surface modifications can occur. The model also showed that orientation only affected the development of He clusters and bubbles in the first 3 nm from the surface. The variation in the formation of vacancies and bubbles with orientation could result in variation in fuzz growth; with the {111} and {211} more likely to develop surface modifications, in comparison to the {001} and {011} surfaces [272]. However if this is the case, then the results of Hammond and Wirth and Ohno *et al.* do not appear to agree. Ohno *et al.* observes wave like growth (precursor to full fuzz growth), on the {111} crystal face, however, Ohno *et al.* predict that the {001} should produce a more ordered wavy structure

than the {111} [271]. From the experimental observations of Ohno *et al.* wavy structures are observed on both {001} and {111} surfaces, giving support to Ohno's model. However, it should be noted that there are no {211} or {011} surfaces to compare to [271], so the Hammond and Wirth model cannot be discounted.

2.4.2.4.4 Variation of Fuzz Growth with Grain Size

In addition to grain orientation, grain size has been observed to influence fuzz growth. Baldwin *et al.* compared fuzz growth in various different tungsten samples [221]. The samples compared were a standard 99.97% pure W sample, stress annealed at 1000 °C for 1 hour (SR W), a ⟨100⟩ single crystal sample produced via a floating-zone-melting method (SC W ⟨100⟩), a W sample produced to the ITER ASTM B760 standard (ITER Grade W), a vacuum plasma sprayed (VPS) W sample (VPS W), and a W sample produced via powder metallurgy and subsequently heat treated at 1527 °C (i.e. above the temperature of recrystallization for W) (RC W). They were all exposed to He plasmas with a flux of ~5×10^{22} m^{-2} s^{-1} at a temperature of 847 °C for one hour. A summary of the thickness of the fuzz layers observed is shown in Figure 2.53. For the recrystallized sample it should be noted that the 'surface' layer thickness is provided in the plot, however unusually, compared to all other samples, fuzz was observed at depths of 200-300 μm, and it was only after 1000 μm that no further nano-structuring was present. It was suggested that the nano-structuring just occurred at grain boundaries deep into the sample, not in the whole grains themselves. The observation of nano-structuring so deep into the sample was suggested to be a result of recrystallization. It was proposed that the increased trapping sites induced by the recrystallization process at the grain boundaries may have allowed for He bubble growth and hence fuzz formation at the grain boundaries. This was related to previous TEM observations where preferential

He bubble growth had been observed at surface grain boundaries. The reason for the nano-structuring to occur so deep into the sample however, was still not clear, but it was suggested that by extrapolating the He diffusion coefficient reported in [273] to 847 °C, He could diffuse up to 2.07 cm after an exposure time of 1 hour, which is of the same order as the depth of observation in the sample [221]. Going back to Figure 2.53, although specific grain sizes are not provided, it is observed that the fuzz growth is reduced in the single crystal W, in comparison to the standard polycrystalline sample. Estimating via metallography techniques, the VPS W, appears to have a smaller grain size in comparison to the standard sample and has a much thicker fuzz layer. However, there is also the recrystallized sample, which presumably has a larger grain size than the standard sample, not only has a thicker 'surface' layer of fuzz, but also has fuzz up to 100s of microns into the depth of the sample. Therefore although the grain size does appear to be impacting fuzz growth, it cannot definitively be said what this effect is, and the variation in manufacturing method for all the samples also adds further complications to the comparison [221]. It could also be that the concentration of defects in each sample is effecting the fuzz growth, with high concentrations of defects acting as sinks for He (He is known to get trapped at vacancies, grain boundaries, dislocations and voids [165], [199], [200]), which may encourage He bubble growth.

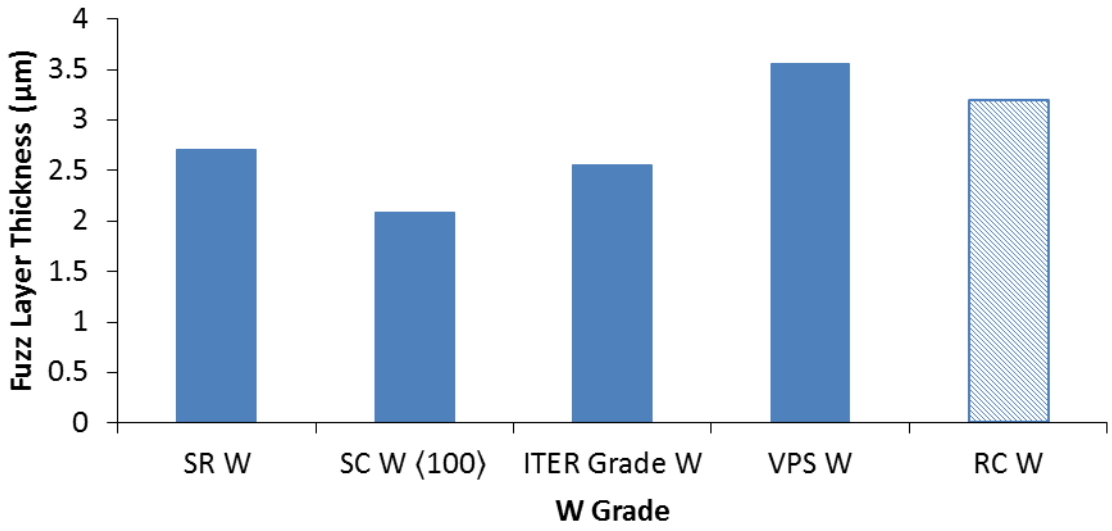

Figure 2.53: Variation of fuzz layer thickness for different W grades, using data from [221].

2.4.2.5 Fuzz Growth in Other Materials

Fuzz growth has not only been observed in W, it has been seen in W alloys as well as other materials. In terms of alloys, Baldwin *et al.* observed fuzz growth in W-La_2O_3 (1% wt), ultra fine grained (UFG) W doped with TiC (1.5% wt), as well as W doped with 5% wt Re, and a chemical vapour deposition (CVD) sample doped with 10% wt Re exposed to He plasmas [221]. Tokunaga *et al.* also observed fuzz growth in W-(0.5,1.5)wt%TiC alloys exposed to D-He mixed plasmas, which in some cases were also seeded with Be [274]. Takamura *et al.* have also observed fuzz on Re wires exposed to He plasmas with an ion energy of 105 eV, flux of 2.5×10^{21} $m^{-2}s^{-1}$, fluence of 1.9×10^{25} m^{-2}, at a temperature of 977 °C [263]. Takamura *et al.* also observed fuzz growth in tantalum sheet, nickel sheet and molybdenum [263]. Fuzz growth has also been observed in iron and pure titanium by Kajita *et al.* [275]. The formation conditions required for fuzz growth in all these samples have not been quantified to the same extent as W, due to the lack of interest for ITER.

Kajita *et al.* [203] suggested that the temperature band where fuzz growth was possible was controlled by the ratio of the surface temperature (T) to the melting temperature of the material (T_m), and using this, Petty suggested temperature windows for various other metals, based on observations in W, of 0.25-0.55 T/T_m in K [222]. Petty also noted that for materials with a lower sputtering threshold than tungsten there would be more competition between fuzz growth and sputtering, resulting in thinner layers of fuzz [222]. Takamura *et al.* [263] have suggested that whether fuzz will grow on a metal is based on a critical range of shear modulus values, which coincide with a temperature band for fuzz growth that is wide enough, and is within the range where He mobility in the bulk material is ensured, and have suggested the potential relationship between a material's properties and the conditions for fuzz growth (Table 2.5). The fluences used to grow fuzz in other materials (typically ~10^{25}-10^{26} m^{-2}) have been of a similar order to those used in pure W.

Table 2.5: Physical properties of materials and the relation to nanostructure growth, where ΔT is the temperature band at which fuzz formation can occur. The shear modulus given is for room temperature, without any effect of He content. Taken from [263] .

Z	Material	Crystal Structure	Melting Point (K)	Shear Modulus (GPa)	Nanostructure Growth	Temperature Range ($\Delta T/T_m$)
74	Tungsten (W)	bcc	3695	161	Well developed fuzz [228]	0.27-0.5
75	Rhenium (Re)	hcp	3459	178	Well developed fuzz[276]	0.36
42	Molybdenum (Mo)	bcc	2896	126	Well developed fuzz	0.28-0.36
73	Tantalum (Ta)	bcc	3290	69	Loops and/or loops with short protrusions	~0.29
28	Nickel (Ni)	fcc	1728	76	Well developed fuzz	~0.37
26	Iron (Fe)	bcc,fcc	1811	82	Well developed fuzz [275]	0.44-0.50
22	Titanium (Ti)	hcp	1941	41-44	Two types of fuzz depending on surface temperature [275]	0.26-0.44

2.4.2.5.1 Fuzz growth in Re doped samples

The effect of fuzz growth on Re and Re doped materials is of interest, as Re is a transmutation element that will be present in ITER and DEMO. Data from Baldwin *et al.* [221]suggested that Re addition inhibits fuzz growth (Figure 2.54). However, it should be noted that the manufacturing method of each sample was different, with the pure W being a rolled sample that was stress annealed for an hour at 1000 °C, the W-5%Re was simply stated to be doped with no further information, and the W-10%Re was prepared by CVD and therefore the manufacturing processes could also have an impact. Takamura and Uesugi have also observed the growth of a fuzz like structure on pure Re wire exposed to 105 eV He ions up to a fluence of 1.9×10^{25} m^{-2}, at a temperature of 977 °C. However, in this case the nanostructural modifications were thinner, straight and needle like in comparison to those observed in pure W or W-Re alloys, but this suggests that Re will never completely supress fuzz formation [263]. DFT simulations have shown that transition elements such as Re are more likely to occupy substitutional sites, impurities such as C and N are more likely to occupy octahedral interstitial sites, and He and O tetrahedral interstitial sites [277]. The binding energy between Re and He is close to 0, and in contrast to other substitutional atoms, Re will not trap He atoms [277]. Therefore in theory Re should behave in the same way as W, however, experimental observations reported in the literature indicate that Re may be inhibiting fuzz growth in W.

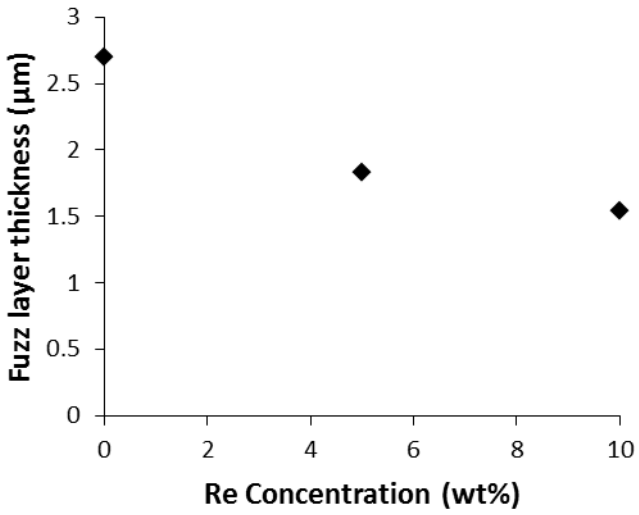

Figure 2.54: Effect of Re addition of fuzz formation, using data from [221].

2.4.2.6 Effect of Fuzz on Tungsten Properties

The most immediate effect of fuzz growth visible to the naked eye is that the surface of the exposed material turns black (Figure 2.55), as opposed to a shiny metallic finish like bulk W. Kajita *et al.* conducted a study into the effect of fuzz growth on optical reflectivity in W[278]. For W samples with fully developed fuzz, the optical reflectivity was observed to fall from 46% for the pristine sample to 1%, which corresponds to a 99% absorption of the incident light [278]. It was estimated that the fuzzy structure is capable of absorbing 98% of total solar light and suggested that it was the ‘darkest man-made metal’[278].

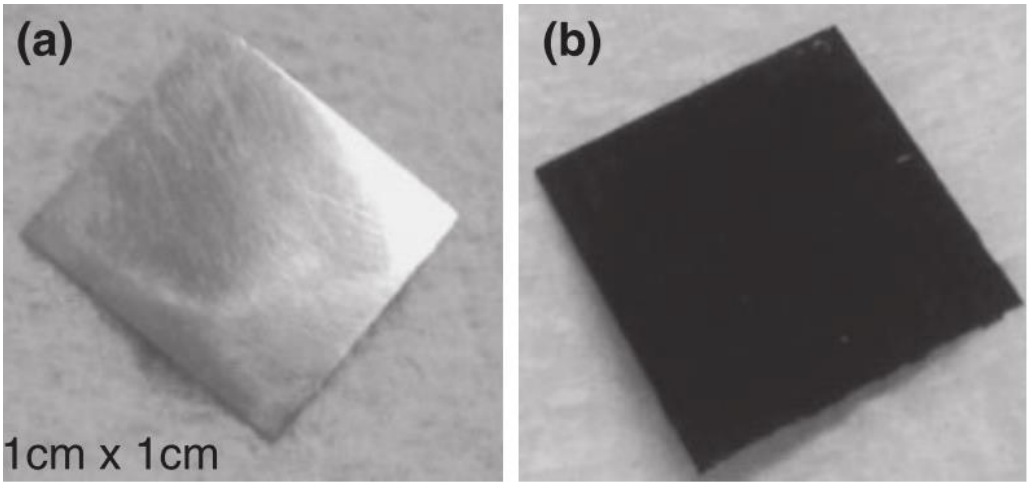

Figure 2.55: Tungsten sample before and after He plasma exposure in NAGDIS-II LPD, where sample b) has grown fuzz, taken from [279].

Investigations by Nishijima *et al.* [280] in the PISCES-B LPD have revealed that fuzz reduces the sputtering yield of tungsten. The thickness of the fuzz layer and the energy of the incident ion were found to influence the sputtering yield of W, and the ratio of the sputtering yield of the fuzzy layer compared to a smooth surface was observed to decrease with increased fuzz layer thickness and saturate when the fuzz layer thickness was >1 μm at ~10%. As an example, the sputtering yield for W with Ar ions at an energy of 110 eV, reduced from $\sim 5\times10^{-2}$ for a smooth surface to $\sim 9\times10^{-3}$ for tungsten with a 1 μm thick fuzz layer [280]. It was suggested that the reduced sputtering yield was due to the increase in porosity with fuzz layer thickness. The particles sputtered get trapped in between the fuzz tendrils and do not escape. At the beginning of fuzz formation the structure is more coarse and less porous so the sputtered particles have a greater chance of escaping the surface. As the fuzz develops, it becomes finer, with an increased porosity, allowing for more sputtered particles to be trapped [280]. A small decrease in the ratio was also predicted with a reduction in the incident energy of the ions due to the larger angle of sputtering of more W atoms at reduced energies, resulting in an increased likelihood of deposition onto the surrounding nanostructure [280]. Takamura *et al.* [281] also

observed the sputtering yield to decrease with fuzz growth, and suggested that the suppression of sputtering was qualitatively related to the ratio between the surface area at the top surface of the tendrils, facing the incident ions and the surface area at the bottom of the troughs of the fuzz [281].

Another advantageous property of fuzz as reported by Baldwin *et al.* [282] is that the presence of fuzz results in W to retain less D (where D exposures are at temperatures between 150-250 °C at fluences between 5-8 $\times 10^{25}$ m^{-2}) in comparison to bulk W. D retention was observed to be 250 times lower in a sample that had pre-grown fuzz in comparison to a sample that had not been previously exposed to a He plasma. It was suggested that this was due to He bubbles close to the surface, growing and interconnecting with each other, resulting in the production of pathways to the surface of the sample, which inhibits the diffusion of D to the bulk [282]. One of the main reasons W has been chosen as a divertor material is for its favourable tritium retention properties in comparison to other materials, the fact that fuzz could form may further decrease this retention (assuming D and T behave in the same manner) which could be desirable.

Nishijima *et al.* have also suggested that fuzz is more resistant to surface cracking in comparison to bulk W with a mirror finish, where cracks were seen following a single ~0.7 MJ m^{-2} plasma pulse. However samples with fuzz growth layers between 1 and 3 μm in thickness did not crack even after 10 pulses at the same energy [283]. It was suggested that this was due to the increased surface area that resulted from the presence of fuzz allowing for increased efficient dissipation of energy [283].

Takamura *et al.* also suggested that fuzz resulted in a reduced secondary electron emission in comparison to bulk W, due to the observed deepening of floating

potential during He exposure [284].

Kajita *et al.* have reported that fuzz exhibits a different thermal response in comparison to bulk tungsten [229]. Initially studies were carried out in the NAGDIS-II LPD where fuzzy samples were exposed to 0.6 ms ruby laser pulses. Surface melting was observed. Numerical calculations suggested that the fuzz resulted in a thermal conductivity of almost zero close to the surface, a reduction of more than two orders of magnitude of the thermal conductivity of bulk tungsten [229].

Following this, fuzz was initially grown on samples in the NAGDIS-II LPD, and then exposed to a high power laser pulse in the MAGNUM-PSI device [225]. Additionally pulsed plasmas were used to investigate the thermal response of fuzz in MAGNUM-PSI. A much higher temperature increase was observed in both cases in the fuzzy samples (400-500 °C for pulsed plasma) in comparison to bulk samples (<100 °C for pulsed plasma). Again melting was observed on the surface of the fuzzy samples subject to either the laser or plasma pulses, despite measurements with an infra-red camera showing that the temperatures reached were below the melting point of W and the energy of the pulses used was below that required for melting. Three suggestions on changes to thermo-physical properties were made as to why the tungsten would melt below the melting point, including a decrease in melting point due to the small size of the nanostructure, a decrease in the thermal conductivity (this time also taking into account porosity, which was not considered before) and finally non-uniform surface heating [225].

It was suggested that the decrease in melting point for the nanostructure would not be sufficient enough to explain the melting observed and that although the reduction in thermal conductivity would result in a temperature increase, this again would be

insufficient to cause melting [225]. The theory that parts of the fuzz were thermally isolated close to the surface, resulting in non-uniform surface temperatures was suggested. This meant that the average temperature across the whole surface was actually less than that measured via the IR camera, but localised heating in certain areas resulted in the increased measured temperature. It was suggested that in the locally heated areas, temperatures high enough for melting could be reached. However, with the current experimental observations with the IR camera limited to a 0.5 mm resolution, further experiments with a higher resolution camera are necessary [225]. Direct measurements of the thermal conductivity of fuzz will also be of interest. There was also a suggestion that vaporisation of a depth of between 2-7.5 nm of the fuzz could occur for a single ELM event in ITER, and as W contamination cools the plasma this could be an issue. However this estimation did not take into account vapour-shielding, pulse accumulation and re-deposition that could also occur which may mitigate the erosion [225].

Kajita *et al.*[285] and Tokitani *et al.*[286] both observed arcing on fuzzy samples at heat fluxes of ~10^{10} W m^{-2} (similar to power of type-I ELM) and 4.2×10^{6} W m^{-2} respectively. Further studies by Kajita *et al.* observed that for a sample exposed to a plasma with a He fluence of 2×10^{24} m^{-2}, where only the early stages of fuzz will have formed, the probability of ignition of arcing was >90% [287]. This is in contrast to a pristine sample where no arcing was observed [287]. Therefore fuzz is seen to increase likelihood of arcing, which is problematic as it could contribute to erosion in ITER, affecting the performance of the plasma. Kajita *et al.* have estimated, following pulsed laser exposures in the NAGDIS-II device that arcing could cause erosion at the rate of 10 mg s^{-1} [257]. The likelihood of arcing was also observed to be dependent on electron density as well as sheath potential [288].

2.5 Work required

Tungsten has been confirmed as the material of choice for the divertor in ITER. It will also be used in DEMO. Considerable research has been undertaken in order to try and predict the behaviour of W in these two extreme environments. The main threats to performance come from damage induced by bombardment of 14 MeV neutrons, including cascade damage and transmutation, bombardment from other ions in the plasma, including He and H ions, and the high temperatures, both during steady state operation and sudden high heat fluxes during disruptions. Currently there is no dedicated fusion materials testing device, so several techniques have been used in order to try and predict the behaviour of W, including the use of ion beam accelerators and LPDs. Further research is required in all these areas in order to develop a more comprehensive database of material properties and better predict any issues that may arise while using W in ITER or DEMO. The aim of this project will be to further develop methods to study degradation of W for fusion applications. The two main topics of interest arise from the products of the D-T reaction; 14 MeV neutrons and He ions (Figure 2.56).

The aim of this project is to study aspects of degradation of W arising from the products of the D-T reaction.

Three areas of research that will be of use in this regard have been identified and are outlined below.

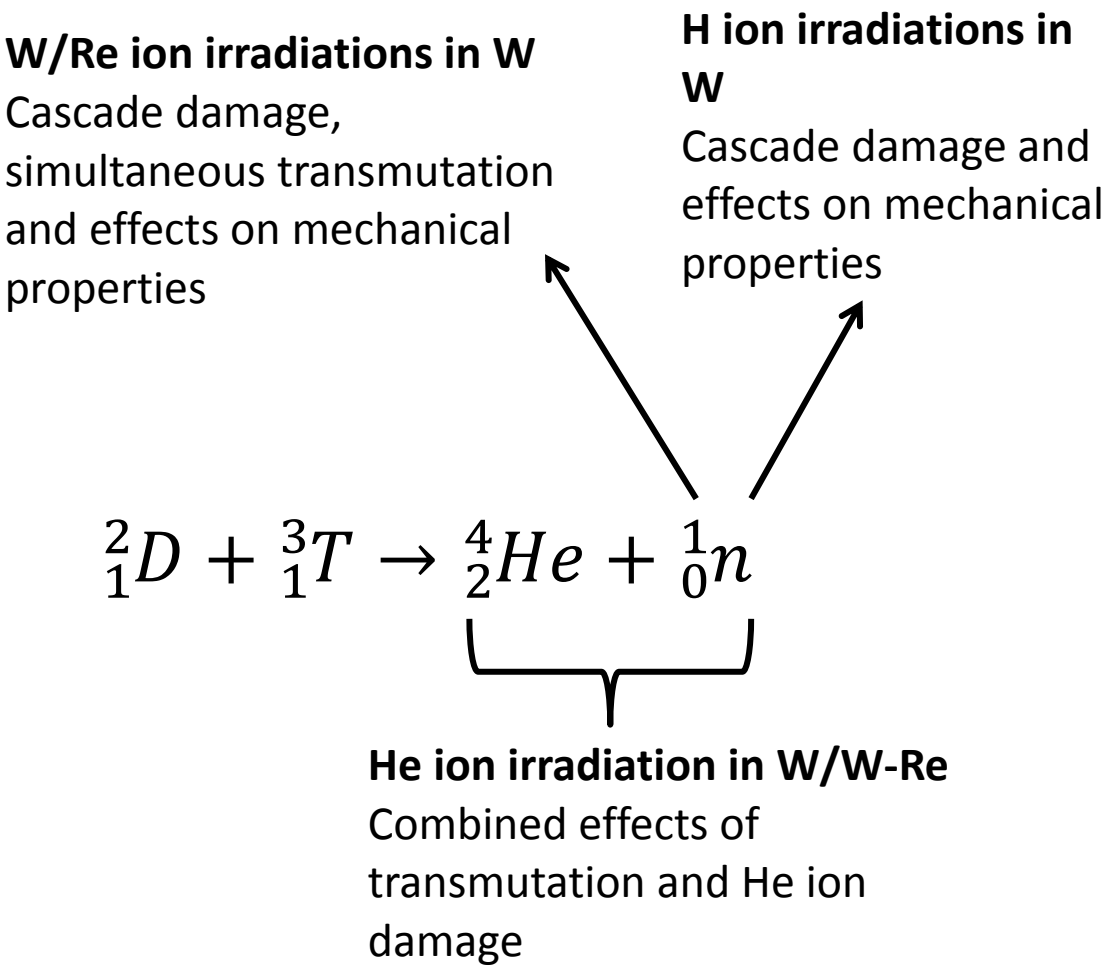

Figure 2.56: Overview of areas of investigation.

2.5.1 Study the effect of Re on the growth of fuzz in W exposed to He plasmas

It is not clear if fuzz will form during ITER or DEMO operation, due to uncertainties with regards to the final operating conditions. In terms of fluence and temperatures required for fuzz formation being reached; this is certain for some areas of the divertor in ITER. However, the energies, particularly during detached plasma operations (required to keep the steady state heat flux at 10 MW/m^2) could be too low. Although, ultimately until experiments begin on ITER or a DEMO reactor is constructed, the energy of He ions cannot be quantified for certain. Additionally the impact of neutron irradiation on the properties of tungsten and the influence this will have on the likelihood of fuzz growth has not been investigated. Re is a transmutation product that will form during nuclear operation in ITER to levels of

0.18% following 2 D-D and 12 D-T years of operation, and also in DEMO, up to levels of 3.8% following 5 years of operation [133]. As seen in Figure 2.54, Re addition seems to be inhibiting fuzz growth in W, however as was mentioned in section 2.4.2.5.1, the manufacturing process of the W-Re alloys was also different, which could have had an effect on the fuzz growth. Re is a transmutation product that will be present, at lower but not insignificant concentrations in ITER, and up to 3.8% after 5 years in a DEMO reactor. Therefore it is of vital importance that the effect of Re on the formation of fuzz is further investigated. Predicting the impact of Re on fuzz growth is important, as fuzz could be detrimental to plasma performance in ITER or DEMO if it were to break of or vaporise as has been suggested in section 2.4.2, which would lead to cooling of the plasma. This topic of research will look to combine the effects of fusion neutron damage with He ion bombardment, through the introduction of Re, to mimic transmutation and exposure to ITER and DEMO relevant He fluxes. This area of research will be addressed in Chapters 4 and 5.

2.5.2 Investigating the use of Re as an implanted species in ion irradiations as opposed to an alloying element

As has been observed in the JOYO fast reactor [67], [134], [162], the mechanism for neutron damage differs significantly if Re is an alloying element, present in W prior to neutron irradiation or if it is created via transmutation during neutron irradiation. If Re is present prior to irradiation, then irradiation hardening has been observed to occur via a precipitation mechanism, whereas if the starting material is pure W, then a void formation mechanism is responsible for irradiation hardening. W ion irradiations in W-5%Re have been compared to those in pure W by Armstrong *et al.* [145], but there is still a gap in the research to simultaneously introduce displacement damage and Re ions during ion irradiation. Re ion irradiations should be carried out in W, and compared to W ion irradiations. Using micro-scale

techniques, it would be interesting to investigate if there would be a variation in the irradiation damage induced through simultaneous introduction of Re during irradiation, as would be the case in ITER or DEMO, as opposed to Re already existing in the matrix. Nanoindentation should be used to look at hardness changes, and SEM and EBSD to look at microstructural changes. This could help to further predict the performance of W in a fusion environment. This topic of research will be addressed in Chapter 6.

2.5.3 Further investigate the use of proton irradiations as a proxy to neutron damage

As discussed in section 2.3.3.5, there have been limited studies into the effect of proton irradiations as a technique to mimic neutron irradiation, particularly if we compare it to the research into heavy ion irradiations and neutron irradiations. The only major study comparing proton irradiations to neutron irradiations, specifically for fusion applications has been carried out by He *et al.* [185]. However, these have only been carried out at temperatures of 500 and 600 °C. Therefore there is scope to further investigate the use of protons as a proxy for neutron irradiation, specifically for fusion applications. In ITER the temperatures reached on the outer target of the divertor could vary between 200-1150 °C [1]. It would therefore be beneficial to further study the impact of temperature by conducting irradiations at temperatures either side of the temperatures used by He *et al.*, to look at the impact on irradiation induced damage. Irradiation hardening should be investigated using nanoindentation and SEM techniques should be used in order to observe microstructural changes.

From the literature it is observed that there is a discrepancy between the hardness increases observed in W following neutron or self-ion irradiation at equivalent doses. For example, comparing the hardness following a dose of 0.4dpa, there is a ~60%

decrease in the hardness increase observed in self-ion irradiated W in comparison to neutron irradiated W (Figure 2.32) [25], [67], [68], [145]. If a comparison of proton and neutron irradiated material to doses of 0.15 dpa is carried out, the proton irradiated material only shows ~10% lower hardness increase in comparison to the neutron material (Figure 2.36) [185]. These are only single data points, and therefore should be compared with caution. It should also be noted that typically micro hardness tests were carried out in the neutron and proton irradiated samples, whereas nanoindentation was used in the ion irradiated material. However, the data seem to suggest that the difference in hardness increases between proton and neutron irradiated material is not as significant as that between self-ion irradiated and neutron irradiated material. Considering that self-ion irradiations should produce cascades more similar to neutron irradiations and proton cascades are smaller and more spaced out [130], it is interesting that in terms of hardness, protons seem to produce hardness results closer to neutron damage. This makes it even more important to continue to study proton irradiations as a proxy for fusion neutron damage. The increased recombination typically associated with the denser cascades in heavy ion irradiations could be contributing to the reduced hardness increase. Additionally, the penetration depth in proton irradiation experiments is greater than in heavy ion irradiation experiments, and therefore indentation measurements are less likely to be influenced by a non-irradiated substrate. Investigating the response of W to proton irradiations shall be carried out in Chapter 7.

3 Methods

3.1 Materials

During the course of this thesis, 6 different materials were utilised:

- 99.95 % purity as received 2 mm thick tungsten sheet purchased from Goodfellow (Ermine Business Park, Huntingdon, England PE29 6WR) with an average grain size of ~1 µm and an inhomogeneous microstructure.
- 99.95 % purity 2 mm thick tungsten sheet from Goodfellow that was annealed for 18 hours at 1400 °C in vacuum in order to get a more uniform microstructure with an average grain size of ~21 µm.
- 30 mm diameter, 1 mm thick 99.97 % purity tungsten discs provided by Plansee (Metallwerk-Plansee-Str. 71, 6600 Reutte, Austria).
- 20 mm diameter, 99.95 % purity tungsten rod purchased from Ultra Minor Metals. The rod produced by a swaging process, using tungsten powder with an average particle size of 4-5 µm.
- 15 mm diameter, 99.95 % purity W-3wt% Re rod purchased from Ultra Minor Metals (C3-603,Emerging Technology Industrial Park,Muyun Industrial Park,Changsha,410118,Hunan,China). The rod produced by a swaging process, using tungsten-rhenium powder with an average particle size of 4-5 µm.
- 15 mm diameter, 99.95 % purity W-5wt% Re rod purchased from Ultra Minor Metals. The rod produced by a swaging process, using tungsten-rhenium powder with an average particle size of 4-5 µm.

For the ion irradiation experiments the as received and annealed sheet was utilised and for the plasma experiments the rod material was utilised.

3.1.1 Sample Preparation

3.1.1.1 Polishing Procedure

In order to prepare the tungsten sheet samples for ion irradiations and mechanical and microstructural analysis, 10 × 10 mm samples were cut from the bulk sheet using electrical discharge machining (EDM). The EDM process resulted in a damage layer, typically a few µm in thickness, that was removed via grinding. Following this half of the samples were annealed under vacuum (~1.9×10^{-3} mbar) for a period of 18 hours at a temperature of 1400 °C. In order to complete the heat treatment, the samples were heated at a rate of 300 °C/hour, up to a temperature of 300 °C, where the temperature was held for 1 hour, following which the samples were again heated at a rate of 300 °C/hour up to a temperature of 1400 °C. This temperature was held for 18 hours, after which the samples were cooled to room temperature at a rate of 350 °C/hour.

The samples of as received and annealed tungsten sheet were ground using 240, 400, 800, 1200 and 2400 grit SiC paper. They were polished on a TexMet cloth using 3 µm diamond suspension (for 30-50 minutes) and with 1 µm diamond suspension (for 10-20 mins), while also using MetaDi Fluid lubricant from Buehler. Initially, the cloth was sprayed three to four times with suspension and 4-6 times with lubricant, checking that there was enough lubricant every five minutes and adding some more diamond suspension every 10 minutes. The samples were then polished, using a damp Maya polishing pad and 0.05 µm colloidal alumina suspension. The samples were polished for 40 minutes, adding a few drops of colloidal alumina every five minutes. This procedure was completed manually. This resulted in a sample surface suitable for electron backscattered diffraction (EBSD) applications.

After the polishing procedure all samples were cleaned ultrasonically using the procedure shown in Table 3.1, before being wrapped in optical tissue and stored in a membrane box in a desiccator.

Table 3.1: Ultrasonic Cleaning Procedure.

Solution	Duration (minutes)
Acetone	10
Ethanol	10
Deionized water	10
Acetone	2

For the material used for plasma exposures, the rods were cut using EDM to produce samples with a thickness of ~1 mm. Again the EDM resulted in a few μm worth of damage that was removed via grinding. These discs, as well as the discs from Plansee were ground and polished using an automatic Struers Planopol-2 and the methodology is highlighted in Table 3.2. This ensured that the samples were prepared to a mirror finish. After polishing, the samples were cleaned ultrasonically, using the procedure in Table 3.1. The samples were then outgassed in a vacuum furnace for 15 minutes at a temperature of 1000 °C. There was no direct cooling used, and it took approximately 7 hours for the temperature to cool from 1000 °C to 100 °C. All samples used throughout this project were prepared to a mirror finish, suitable for EBSD applications. Although in a fusion reactor the tungsten would not be prepared in such a way, for these experiments this process was necessary for two main reasons. Firstly to ensure that the damage profile induced in all samples via ion irradiations or plasma exposures was uniform across the sample. When damage layers of the order of microns are being induced, it is important that the starting condition of material under observation is uniformly flat. Furthermore several of the

tests and analyses used within this thesis require a flat, uniform finish, where the grains are clearly visible.

Table 3.2: Polishing procedure for Tungsten and Tungsten Rhenium Discs [289].

Step 1: Grinding with automatic Struers Planopol-2. Check and rinse sample with water between each step						
	Material	Time/paper	Number of papers	Rotation speed	Force (machine setting)	Comments
a	180 SiC	2-3 min	3	300	4 to 6	
b	320SiC	2-3 min	3	300	6	
c	500SiC	2-3 min	3	300	6	
d	1000SiC	2-3 min	3	300	6	
e	2400SiC	2-3 min	3	300	6	
	Solution	Time	Number of Times	Speed of Rotation	Force (machine setting)	Comments
a	Green 3 µm	10 min	3 to 5	150	3 to 5	Use TexMet cloth. Spray 3-4 times with green suspension and 4-6 times with lubricant. Check every 5 minutes that there is enough lubricant (i.e ensure that there are droplets on the samples). After each 10 minutes add some more green suspension. Following this step the sample should have a mirror finish, if not, then the step should be prolonged.
b	Blue 1 µm	10 min	2 to 4	150	3 to 5	Use TexMEt cloth. Check that there is enough fluid left every 5 minutes. Add some more diamond suspension every 10 minutes cycle.
c	White 0.05 µm	10 min	2 to 4	150	3 to 5	Use MicroCloth (no lubricant required). Add some more suspension after 5 minutes.

3.1.1.2 Focused Ion Beam (FIB)

Focused Ion Beam (FIB) was utilised in this project to determine the thickness of the fuzz layers produced in samples exposed to helium plasmas discussed in Chapters 4 and 5. A FIB can machine features at the nm-µm scale, using gallium (Ga) ions to mill the sample via a sputtering process. Inherently it is a destructive process, and a compromise is required between removing material quickly, while also limiting damage to the specimen under analysis. The systems used in this research were the Quanta 3D and Nova. Both systems are DualBeam, which means that they have both a FIB and an SEM, so that imaging as well as machining can occur. In order to obtain thickness measurements, initially a layer of platinum was deposited on the region of interest of the sample via chemical vapour deposition (CVD) [290], in order to protect the fuzz from ion beam damage. The platinum did slightly obscure the top of the fuzz, however as the same technique was used for all the samples, it can be assumed that all fuzz thicknesses measured were slightly lower than they actually were. If no platinum was used, a greater amount of fuzz would be removed via ion beam damage. Following this a regular cross section using high current gallium ions was cut into the sample close to the region of interest. The cross section was then ‘cleaned’ by performing cleaning cross sections at lower and lower current gallium ions until a smooth surface is achieved, where the microstructure and fuzz were clearly observable. The platinum deposition, rough cut and cleaning cut process are shown in Figure 3.1and the final cross section produced is shown in Figure 3.2.

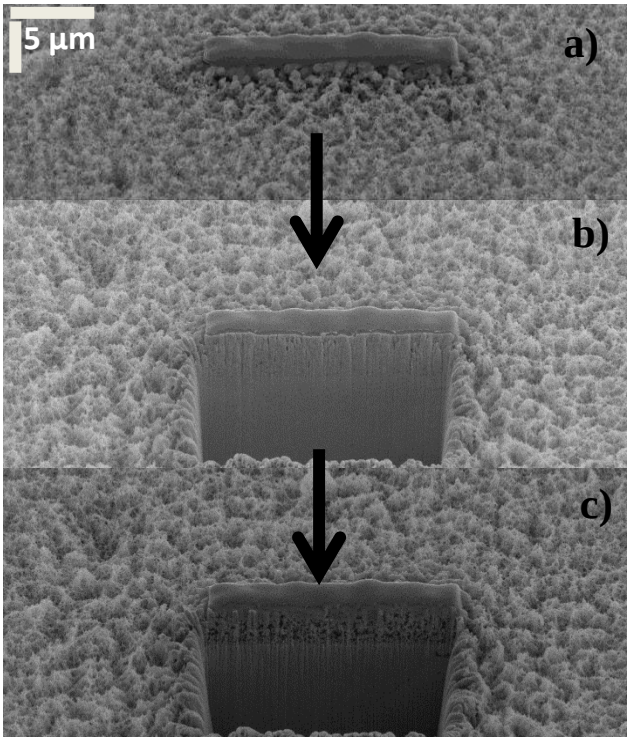

Figure 3.1: Procedure to produce cross sections, starting with a) Pt deposition, b) rough cut and c) cleaning cross section. All images are taken at a tilt of 52°. The original and tilt corrected scales are provided.

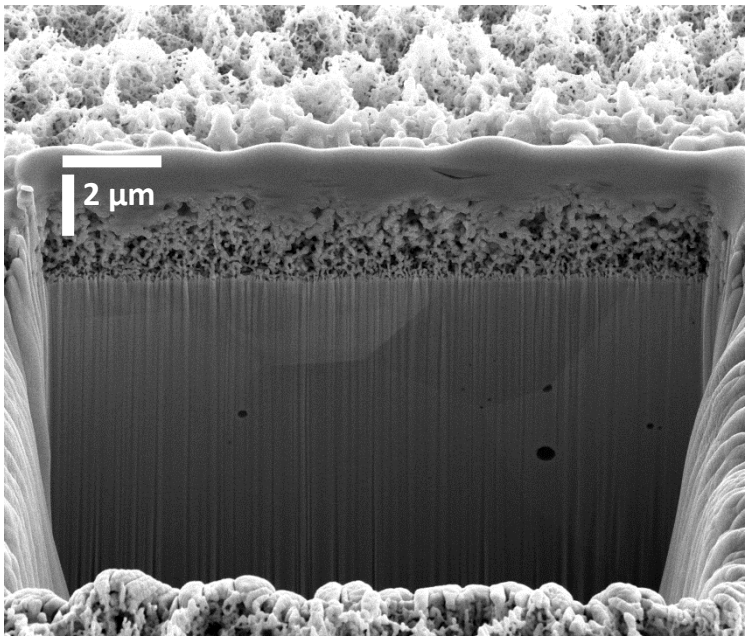

Figure 3.2: Final cross section of plasma exposed W-5%Re sample, revealing the thickness of the 'fuzz' layer. Image is taken at a tilt of 52°. The original and tilt corrected scales are provided.

FIB was also utilised in this project to prepare TEM specimens. This procedure was carried out by Dr. Michael Ward at the University of Leeds, LENNF facility. Again this involves firstly depositing platinum over the region of interest. Trenches are then milled on either side of the lamella and cuts are made to detach it from the bulk so that it can be lifted out from the sample. It is then attached using platinum to a copper grid. Following which it is thinned to electron transparency (<100 nm). The process is illustrated in Figure 3.3.

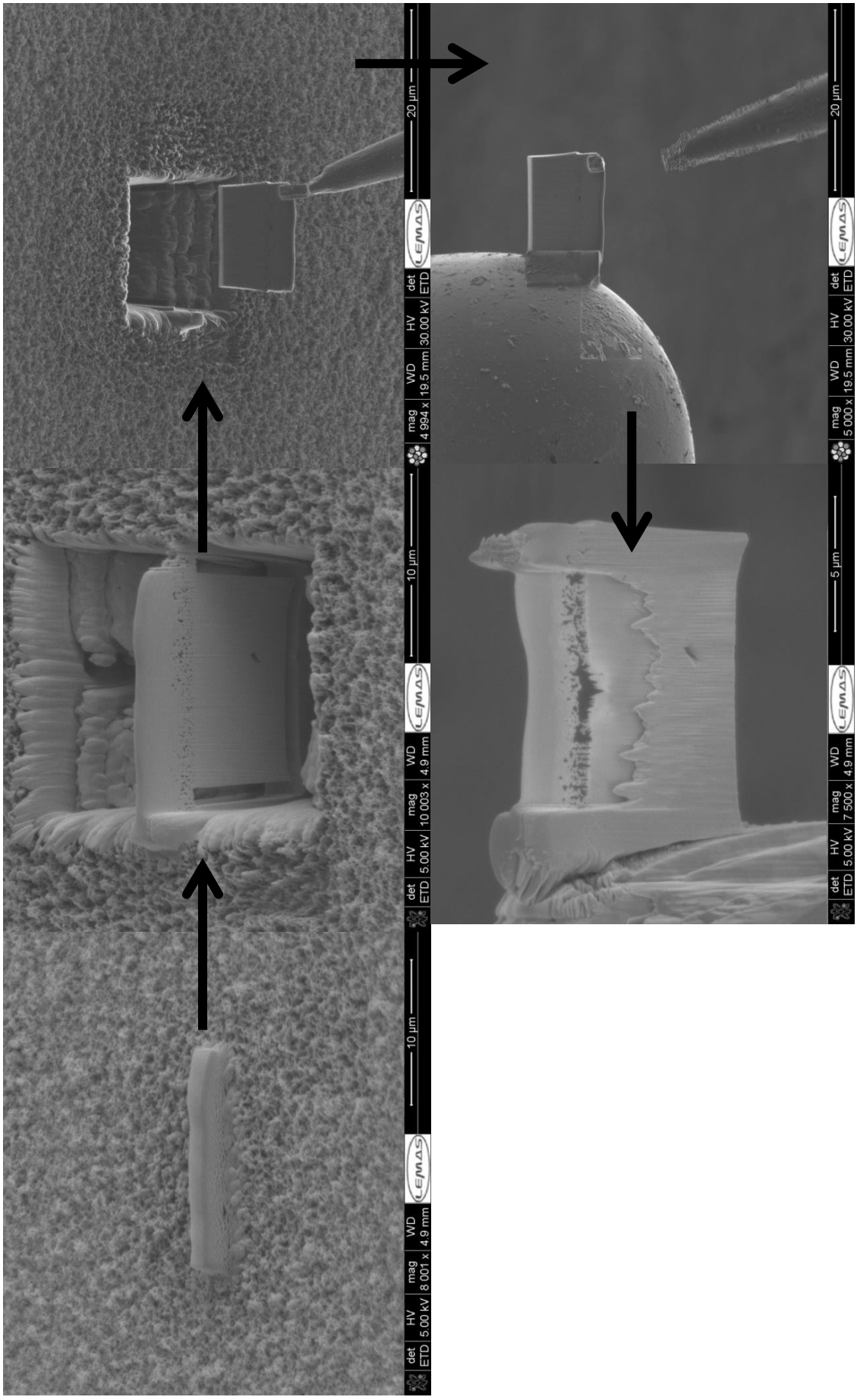

Figure 3.3: Procedure to produce TEM lift outs using FIB (Images taken by Dr. Michael B. Ward)

3.2 Linear Plasma Devices

During this PhD, a collaboration was established with the FOM Institute DIFFER (Dutch Institute For Fundamental Energy Research) with access to two linear plasma devices: Magnum-PSI and Pilot-PSI. Both devices were utilised to obtain the data reported in Chapter 4 ("Effect of Rhenium Addition on Tungsten Fuzz Formation in Helium Plasmas") and Pilot-PSI was used to obtain the data for Chapter 5 ("Effect of Rhenium Concentration on Tungsten Fuzz Growth in Helium Plasmas at High Fluence").

Schematics of Magnum-PSI and Pilot-PSI are shown in Figure 3.4 [248] and Figure 3.5 [291], respectively. Magnum-PSI is capable of reaching fluxes of the order of 10^{23} $m^{-2}s^{-1}$ and Pilot-PSI is capable of 10^{24} $m^{-2}s^{-1}$. This corresponds to the 10^{24} $m^{-2}s^{-1}$ expected in ITER [248]. Pilot PSI uses a cascaded arc source in order to generate the plasma which is confined via an axial magnetic field, resulting in a cylindrical shaped plasma beam that is strongly magnetised [218]. Magnum-PSI operates in a similar way [248]. During the course of this PhD, Magnum-PSI was used in 10 second pulses. For the results reported in Chapter 4, Pilot-PSI was used in 100 second pulses, and for Chapter 5 it was used in 800, 1600 and 3200 s pulses. It would have been ideal to also run the exposures in Chapter 4 continuously, however due to the constraints of the magnetic field this was not possible. This meant that the shots reported in Chapter 4 took longer to complete, as a cooling down period was required between them. Petty *et al.* have investigated the differences between discrete and continuous exposures to plasma in a Magnetron sputtering device [253], and suggested direct comparison between pulsed and continuous exposures may be difficult, due to the fact between pulses helium could escape from the sample and annealing of the fuzz could also occur [253]. However, generally in LPDs, the time

between pulses is of the order of minutes rather than hours, so it could be that the effect is not as important on such timescales.

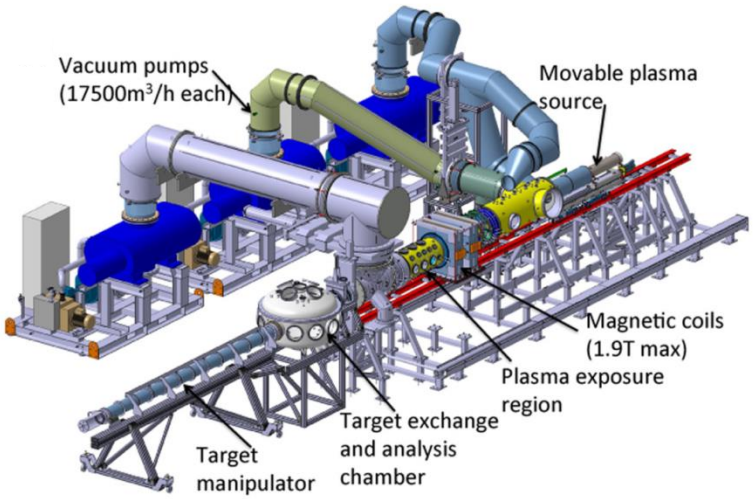

Figure 3.4: Schematic of Magnum-PSI linear plasma device [248].

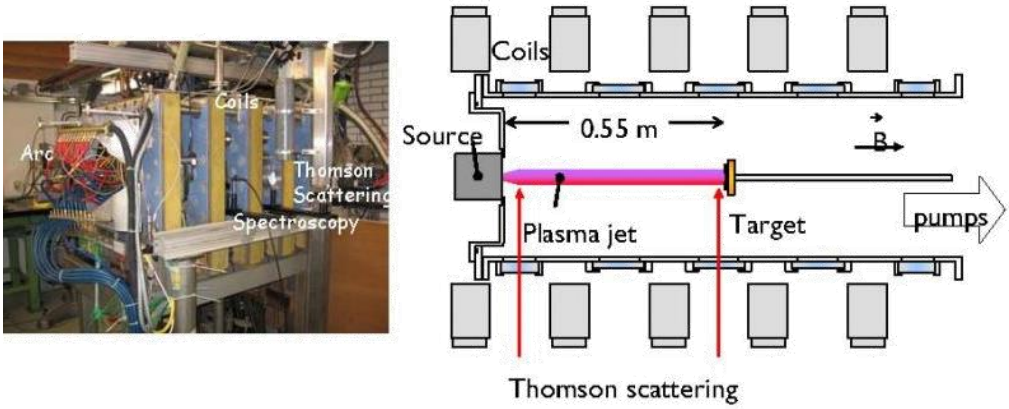

Figure 3.5: Schematic of Pilot-PSI linear plasma device [291].

3.3 Ion Irradiations

During this PhD collaborations were established with the Australian National University (ANU) and Notre Dame University in order to carry out heavy ion (W and Re) and proton irradiations respectively.

3.3.1 Simulation of Ion Irradiation Damage

In order to determine the parameters for irradiation damage, damage profiles were calculated using the Monte Carlo simulation code, SRIM [121]. To determine the

damage profiles for heavy ion irradiations a detailed calculation with full damage cascades was utilised and for proton irradiations the Kinchin-Pease model was used [128]. The full damage model was used for the heavy ion irradiations as this is what had been employed by previous experiments to which the results generated in this project were to be compared [145]. Therefore for ease of comparison the full damage model was used. For proton irradiations, the Kinchin-Pease model was used as this produces the most accurate results [292]. In both cases a displacement energy of 68 eV was assumed for tungsten as this is the minimum displacement threshold in the <100> direction [293]. Additionally, for ease of comparison to previous studies, a value of 68 eV was used [145], [179]. For all simulations 10,000 ions were utilised in order to get an output without noise. From the output files the total number of displacements and hence dpa for a particular fluence was calculated.

For the full damage simulations the total number of displacements was calculated using Equation 3.1.

Equation 3.1

$$Total\ displacements = vacancies + repalcement\ collisions$$

For the Kinchin-Pease model, the total displacements were simply equal to the total number of vacancies at equilibrium.

Relevant fluences were then chosen to obtain dpa values relevant for fusion. Additionally the atomic parts per million (appm) of the implanted ion species was calculated from the output files.

3.3.2 Heavy Ion Irradiations

Heavy ion irradiations (W and Re) were carried out using the tandem accelerator (National Electrostatic Corporation 5SDH) at ANU (Figure 3.6). The accelerator

utilised a SNICS-II source from NEC [294]. The ion accelerator works on the principle that a negatively charged ion beam is accelerated towards a positively charged terminal, where the ions are stripped of their electrons. This results in a positively charged beam that is accelerated away from the terminal towards the target. Further information about the set up can be accessed from [294]. For these irradiations the samples were clamped to a holder made of stainless steel, which was heated to a temperature of 400 °C during irradiation. The temperature of 400 °C was chosen as this is the temperature predicted at the surface of the outer target in ITER [1]. As discussed in Section 2.3.3.6.2, due to the difference in dose rate between 14 MeV neutron damage and heavy ion irradiation damage, a temperature shift should be used to get similar defects. However for this specific case, information is lacking, preventing the link between shift and dose being made.

Figure 3.6: Tandem accelerator at ANU.

3.3.3 Proton Irradiations

Proton irradiations were carried out utilising the 5 MV pelletron accelerator in the Nuclear Science Laboratory (NSL) at the University of Notre Dame (Figure 3.7). It works on the principle that a large positive charge is applied to the terminal (which is

essentially a centralised electrode), which causes a negatively charged ion beam produced outside the accelerator to accelerate as it travels towards the terminal. When the ion beam travels through the location of the terminal, the ions in the beam are stripped of their electrons as they pass through a thin carbon foil. The ion beam is now positively charged and hence accelerated away from the terminal, from where it leaves the accelerator and is incident on a target [295]. In this project, samples were mounted on a high temperature irradiation station which was heated to either 400 or 800 °C. These temperatures were chosen as they lie within the operating range for tungsten within ITER [1]. Again, due to lack of information the temperature shift was not determined. Further information is provided in Chapter 7 ("Effect of Proton Irradiations on the Mechanical Properties of Tungsten for Nuclear Fusion Applications").

Figure 3.7: The Tandem Van de Graaff Accelerator at Notre Dame University [295]

3.4 Measurement of Mechanical Properties

In order to measure mechanical properties of the irradiated layers obtained from the heavy ion and proton irradiations, nanoindentation was utilised. In both cases a displacement control method was employed.

For the heavy ion irradiations, where the damage profile was ~500 nm deep, low load nanoindentation (<10 mN) using a Hysitron triboindenter fitted with a Berkovich tip was utilised. This indenter provides data accurate for displacements between 50-200 nm. A displacement controlled method was utilised to produce indents in the displacement range of 50-200 nm, which was within the irradiated damage layers of the samples. The methodology is described in more detail in Chapter 6 ("Effect of Rhenium Irradiations on the Mechanical Properties of Tungsten for Nuclear Fusion Applications").

For the proton irradiated samples, where the damage layer extended up to a depth of 6 µm with a uniform damage region between 500-2000 nm into the sample, an MTS indenter, fitted with an XP Berkovich tip was utilised that could reach displacements of up to 2000 nm in a silica reference sample. In this case continuous stiffness measurement (CSM) indents with a 2000 nm displacement were used. The quoted load resolution from the manufacturer is 50 nN [296]. The CSM method provides modulus and hardness data throughout the depth of the indent by imposing small dynamic oscillations and allowing for stiffness to be continually measured throughout the depth, rather than just from an unload curve [297]. The advantage of CSM indents is that data is obtained at a range of depths in just one indent, however the results may not be accurate for materials with a high contact stiffness [297] [298].

Nanoindentation is typically used to determine elastic modulus and hardness values of a material by analysing the load displacement curve after applying and unloading the sample using a nanoindenter tip, such as the Berkovich geometry. A Berkovich tip is a 3-sided pyramid that is suitable for analysis of the samples produced in this thesis. This tip is routinely used for nanoindentation and previous work to which

results reported in this thesis were compared also made use of the Berkovich tip [145]. Springs are used to maintain the alignment of the indenter and prevent sideways movement. A typical load-unload curve is shown in Figure 3.8. In this diagram, P is the applied load and h is the displacement into the sample (relevant to the initial deformed surface) [297]. P_{max} is the maximum applied load, h_{max} is the maximum displacement into the sample, h_f is the permanent depth of the indent following the unloading stage, and S is the contact (elastic loading) stiffness. In the loading part of the curve the deformation is assumed to be both elastic and plastic, while in the unload portion only elastic deformation is assumed. Due to the fact that the unload portion of the curve is elastic, it is from this part of the curve that the material's elastic modulus is calculated [297]. A schematic diagram of the load-unload process, using a Berkovich tip is shown in Figure 3.9. In the case of a Berkovich indenter, it is assumed that φ (the half induced angle) has a value of 70.3°, h_c is the contact depth between the indenter tip and the sample, h_s is sink-in (the elastic deformation of the sample surface that surrounds the indent [299]).

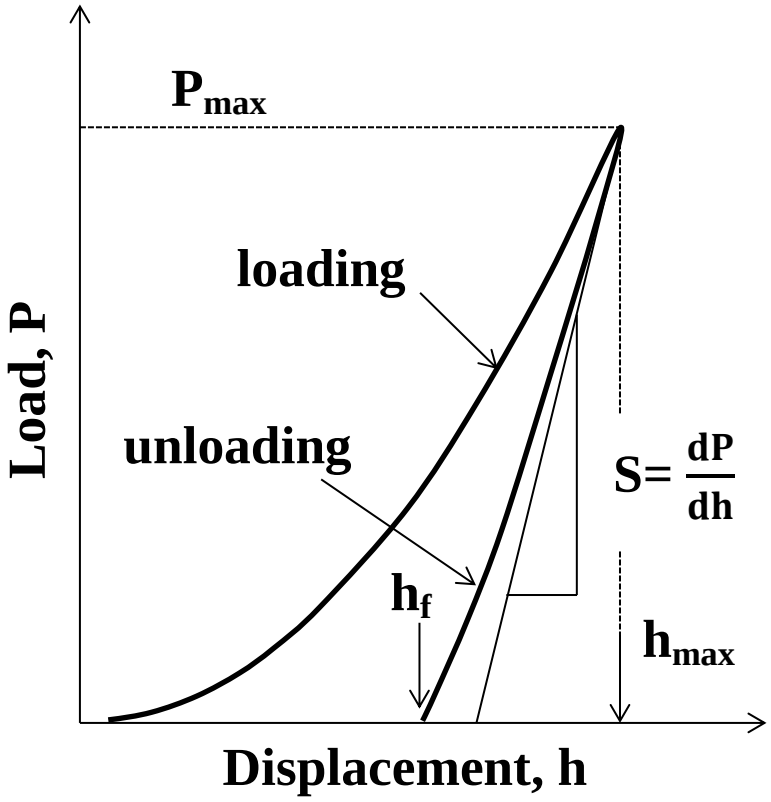

Figure 3.8: Load-displacement curve redrawn from [297].

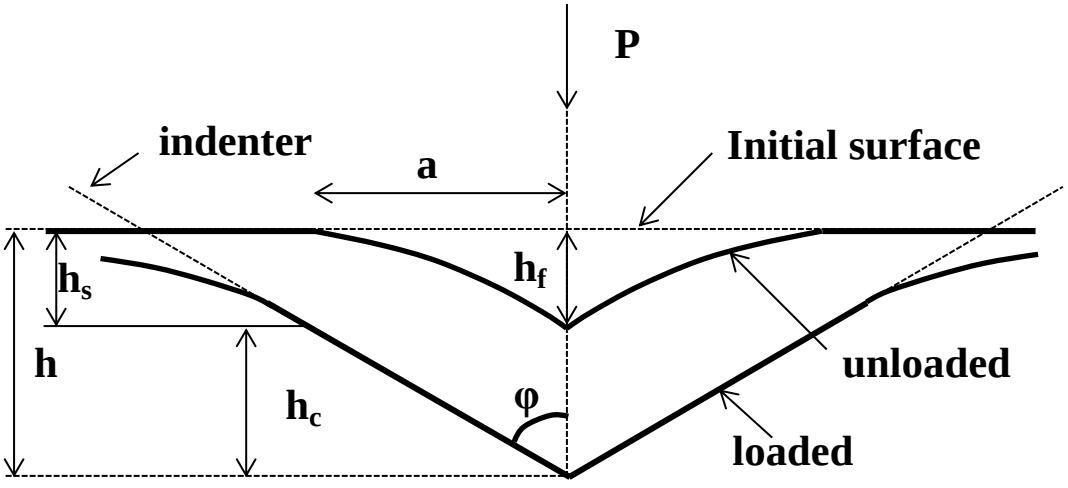

Figure 3.9: Schematic of load/unload process redrawn from [297].

The indenter tip approaches the sample, until it reaches the sample surface resulting in a change in stiffness response of the system. The measured load is corrected for the stiffness of the support spring of the system, using Equation 3.2. P_{raw} and P_0 are the raw load and the raw load at the sample surface respectively. h_{raw} and h_0 are the raw displacement and the raw displacement at the sample surface. K_{spring} is the stiffness of the spring. Hence the first term corresponds to total load and the second term to the reaction force of the springs.

Equation 3.2

$$P = (P_{raw} - P_0) - K_{spring}(h_{raw} - h_0)$$

The measured displacement also requires correction, specifically for thermal drift and frame displacement (Equation 3.3).

K_{frame} is the frame stiffness and is very sensitive to the method of mounting of the sample. It is for this reason that all samples during this thesis were mounted in the same way to ensure consistency and repeatability. All samples were mounted on an SEM stub using cyanoacrylate adhesive, which was in turn mounted in a specially designed aluminium holder and made secure using a grub screw. In order to determine whether the samples were mounted correctly, the modulus- displacement graphs were checked, ensuring that the modulus values remained constant with depth (except where surface effects dominated). This meant that samples could easily be transferred between the nanoindenter and the SEM, without any need to change mounting. The silica references that were used for both indentation systems used in this thesis were also mounted on stubs using cyanoacrylate adhesive to ensure consistency. Although it is impossible to completely remove the effects of system compliance, this method limited the effects. The first term of Equation 3.3

corresponds to the total displacement of the tip; the second term corresponds to the frame displacement and the final term to thermal drift, where Q is the thermal drift coefficient and is calculated via a least squares fit and $t - t_0$ is the duration of the indent. The thermal drift is calculated during the hold segment of each indent, at 10 % of the maximum load. For the both systems, thermal drift was typically less than 0.05 nm/s.

Equation 3.3

$$h_c = (h_{raw} - h_0) - \frac{P_{raw} - P_0}{K_{frame}} - Q(t - t_0)$$

In order to determine the elastic modulus of the sample, Equation 3.4 is used, where β is a dimensionless correction factor, which is typically taken to be ~1.05 ±0.05 [297] (obtained from experiments and 3D finite element analysis) and E_r is the reduced modulus [297]. The reduced modulus is essentially the combined properties of the system and the material under investigation.

Equation 3.4

$$E_r = \frac{\sqrt{\pi}S}{2\beta\sqrt{A}}$$

From the reduced modulus, the actual modulus, E can be obtained using Equation 3.5. This requires the Poisson's ratio of the sample, ν, as well as of the indenter ν_i. The modulus of the indenter material, E_i is also required [297].

Equation 3.5

$$\frac{1}{E_r} = \frac{(1 - \nu^2)}{E} + \frac{(1 - {\nu_i}^2)}{E_i}$$

This can be re-arranged to give Equation 3.6.

Equation 3.6

$$E = \frac{(1-\nu^2)}{\frac{1}{E_r} - \frac{(1-\nu_i{}^2)}{E_i}}$$

It is also necessary to callibrate for compliance in the system using Equation 3.7 [297]. The total compliance, C is equal to the sum of the load frame compliance, C_f and the compliance of contact which is the second term in the equation. Essentially the system is equivalent to two springs in series.

Equation 3.7

$$C = C_f + \frac{\sqrt{\pi}}{2E_r}\frac{1}{\sqrt{A}}$$

Equation 3.8

$$A = \left(\frac{\sqrt{\pi}}{2E_r \times (C - C_f)}\right)^2$$

Following this, Equation 3.7 is rearranged (Equation 3.8) in order to obtain values of the indentation area (A) at various depth, which in turn feed into the area function equation (Equation 3.9). C_n are constants used to get a good fit for the area function [297].

Equation 3.9

$$A = \sum_{n=0}^{8} C_n (h_c)^{2-n} = C_0 {h_c}^2 + C_1 h_c + C_2 {h_c}^{1/2} + C_3 {h_c}^{1/4} + \cdots C_8 {h_c}^{1/128}$$

Once the area function has been determined, the hardness of the material under analysis can be obtained, using the maximum load, P_{max} and the contact area, A as shown in Equation 3.10 [297].

Equation 3.10

$$H = \frac{P_{max}}{A}$$

In all cases the indenter tip area coefficients and compliance were calibrated by using data obtained from indenting a fused silica standard. Fused silica is used as it exhibits ideal behaviour, due to its low E/H value. For more information on nanoindentation, the reader is directed to [297] and [299].

3.5 Microstructural Evaluation

3.5.1 Scanning Electron Microscopy (SEM)

SEM was used extensively in this project for microstructural and surface characterisation of both the plasma and ion irradiated samples. Three functions of SEM used in this project are highlighted below. The SEMs used in this project were the Quanta 200, Quanta 650, Philips XL30 and Zeiss Sigma. Apart from the Quanta 200, which is a filament SEM, these are all FEG (Field Emission Gun) SEMs.

3.5.1.1 Imaging

SEM was utilised to obtain data reported in all the results chapters of this thesis. The Quanta 200 was used for low magnification imaging and to check that sample preparation was adequate before ion irradiations. Field emission gun (FEG) SEMs were utilised in order to conduct high magnification work. A schematic diagram of an SEM is shown in Figure 3.10 [300].

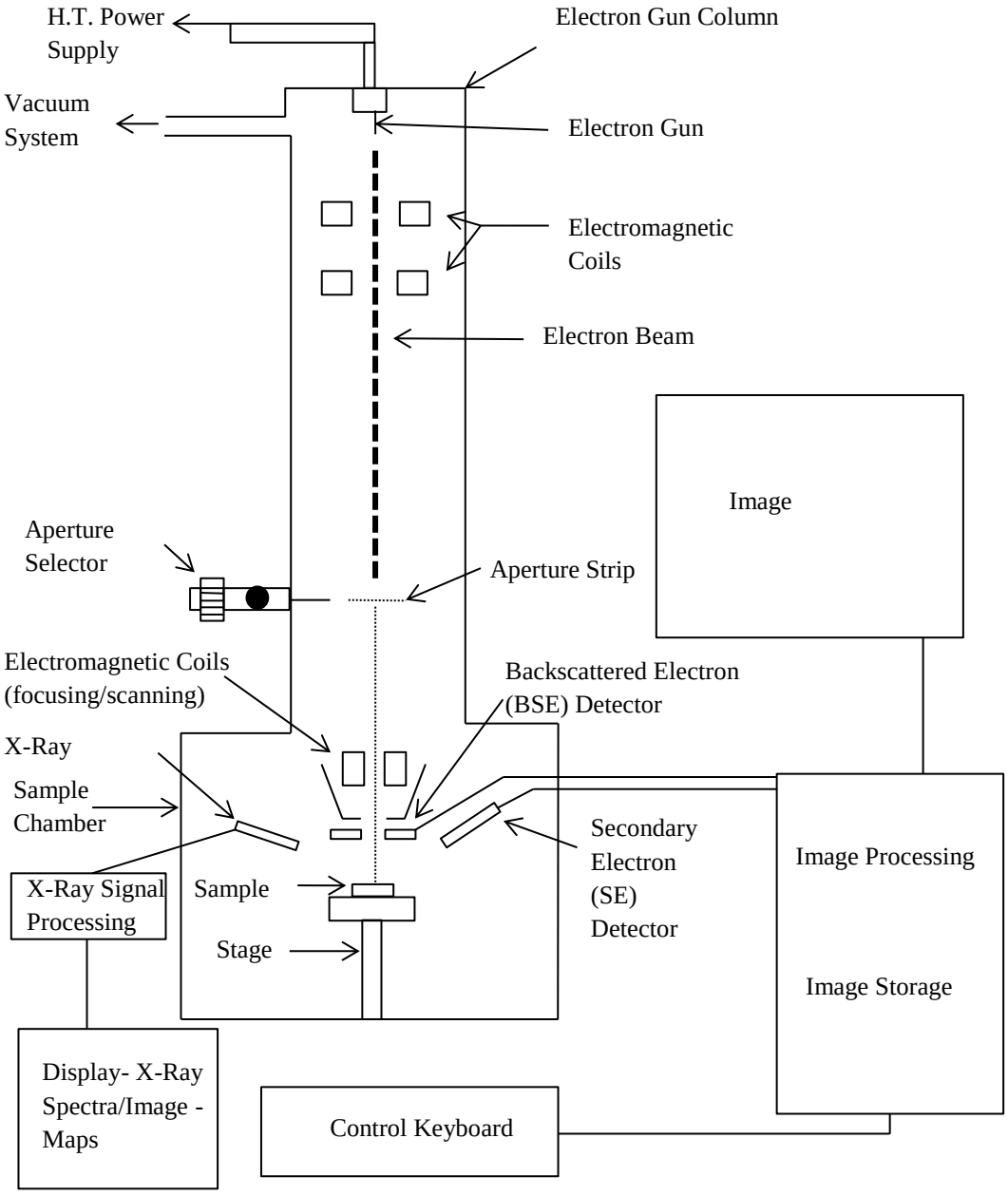

Figure 3.10: Schematic Diagram of SEM adapted from [300].

When using a SEM, the sample under inspection is irradiated with a beam of electrons, resulting in signals from secondary electrons, backscattered electrons, Auger electrons, X-rays and photons being emitted from different depths of the sample [301]. The interaction volume of the electrons with the sample is typically a tear drop shape. Figure 3.11 illustrates the types and locations of the signals generated from the electron beam interaction with the sample under investigation. It should be noted that the interaction volume increases with increasing accelerating

voltage of the incident electron beam. This means with lower accelerating voltages more surface information is obtained, and with higher voltages the information comes from deeper into the sample. Secondary electrons provide information close to the surface of the sample. Electrons from the incident beam interact with electrons in the sample, resulting in the incident electron changing direction and the electron in the sample being ejected from its original atom. This ejected electron is referred to as a secondary electron and has an energy of less than 50 eV [302]. Backscattered electrons are generated deeper in the sample in comparison to secondary electrons. Due to a large number of large angle elastic scattering events, primary electrons incident on the sample can be back scattered out of the sample, and hence are referred to as back scattered electrons [302]. The different signals can provide us with information from different regions within the sample, and combined together a complete picture is created.

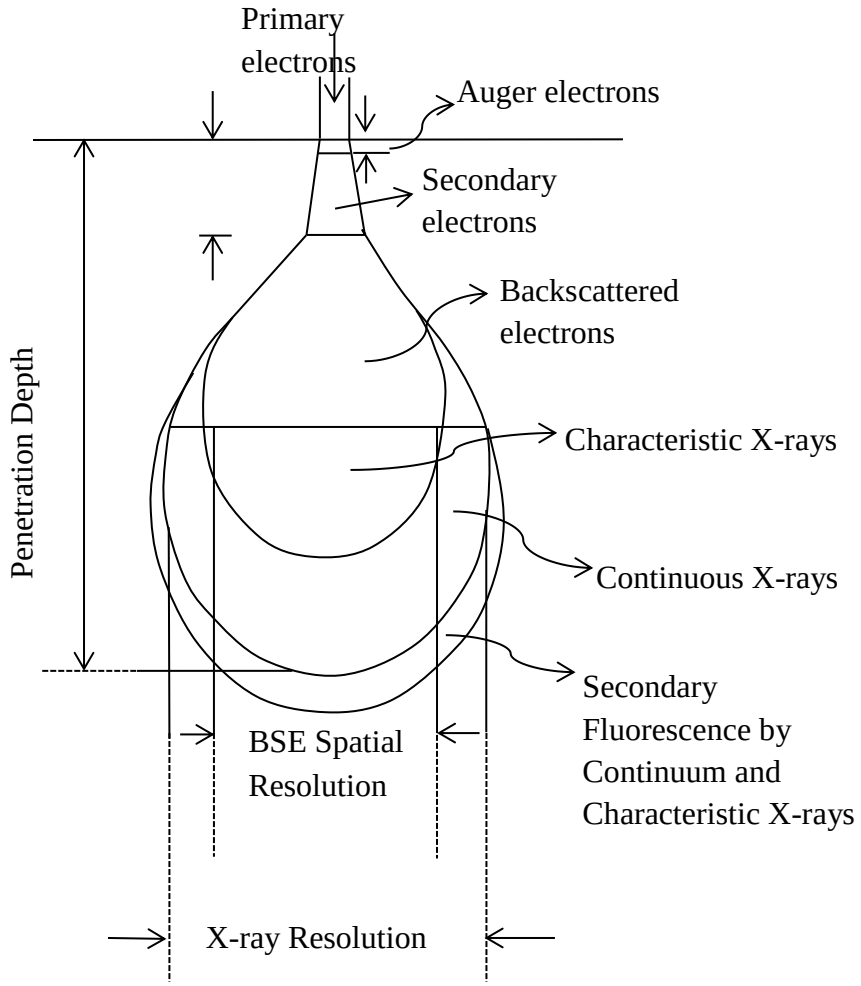

Figure 3.11: Teardrop model of electron penetration into sample and location and type of signals generated, adapted from [302]. The interaction volume depends on electron energy and the sample under analysis. Typically the secondary electrons come from the first 10 nm. For electron energies between 15-30 kV in a flat W sample, the peak back scattered electron penetration depth is between 190-500 nm and the total peak penetration depth is between ~400-1300 nm, as calculated with CASINO v 2.48 [304].

3.5.1.2 Electron Backscattered Diffraction (EBSD)

3.5.1.2.1 Experimental Technique

In order to conduct EBSD analysis on a sample, the primary electron beam (stationary) is incident on a sample tilted to 70°. This results in electrons to be diffracted from the sample, resulting in a characteristic diffraction pattern being observed (Kikuchi patterns), depending on the crystal structure and grain orientation of the sample under investigation [303]. This allows us to differentiate and identify grains of certain orientations and phases.

3.5.1.2.2 Simulation of Electron Penetration Depths

The depth from which the signal originates is dependent on the voltage of the incident electron beam. The higher the voltage, the higher the penetration depth and hence the deeper from the sample the signal is obtained. In order to correlate the electron beam voltage with the penetration depth of the back scattered electrons, and incidentally the depth into the sample from which the signal is coming from, CASINO (monte CArlo Simulation of electron trajectory in sOlids) software can be utilised. In this project version 2.48 was utilised [304]. This Monte Carlo simulation can be used to calculate the penetration depth of back scattered electrons with varying electron beam voltage, as used in Chapter 6. In this particular case irradiation damage was correlated with the penetration depth of the electrons, and hence revealed orientation specific damage due to ion irradiation.

3.5.1.3 Energy-Dispersive X-ray spectroscopy (EDX)

When electrons from the incident electron beam interact with inner shell electrons of atoms in the sample under observation and a secondary electron is released, an outer shell electron will then drop down in order to fill the vacancy created by the ejected secondary electron. As the outer shell electron drops down to fill the vacancy, a characteristic X-Ray is emitted from the sample. Due to the fact that the X-ray is characteristic of an element, X-rays can be used to identify elements present in a sample [302]. This is the basis of EDX. EDX was used to identify carbides that had formed on the surface of proton irradiated samples; this work is presented in Chapter 7.

4 Effect of Rhenium Addition on Tungsten Fuzz Formation in Helium Plasmas

A paper published in the peer reviewed journal: Journal of Nuclear Materials

Presented as an adaptation of the published form.

doi:10.1016/j.jnucmat.2016.03.016

Authors
Aneeqa Khan, Gregory De Temmerman, Thomas W. Morgan, Michael B. Ward

Effect of Rhenium Addition on Tungsten Fuzz Formation in Helium Plasmas

Aneeqa Khan[a], Greg De Temmerman[b] ,Thomas W. Morgan[c] , Michael Ward[d]

[a]*School of Mechanical, Aerospace and Civil Engineering, The University of Manchester, M13 9PL, UK*
[b]*ITER Organization, Route de Vinon-sur-Verdon, CS 90 046 - 13067 St Paul Lez Durance Cedex , France*
[c] *FOM Institute DIFFER – Dutch Institute for Fundamental Energy Research, Partner in the Trilateral Euregio Cluster, Eindhoven, the Netherlands*
[d]*Institute for Materials Research, School of Chemical Process Engineering, University of Leeds, Leeds, LS2 9JT, UK*

Abstract

The effect of the addition of rhenium to tungsten on the formation of a nanostructure referred to as 'fuzz' when exposed to helium plasmas at fusion relevant ion fluxes was investigated in the Magnum and Pilot PSI devices at the FOM Institute DIFFER. The effect rhenium had on fuzz growth was seen to be dependent on time, temperature and flux. Initial fuzz growth was seen to be highly dependent on grain orientation, with rhenium having little effect. Once the fuzz was fully developed, the effect of grain orientation disappeared and the rhenium had an inhibiting effect on growth. This could be beneficial for inhibiting fuzz growth in a future fusion reactor, where transmutation of tungsten to rhenium is expected. It also appears that erosion or annealing of the fuzz is limiting growth of fuzz at higher temperatures in the range of ~1340 °C.

4.1 Introduction

Tungsten will be the main plasma facing material used for the divertor within the experimental fusion reactor, ITER [3]. This is due to its high melting point of 3420 °C [4], low rate of sputtering [5] and also its strength at elevated temperatures [6]. However there are some unresolved issues. It is expected that temperatures of 1000-1200 $^{\circ}$C will be reached at the strike point during a Q=10 discharge [7]. Extensive work has been completed in regards to the damage pure tungsten will undergo when exposed to helium plasmas. Exposure to helium plasmas results in a nanostructure formation on the surface of tungsten (referred to as 'fuzz' in literature) [8] [9]. The rate of formation of such nanostructures has previously been observed to increase with increasing fluxes of helium ions until a value of 10^{22} $m^{-2}s^{-1}$ after which the incoming flux does not play a role anymore[10]. However, recently Petty et al. have observed that this is due to the fact above fluxes of $10^{22}m^{-2}s^{-1}$ impurity fractions set up a growth-erosion equilibrium [1]. It has also been found that increasing the temperature of exposure results in an increase in the diameter of the helium bubbles on the surface of pure tungsten. The surface temperature also heavily influences the kinetics of the surface modification process. The modified layer thickness is dependent on the square root of the exposure time [9] [2].

In ITER and beyond to DEMO, there will also be 14 MeV neutrons present from the D-T (Deuterium-Tritium) reaction and it has been determined by Gilbert and Sublet that tungsten will transmute to W-3.8at%Re-1.4at%Os following five years of power plant conditions [11].

With typical first wall components in a DEMO reactor set to have a lifetime of at least five years [12], the effect of transmutation products is of great interest. Rhenium addition, while having a ductilising effect in non-irradiated tungsten has been found to increase the brittle nature of tungsten following neutron irradiation [13]. Initial work on the effect of rhenium on plasma-induced surface damage has been completed by Baldwin et al., suggesting that rhenium addition may result in decreased efficiency of formation of the helium induced nanostructure [14]. Due to the transmutation of tungsten in a fusion reactor, further investigation of the effect of rhenium on plasma damage of tungsten is of great interest.

It is the aim of this work to investigate the effect of rhenium addition on the kinetics and process of helium induced damage creation in tungsten under fusion relevant plasma conditions.

4.2 Materials and Methods

In order to investigate the effect of rhenium addition, samples of tungsten with varying rhenium concentrations were exposed to ITER relevant helium plasmas in the Magnum and Pilot PSI linear plasma devices at DIFFER.

Rods of 99.95% commercial purity polycrystalline tungsten, with an average grain size of 1.6 μm, tungsten-3% rhenium, with an average grain size of 5 μm and tungsten-5% rhenium (weight percentage), with an average grain size of 5 μm were purchased from Ultra Minor Metals. The rods were produced by a swaging process, using a tungsten or tungsten-rhenium powder with an average particle size of 4-5 μm. The pure tungsten rod was 20 mm in diameter and 30 mm long, and the tungsten rhenium rods were 15 mm in diameter and 100 mm long. Discs of approximately 1 mm thickness were cut from the rods, using Electrical Discharge Machining (EDM) and then polished to a mirror finish and cleaned ultrasonically using ethanol and acetone. Following this they were outgassed at 1000 °C for a duration of 15 minutes. A 30 mm diameter, 1 mm thick tungsten disc of 99.95% commercial purity of pure tungsten obtained from Plansee was also used for the Pilot-PSI experiment, with an average grain size of 1.2 μm. Concentrations of 3 and 5% rhenium were selected as they were values close to the 3.8% concentration of rhenium expected due to transmutation of tungsten after five full years of power plant conditions in DEMO [11].

4.3 Experimental

One set of experiments was conducted in the Magnum PSI linear plasma device, exposing the samples to pure helium plasmas at fluxes of the order of 10^{23} ion·$m^{-2}s^{-1}$ and energy of 30 eV, where discs of each alloy composition were exposed to the plasma for between 40 and 200 seconds at temperatures of approximately 970 °C. The exposures were conducted in pulses of 10 seconds. The temperature was measured using an infrared camera, and a pyrometer was used to confirm the data. The pyrometer temperature is accurate at all conditions, however when the emissivity of the sample changes as a result of fuzz growth, then the temperature measured by the infrared camera will be much higher than the real temperature the sample is exposed to. The pyrometer is then used to adjust the infrared data. Hence, when there appears to be a discrepancy between the two, this is an indicator that fuzz is growing. There

is a radial variation of temperature across the surface of the sample, which can be analysed from the infrared data.

The second set of experiments was conducted in the Pilot PSI device. A disc of each alloy composition was exposed for 400 s at a temperature of approximately 1400 °C to helium plasma with fluxes of the order of 10^{24} ion·$m^{-2}s^{-1}$ and energies of 30 and 35 eV. The exposures were conducted in pulses of 100s. The Magnum exposures were for monitoring the effect of rhenium concentration on the early stages of fuzz formation, and the Pilot exposures aimed at studying the effect of higher fluence. The exposure conditions for each sample are shown in Table 4.1. The average temperature is the average of the temperature reading from the pyrometer over all the pulses each sample was exposed to.

Table 4.1: Sample Exposure Conditions

Material	Average Temperature (°C)	Fluence (ions m^{-2})	Duration (s)	Energy (eV)
Pure Tungsten	1106±11	$1.4\times10^{25}\pm2.9\times10^{23}$	40	30
	990±23	$3.5\times10^{25}\pm7.5\times10^{24}$	100	30
	960±30	$4.1\times10^{25}\pm1.4\times10^{25}$	200	30
	1340±120	$7.6\times10^{26}\pm9.5\times10^{25}$	400	30-35
Tungsten-3% Rhenium	960±20	$1.6\times10^{25}\pm2.7\times10^{24}$	40	30
	960±40	$3.6\times10^{25}\pm5.5\times10^{24}$	100	30
	930±80	10^{25}	200	30
	1460±60	$1.1\times10^{27}\pm3.34\times10^{25}$	400	30
Tungsten-5% Rhenium	970±24	10^{25}	40	30
	930±30	10^{25}	100	30
	940±30	7.8×10^{25}	200	30
	1420±150	10^{27}	400	30

Following the plasma exposures of the samples, Scanning Electron Microscopy (SEM) was utilised to analyse all exposed surfaces. Focused Ion Beam (FIB) was used to obtain cross sections. 15 μm length cross sections were cut in each area of interest and the average depth was determined by taking depth measurements at 1 μm intervals. FIB was also utilised to produce Transmission Electron Microscopy (TEM) foils that were 15 μm in length, from the discs exposed to helium plasma for 400 s, in order to analyse the internal pore structure. Bright Field TEM imaging, as well as High Angle Annular Dark Field (HAADF) Scanning TEM (STEM) imaging was used to image the TEM foils. Diffraction patterns were also used to identify the crystal structure of the fuzz.

4.4 Results and Discussion

Figure 4.1 illustrates the fuzz production at the centre of the targets in pure W, W-3%Re and W-5%Re at a flux of ~10^{23} m^{-2} s^{-1} and at a temperature of approximately 970 °C. Images have been taken at low and high magnifications. It is observed that the initial stages of fuzz growth in all cases (up to 100 s), is highly orientation dependent. In the low magnification images of the 40 s exposures, it can be observed that the direction of the fuzz growth varies from grain to grain. The fact that the grain boundaries become less visible as the fuzz develops and are almost invisible after 200 s indicates that the grain orientation impact on fuzz growth diminishes over time. The fuzz growth has a clear wave-like structure aligned in one direction during early stages of formation, which is clearly observed in the high magnification SEM images up to 100 s. Different structures are observed in different grains... At these early stages of fuzz formation it is seen that the initial fuzz formation is highly dependent on grain orientation, which has also been observed by De Temmerman et al. [15], however there is no clear indication if rhenium is affecting the growth at these early stages. The tendrils in the rhenium alloyed samples appear to be thicker in comparison to the tendrils observed in the pure tungsten samples.

Figure 4.2 refers to the fuzz produced at the higher temperature of 1400 °C, at a flux of 10^{24} m^{-2} s^{-1} for a duration of 400 s. The FIB cross sections shown in Figure 4.2 a)-c) indicate that there is only a 0.25 μm decrease in fuzz depth between pure W and W-3%Re. There is a significant decrease between W-3%Re and W-5%Re, with the depth observed in W-5%Re being approximately a quarter of that seen in the W-3%Re. However, it should be acknowledged that the temperature the pure tungsten sample was exposed to was approximately 100°C lower than that of the rhenium samples. It should also be noted that the platinum deposition procedure from the FIB process may obscure the very top of the fuzz, resulting in all values of thickness measured being slightly lower than they actually are.

From Figure 4.2 d) we can see that the addition of rhenium is having an inhibiting effect on the thickness of the fuzz layer. Combined with the SEM images of the surface of the fuzz (Figure 4.2 e)-g)) which show a finer structure in the pure W, compared to the W-3%Re and W-5%Re cases, it can be said that at these conditions the rate of fuzz growth appears more inhibited with increasing rhenium addition. This trend is consistent with experiments by Baldwin et al. that suggested alloying W with increasing Re concentration resulted in a reduction in the efficiency of nanostructure formation [14], however the rate of reduction with only 5% rhenium seems to far exceed that observed by Baldwin et al, where the growth of the 5% and 10% rhenium alloyed samples fuzz layer thickness were 0.66 and 0.56 of the thickness of the pure W case respectively [14]. It is suggested that this is due to the higher temperatures used in our experiments (the 5% Re alloy fuzz thickness is ~0.21 of the thickness of the pure W case), meaning that annealing and erosion could also be having an effect on the fuzz formation mechanism.

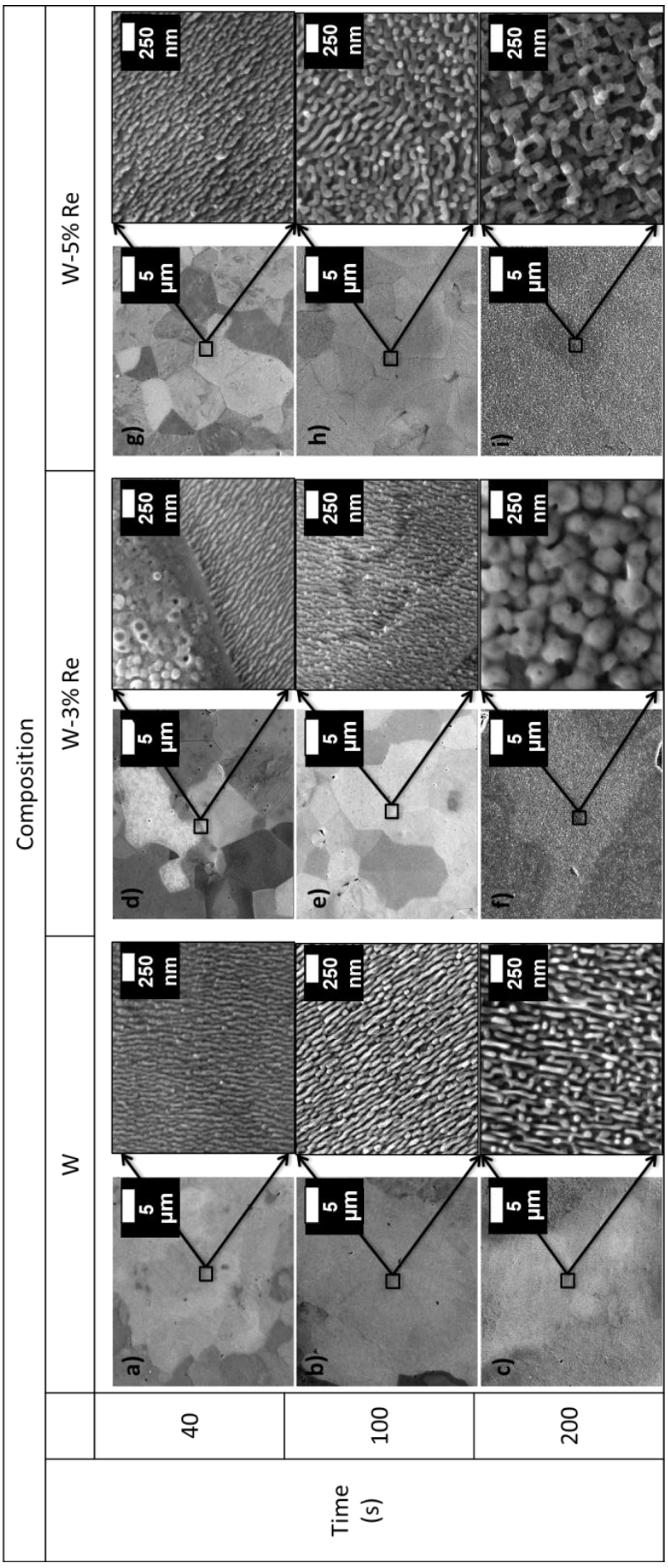

Figure 4.1: SEM images at low and high magnifications of W, W-3% Re and W-5% Re samples exposed for 40, 100 and 200s at a flux of 10^{23} m^{-2} s^{-1} and at a temperature of approximately 970 °C in Magnum PSI

Recently work has been done by Petty et al. that provides a way to compare the thickness of fuzz layers, taking into account both fluence (Φ) and temperature. This utilises Equation 1, which is defined for $x(\Phi): \Phi > \Phi_0$, where x is the thickness for the fuzz layer, $C = 2D/\Gamma$ (D is the diffusion coefficient and Γ is flux) and is a constant specific for a certain temperature. Φ_0=2.5×10^{24} ionsm^{-2} and α=$\frac{1}{2}$ [1].

$$x(\Phi) = (C(\Phi - \Phi_0))^{1/2} \quad (1) \text{ [1]}$$

A value of C can be determined from the values of the diffusion coefficient, D found by Baldwin et al. in [2], resulting in C=2.64×10^{-38} m^4 at 847 °C and C= 8×10^{-38} m^4 at 1047 °C, where the flux is 5×10^{22} ionsm^{-2}s^{-1} in both cases. However in this experiment, for the pure W case, our flux and temperature are both higher than these values. Using Equation 1, we can determine C for the pure W case at 1340°C, where the fluence is 7.6×10^{26} ionsm^{-2} , using the measured fuzz layer thickness value of 2.346 μm, as having a value of 7.27 ×10^{-39} m^4, which is an order of magnitude lower than that calculated with the Baldwin data. This suggests that at the higher temperatures of ~1340 °C, annealing and or erosion is also playing a role and resulting in a layer of fuzz that is not as thick as that observed at lower temperatures. It has been observed by Kajita et al. that annealing can occur within the range of temperatures and fluxes required for fuzz growth [16]. This can also explain why the rhenium alloyed samples (exposed at temperatures around 100 °C higher than the pure W case), especially the 5% rhenium case show such significant decrease in thickness of the fuzz layer in comparison to the pure tungsten case, which as a percentage of the thickness of the pure W fuzz layer is much lower than that observed at 847 °C by Baldwin et al. [14].

Interestingly, recently Takamura et al. have observed the growth of thin, needle like fuzz structures on pure rhenium wire, which suggests that although rhenium has been seen to inhibit fuzz growth, it will never completely suppress it , even at higher concentrations [17].

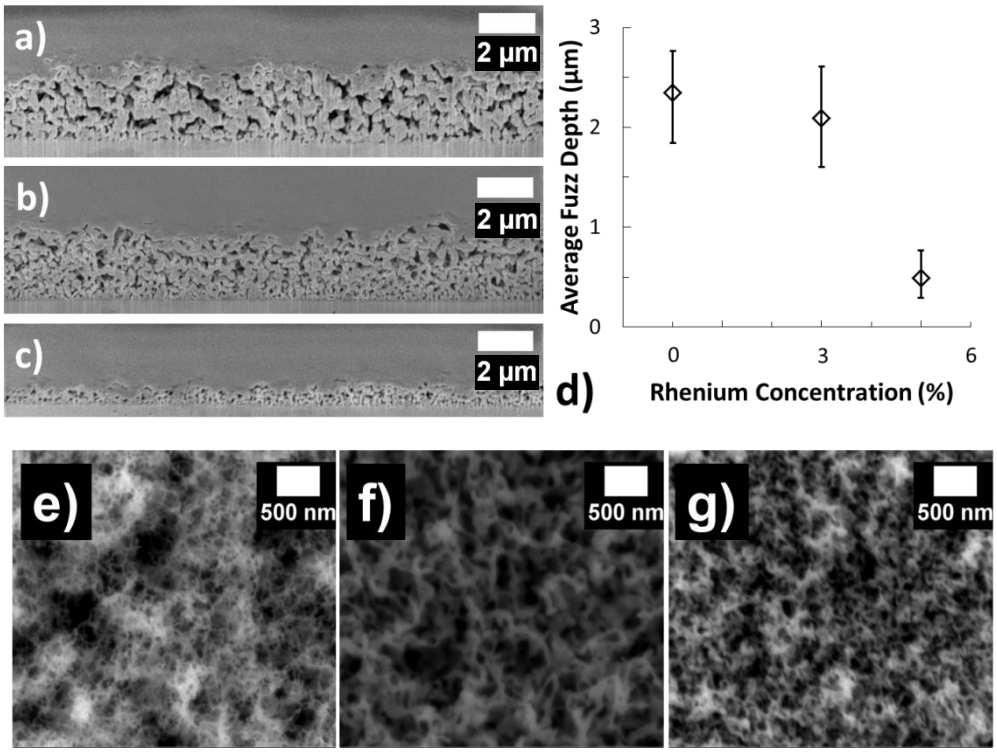

Figure 4.2: Cross sections of fuzz in a) W, b) W-3% Re and c) W- 5% Re and d) plot of the variation of fuzz depth with rhenium concentration and SEM images of fuzz in e) W f) W-3%Re, g) W- 5% Re for samples exposed for 400 s at a flux of 10^{24} m^{-2} s^{-1} and temperature of 1400 °C in Pilot PSI

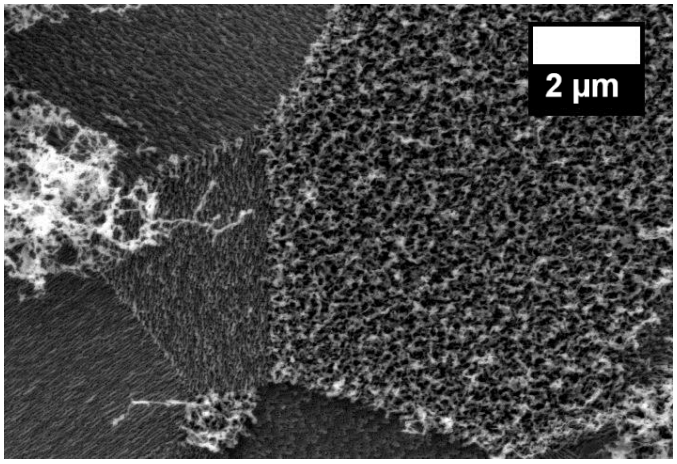

Figure 4.3: Grain dependence of fuzz growth at edge of plasma in W-3% Re exposed for 400 s at a flux of ~ 0.9 ×10^{24} $m^{-2}s^{-1}$and temperature of 1400 °C in Pilot PSI.

At the edge of the plasma exposed-area, where the temperatures and fluxes were lower (the flux was ~2.5 lower than at centre of plasma beam, with a value of 0.9 ×10^{24} $m^{-2}s^{-1}$), the fuzz growth is again seen to be initially dependant on grain orientation, as shown in Figure 4.3. Taking the W-3%Re sample as an example, the fuzz is seen to grow faster in some grains, as well as growing in different directions. This difference in fuzz growth on different grain

orientations has also been observed in pure W by Yamagiwa et al., as well as Ohno et al. among others [18] [19].The early stages of fuzz growth are also observed, as indicated in Figure 4.4. This structure appears platelet like.

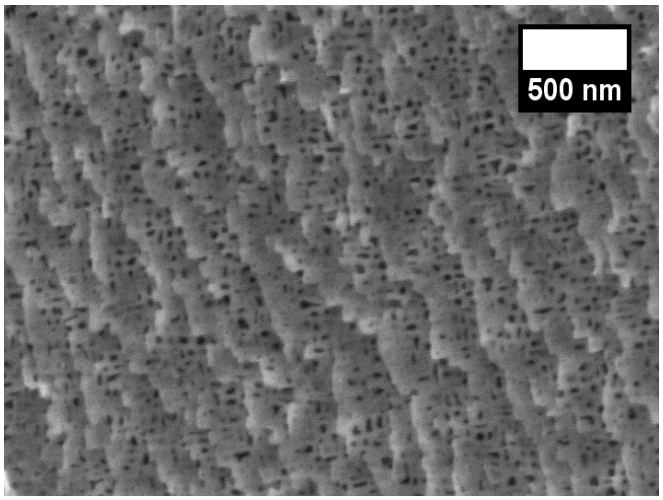

Figure 4.4: Early stage of fuzz growth at edge of plasma in W-3% Re exposed for 400 s at a flux of ~ 0.9×10^{24} $m^{-2}s^{-}$and temperature of 1400 °C in Pilot PSI.

TEM has been carried out to explore the formation mechanism of fuzz in the samples exposed for 400 s at a flux of 10^{24} m^{-2} s^{-1} and temperature of 1400 °C, as illustrated in Figure 4.5. Bright field images use the signal from on-axis un-diffracted electrons, whereas high-angle annular dark-field images utilise the signal from incoherently scattered electrons at high (< 50 mrad) angles [20]. The absence of diffraction contrast in HAADF images makes it a more suitable technique for the visualisation of the pore structure within the fuzz. It should be noted that in all the TEM images the white bubbly regions correspond to the fuzz structure, and the granular material surrounding this is platinum deposit from the sample preparation process, using FIB. It can be seen that in all cases there are a wide range of bubble sizes visible. In all cases coarser bubbles are observed at the base of the fuzz, which get smaller and smaller further up the tendrils. There are some areas where two separate strands of fuzz have formed around a large bubble, as labelled at position 1 of Figure 4.5 d) iii. It is possible that originally there was one strand of fuzz, encircling the bubble that has split into two parts or that the two strands formed independently of each other. It is not clear whether the bursting of the bubble has resulted in this separation, or there is another mode of growth at work here. It is also a possibility that this could be an artefact of production of the TEM sample via the use of FIB. At the base of the fuzz structure there are also multiple small bubbles. It is proposed that these will eventually coalesce to form larger bubbles. Such large bubbles are not observed at the top of the fuzz structure. In the case of W-3%Re bubbles are also observed up to 1 μm below the surface of the sample as highlighted in Figure 4.5 b). Such bubbles were not observed below the surface of the pure W and W-5% Re cases, however, this may be due to the fact we are only sampling a small volume. Again, the tendrils of fuzz in the pure W are seen to be much thinner than those in the rhenium

alloyed cases. Using the TEM images, close to the base of the fuzz, in the case of pure W, the tendrils vary in width between 17-40 nm, in the 3% Re case 22-45 nm and in the 5% case 30-54 nm, and from the HAADF imaging the bubbles within the pure W tendrils are seen to be much smaller than in the rhenium alloyed samples, reiterating the fact that the pure W fuzz is more developed than the W-3%Re and W-5%Re fuzz. The fact that the thinner the tendrils, the more developed the fuzz, is something that is also observed by Kajita et al. [14], where the fuzz depth increases with helium fluence, while the thickness of the tendrils decreases. It should also be acknowledged that the higher temperature of exposure for the rhenium alloyed samples may also be contributing to the thicker fuzz observed in these cases. The size of the helium bubbles formed is dependent on temperature and therefore the tendrils may be thicker in the rhenium alloyed samples, because of the larger bubbles being formed at higher temperatures.

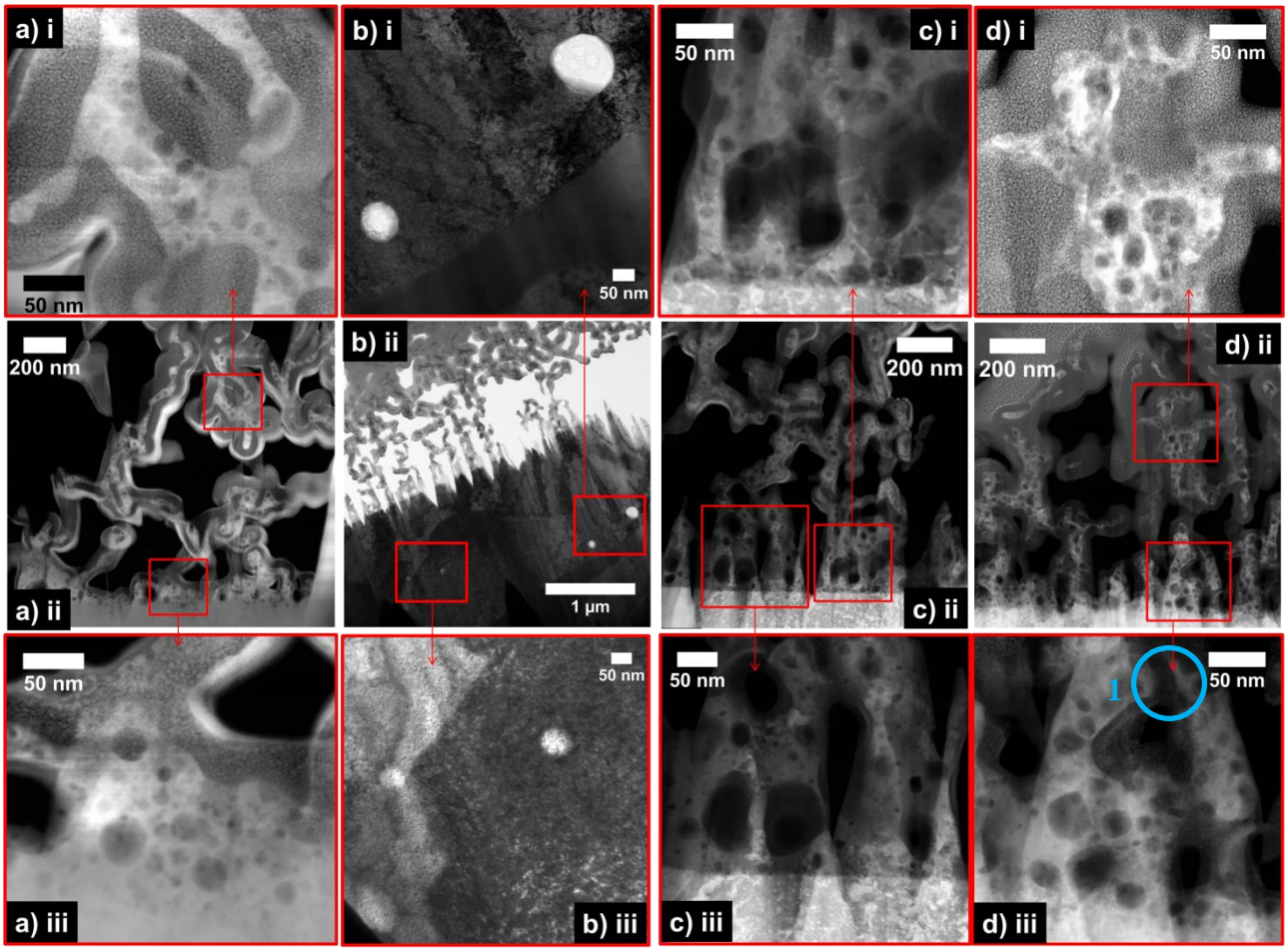

Figure 4.5: TEM images of fuzz in a) W (HAADF) b) W-3% Re (bright field) and c) W-3% Re (HAADF) and d) W-5% Re (HAADF) for samples exposed for 400 s at a flux of 10^{24} m^{-2} s^{-1} and temperature 1400 °C in Pilot PSI.

Selected area electron diffraction patterns (SADPs) were also taken from the fuzz tendrils of samples exposed in Pilot PSI, as shown in Figure 4.6. Apart from the continuous diffuse rings which index to FCC Pt (deposited during FIB preparation) all reflections (the bright dots) match to BCC polycrystalline tungsten (α phase), i.e. identical to bulk tungsten in its atomic structure (all the patterns have a common set of spacings, around 2.1, 1.5, 1.25 and 1.1

angstroms). This indicates fuzz formation is not related to any phase shift to the β phase and its associated columnar habit (elongated prism structure). The disparity in the position and frequency of reflections in each of the patterns is due to the generally low number and variation in orientation of the crystallites within the analysed areas.

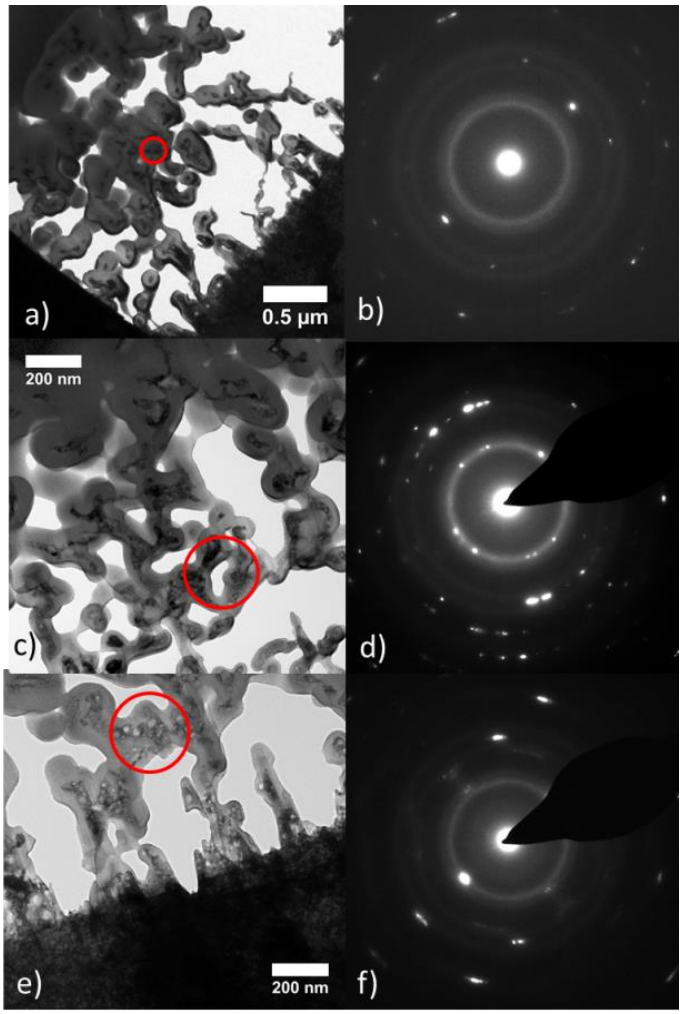

Figure 4.6: Bright field TEM images and corresponding diffraction pattern of fuzz in a) b) W c) d) W-3% Re and e) f) W-5% Re for samples exposed for 400 s at a flux of 10^{24} m^{-2} s^{-1} and temperature 1400 °C in Pilot PSI.

4.5 Conclusions

The effect of rhenium on the development of tungsten fuzz was investigated at a range of times, temperatures and fluxes by exposing pure W, W-3%Re and W-5%Re samples to helium plasmas, using the Magnum and Pilot PSI devices. In all cases it was seen that fuzz growth is dependent on grain orientation in the initial stages, however this effect disappears after some time. At these early stages, due to the strong orientation dependence, it was not clear what the effect of the rhenium addition was, with the grain to grain variation being more pronounced than the variation between rhenium concentrations. For 400 s exposures at 1400 °C and a flux of 10^{24} m^{-2} s^{-1} , rhenium addition appears to impede fuzz growth. TEM also

shows that in all cases, small bubbles coalesce together to form larger bubbles at the base of the tendrils. The bubbles get progressively smaller, further away from the base. Rhenium does seem to be affecting fuzz growth, but this effect differs depending on time, temperature and flux. Therefore it would be beneficial to conduct further plasma exposure experiments in order to build up a more detailed picture. For fully developed fuzz conditions, rhenium is seen to inhibit fuzz growth, which could be beneficial if fuzz was to form in DEMO, where it is known there will be transmutation of tungsten to rhenium. High temperatures of the order of 1340-1440 °C also appear to be having an inhibitive effect on fuzz growth and it is proposed that this is due to annealing and or erosive processes that are not observed when fuzz grows at lower temperatures.

Acknowledgements

The authors gratefully acknowledge the help and support from all the staff at DIFFER, without whom this work would be impossible. This work was supported by the Engineering and Physical Sciences Research Council [EP/K504178/1]. Acknowledgements are also given to the Leeds EPSRC Nanoscience and Nanotechnology Facility (LENFF). The author would also like to thank the referees for their insightful comments and thank TJ Petty for the useful conversations. The views and opinions expressed herein do not necessarily reflect those of the ITER Organization.

References

[1] T.J. Petty, M.J. Baldwin, M. Hasan, R.P. Doerner, J.W. Bradley, Nucl. Fusion 093033 (2015) 93033.

[2] M.J. Baldwin, R.P. Doerner, Nucl. Fusion 48 (2008) 035001 (5pp).

[3] R.A. Pitts, S. Carpentier, F. Escourbiac, T. Hirai, V. Komarov, S. Lisgo, A.S. Kukushkin, A. Loarte, M. Merola, A. Sashala Naik, R. Mitteau, M. Sugihara, B. Bazylev, P.C. Stangeby, J. Nucl. Mater. 438 (2013) S48.

[4] PLANSEE, "Materials: Tungsten," 2013. [Online]. Available: http://www.plansee.com/en/Materials-Tungsten-403.htm. [Accessed: 02-Jul-2013].

[5] Y. Ueda, H.T. Lee, N. Ohno, S. Kajita, a Kimura, R. Kasada, T. Nagasaka, Y. Hatano, a Hasegawa, H. Kurishita, Y. Oya, Phys. Scr. T145 (2011) 14029.

[6] M. Rieth, J.L. Boutard, S.L. Dudarev, T. Ahlgren, S. Antusch, N. Baluc, M.-F. Barthe, C.S. Becquart, L. Ciupinski, J.B. Correia, C. Domain, J. Fikar, E. Fortuna, C.-C. Fu, E. Gaganidze, T.L. Galán, C. García-Rosales, B. Gludovatz, H. Greuner, K. Heinola, N. Holstein, N. Juslin, F. Koch, W. Krauss, K.J. Kurzydlowski, J. Linke, C. Linsmeier, N. Luzginova, H. Maier, M.S. Martínez, J.M. Missiaen, M. Muhammed, A. Muñoz, M. Muzyk, K. Nordlund, D. Nguyen-Manh, P. Norajitra, J. Opschoor, G. Pintsuk, R. Pippan, G. Ritz, L. Romaner, D. Rupp, R. Schäublin, J. Schlosser, I. Uytdenhouwen, J.G. van der Laan, L. Veleva, L. Ventelon, S. Wahlberg, F. Willaime, S. Wurster, M. a. Yar, J. Nucl. Mater. 417 (2011) 463.

[7] V. A. Soukhanovskii, R.E. Bell, a. Diallo, S. Gerhardt, S. Kaye, E. Kolemen, B.P. LeBlanc, A. McLean, J.E. Menard, S.F. Paul, M. Podesta, R. Raman, D.D. Ryutov, F. Scotti, R. Kaita, R. Maingi, D.M. Mueller, a. L. Roquemore, H. Reimerdes, G.P. Canal, B. Labit, W. Vijvers, S. Coda, B.P. Duval, T. Morgan, J. Zielinski, G. De Temmerman, B. Tal, J. Nucl. Mater. 438 (2013) S96.

[8] Y. Ueda, K. Miyata, Y. Ohtsuka, H.T. Lee, M. Fukumoto, S. Brezinsek, J.W. Coenen, a. Kreter, a. Litnovsky, V. Philipps, B. Schweer, G. Sergienko, T. Hirai, a. Taguchi, Y. Torikai, K. Sugiyama, T. Tanabe, S. Kajita, N. Ohno, J. Nucl. Mater. 415 (2011) S92.

[9] G. De Temmerman, K. Bystrov, J.J. Zielinski, M. Balden, G. Matern, C. Arnas, L. Marot, J. Vac. Sci. Technol. A Vacuum, Surfaces, Film. 30 (2012) 41306.

[10] M.J. Baldwin, R.P. Doerner, D. Nishijima, K. Tokunaga, Y. Ueda, J. Nucl. Mater. 390-391 (2009) 886-890.

[11] M.R. Gilbert, J.-C. Sublet, Nucl. Fusion 51 (2011) 43005.

[12] A. Möslang, E. Diegele, M. Klimiankou, R. Lässer, R. Lindau, E. Lucon, E. Materna-Morris, C. Petersen, R. Pippan, J.. Rensman, M. Rieth, B. Van Der Schaaf, H.-C. Schneider, F. Tavassoli, Nucl. Fusion 45 (2005) 649.

[13] J. Davis, V. Barabash, A. Makhankov, J. Nucl. Mater. 263 (1998) 308.

[14] M.J. Baldwin, R.P. Doerner, J. Nucl. Mater. 404 (2010) 165.

[15] G. De Temmerman, K. Bystrov, J.J. Zielinski, M. Balden, G. Matern, C. Arnas, L. Marot, J. Vac. Sci. Technol. A Vacuum, Surfaces, Film. 30 (2012) 041306.

[16] S. Kajita, N. Ohno, M. Yajima, J. Kato, J. Nucl. Mater. 440 (2013) 55.

[17] S. Takamura, Y. Uesugi, Appl. Surf. Sci. 356 (2015) 888.

[18] M. Yamagiwa, S. Kajita, N. Ohno, M. Takagi, N. Yoshida, R. Yoshihara, W. Sakaguchi, H. Kurishita, J. Nucl. Mater. 417 (2011) 499.

[19] N. Ohno, Y. Hirahata, M. Yamagiwa, S. Kajita, M. Takagi, N. Yoshida, R. Yoshihara, T. Tokunaga, M. Tokitani, J. Nucl. Mater. 438 (2013) S879.

[20] D. Williams, C. Carter, Transmission Electron Microscopy, 1996.

5 Effect of Rhenium Concentration on Tungsten Fuzz Growth in Helium Plasmas at High Fluence

A paper accepted by the peer reviewed journal: Journal of Nuclear Materials

Presented as an adaptation of the accepted form.

Authors
Aneeqa Khan, Thomas W. Morgan, Thomas J. Petty, Michael B. Ward, Paul Mummery

Effect of Rhenium Concentration on Tungsten Fuzz Growth in Helium Plasmas at High Fluence

Aneeqa Khan[a], Thomas W. Morgan[b], Thomas J. Petty[c], Michael B. Ward[d], Paul Mummery[a]

[a] *School of Mechanical, Aerospace and Civil Engineering, The University of Manchester, M13 9PL, UK*
[b] *FOM Institute DIFFER – Dutch Institute for Fundamental Energy Research, Partner in the Trilateral Euregio Cluster, 5612 AJ Eindhoven, the Netherlands*
[c] *Department of Electrical Engineering and Electronics, University of Liverpool, Brownlow Hill, Liverpool L69 3GJ, UK*
[d] *Institute for Materials Research, School of Chemical Process Engineering, University of Leeds, Leeds, LS2 9JT, UK*

Abstract

The effect of rhenium addition on tungsten fuzz growth in fusion relevant helium plasmas at high fluences is investigated. Previous work at temperatures of ~1340-1440 °C indicated that rhenium was having an inhibiting effect on growth. However, possibly due to the effect of annealing, and the early-stage W-fuzz growth observed, the relationship between rhenium concentration and fuzz growth was unclear. A study was conducted at lower temperatures of 1025 °C, so that the rhenium concentration would be the dominant factor. Re is observed to have an inhibitory effect on fuzz growth, with exception of a W-3%Re sample exposed to a fluence of ~1 $\times 10^{26}$ m^{-2}. It was suggested that the reduced growth could be due to the increased ductility of W-Re over W. Alternatively it could be due to a retardation of $\mathbf{b}=1/2\langle 111\rangle$ loop motion by Re, which could slow bubble growth and hence the formation of fuzz. Evidence for an incubation time for fuzz growth was also provided.

5.1 Introduction

Tungsten (W) is a candidate material for plasma facing components, including the divertor, in demonstration fusion power plants (DEMO) due to its high melting temperature, resistance to sputtering, and its strength at high temperatures [1]–[3]. In DEMO, 14 MeV neutrons have been predicted to cause transmutation of W to rhenium (Re) and osmium (Os), becoming W-3.8at%Re-1.4at%Os after five years of operation [4]. Over the past several years a phenomenon known as fuzzy W has been observed in linear plasma devices and also within the C–Mod tokamak at MIT [1]. Fuzzy W is the surface modification of a W sample upon bombardment by helium (He) ions at elevated temperatures. Previous work by the authors at temperatures of ~1340-1440 °C and fluences of the order of 10^{27} m^{-2} revealed that Re has an inhibiting effect on fuzz growth [5]. However, due to the high temperatures, and the additional contribution of annealing and erosion processes to the fuzz formation mechanism that are not well understood, it was not clear what was driving the inhibiting effect of Re. Therefore the present study has systematically investigated the effect of Re addition to pure W, using W-3wt%Re and W-5wt%Re at lower temperatures, in order to try and discern how Re is effecting the fuzz formation mechanism. The variation of fuzz development across the plasma beam profile has also been addressed.

5.2 Materials

Throughout this study three different materials were used; 99.97% purity W discs (Plansee), and 99.95% commercial purity W-3wt%Re and W-5wt%Re rods (Ultra Minor Metals). Re concentrations of 3 and 5wt% were used in order to give a representation of the 3.8at% Re predicted in DEMO after five years of operation at full power [4]. All percentages from now on should be considered as weight percentages unless otherwise stated. The rods were manufactured via a swaging process, utilising W and Re powder, with particles ~4-5 μm in size. The pure W discs were 30 mm in diameter and 1 mm thickness (average grain size of ~1.2 μm). The W-Re rods were 15 mm in diameter and were cut using electrical discharge machining (EDM) into discs ~1 mm in thickness. All the discs were polished using SiC grinding paper, 3 μm and 1 μm diamond suspension and finally colloidal alumina with a particle size of 0.05 μm. Following this they were ultrasonically cleaned, utilising ethanol and then acetone. Before exposure the samples were outgassed for 15 minutes at a temperature of 1000 °C.

5.3 Experimental

All samples were exposed to helium plasmas within the Pilot-PSI linear plasma device [6]. Samples of pure W, W-3%Re, and W-5%Re were exposed to He plasmas at an average temperature of 1025 °C, and fluxes of the order of 10^{23} $m^{-2}s^{-1}$. The bias was maintained at -50 V, T_e was ~0.3 eV and n_e was ~0.8×10^{20} m^{-3} for each exposure. This corresponds to a He ion energy of 45 eV. The profile of the beam was Gaussian with a full width half maximum (FWHM) of ~ 10 mm. Three samples of each alloy were studied, exposing one sample of each alloy for 800, 1600, and 3200 s. All experiments were carried out in a single continuous exposure. The samples were weighed before and after exposure. An overview of the experimental conditions for each alloy is shown in Table 5.1. The flux in the table is the flux in the centre of the sample, i.e. the peak in the flux graph. The flux variations for all the samples, across the profile of the sample for 800, 1600 and 3200 s exposures are shown in Figure 5.1. There is some variation between the fluxes used on each sample. There is ~3×10^{22} $m^{-2}s^{-1}$ and a 7×10^{22} m^{-2} s^{-1} difference between pure W and W-3%Re and W-5%Re respectively at the peak in the 800 s shot. For the 1600 s samples, the Re samples have extremely similar fluxes, and the pure W has a flux that is ~ 3×10^{22} $m^{-2}s^{-1}$ greater. For the 3200 s, the fluxes are all within ~0.4×10^{2} $m^{-2}s^{-1}$ of each other at the peak. This variation in flux is something that has also been observed in other LPDs such as PISCES-A[7].

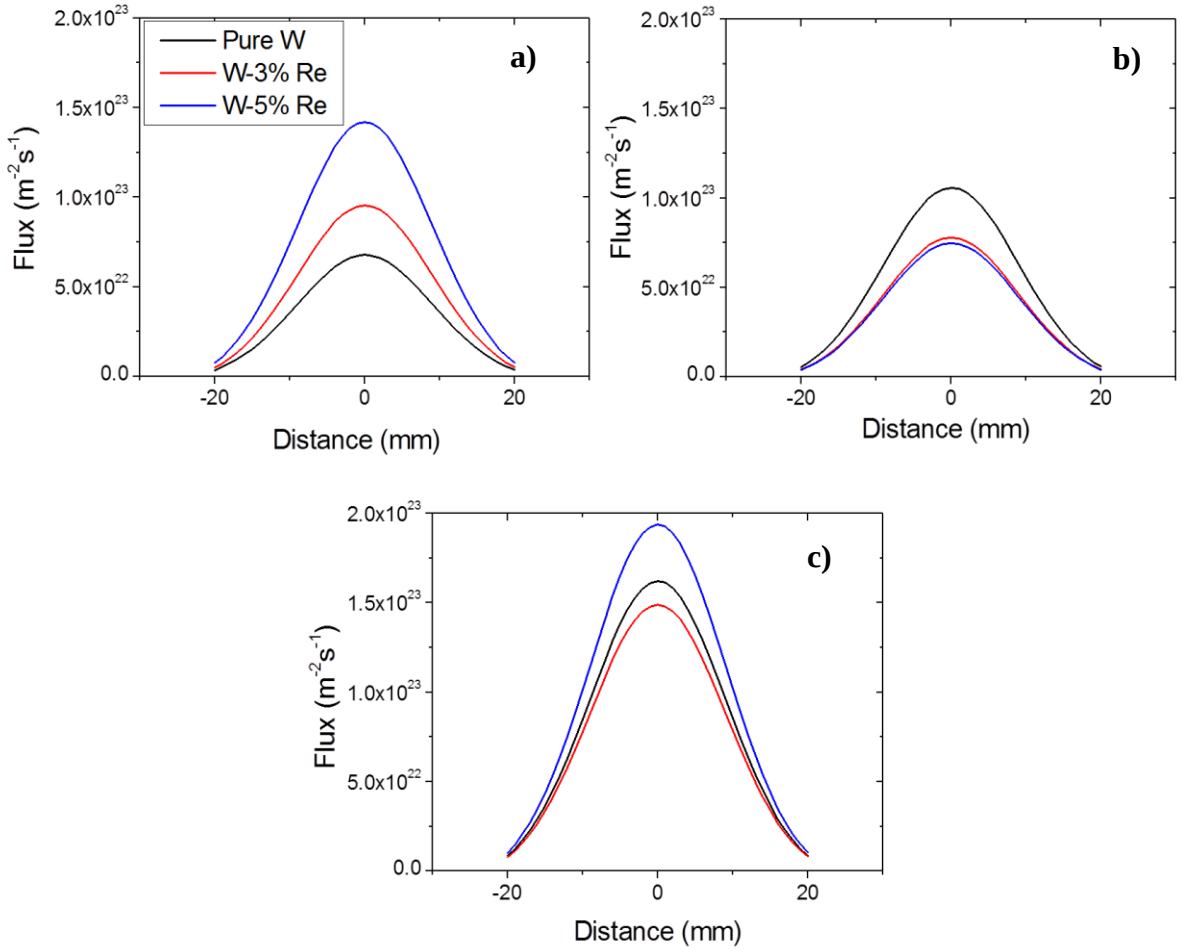

Figure 5.1: Variation in flux across the sample for pure W, W-3%Re and W-5%Re exposed for a) 800 s, b) 1600 s and c) 3200 s.

Table 5.1: Plasma exposure conditions.

Material	Flux ($m^{-2}s^{-1}$)	Duration (s)	Fluence (m^{-2})
W	$6.8\pm0.8\times10^{22}$	800	$5.4\pm0.6\times10^{25}$
	$1.1\pm0.2\times10^{23}$	1600	$1.7\pm0.3\times10^{26}$
	$1.6\pm0.5\times10^{23}$	3200	$5.2\pm1.4\times10^{26}$
W-3%Re	$9.5\pm1.1\times10^{22}$	800	$7.6\pm0.9\times10^{25}$
	$7.8\pm1.6\times10^{22}$	1600	$1.2\pm0.3\times10^{26}$
	$1.5\pm0.5\times10^{23}$	3200	$4.8\pm1.5\times10^{26}$
W-5%Re	$1.4\pm0.3\times10^{23}$	800	$1.1\pm0.2\times10^{26}$
	$7.5\pm1.0\times10^{22}$	1600	$1.2\pm0.2\times10^{26}$
	$1.9\pm0.5\times10^{23}$	3200	$6.2\pm1.6\times10^{26}$

In order to accurately measure the temperature of the samples during exposure, both an infra-red camera and pyrometer were used.

Following the plasma exposures, scanning electron microscopy (SEM), and focused ion beam (FIB) was conducted at a series of positions across the profile from the centre of the plasma

beam to the edge. This allowed the variation of the thickness of the fuzz layer and surface morphology across the surface to be analysed. The method is described in more detail in the results section.

5.4 Results

The measurements of the mass loss are shown in Figure 5.2. It should be noted that measurements for the 1600 s pure W exposure, and the 3200 s W-3%Re exposure were erroneous and thus have been omitted from the figure. The energies in this study (~45 eV) are below the sputtering threshold for W (~109 eV [8]), however, mass loss is still observed. This is assumed to be due to trace impurities within the plasma and has also been observed in other machines [9]. At temperatures of ~1000 °C and energies of 50 eV a yield of 5×10^{-5} atoms/ion has been reported for Pilot PSI in tungsten [6]. For the pure tungsten samples, at the fluences employed (taking into account the Gaussian beam profile), this corresponds to a mass loss of ~ 4.5×10^{-4} g after 3200 s, which is close to the experimentally observed values. In general there is an increase in mass loss with increased fluence. Although it is difficult to see a large difference in the mass loss of the lower fluence samples, there is a suggestion at the highest fluences that the mass loss is greater in W-5%Re in comparison to pure W. Even though the data is limited, this hints that the Re could be inhibiting erosion.

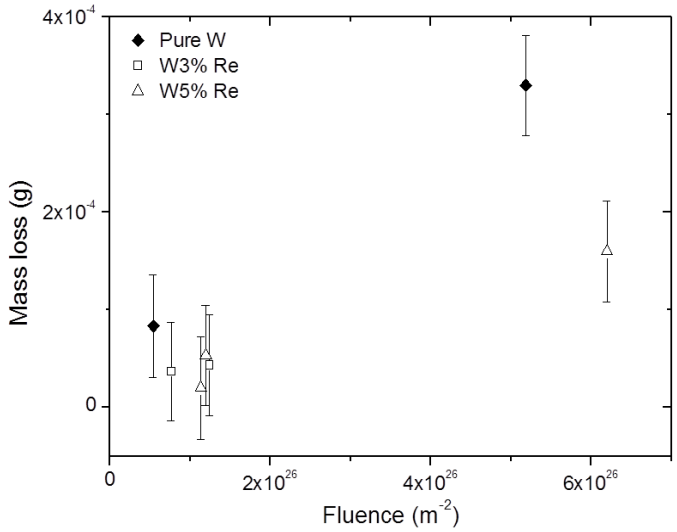

Figure 5.2: Plot of mass loss against fluence for pure W, W-3%Re, and W-5%Re.

FIB cross-sections were carried out at various positions on the samples. The plasma beam has a non-uniform intensity across the surface of the samples. The variation of flux across the beam for all the samples is highlighted in Figure 5.1. As such, different positions on the sample reflect different fluences, thereby giving multiple data points for each sample. Each cross section was 15 µm in length, an example of which is shown in Figure 5.3. High and low magnification SEM images close to the region of the FIB cross sections were also taken to reveal the nature of the fuzz on the surface of the samples. Detailed images for all the samples can be found in Figure 5.4-Figure 5.9. Values for the thickness of the fuzz layer were obtained by taking several measurements across the FIB cross section (higher magnification images were used to accurately determine thickness of thinner fuzz layers). Following work by Petty *et al.* [9], the relationship between fluence and fuzz thickness is illustrated in Figure 5.10. A fluence profile across all samples was determined from the Thomson scattering values for T_e and n_e across the beam profile. For this plot, data was taken from 0-5 mm across the profile, where the temperature measured using the IR camera was observed to be fairly uniform (~1025 ±50 °C). The position for each cross section was correlated to the fluence at that position. The error bars on these plots represent the standard deviation of the range of thickness measurements across the section. It can clearly be seen that fuzz growth, and the effect of Re is dependent on fluence.

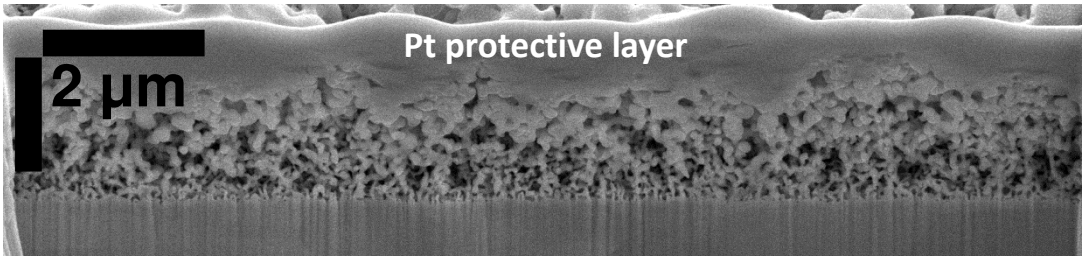

Figure 5.3: FIB cross section for W-5w%Re exposed for 3200 s at ~1025 °C and flux of 1.9± 0.5×10^{23} $m^{-2}s^{-1}$. The image was taken at 45° and therefore a tilt corrected vertical scale bar is also included. There is a layer of platinum across the top to protect the fuzz.

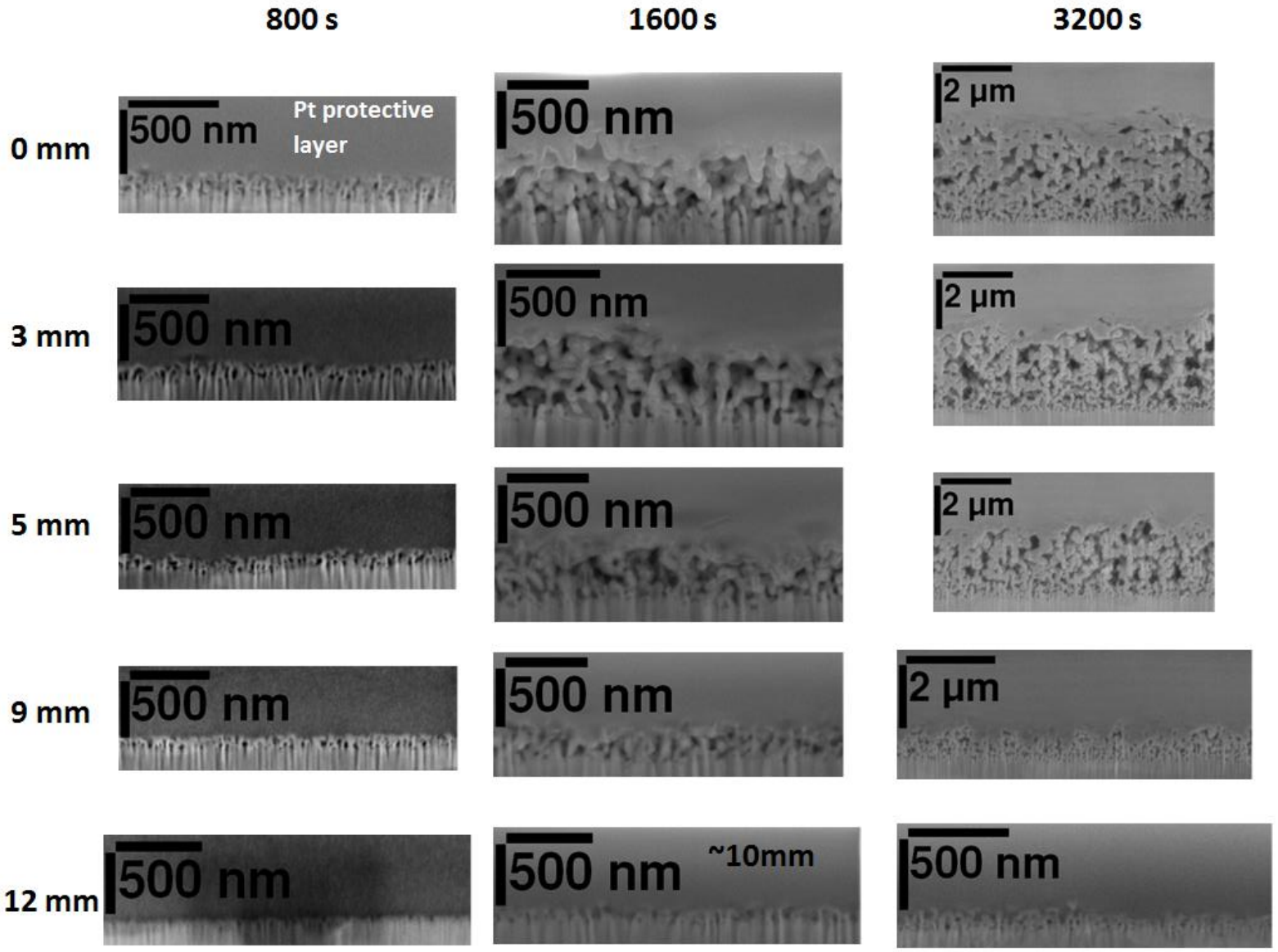

Figure 5.4: FIB Cross Sections at 0, 3, 5, 9 and 12 mm (with exception of the 1600s sample, where the final measurement is taken at 10 mm) from the centre of the plasma beam in Pure W exposed for 800, 1600 and 3200 s at 1025 °C and a peak flux of ~ 1-2×10^{23} $m^{-2}s^{-1}$. In all images there is a platinum protective layer at the top, which is labelled in the image for the 800 s exposed sample at 0 mm. As the images were taken at a tilt of 45°, a tilt corrected scale bar is also given in the vertical direction in all images. The fuzz layer thickness is seen to decrease away from the centre of the sample, and the fuzz layer thickness is seen to increase with exposure time.

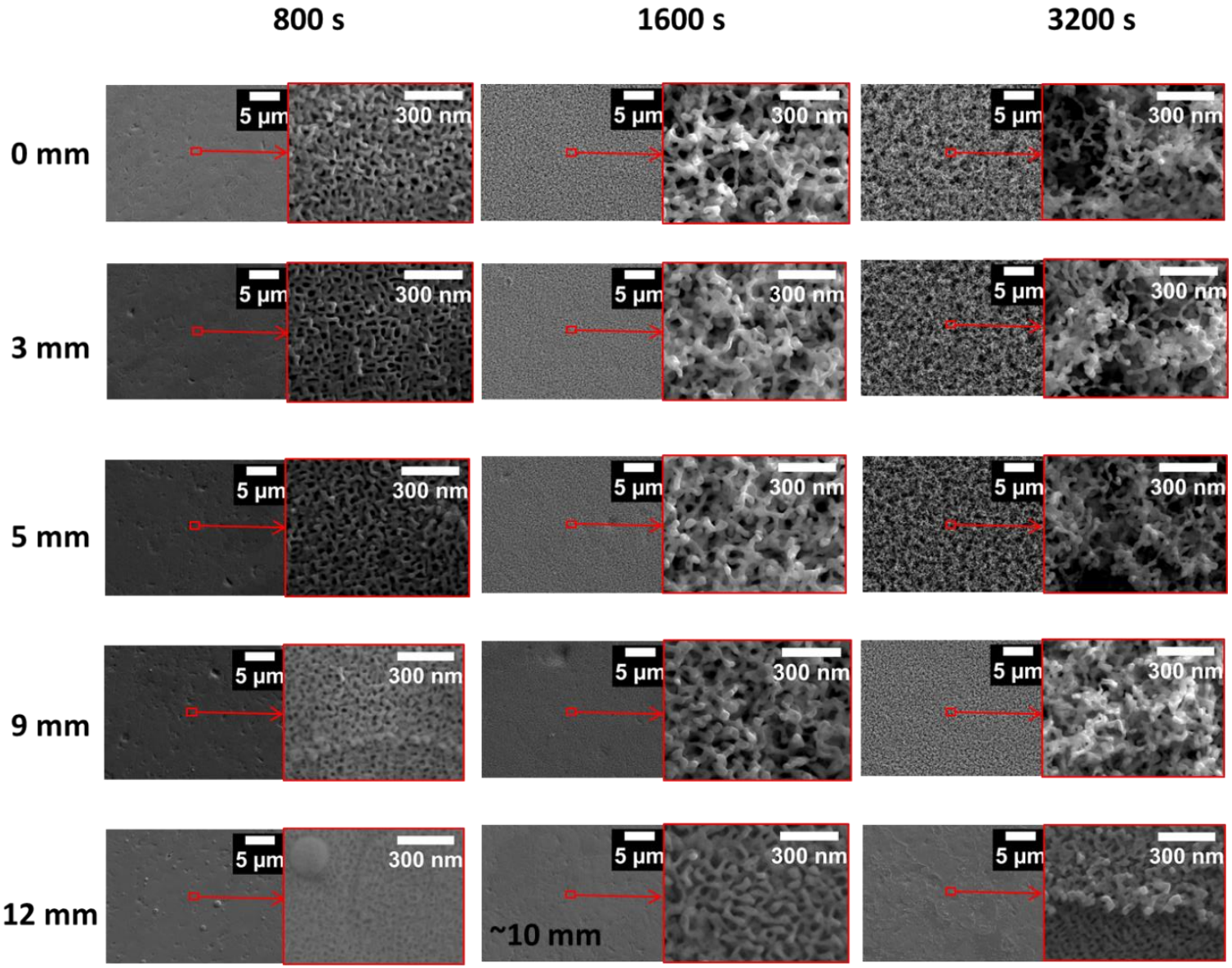

Figure 5.5: High and low magnification SEM images of the surface at 0, 3, 5, 9 and 12 mm (with the exception of the 1600 s exposure where the final measurement is taken at 10 mm) from the centre of the plasma beam in Pure W exposed for 800, 1600 and 3200 s at 1025 °C and a peak flux of ~ 1-2×10^{23} $m^{-2}s^{-1}$. The fuzz tendrils are angular and coarse, even in the middle of the sample following the 800 s exposure, where the grain boundaries are still slightly visible at low magnification. Some sort of blisters are visible at 12 mm. At 1600 s and 3200 s the fuzz becomes more disordered and the tendrils appear to get thinner. Across the sample the tendrils get thicker and more angular, and at 12 mm in the 3200 s sample the grains appear to be visible again.

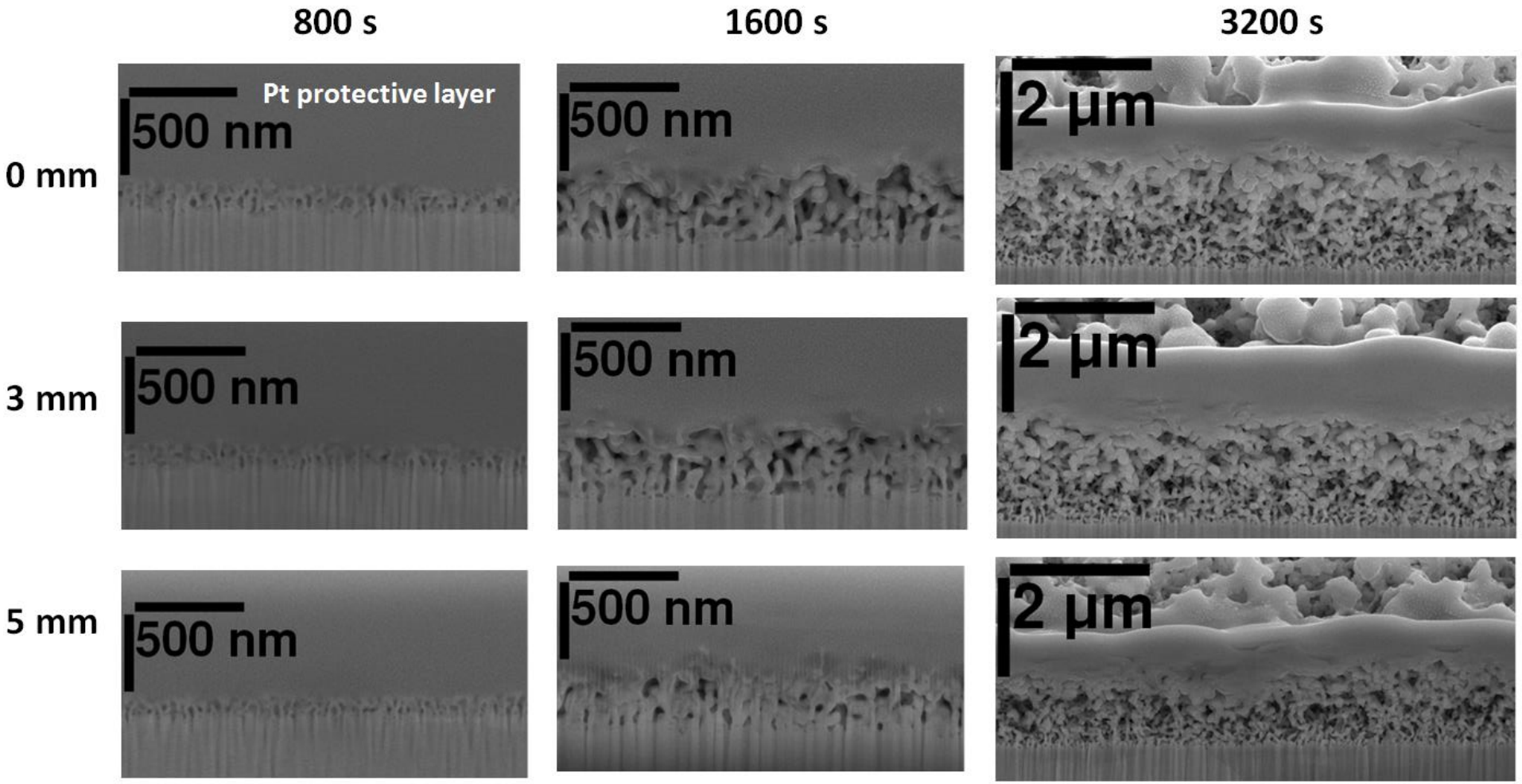

Figure 5.6: FIB Cross Sections at 0, 3, and 5 mm from the centre of the plasma beam in W-3%Re exposed for 800, 1600 and 3200 s at 1025 °C and a peak flux of ~ 1-2×10^{23} $m^{-2}s^{-1}$. In all images there is a platinum protective layer at the top, which is labelled in the image for the 800 s exposed sample at 0 mm. As the images were taken at a tilt of 45°, a tilt corrected scale bar is also given in the vertical direction in all images. There is a slight decrease in thickness across the sample in all cases. The fuzz thickness noticeably increases with exposure time.

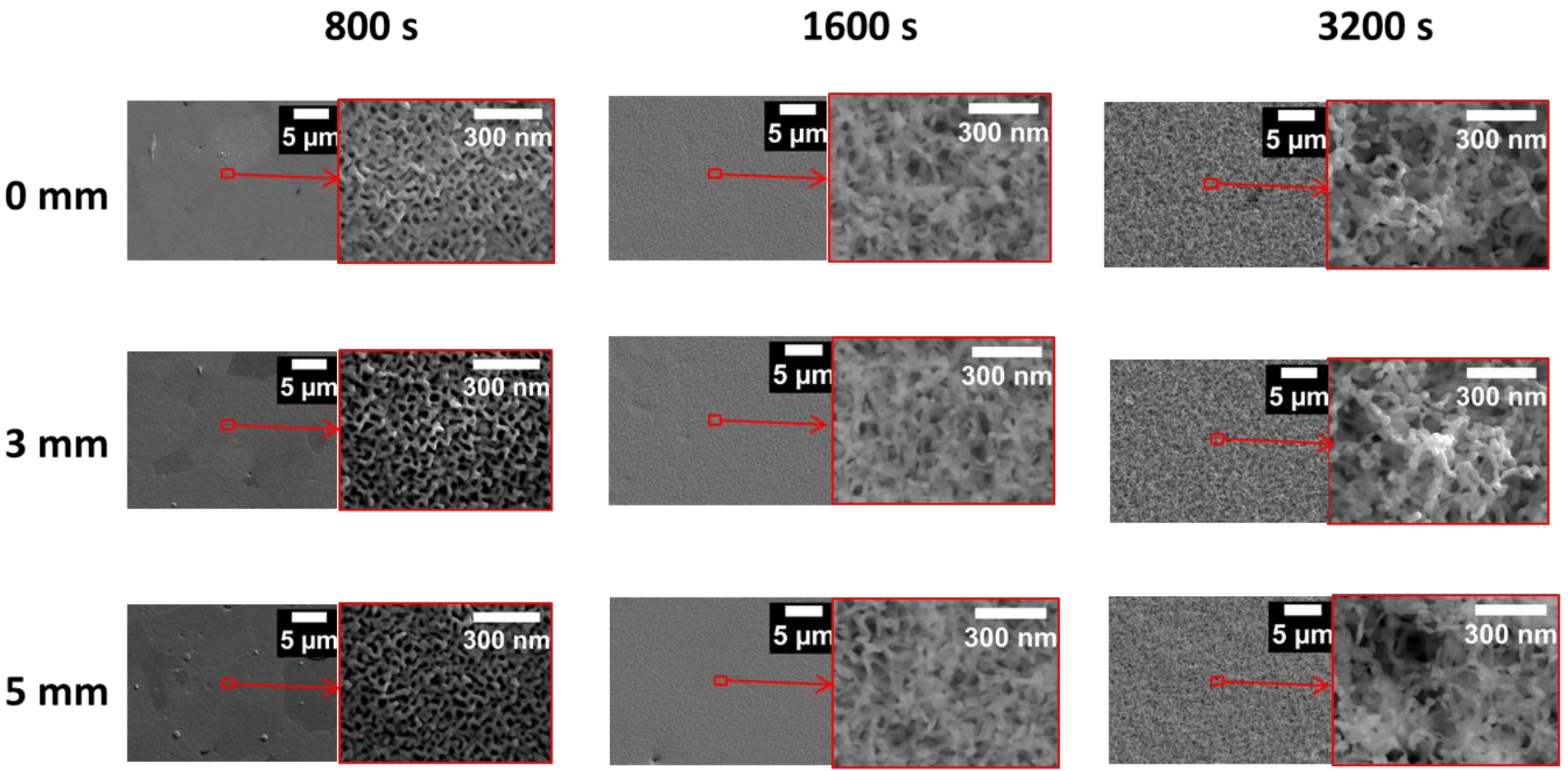

Figure 5.7: High and low magnification SEM images of the surface at 0, 3, and 5 mm from the centre of the plasma beam in W-3%Re exposed for 800, 1600 and 3200 s at 1025 °C and a peak flux of ~ 1-2×10^{23} $m^{-2}s^{-1}$. For the 800 s exposures the fuzz is thicker and very angular, with large voids visible in between the tendrils. At low magnifications the grains are visible, especially at 3 and 5 mm. At 5mm some blister like features are also observed. The tendrils become thinner and more disordered and the regular spaced black holes less visible with increased exposure time. However, in this case the tendrils appear thicker than those seen in pure W under similar conditions.

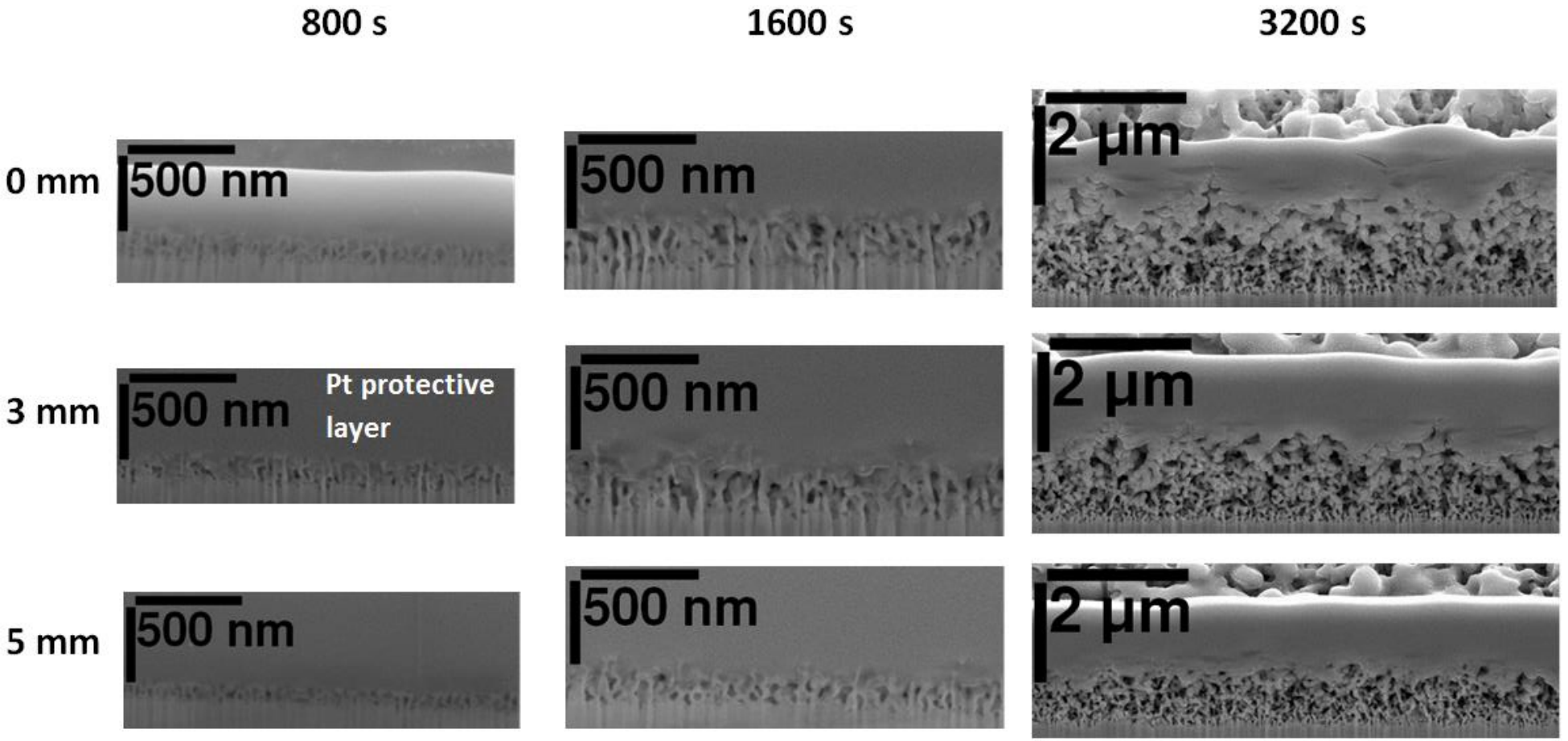

Figure 5.8: FIB Cross Sections at 0, 3, and 5 mm from the centre of the plasma beam in W-5%Re exposed for 800, 1600 and 3200 s at 1025 °C and a peak flux of ~ 1-2×10^{23} $m^{-2}s^{-1}$. In all images there is a platinum protective layer at the top, which is labelled in the image for the 800 s exposed sample at 3 mm. As the images were taken at a tilt of 45°, a tilt corrected scale bar is also given in the vertical direction in all images. Again it is observed that the fuzz thickness is seen to decrease with distance from the centre of the sample, however this effect is more pronounced for the 3200 s exposure. The fuzz layer thickness is greater with increased exposure time, with the 3200 s sample having a significantly thicker layer in comparison to the other samples.

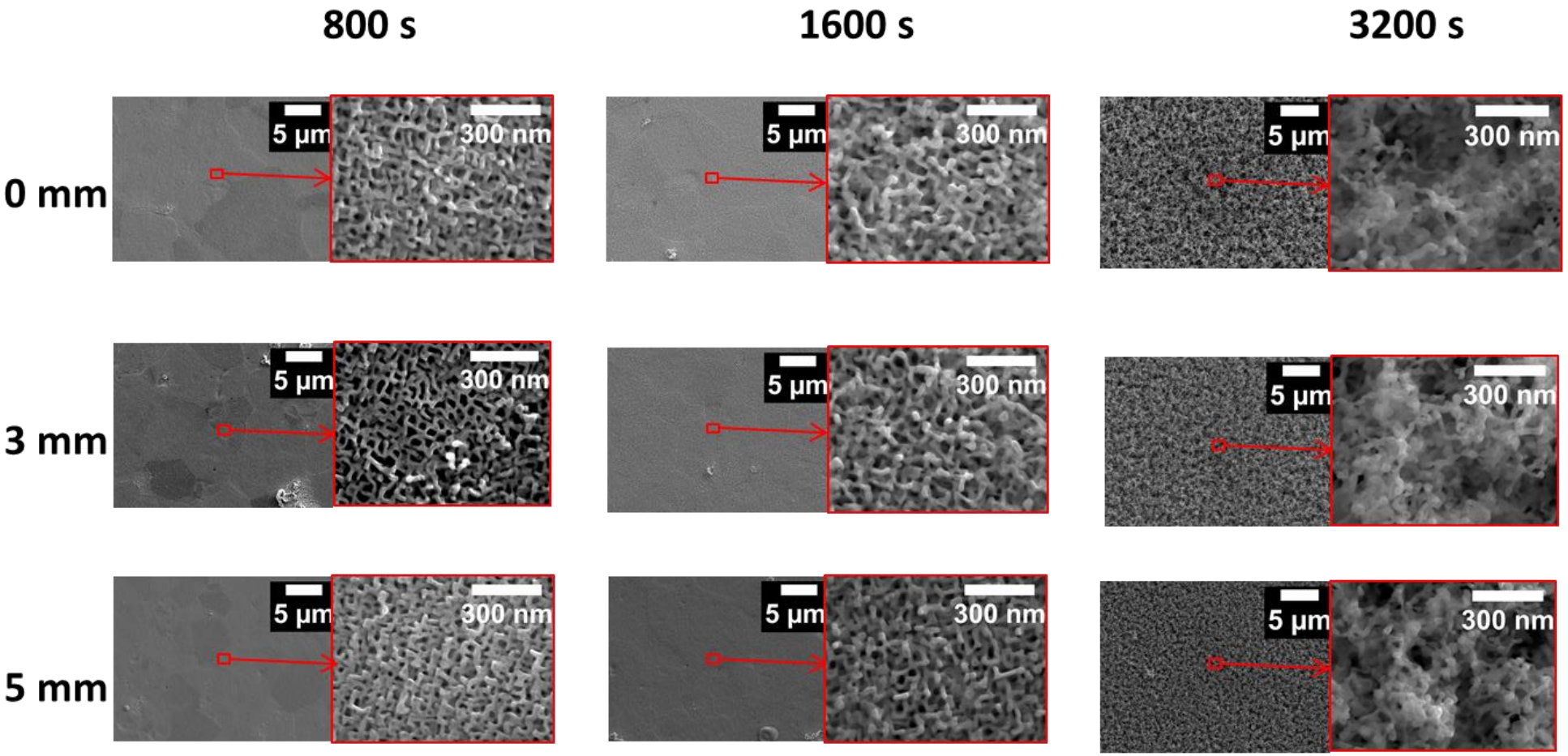

Figure 5.9: High and low magnification SEM images of the surface at 0, 3, and 5 mm from the centre of the plasma beam in W-5%Re exposed for 800, 1600 and 3200 s at 1025 °C and a peak flux of ~ 1-2×10^{23} $m^{-2}s^{-1}$. As seen in previous samples the grain boundaries are visible for the 800 s sample, however for the W-5% Re, they are also slightly visible even at 1600 s, suggesting a slower rate of growth. Again the fuzz growth at 800 s is observed to be coarse and angular in nature, with visible regular black holes in between tendrils. Although the fuzz appears to be slightly more disordered at 1600 s, it is not as disordered as that seen for the pure W and W-3%Re samples, By 3200 s the grain boundaries are no longer visible, and the fuzz tendrils are thinner and more disordered than the shorter exposures, but still thicker than those seen in pure W under similar conditions.

5.5 Discussion

5.5.1 Mass loss

It has been extensively observed in the literature that fuzz growth increases with fluence [9], and this experiment shows the same trend. Fuzz growth does not typically involve a mass loss as it is a growth process [10]. As has been mentioned previously the energy of the incoming He particles is less than the sputtering threshold for tungsten, and it is therefore suggested that the mass loss is due to trace impurities in the plasma. These impurities could include N, O or W. If we use equation 1, we can determine the sputtering threshold for such impurities [8].

$$E_{th} = \frac{(M_i+M_t)^2}{4M_iM_t} E_s \qquad (1)$$

E_{th} is the threshold sputtering energy, M_i is the mass of the incident ion, M_t is the mass of the target and E_s is the surface binding energy, which for W is taken to be 8.68 eV [11], [12]. The calculated sputtering thresholds for N, O and W are thus calculated as 33, 29 and 8.68 eV respectively. This is clearly less than the energies of 45 eV used in this experiment, and therefore sputtering by these impurities is a distinct possibility.

At higher fluences there will be an increased number of impurity particles incident on the samples, and consequently increased sputtering. This explains why in total there is a higher mass loss at increased fluences (Figure 5.2). This increased effect of erosion by impurities at higher fluences is something that has also been observed by Petty *et al.* [9]. Typically in the literature, fuzz has been observed to inhibit sputtering, as particles sputtered from the bulk are trapped within the fuzz [13]. The rate of loss for pure W at the lower fluence (and hence a thinner layer of fuzz) is estimated as ~0.15 mg/10^{26} particles, and as ~ 0.06 mg/10^{26} particles at the higher fluence. This is consistent with the findings in the literature [13]. Figure 5.2 hints that there may be reduced erosion in the Re samples, however there is only one data point and therefore it is difficult to make a firm conclusion.

5.5.2 Variation of Fuzz Growth with Time and Fluence

From the top surface and cross sectional SEM images (Figure 5.4-Figure 5.9) , it is observed that for all the samples exposed for 800 s, the fuzz growth is dependent on orientation, which has been previously observed by several other authors [5], [14]–[16]. The nanostructure is ordered on the underlying grain orientation, very angular, and coarse in nature. Regularly spaced black holes are visible between the tendrils. This corresponds to fuzz layers that are all less than 200 nm in thickness. The thickness decreases at an increasing rate across the plasma beam profile and at the centre of the plasma beam the thickness of the fuzz layer in the W-3%Re and W-5%Re cases is 89% and 85% of the pure W case, respectively.

At 1600 s, in the pure W case, at 0 mm the grain boundaries are barely visible, as is the case with W-3%Re. However, for the W-5%Re cases the grains are more visible, indicating that the growth is still orientation dependant and that it is at an earlier stage of growth, which is reiterated by the fact the fuzz thickness is 49% of the pure W. For W-3%Re the fuzz thickness is 72% of the pure W at 0 mm. From the SEM images it can be seen that the fuzz is

more disordered (it is less angular in nature and there is more variation in the tendril thickness and direction of growth) in comparison to the fuzz observed at 800 s. The fuzz in the pure W and W-3%Re is more disordered than the W-5%Re exposed for 1600 s. The fact the fuzz is more disordered is another indication of increased growth, which fits with the observed increase in layer thickness, again providing an indication that Re is inhibiting fuzz growth.

At 3200 s the grain dependence has all but disappeared in all cases, and the fuzz is extremely disordered at the centre of the plasma beam for all samples. There is a significant increase in thickness, from the 1600 s exposure with the pure W and W-3%Re being 4.6 times thicker in the centre of the beam and the W-5%Re, 6 times thicker in comparison to the 1600 s exposure. The W-3%Re and W-5%Re thicknesses are 71% and 66% of that of the pure W layer, respectively.

In all cases the fuzz thickness is seen to increase with fluence, with fuzz growth being highest in the centre of the samples (Figure 5.10). There is an indication that Re is inhibiting fuzz growth, with all samples containing Re, with exception of the 3%Re sample in the 1600 s exposure lying below the line created by the pure W samples. For the specific data produced in this experiment, the fuzz layer thickness for pure W appears to increase with a power law trend with fluence ($x(\Phi) = (1.03 \times 10^{-32}) \times \Phi^{1.22}$).

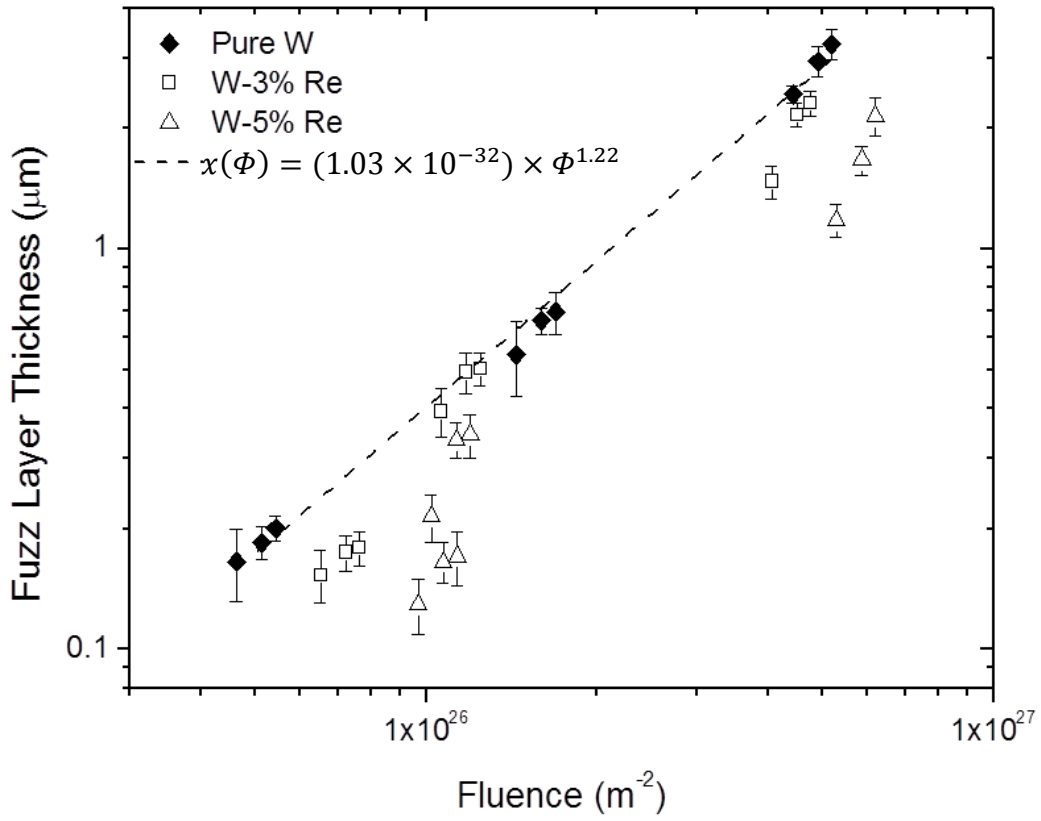

Figure 5.10: Variation of fuzz thickness with fluence for pure W, W-3%Re, and W-5%Re. Fluence was calculated as a function of the radius of the sample. Variation of fluence across 5 mm only was considered, as in this region the temperature was fairly uniform and was ~1025 °C.

A comparison of our results to those from experiments in other devices in the literature, and also to the thickness values expected from the constant, C ($x(\Phi) = (C(\Phi - \Phi_0))^{1/2}$, where x is the thickness of the fuzz layer, Φ is fluence and $\Phi_0$is incubation fluence) determined by Petty *et al.* [9] has been conducted. This is illustrated in Figure 5.11.The majority of the literature data comes from experiments carried out at temperatures between ~800-930 °C [9], [17], which is lower than the 1025 °C used in this study. The C model predicts that fuzz growth will increase at higher temperatures, and the present data obtained at ~1025 °C should be close to that predicted for temperatures of 1047 °C. However, our data falls well below the prediction and even below the model for 847 °C. This could be because the model does not take into account annealing. Annealing out of fuzz is something that has been observed extensively in the literature, and it has been seen that fuzz thickness is lower at higher temperatures, past a certain threshold for annealing. Kajita *et al.* found this temperature to be 1127 °C [18], and Baldwin and Doerner observed annealing up to temperatures of 1627 °C [10], [17]. However, it is not clear why annealing would have a larger impact in the present study compared to literature values at similar temperatures. Something else may be affecting the growth rate.

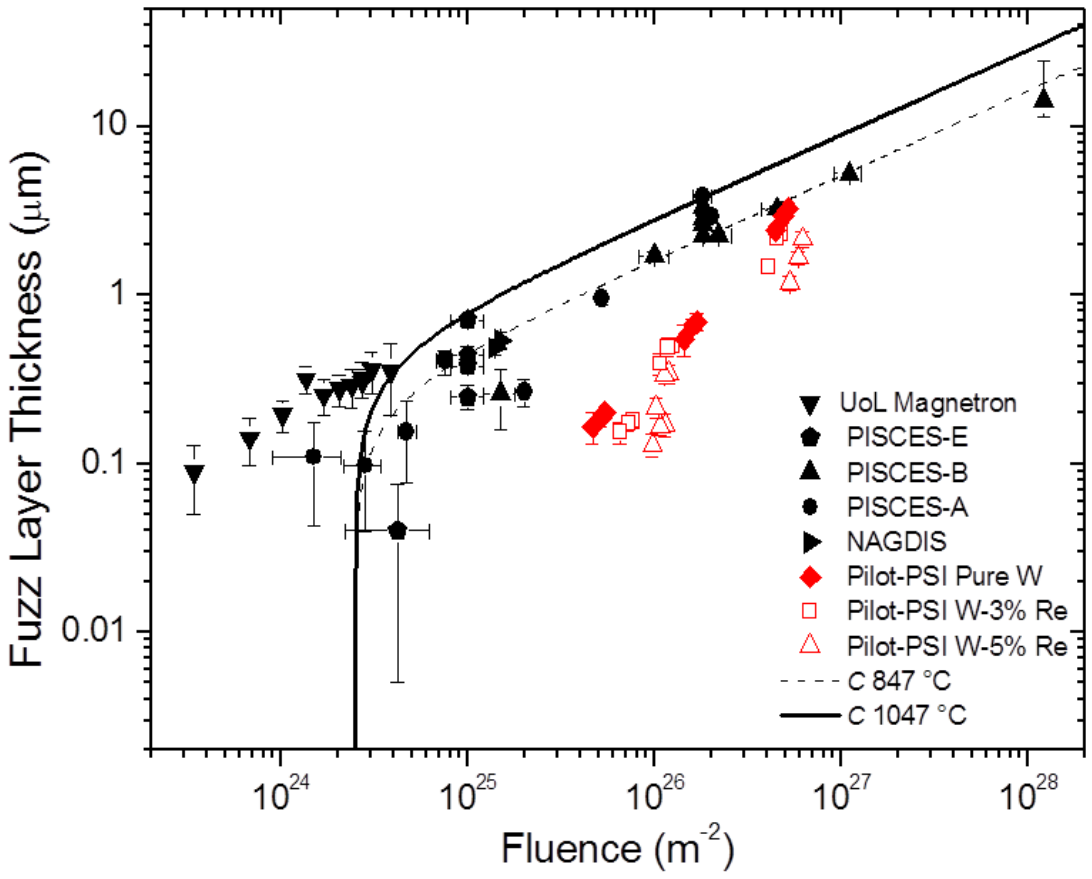

Figure 5.11: Variation of fuzz thickness with fluence, in comparison to experiments in literature and C values determined from diffusion coefficients at 847 °C and 1047 °C. For references for the literature data points see [9], [17]. Data to calculate C is obtained from [17].

5.5.3 Incubation Time

It has been observed by Baldwin *et al*. that the growth rate of fuzz is limited at higher fluxes, which could also be a reason for the reduced growth , in comparison to the rest of the literature [19]. Baldwin *et al.* found that at fluxes greater than 10^{22} $m^{-2}s^{-1}$, following a 3600 s exposure there was no change in the thickness of the fuzz layer. This suggests that at such fluxes something other than the supply of He could be limiting fuzz growth. In the current study the flux of 10^{22} $m^{-2}s^{-1}$ is exceeded in all cases. Therefore it may that rather than fluence or flux, time may be the important quantity when trying to predict fuzz growth.

Baldwin *et al*. have suggested that rather than an incubation fluence, there is an incubation time before fuzz can grow [19]. Therefore another possibility is that due to the fact the fluxes used in Pilot-PSI are higher compared to the other devices (Figure 5.12, Figure 5.13), the incubation time is longer as a proportion of the total time required to get the desired fluences (resulting in the data from Pilot-PSI being shifted to the right of the data in the literature (Figure 5.11)). The fact that the growth at higher fluences (corresponding to longer exposure times) is closer to that expected from the literature compared to the lower fluence samples provides some credence to this theory. The lower fluence exposures would not have exceeded the incubation time enough to reach the levels of growth seen at lower fluxes for the same fluence, however at higher fluences the incubation time may have been more significantly exceeded, resulting in growth levels closer to those observed at lower fluxes.

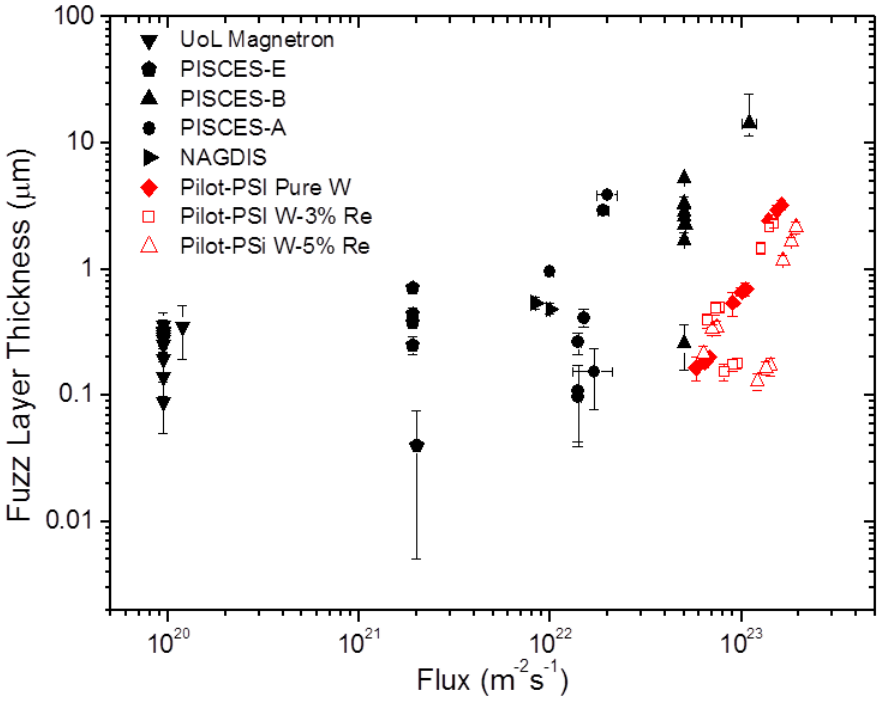

Figure 5.12: Variation of fuzz layer thickness with flux, in comparison to literature values. For references for the literature data points see [9], [17].

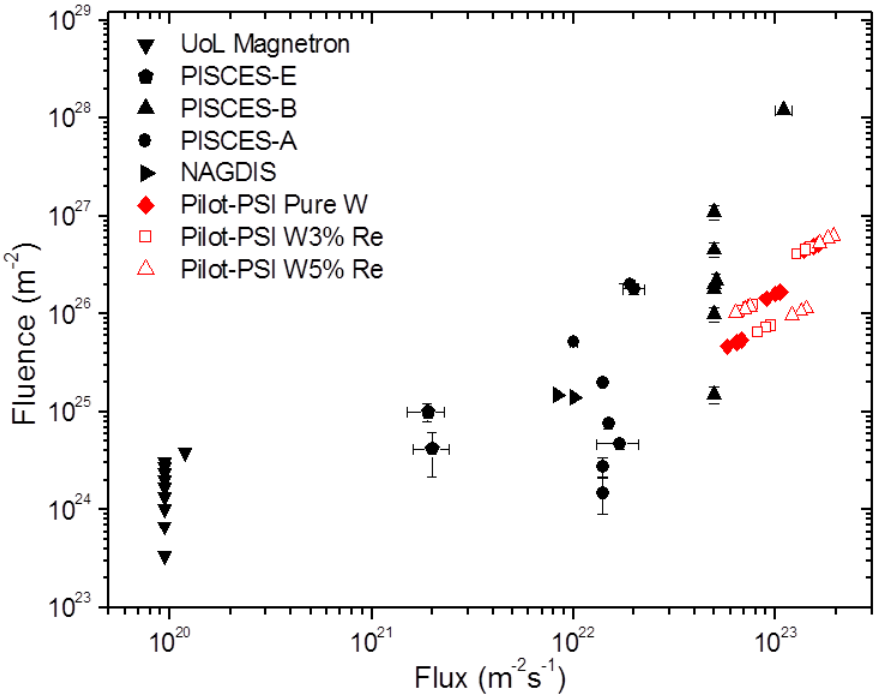

Figure 5.13: The fluxes used to achieve certain fluences for this experiment and in the literature. For references for the literature data points see [9], [17].

Furthermore it should be noted that similar fluences were achieved for the W-5%Re sample in the 800 s and 1600 s exposures, however, the fuzz thickness achieved after the 1600 s exposure was still higher than that after 800 s. The 1600 s exposure time used a lower flux to achieve a similar fluence to the 800 s exposure time, and therefore following the incubation time theory, the 1600 s exposure had a greater amount of time to exceed the incubation time, resulting in a thicker fuzz layer.

The data from the magnetron device, where the experiments were carried out at 827 °C[17], lies above the expected value for exposures even at 1047 °C, and these thicknesses are reached at fluences below the incubation fluence of 2.5×10^{24} m^{-2} suggested by Petty *et al.* [9]. This also points towards the existence of an incubation time. The fluxes in the magnetron are an order of magnitude lower than those used in other devices (Figure 5.12), resulting in exposure times of the order of hours in order to achieve fluences lower than other literature data, and fuzz thickness layers greater than expected. De Temmerman *et al.* conducted previous work in Pilot-PSI at fluxes between $0.7\text{-}3\times10^{24}$ $m^{-2}s^{-1}$, which is an order of magnitude higher than that used in the current experiment, at temperatures between 1400-2000 °C[20]. It was suggested that the shorter exposure times used in these experiments in comparison to previous studies by Baldwin and Doerner [21] and Kajita *et al.*[22] could result in a greater deviance from previous data [20]. This again highlights the importance of time, rather than just fluence.

The concept of incubation time is intuitive. For example, if theoretically a sample was exposed to a flux of 2.5×10^{24} m^{-2} s^{-1} for 1 s (giving the predicted incubation fluence of 2.5×10^{24} m^{-2}), one would assume that there would not be sufficient time for all the

mechanisms required for fuzz growth to take part. This suggests that there is a relationship between exposure time and fluence on the fuzz layer thickness.

5.5.4 Influence of Flux

He retention has been suggested to be dependent on flux of the incoming ions by Hammond and Wirth [23].At the 800 s exposures the fluxes were slightly higher for the W-3%Re and even higher for the W-5%Re in comparison to the pure W, resulting in higher total fluences for the Re samples (Figure 5.13). Despite this the fuzz thickness was fairly similar for all the samples. Therefore for these samples it appears that Re at 3% and 5% concentrations is inhibiting fuzz growth, as despite the increased fluence achieved in the Re samples, the fuzz growth does not exceed that observed in pure W.

For the 1600 s exposures the fluxes employed for both Re alloyed samples are similar, and consequently similar fluences are achieved (Figure 5.13). Whereas for the pure W sample the flux used and therefore the fluence achieved is higher. Here it is observed that the fuzz layer thickness is higher in the pure W. However, considering that a lower flux was used for the W-3%Re and the thickness is lower, it lines up with the pure W samples. Therefore in this scenario it is not clear that for a 3% concentration, Re is inhibiting fuzz growth. The W-5%Re however still has a smaller fuzz layer thickness than the W-3%Re, which is particularly noticeable at the lowest fluence, where the fuzz layer thickness is ~ 0.5 that of the 3% alloy.

At 3200 s the flux and fluences used are fairly similar for the W and W-3%Re samples (hence the points overlap in the flux fluence graph in Figure 5.13), with only a higher flux used for the W-5%Re sample. Therefore in this case it is easy to make a direct comparison. Here we see that the thickness of the W-3%Re is slightly less than the W values, and the W-5%Re shows significantly less fuzz growth.

For the specific data produced in this experiment, the fuzz layer thickness for pure W appears to increase with a power law trend with fluence. However, this is not so clear for the Re alloys. This could be due to the fact the flux employed for the 1600 s shots in the Re alloys is less than that employed in the 800 s shots. For the pure W the flux and fluence increase at regular intervals. The flux variation with fluence in the case of W-3%Re is not as uniform as pure W, but there is less deviation in comparison to the 5%Re. This may indicate why there is a more uniform increase in fuzz thickness with fluence for the W-3%Re, in comparison to W-5%Re.

An important thing to remember is that it has been observed that there can be variation in fuzz growth in the literature, and it doesn't always follow the same trend. For example in Figure 5.11, we see that at fluences of ~10^{25} and ~2×10^{26} m^{-2} there is a variation in the fuzz thickness at similar fluences despite the similar temperatures employed (typically 827-867 °C [9]) and in some cases also similar fluxes.

5.5.5 Effect of Re on Fuzz Growth

It is important to consider what is the mechanism behind the Re having an inhibitory effect on fuzz growth and how this varies with fluence and flux. The most recent theory on the mechanism of fuzz formation based on experimental observations by Takamura *et al.* [24] states that the fuzz growth mechanism is initiated by pitting of the surface of the bulk metal due to the formation of holes [24]. Following this, He bubbles from the bulk material thermally migrate to the surface of the sample and then they burst, releasing He in the process. As the fluence of the impinging He ions increases, the area of the holes grow and 'nano-walls' are formed. Holes can also form in the centre of the nano-walls, due to the presence of nano-bubbles, which produces a loop structure. These loops then grow in size as the fluence of He continues to increase. Finally, once the surface tension of the nano-bubbles in the loops is broken, the loops fracture and branch out, leading to the formation of the nano structure referred to as fuzz [24]. Ito *et al*. [25] note the main processes occurring during helium plasma irradiation as penetration of the helium ions, agglomeration and diffusion of the He, bubble growth, which it is suggested occurs via strain around He bubbles, and dislocation loop punching, finally followed by the fuzz formation.

From our results it is observed that at the lowest fluences ($0.5\text{-}1\times10^{26}$ m^{-2}), both concentrations seem to have an inhibitory effect on the formation mechanism, as despite the fluences being higher than those for pure W, the total thickness of the fuzz layer is quite similar. At fluences of $\sim1\text{-}2\times10^{26}$ m^{-2}, the 3%Re does not seem to show an inhibitory effect, whereas the 5%Re does. At fluences of $\sim4\text{-}6\times10^{26}$ m^{-2}, the 3%Re samples show slightly less fuzz growth in comparison to pure W, with a more significant effect seen in the 5%Re samples.

At lower fluences ($0.5\text{-}1\times10^{26}$ m^{-2}), the early stages of the mechanism of formation are taking place (grain boundaries are still observed in the 800 s SEM images in Figure 5.5, Figure 5.7 and Figure 5.9). Initially it was thought that grain size may be what is causing the difference in fuzz growth. Baldwin *et al.* looked at fuzz growth in various grades of tungsten at a temperature of 847 °C and fluxes of $\sim5\times10^{22}$ $m^{-2}s^{-1}$. They observed that fuzz growth appeared to be lower in single crystal W, in comparison to a standard rolled polycrystalline W target [10]. However, this would not explain the decrease in growth observed in the W-5%Re in comparison to W-3%Re, as these samples have similar grain sizes.

According to Kajita *et al.* the shear modulus for W and Re is very similar at the temperature range of 0.25-0.5 T_m (T_m is the melting point in K**)** [26]. Takamura *et al.* had stated that the shear modulus could be a critical value for fuzz growth being sustained [24], and as they should be similar for all the samples, it is likely the differences in fuzz growth are driven by another process.

It was then considered whether the trapping probability for He differed for Re atoms in comparison to W atoms. Becquart conducted DFT (density functional theory) calculations, showing that the binding energy between Re and He is close to zero, and unlike other substitutional atoms, Re will not act as a trap for He [27]. This suggests that Re as a substitutional atom would behave in a similar manner to W with respect to He. Wu *et al.* also

obtained similar results from DFT calculations [28]. It should be noted however, these calculations do not take into account temperature, and are performed at 0 K, which would have an impact [27], [28].

It is well established that it non-irradiated W, the addition of Re in solid solution results in improved ductility [29], [30]. Therefore another consideration was the microstructural processes behind the improved ductility of W-Re alloys over pure W. DFT has been utilised in order to explain the improved ductility of W-Re, where it has been observed that the addition of Re results in a change in the $1/2\langle 111\rangle$ screw dislocation properties, a change in the core symmetry, the Peierls stress is reduced, and the number of slip planes increases [31].This could therefore be impacting the data, but first we must consider whether this is valid in irradiated material.

Other work on W-Re alloys following ion irradiation, albeit at much higher energies (of the order of MeV), has shown embrittlement post irradiation [32]–[34]. Recent work by Armstrong *et al.* [32] has shown that ion irradiation at 300 °C using W ions results in significant hardening and embrittlement in W-5%Re alloys with a grain size of 10-100 µm. Up to dose levels of 1.2 dpa, although there is a slightly greater increase in hardness in the W-Re alloys, in comparison to pure W with a grain size of 50-500 µm, the actual raw hardness value in the W-Re is less than that of W. Experiments in W-5%Re with a smaller grains size of ~2 µm, shows a slightly lower increase in hardness in comparison to the pure W, however this time the actual raw hardness is higher than that of the pure W [33].

More relevant to the experiments in this paper, Beck *et al.*[34] have conducted He ion irradiations at energies between 0.05-1.8 MeV, up to levels of ~3000 appm at a temperature of ~ 300 °C, in pure W, W-1%Re and W-5%Re. All the materials had grain sizes between ~50-500 µm, and therefore are more directly comparable to the heavy ion irradiations. The hardness increases were much greater than in the self-ion irradiated material and this time the hardness increase was greater in the pure W, in comparison to the W-Re alloys, where the 5% Re had a greater raw increase than the 1%Re alloy. The total raw hardness was still slightly less in the W-1%Re samples post He irradiation in comparison to pure W. The W-5%Re and pure W and had similar levels of raw hardness post irradiation [34].

It is quite complex to compare the mechanisms of damage in high energy and low energy ion irradiations. The mechanisms of hardening induced by high energy W or He ions would be different to that induced by the lower energy (45 eV) used in our experiment. At energies ≥1 keV vacancies will be produced with the penetration of the He ions [25] and sputtering will also be an issue. In the He irradiations by Beck *et al.*(0.05-1.8 MeV) [34], and in another study by Armstrong *et al.*(2 MeV) [35] no He bubbles were observed in TEM micrographs, and it was suggested that He was trapped in small He vacancy clusters. This is in contrast to the low energy irradiations used to produce fuzz, where the energies are too low to form vacancies and He self-traps in He clusters, which can grow via a loop punching mechanism, in order to form bubbles. These bubbles have been observed in the tendrils, and also below the surface of the fuzz [22]. Additionally there is a significant temperature difference between these experiments and the experiment in this paper, which would result in a variation in the

damage mechanisms. At the low energies employed in this experiment the mobility of He is related to the temperature rather than the energy of the ion, and at higher temperatures there will be increased mobility. Therefore it is quite difficult to correlate the observations in higher energy, lower temperature experiments to observations in this experiment.

If we are to assume that in the case of our experiment that there is not increased embittlement of the W-Re samples in comparison to the pure W, and that W-Re is more ductile than pure W, this could be a factor in effecting the fuzz growth. Therefore according to the models of Romaner *et al.* [31] there will be more slip planes and therefore the W-Re samples can behave more plastically. As bubbles grow via a plastic deforamtion process, it could be that in the W-Re alloys that bubbles can continue to grow without bursting for longer in comaprison to the pure W. Bubble formation and bursting has repeatededly been said to be a vital step in fuzz formation [22], [24], [36]. Therefore, the reduced speed of bubble bursting could result in a slower rate of fuzz growth.

Additionally, work by Muzyk *et al.* [37] suggests that Re can trap SIA defects in bcc-W, which is suggested could affect the response to irradiation. Also in W ion irradiated W-5%Re, Re has been observed to impede $\mathbf{b}=1/2\langle 111\rangle$ loop motion [38]. Kobayashi *et al.*[39] have said that He bubbles grow by a process of absorption of He interstitials, whereby the W atoms that surround the bubble are pushed away resulting in a cloud of SIAs around the bubble. The bubble then grows and the dislocation loop is punched [25]. Kobayashi *et al.* [39] state that the edge dislocation making up the loop has $\mathbf{b}=1/2\langle 111\rangle$. Therefore, it may be that as Re has been observed to inhibit $\mathbf{b}=1/2\langle 111\rangle$ loop motion, the loop punching process takes place more slowly in the Re alloyed samples, resulting in a slower rate of bubble growth and therefore it takes longer for the bubbles to burst and form fuzz. It is not clear why the W3%Re sample exposed for 1600 s does not show the reduced fuzz growth as seen in the other Re samples.

5.6 Conclusions

An investigation into the effect of Re addition on the fuzz formation mechanism was conducted at ~1025 °C. There is an increase in mass loss with increasing exposure time and fluences. The mass loss is suggested to be due to impurities with sputtering thresholds that are below the 45 eV used in this experiment. It is suggested that the mass loss increases with fluence due to the increased number of impurity particles impacting on the samples.

This effect of Re addition across a range of fluences from $0.5\text{-}6.2\times10^{26}$ m^{-2} has been studied. Re has been seen to inhibit fuzz growth, with the exception of the W-3%Re sample exposed to a fluence of $\sim1\times10^{26}$ m^{-2}. The inhibitory effect of Re is observed to increase with Re concentration .It is suggested that this may be due to the increased ductility of W-Re over W. It could also be due to the retardation of $\mathbf{b}=1/2\langle 111\rangle$ motion by Re, which may slow the loop punching process by which bubbles grow.

Additionally evidence has been provided for the incubation time theory, as opposed to the incubation fluence theory. This provides an explanation for the thickness of the fuzz layer

data in this experiment lying below that expected using the equation from Petty *et al.* and other literature values at similar fluences [9].

Acknowledgements

The authors gratefully acknowledge the help and support from all the staff at DIFFER, without whom this work would be impossible. This work was supported by the Engineering and Physical Sciences Research Council [EP/K504178/1]. Acknowledgements are also given to the Leeds EPSRC Nanoscience and Nanotechnology Facility (LENNF) (EP/K023853/1).

References

[1] R. A. Pitts, S. Carpentier, F. Escourbiac, T. Hirai, V. Komarov, S. Lisgo, A. S. Kukushkin, A. Loarte, M. Merola, A. Sashala Naik, R. Mitteau, M. Sugihara, B. Bazylev, and P. C. Stangeby, "A full tungsten divertor for ITER: Physics issues and design status," *J. Nucl. Mater.*, vol. 438, pp. S48–S56, Jul. 2013.

[2] Y. Ueda, H. T. Lee, N. Ohno, S. Kajita, A. Kimura, R. Kasada, T. Nagasaka, Y. Hatano, A. Hasegawa, H. Kurishita, and Y. Oya, "Recent progress of tungsten R&D for fusion application in Japan," *Phys. Scr.*, vol. 2011, no. T145, pp. 1–6, Dec. 2011.

[3] M. Rieth, J. L. Boutard, S. L. Dudarev, T. Ahlgren, S. Antusch, N. Baluc, M.-F. Barthe, C. S. Becquart, L. Ciupinski, J. B. Correia, C. Domain, J. Fikar, E. Fortuna, C.-C. Fu, E. Gaganidze, T. L. Galán, C. García-Rosales, B. Gludovatz, H. Greuner, K. Heinola, N. Holstein, N. Juslin, F. Koch, W. Krauss, K. J. Kurzydlowski, J. Linke, C. Linsmeier, N. Luzginova, H. Maier, M. S. Martínez, J. M. Missiaen, M. Muhammed, A. Muñoz, M. Muzyk, K. Nordlund, D. Nguyen-Manh, P. Norajitra, J. Opschoor, G. Pintsuk, R. Pippan, G. Ritz, L. Romaner, D. Rupp, R. Schäublin, J. Schlosser, I. Uytdenhouwen, J. G. van der Laan, L. Veleva, L. Ventelon, S. Wahlberg, F. Willaime, S. Wurster, and M. A. Yar, "Review on the EFDA programme on tungsten materials technology and science," *J. Nucl. Mater.*, vol. 417, no. 1–3, pp. 463–467, Oct. 2011.

[4] M. R. Gilbert and J.-C. Sublet, "Neutron-induced transmutation effects in W and W-alloys in a fusion environment," *Nucl. Fusion*, vol. 51, no. 4, p. 43005, Apr. 2011.

[5] A. Khan, G. De Temmerman, T. W. Morgan, and M. B. Ward, "Effect of rhenium addition on tungsten fuzz formation in helium plasmas," *J. Nucl. Mater.*, vol. 474, pp. 99–104, 2016.

[6] G. De Temmerman, K. Bystrov, R. P. Doerner, L. Marot, G. M. Wright, K. B. Woller, D. G. Whyte, and J. J. Zielinski, "Helium effects on tungsten under fusion-relevant plasma loading conditions," *J. Nucl. Mater.*, vol. 438, pp. S78–S83, Jul. 2013.

[7] T. Petty, "Private Communication." 2016.

[8] E. Hotston, "Threshold energies for sputtering," *Nucl. Fusion*, vol. 15, no. 3, pp. 544–547, 1975.

[9] T. J. Petty, M. J. Baldwin, M. Hasan, R. P. Doerner, and J. W. Bradley, "Tungsten 'fuzz' growth re-eaxmined: The dependence on ion fluence in erosive and non-erosive helium plasma," *Nucl. Fusion*, vol. 55, no. 9, pp. 1–11, 2015.

[10] M. J. Baldwin and R. P. Doerner, "Formation of helium induced nanostructure 'fuzz' on various tungsten grades," *J. Nucl. Mater.*, vol. 404, no. 3, pp. 165–173, Sep. 2010.

[11] Y. Kudriavtsev, A. Villegas, A. Godines, and R. Asomoza, “Calculation of the surface binding energy for ion sputtered particles,” *Appl. Surf. Sci.*, vol. 239, no. 3–4, pp. 273–278, 2005.

[12] W. Eckstein, “Calculated Sputtering, Reflection and Range Values,” IPP Report, Max-Planck-Institut für Plasmaphysik, 2002.

[13] D. Nishijima, M. J. Baldwin, R. P. Doerner, and J. H. Yu, “Sputtering properties of tungsten ‘fuzzy’ surfaces,” *J. Nucl. Mater.*, vol. 415, pp. S96–S99, 2011.

[14] M. Yamagiwa, S. Kajita, N. Ohno, M. Takagi, N. Yoshida, R. Yoshihara, W. Sakaguchi, and H. Kurishita, “Helium bubble formation on tungsten in dependence of fabrication method,” *J. Nucl. Mater.*, vol. 417, no. 1–3, pp. 499–503, Oct. 2011.

[15] N. Ohno, Y. Hirahata, M. Yamagiwa, S. Kajita, M. Takagi, N. Yoshida, R. Yoshihara, T. Tokunaga, and M. Tokitani, “Influence of crystal orientation on damages of tungsten exposed to helium plasma,” *J. Nucl. Mater.*, vol. 438, pp. S879–S882, 2013.

[16] G. De Temmerman, K. Bystrov, J. J. Zielinski, M. Balden, G. Matern, C. Arnas, and L. Marot, “Nanostructuring of molybdenum and tungsten surfaces by low-energy helium ions,” *J. Vac. Sci. Technol. A Vacuum, Surfaces, Film.*, vol. 30, no. 4, p. 041306, 2012.

[17] T. J. Petty, “Tungsten nanostructure formation in a magnetron sputtering device,” University of Liverpool Thesis, 2015.

[18] S. Kajita, N. Ohno, M. Yajima, and J. Kato, “Growth annealing equilibrium of tungsten nanostructures by helium plasma irradiation in non-eroding regimes,” *J. Nucl. Mater.*, vol. 440, no. 1–3, pp. 55–62, 2013.

[19] M. J. Baldwin, R. P. Doerner, D. Nishijima, K. Tokunaga, and Y. Ueda, “The effects of high fluence mixed-species (deuterium, helium, beryllium) plasma interactions with tungsten,” *J. Nucl. Mater.*, vol. 390–391, pp. 886–890, Jun. 2009.

[20] G. De Temmerman, K. Bystrov, J. J. Zielinski, M. Balden, G. Matern, C. Arnas, and L. Marot, “Nanostructuring of molybdenum and tungsten surfaces by low-energy helium ions,” *J. Vac. Sci. Technol. A Vacuum, Surfaces, Film.*, vol. 30, no. 4, p. 041306, 2012.

[21] M. J. Baldwin and R. P. Doerner, “Helium induced nanoscopic morphology on tungsten under fusion relevant plasma conditions,” *Nucl. Fusion*, vol. 48, pp. 1–5, Mar. 2008.

[22] S. Kajita, N. Yoshida, R. Yoshihara, N. Ohno, and M. Yamagiwa, “TEM observation of the growth process of helium nanobubbles on tungsten: Nanostructure formation mechanism,” *J. Nucl. Mater.*, vol. 418, no. 1–3, pp. 152–158, Nov. 2011.

[23] K. D. Hammond and B. D. Wirth, “Crystal orientation effects on helium ion depth distributions and adatom formation processes in plasma-facing tungsten,” *J. Appl. Phys.*, vol. 116, no. 14, p. 143301, Oct. 2014.

[24] S. Takamura and Y. Uesugi, “Experimental identification for physical mechanism of fiber-form nanostructure growth on metal surfaces with helium plasma irradiation,” *Appl. Surf. Sci.*, vol. 356, pp. 888–897, 2015.

[25] A. M. Ito, A. Takayama, Y. Oda, T. Tamura, R. Kobayashi, T. Hattori, S. Ogata, N.

Ohno, S. Kajita, M. Yajima, Y. Noiri, Y. Yoshimoto, S. Saito, S. Takamura, T. Murashima, M. Miyamoto, and H. Nakamura, "Hybrid simulation research on formation mechanism of tungsten nanostructure induced by helium plasma irradiation," *J. Nucl. Mater.*, vol. 463, pp. 109–115, 2015.

[26] S. Kajita, T. Ishida, N. Ohno, D. Hwangbo, and T. Yoshida, "Fuzzy nanostructure growth on Ta/Fe by He plasma irradiation," *Sci. Rep.*, vol. 6, p. 30380, 2016.

[27] C. S. Becquart and C. Domain, "Solute-point defect interactions in bcc systems: Focus on first principles modelling in W and RPV steels," *Curr. Opin. Solid State Mater. Sci.*, vol. 16, no. 3, pp. 115–125, 2012.

[28] X. Wu, X. S. Kong, Y. W. You, C. S. Liu, Q. F. Fang, J. L. Chen, G. N. Luo, and Z. Wang, "First principles study of helium trapping by solute elements in tungsten," *J. Nucl. Mater.*, vol. 455, no. 1–3, pp. 151–156, 2014.

[29] J.-C. Carlen and B. D. Bryskin, "Rhenium - A Unique Rare Metal," *Mater. Manuf. Process.*, vol. 9, no. 6, pp. 1087–1104, 1994.

[30] M. Rieth, S. L. Dudarev, S. M. Gonzalez de Vicente, J. Aktaa, T. Ahlgren, S. Antusch, D. E. J. Armstrong, M. Balden, N. Baluc, M.-F. Barthe, W. W. Basuki, M. Battabyal, C. S. Becquart, D. Blagoeva, H. Boldyryeva, J. Brinkmann, M. Celino, L. Ciupinski, J. B. Correia, a. De Backer, C. Domain, E. Gaganidze, C. García-Rosales, J. Gibson, M. R. Gilbert, S. Giusepponi, B. Gludovatz, H. Greuner, K. Heinola, T. Höschen, a. Hoffmann, N. Holstein, F. Koch, W. Krauss, H. Li, S. Lindig, J. Linke, C. Linsmeier, P. López-Ruiz, H. Maier, J. Matejicek, T. P. Mishra, M. Muhammed, a. Muñoz, M. Muzyk, K. Nordlund, D. Nguyen-Manh, J. Opschoor, N. Ordás, T. Palacios, G. Pintsuk, R. Pippan, J. Reiser, J. Riesch, S. G. Roberts, L. Romaner, M. Rosiński, M. Sanchez, W. Schulmeyer, H. Traxler, a. Ureña, J. G. van der Laan, L. Veleva, S. Wahlberg, M. Walter, T. Weber, T. Weitkamp, S. Wurster, M. a. Yar, J. H. You, and A. Zivelonghi, "Recent progress in research on tungsten materials for nuclear fusion applications in Europe," *J. Nucl. Mater.*, vol. 432, no. 1–3, pp. 482–500, Jan. 2013.

[31] L. Romaner, C. Ambrosch-Draxl, and R. Pippan, "Effect of Rhenium on the Dislocation Core Structure in Tungsten," *Phys. Rev. Lett.*, vol. 104, no. 19, p. 195503, May 2010.

[32] D. E. J. Armstrong, X. Yi, E. A. Marquis, and S. G. Roberts, "Hardening of self ion implanted tungsten and tungsten 5-wt% rhenium," *J. Nucl. Mater.*, vol. 432, no. 1–3, pp. 428–436, Jan. 2013.

[33] D. E. J. Armstrong and T. B. Britton, "Effect of dislocation density on improved radiation hardening resistance of nano-structured tungsten-rhenium," *Mater. Sci. Eng. A*, vol. 611, pp. 388–393, 2014.

[34] C. E. Beck, S. G. Roberts, P. D. Edmondson, and D. E. J. Armstrong, "Effect of Alloy Composition & Helium ion-irradiation on the Mechanical Properties of Tungsten, Tungsten-Tantalum & Tungsten-Rhenium for Fusion Power Applications," *MRS Proc.*, vol. 1514, pp. 99–104, 2013.

[35] D. E. J. Armstrong, P. D. Edmondson, and S. G. Roberts, "Effects of sequential tungsten and helium ion implantation on nano-indentation hardness of tungsten," *Appl. Phys. Lett.*, vol. 102, no. 251901, pp. 1–5, 2013.

[36] S. Kajita, W. Sakaguchi, N. Ohno, N. Yoshida, and T. Saeki, “Formation process of tungsten nanostructure by the exposure to helium plasma under fusion relevant plasma conditions,” *Nucl. Fusion*, vol. 49, no. 9, pp. 1–6, Sep. 2009.

[37] M. Muzyk, K. J. Kurzydłowski, N. L. Baluc, and S. L. Dudarev, “Phase stability , point defects , and elastic properties of W-V and W-Ta alloys,” vol. 104115, pp. 1–17, 2011.

[38] X. Yi, M. L. Jenkins, M. Briceno, S. G. Roberts, Z. Zhou, and M. A. Kirk, “In situ study of self-ion irradiation damage in W and W-5Re at 500oC,” *Philos. Mag.*, vol. 93, no. 14, pp. 1715–1738, May 2013.

[39] R. Kobayashi, T. Hattori, T. Tamura, and S. Ogata, “A molecular dynamics study on bubble growth in tungsten under helium irradiation,” *J. Nucl. Mater.*, vol. 463, pp. 1071–1074, 2015.

6 Effect of Rhenium Irradiations on the Mechanical Properties of Tungsten for Nuclear Fusion Applications

A paper published in the peer reviewed journal: Journal of Nuclear Materials

Presented as an adaptation of the published form.

doi:10.1016/j.jnucmat.2016.05.003

Authors
Aneeqa Khan, Robert Elliman, Cormac Corr, Joven J. H. Lim, Andrew Forrest, Paul Mummery, Llion M. Evans

Effect of Rhenium Irradiations on the Mechanical Properties of Tungsten for Nuclear Fusion Applications

Aneeqa Khan[a,] , Robert Elliman[b], Cormac Corr[b], Joven J. H. Lim[c], Andrew Forrest[c], Paul Mummery[a], Llion Evans[d]

[a] *School of Mechanical, Aerospace and Civil Engineering, The University of Manchester, M13 9PL, UK*
[b] *Research School of Physics and Engineering, The Australian National University, Canberra ACT 2601, Australia*
[c] *School of Materials, The University of Manchester, M13 9PL, UK*
[d] *Culham Centre for Fusion Energy, Culham Science Centre, Abingdon, Oxon, OX14 3DB, UK*

Abstract

As-received and annealed tungsten samples were irradiated at a temperature of 400°C with Re and W ions to peak concentrations of 1600 appm (atomic parts per million) and damage levels of 40 dpa (displacements per atom). Mechanical properties were investigated using nanoindentation, and the orientation and depth dependence of irradiation damage was investigated using Electron Back Scatter Diffraction (EBSD). Following irradiation there was a 13% increase in hardness in the as received sheet and a 23% increase in the annealed material for both tungsten and rhenium irradiation. The difference between the tungsten and rhenium irradiated samples was negligible, suggesting that for the concentrations and damage levels employed, the presence of rhenium does not have a significant effect on the hardening mechanism. Initial qualitative analysis of EBSD pole figures suggested there was an orientation dependence of irradiation damage; however detailed quantitative analysis revealed that this was not the case.

6.1 Introduction

Tungsten is a candidate material for the divertor in future fusion reactors [1], due to its high melting point of 3420°C [2], low sputtering rate [3] and its strength at high temperatures [4]. During the D-T operation of ITER and DEMO, 14MeV neutrons will cause irradiation damage, including displacement cascades and transmutation of the tungsten. This is expected to produce up to 43 dpa (displacements per atom) following three full power years of DEMO operation. The rate of damage production is a strong function of distance from the plasma facing surface, as shown in Fig. 6.1. Within region G of the divertor armour and region F of the divertor structure, ~1500 appm of Re is expected after 3 full power years. (see Fig. 6.2). In ITER the rhenium concentration is expected to be ~1800 appm after 14 years of operation [5].

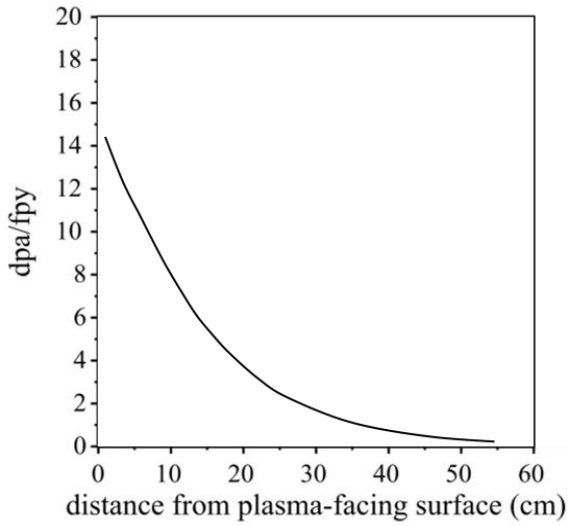

Fig. 6.1: dpa/fpy values for W with distance from plasma facing surface using the latest W-TENDL 2011 neutron library. The data is provided as a function of distance from the surface of region A in Fig. 6.2. Redrawn from [6].

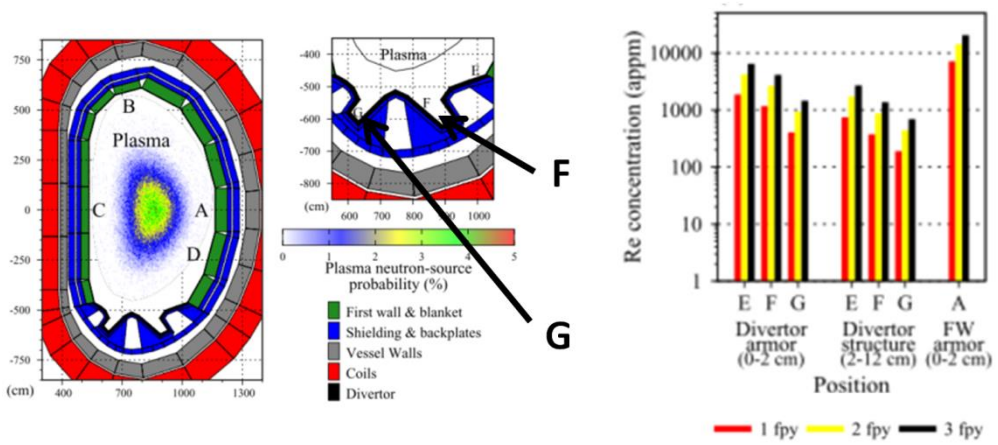

Fig. 6.2: Schematic of DEMO regions and variation in concentration of Re produced in pure W under neutron irradiation as a function of position and distance from the plasma facing surface in different regions of the DEMO design [6].

It is important to investigate the effect transmutation of tungsten to rhenium will have in conjunction with the displacement damage cascades caused by 14MeV neutrons, due to the fact rhenium addition is known to cause embrittlement in neutron irradiated tungsten [7], and this could affect the life of tungsten components within a fusion reactor. Neutron irradiations at damage levels from 0.15 to 1.54 dpa in pure tungsten and tungsten rhenium alloys (ranging from 3-26% concentration of rhenium) have been conducted to investigate the effect of rhenium addition on neutron damage [7]–[9]. The damage mechanism has been observed to differ, depending on whether the pure tungsten transmutates to rhenium, following neutron damage, or if rhenium is already present in the alloys prior to neutron irradiation. These experiments have provided valuable information on the effect of rhenium on the neutron irradiation damage mechanism in tungsten, both as a transmutation product, and also as an alloying element prior to irradiation. However due to the nature of neutron experiments it is

currently unfeasible to reach dpa levels expected in a fusion reactor like DEMO. Also due to the activity of the samples, analysis can be logistically very difficult. For this reason other, faster methods are being pursued in conjunction with neutron damage experiments to obtain more information on irradiation damage in tungsten for fusion relevant conditions.

Recently self-ion irradiations have been used to mimic the 14 MeV neutron damage expected for tungsten in a fusion reactor [10], [11]. Tungsten irradiations in alloys of W-5%Re have also been used to mimic the effects of transmutation to rhenium, while also inducing displacement damage [12]. However, as has been observed in the neutron damage experiments, the damage mechanism in pure tungsten (which transmutates to rhenium) is different to that in samples where rhenium is already present prior to irradiation. Therefore in this experiment, rhenium ions will be implanted in tungsten to simulate transmutation, at the same time as creating defects, rather than inducing damage in a pre-existing tungsten-rhenium matrix.

In addition to the particle damage, irradiation temperature also has an effect on changes to mechanical and microstructural properties [13] , and as it is predicted that temperatures of 400 °C will be reached at the surface of the ITER outer target [1], in this experiment, the mechanical properties of as-received and annealed tungsten samples are studied following irradiation with tungsten and rhenium ions at 400^{o}C.

6.2 Materials and Methods

6.2.1 Sample Preparation

Tungsten samples were prepared from a 2mm thick sheet of commercial purity (99.95%) tungsten supplied by Goodfellow Cambridge Ltd. The as-received sheet had a {100} fibre texture with respect to the common sheet plane (Fig. 6.4). Samples with dimensions 1cm x 1cm were cut from the sheet and half of these were annealed under vacuum for 18 hours at 1400°C in order to produce a uniform microstructure. A slightly stronger {100} fibre texture was observed in the annealed material (Fig. 6.4). All the samples were polished to a mirror finish by firstly grinding the samples with SiC paper with decreasing grit size, then polishing with 3 and 1 μm diamond suspension, and finally polishing with colloidal alumina. The samples were subsequently cleaned ultrasonically in acetone, ethanol and deionised water. The microstructures of as received and annealed samples are shown by the back-scatter SEM images in Fig. 6.3.

These show that the grain size of the as received material is inhomogeneous, with an average grain size of approximately 1μm, while the average grain size in the annealed samples is 21 μm (Fig. 6.3). Both grain sizes were calculated using the Channel 5 software package assuming a 1° misorientation.

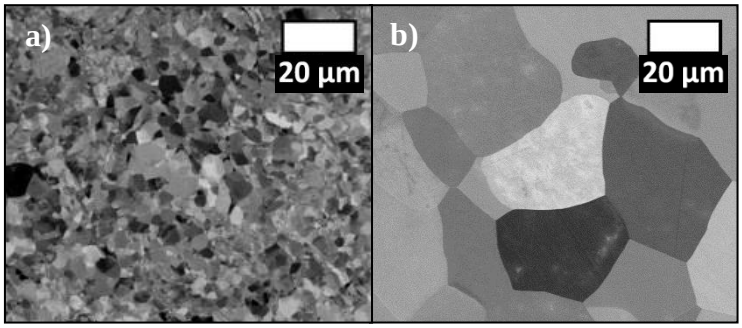

Fig. 6.3: SEM Back Scatter Images for a) as received and b) annealed tungsten sheet.

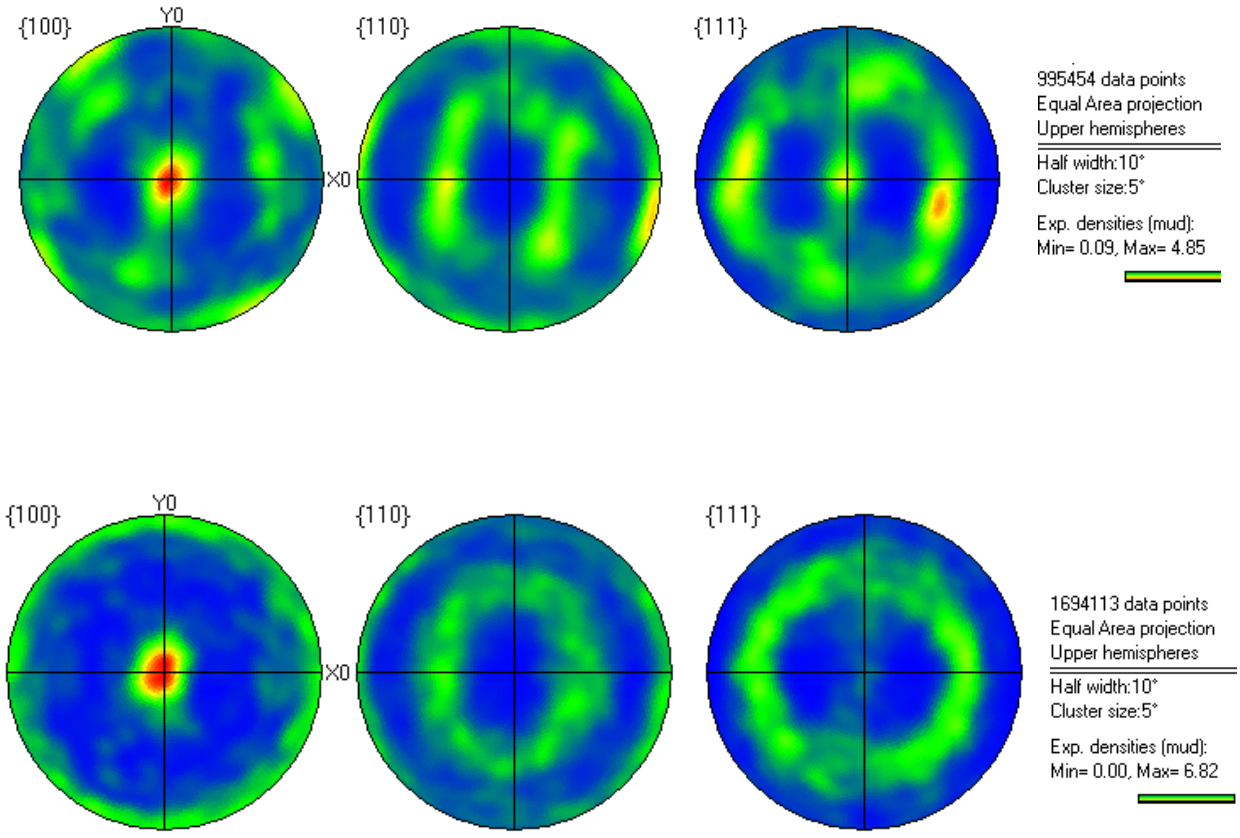

Fig. 6.4: Pole figures for a) as-received and b) annealed material, showing a moderate texture in the {100} direction.

6.2.2 Experimental

One set of as received and one set of annealed tungsten samples were irradiated with W and a second set with Re ions, using a tandem accelerator (National Electrostatics Corporation 5SDH) at the Australian National University (ANU). Samples were clamped to a stainless-steel sample holder and heated to 400°C during irradiation, which is within the operating window of the divertor in ITER [1]. The ion-irradiation conditions are summarised in Table 6.1.

Table 6.1: W and Re Ion Irradiation Conditions on Annealed and As Received Targets.

Species	Energy (MeV)	Fluence (/cm^2)	Temperature (°C)	Charge State	Target Current (nA)	Flux (/cm^2/s)
W	1	4.80E+14	400	1	120	1.7E+11
	2	7.00E+14	400	1	120	1.7E+11
	4	2.80E+15	400	2	120	8.3E+10
Re	1	4.80E+14	400	1	150	2.1E+11
	2	6.50E+14	400	1	500	6.9E+11
	4	2.80E+15	400	2	600	4.2E+11

Ion range and damage distributions were calculated using SRIM (Stopping range of ions in matter, a Monte Carlo simulation code) [14], utilising full damage calculations with 68 eV displacement energies. Multi-energy implant sequences, using a raster scanned beam were chosen to produce a near uniform implanted ion distribution over the depth range from 0.06 μm to 0.3 μm, as shown in Fig. 6.5 (i.e. 1 MeV, 2 MeV and 4 MeV ion implantations were used for each sample). The resulting rhenium concentration in this region is ~1650 appm, which is close to the 1500 appm transmutation concentration anticipated in region G of the divertor armour and region F of the divertor structure in a DEMO concept (Fig. 6.2). The peak damage (~40 dpa) achieved under these conditions is also in the range expected in region A of the DEMO concept shown in Fig. 6.2. There is no data for the dose in specific regions of the divertor. However, there is also transmutation data provided for region A of the first wall armor in a DEMO model [6]. Combined with the dose information in Fig. 6.1, this predicts an appm/dpa ratio of 460 appm/dpa [6]. This is higher than the ratio achieved in this experiment of ~40 appm/dpa. However, due to the fact that in order to implant an increased concentration of Re, an increased dose will be achieved, as the Re acts a PKA, it is impossible to avoid this.

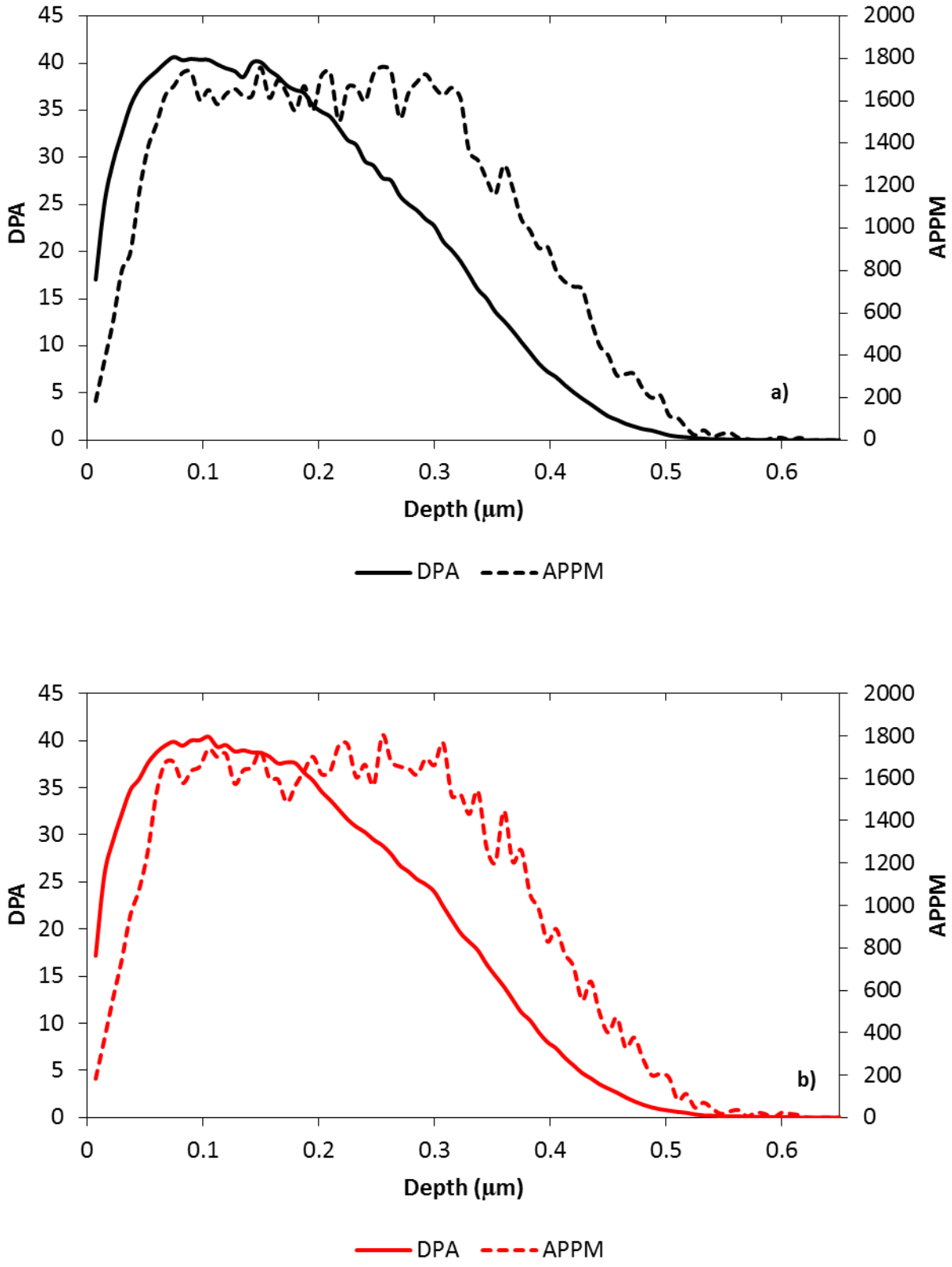

Fig. 6.5: Stopping range of ions in matter (SRIM) calculated profiles of displacements per atom and atomic parts per million of a) rhenium implanted in rhenium irradiated tungsten and b) tungsten implanted in tungsten irradiated tungsten at 1; 2 and 4 MeV using a 68 eV displacement value.

Samples were characterised using Electron Back Scatter Diffraction (EBSD) to characterise the grain-specific irradiation damage in annealed samples, and nanoindentation to determine changes in the mechanical properties of both the as received and annealed samples.

EBSD was performed over an area of 420 by 320 μm on the annealed sample (Fig. 6.6), utilising a step size of 0.5-0.6 μm and accelerating voltages of 15, 20 and 30 kV. EBSD inverse pole figure (IPF) maps of the annealed W and Re irradiated samples were also produced (Fig. 6.7 and Fig. 6.8). Different voltages were used in order to study variations in ion irradiation damage close to the surface. The higher the voltage utilised, the larger the penetration depth of the back scatter electrons. The CASINO program, version 2.48 (monte CArlo Simulation of electron trajectory in sOlids) was used to determine the maximum penetration depth of back scatter electrons [15]. The software is freely available and accessible online [16].

Low load nanoindentation was perfomed with a Hysitron triboindenter using a Berkovich tip and was used to measure the mechanical properties of samples to depths of 200nm. The system is capable of producing reliable results for depths as small as 50 nm. Variation in hardness from depths of 50-200 nm were achieved by performing measurements over an array of 150 indents (15 by 10 array, with 20 μm between each indent), ranging in depth from 50 nm to 200 nm into the sample. The indents were displacement controlled with a 5 second loading segment, followed by a two second hold. The same array of indents was applied to a silica standard in order to calibrate the results.

Measurements of modulus and hardness were calculated for each indent from the unload portion of each load/unload curve. Supplied software was used to calculate the reduced modulus E_r, which was converted to actual modulus using Equation 1 [17].

$$\frac{1}{E_r} = \frac{(1-\nu^2)}{E} + \frac{(1-{\nu_i}^2)}{E_i} \quad [1]$$

Where E_i and ν_i are the modulus and Poisson's ratio of the indenter material and ν is the Poisson's ratio of the material being indented. The indenter tip is made of diamond, where E_i is equal to 1141GPa and ν_i is equal to 0.07 [18]. The Poisson's ratio of tungsten was assumed to be 0.28.

6.3 Results and Discussion

6.3.1 Quality of EBSD results

First we consider the EBSD results for the annealed, non-irradiated samples, as shown in Fig. 6.9. Here, the hit rate (the percentage of Kikuchi patterns that have successfully been indexed) for all samples was above 99% and the Inverse Pole Figure (IPF) maps (Fig. 6.6) were completely indexed across all grains. For the tungsten and rhenium irradiated samples the situation was quite different. In both cases the hit rate was above 94% for 30 keV electrons. However, at 20 kV, significant degradation in the pole figures was observed (Fig. 6.7 and Fig. 6.8). At 15 kV the hit rate for both samples was further reduced to less than 10% in both cases. It should be noted that SRIM calculations indicate a sputtering rate of ~12

atoms/ion, which for the fluences employed corresponds to the removal of <2 nm of W from the surface, therefore even allowing for the orientation dependence of the sputtering rate, no surface roughening is expected. This reduction in hit rate is therefore due to the fact that certain grains are not indexing, and indeed no Kikuchi patterns for W are observed for these grains at the lower voltages. This can be correlated with the penetration depth of the back scatter electrons using the CASINO code [16], as shown in Fig. 6.10. Such analysis shows that although the penetration depth increases with voltage, the majority of the signal in all cases comes from within 100 nm close to the surface. This is within the irradiated layer, but suggests that closer to the surface there is some kind of damage that prevents indexing to W. It could be that some kind of surface layer has formed during the irradiation, although further analysis would be required to confirm this. It has recently been observed that ion irradiations can result in the formation of carbides [19], [20]. It should be investigated whether this is something that could have formed on the samples in this study, resulting in the degradation of the pole figure quality. At 15 and 20 kV, where the most damage is observed, 75% of the back scattered electrons come from the first 40 nm and 60 nm respectively. Qualitatively, there is some indication that this damage could be orientation specific, which will be analysed further. There was no apparent change in grain size or texture for irradiated samples.

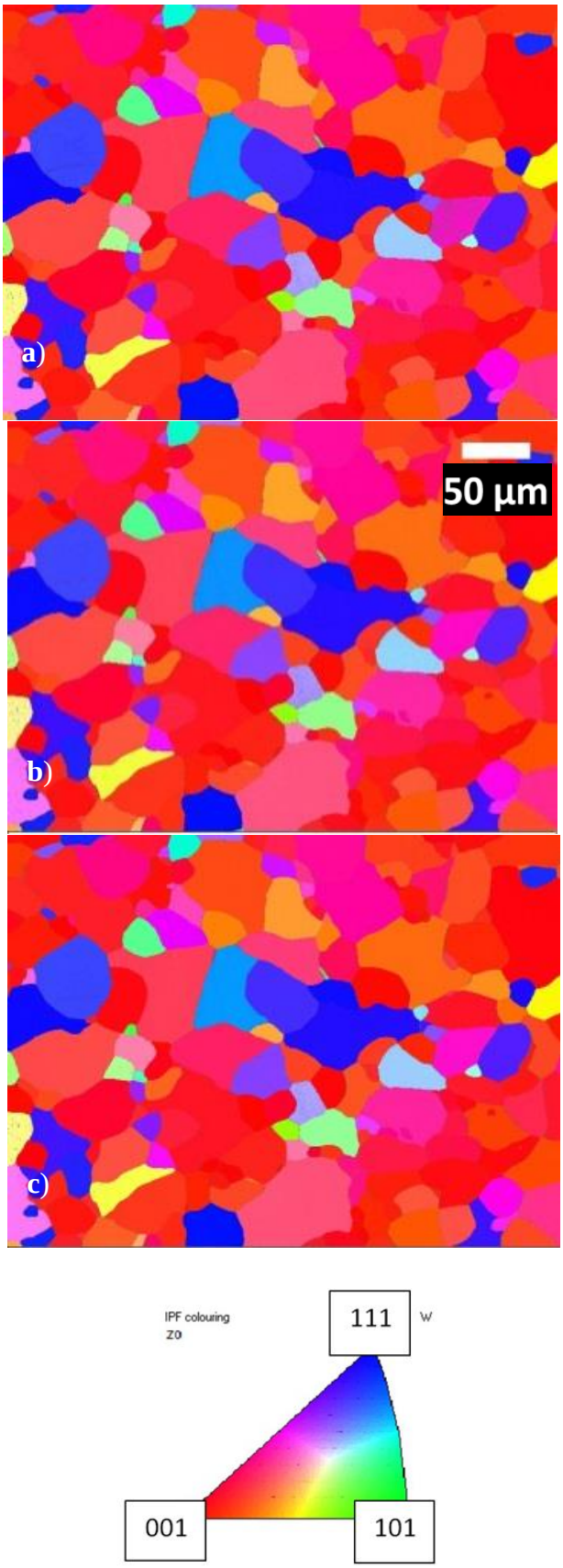

Fig. 6.6: Pole Figures overlaid on band contrast image at a)15 kV, b)20 kV and c) 30 kV in annealed W.

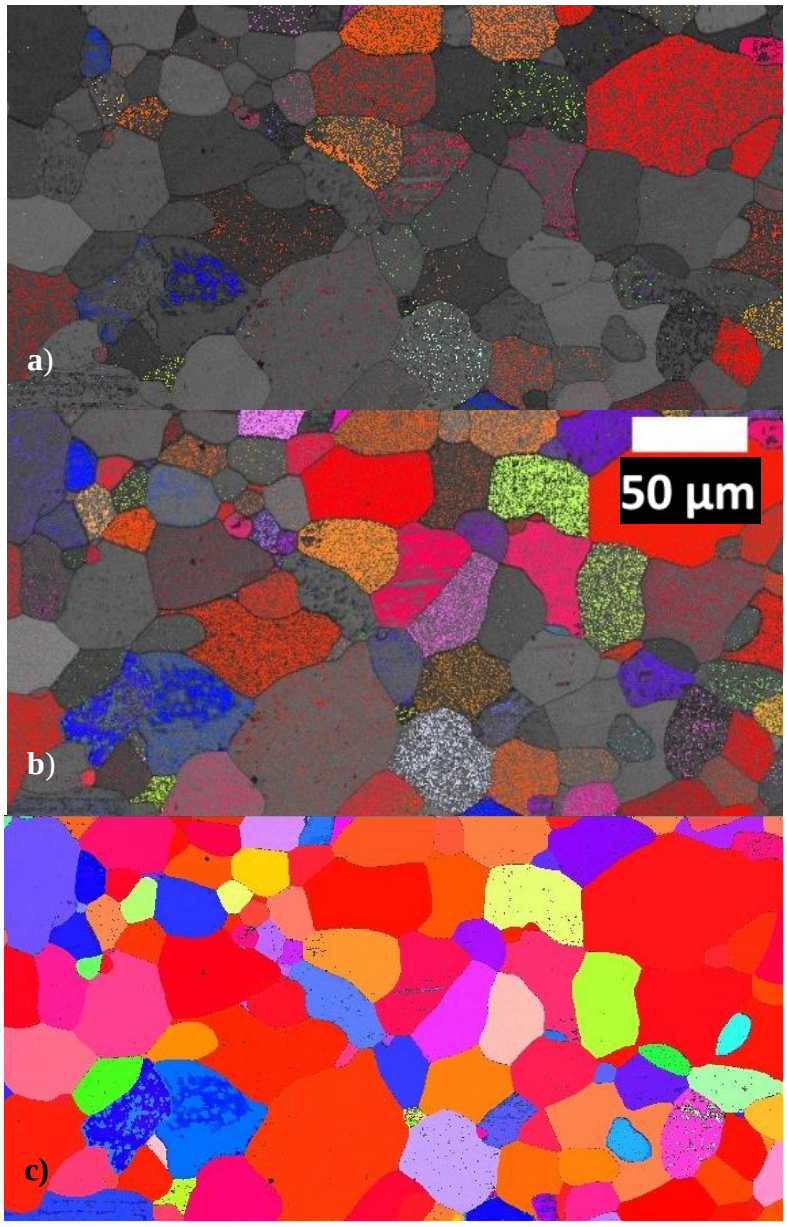

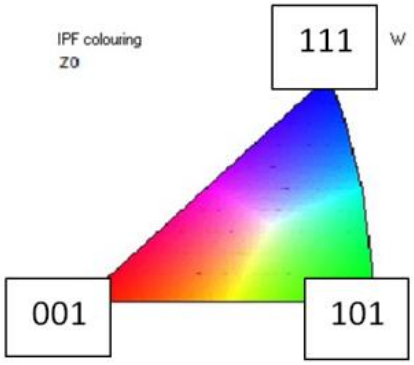

Fig. 6.7: Pole Figures overlaid on band contrast image at a)15 kV, b)20 kV and c) 30 kV in Re irradiated annealed W.

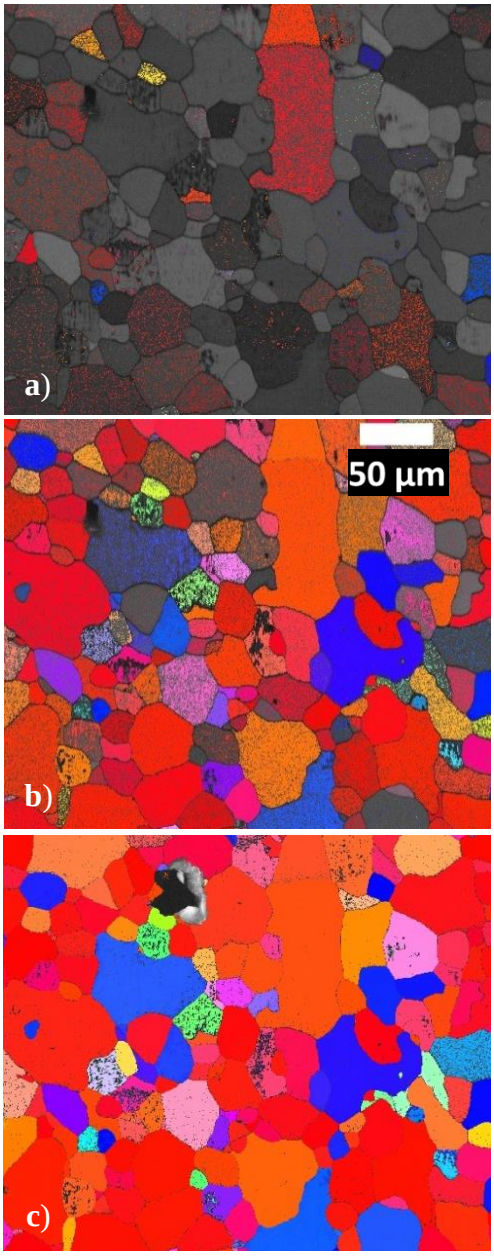

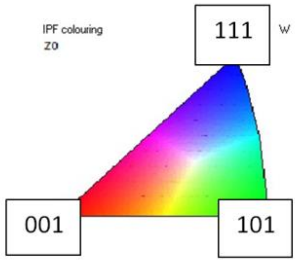

Fig. 6.8: Pole Figures overlaid on band contrast image at a)15 kV, b)20 kV and c) 30 kV in W irradiated annealed W.

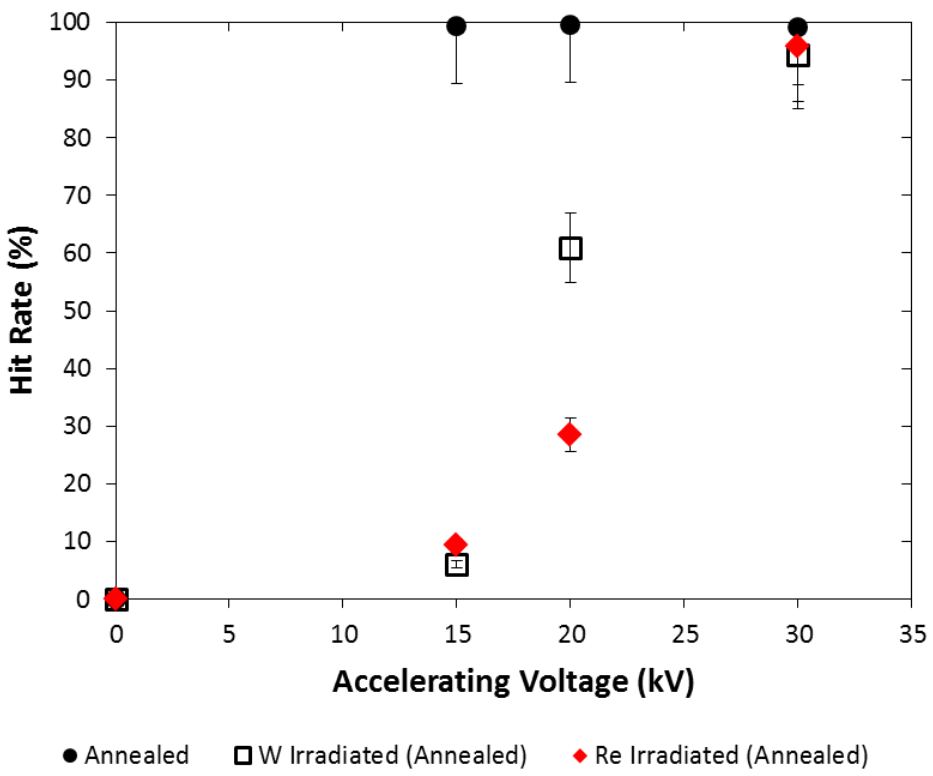

Fig. 6.9: Relationship between Accelerating Voltage and Hit Rate of EBSD map in annealed and irradiated annealed irradiated samples.

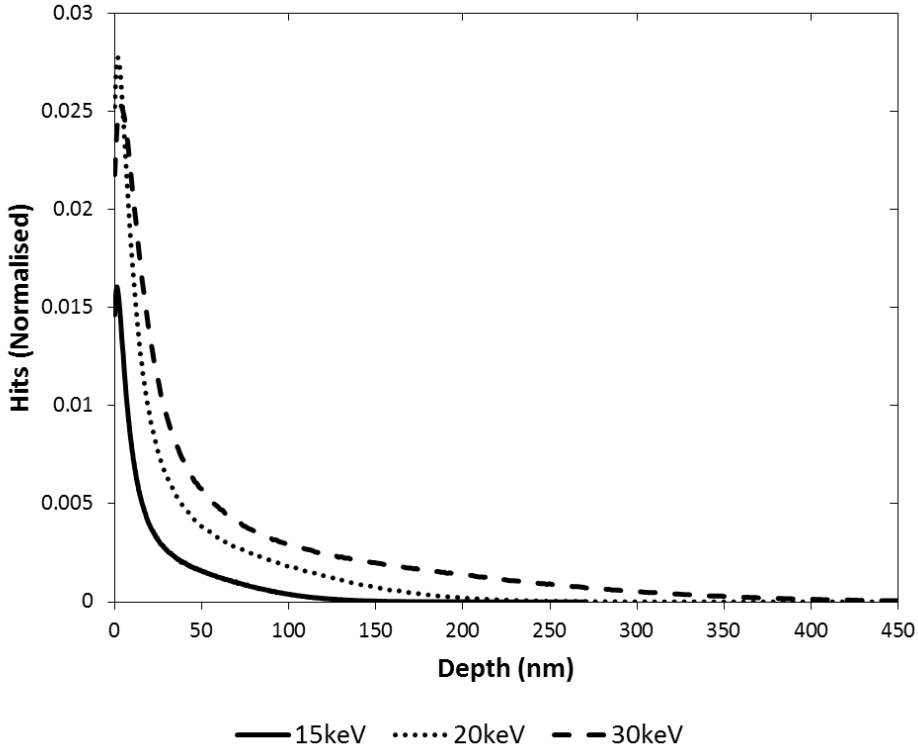

Fig. 6.10: Normalised hits of backscattered electrons vs penetration depth at a) 15 keV, b) 20 keV and c) 30 keV calculated using CASINO.

In order to analyse the orientation dependance of damage, the area covered by all grains with the orientations [001], [111] and [101], within a 10° misorientation (determined using Channel 5 software) were measured at each accelerating voltage for both the W and Re irradiatied samples (Fig. 6.11, Fig. 6.12). Both EBSD scans were carried out using a step size of 0.5-0.6 µm. The area analysed in both samples was ~ 200 000 μm^2. ImageJ software was used to calculate areas. Firstly it should be noted that the samples are textured and that the [001] orientation is the dominant orientation. Secondly, although the areas analysed were of similar sizes in both samples, the area covered by the three considered orientations varied between the samples. A higher proportion of grains indexed to the three orientations in the W irradiated sample, as opposed to the Re irradiated sample. In the case of the W irradiated material, the area covered by the [001] and [111] orientations at 15 kV, as a proportion of that covered at 30 kV, is fairly similar. For the Re irradiated material, as a proportion of the area covered at 30 kV, there is a difference between the areas of [001] and [111] orientations at 15 kV. At 15 kV, the area of the [001] orientation is ~10% of that at 30 kV and the area of the [111] orientation is ~21% of that at 30 kV. But, given that such a small area was covered by [111] grains in the first place, it is not possible to say that this orientation is any more resistant to irradiation damage in comparison to the [001] orientation. In terms of the raw area indexing at 15 kV, in both cases the highest area is that attributed to the [001] orientation. In the W irradiated sample at 15 kV, ~ 5% of the area indexes to [001], and in the Re irradiated sample, ~2.5% of the area indexes to [001]. However, as this was the dominant orientation to begin with, this does not suggest it is any more resistant to the irradaition damage than the other orientations. Therefore, although from the initial EBSD images there was an indication of orientation dependence, the quantitative analysis has revealed that this is not the case. In order to further investigate the effect of orientation it would be beneficial to conduct further irradiation experiments in a fully recrystallised sample without texture.

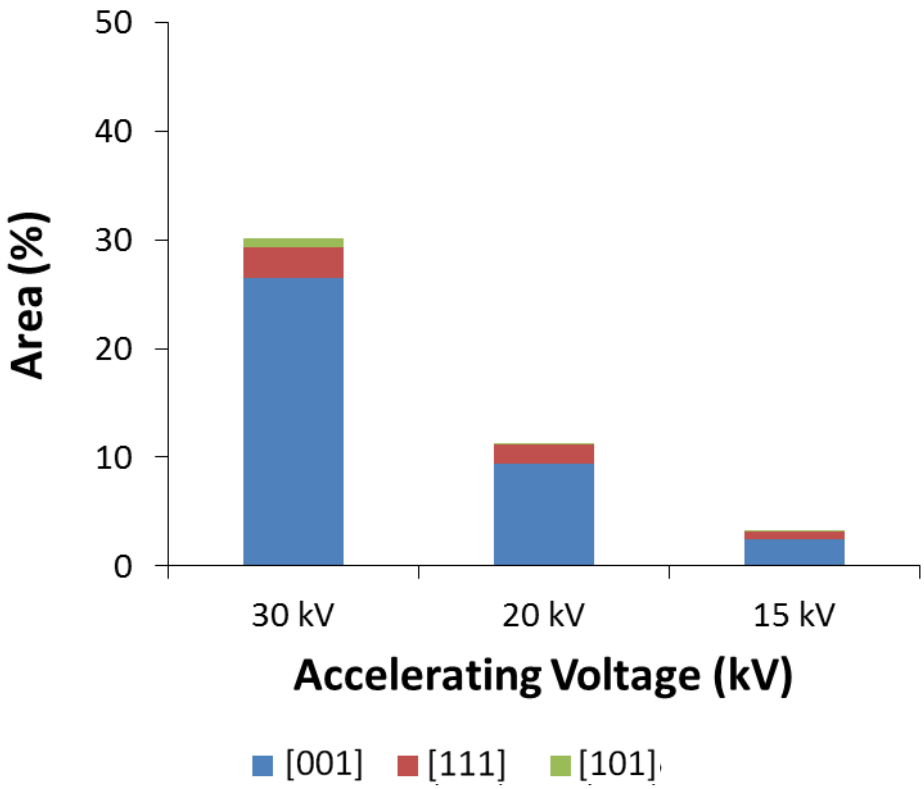

Fig. 6.11: Variation of indexed area covered by [001], [111] and [101] (within a 10° misorientation) orientations with accelerating voltage for Re irradiated annealed W.

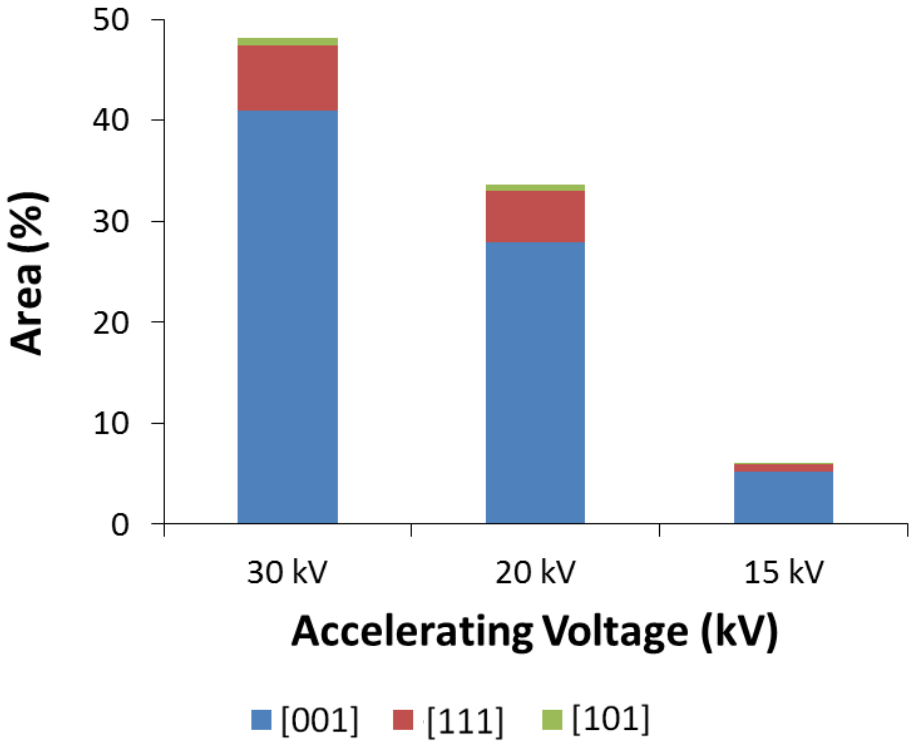

Fig. 6.12: Variation of indexed area covered by [001], [111] and [101] (within a 10° misorientation) orientations with accelerating voltage for W irradiated annealed W.

6.3.2 Change of mechanical properties

The mechanical properties of annealed samples before and after irradiation are summarised in Fig. 6.13, and those for as-received samples before and after irradiation are summarised in Fig. 6.14. Comparison of Fig. 6.13 a) and Fig. 6.14 a) shows that the modulus of both annealed and as received samples is unchanged by irradiation and is approximately constant over the whole depth of measurement. The modulus of all samples is within 5.5% of the expected modulus for tungsten of 410 GPa [2], with the exception of the non-irradiated as-received sample which showed a slightly greater deviation of 8.9%. This is greater than the expected tolerance of the measurement system, which is ±5 %.

Although the modulus is constant over depths of 50-200 nm, there is a clear decrease in hardness with increasing indent depth (Fig. 6.13 b) and Fig. 6.14 b)). This is explained by the Nix Gao relationship. The Nix and Gao model predicts a linear relationship between the square of the hardness and the reciprocal of the depth of the indenter into a polycrystalline sample when the measurement is no longer limited by 'tip effects' (tip blunting or deformities at low loads) [21]. The advantage of this high resolution technique means that this linear relationship holds, even at displacements as small as 50 nm, as illustrated in Fig. 6.13 c) and Fig. 6.14 c).

From Fig. 6.13 b) it can be observed that there is an approximate 23 % increase in hardness for the rhenium and tungsten irradiated annealed samples. This increase is almost the same, regardless of the implanted ion species. For the as received samples, the actual hardness is on average 0.4 GPa higher, but a similar trend is still observed, as shown in Fig. 6.14 b)**.** However, the increase in hardness is only ~13% for the rhenium irradiated and tungsten irradiated as-received samples. In the case of W irradiations, the implanted ions become part of the matrix, indistinguishable from the host atoms. The Re will also substitute for W, forming a substitutional solid solution as we are below the solubility limit of 30 at.% [22]. This indicates that while simultaneously implanting rhenium at concentrations of approximately 1600appm, and inducing cascade damage of approximately 40 dpa the substitution of rhenium atoms into the tungsten matrix, rather than tungsten atoms has a negligible effect on hardness and modulus changes. It is the displacements created, rather than the introduction of a new element into the matrix that is driving the damage mechanism. This is consistent with the fact that the damage from the tungsten and rhenium ion irradiations is comparable due to the fact the mass number of tungsten is 184 and that of rhenium is 187. The greater hardness increase in the annealed samples in comparison to the as-received is consistent with other literature, where W was irradiated with Fe ions, and is due to the fact the grain boundary area (a sink site) in the annealed samples is smaller than in the as-received [23].

If we compare our results to those of Armstrong *et al.*, where irradiations were carried out in pure W and W-5%Re at temperatures of ~300 °C, utilising an energy of 2MeV to achieve a damage level of 33 dpa where there was a 12% increase in hardness in tungsten (50-500 μm grain size) and a 45% increase in hardness of the W-5%Re (10-100 μm grain size). It is interesting that at lower temperatures and a slightly lower dpa level than the data presented in this paper the hardness increase observed in W-5%Re was so large. If we compare to our

rhenium irradiated annealed material, with average grain size of 21 μm, which is comparable to the grain size of the W-5%Re Armstrong *et al.* utilised, the hardness increase is less than half of that observed by Armstong *et al.*, suggesting that the presence of rhenium is dominating the damage mechanism, which is clearly not the case with the lower concentrations we utilised. Armstrong et al. have observed Re clusters at 33 dpa, which it is suggested are precursors to σ phase, which provides a reason for the higher hardness observed [12]. It is predicted that such clusters are not formed with the lower Re concentrations used in this study.

The hardness increase observed in the as received tungsten in this experiment are comparable to that observed by Armstrong *et al.* [12]. However, the annealed tungsten in this study showed double the increase in hardness observed in pure W by Armstrong *et al.* [12]. Considering that the annealed W used in this study has a smaller grain size than the W used by Armstrong *et al.*, and should therefore theoretically show a smaller hardness increase, another factor must be contributing to the higher hardness increase observed. It is unlikely that a 100 °C increase in temperature used in the present study should have such a large effect on the hardness increase. Armstrong *et al.* have shown a small increase in hardness between 13 and 33 dpa, but even if the hardness increase was to increase at the higher dose of 40 dpa, it is unlikely the difference would be as significant as that observed. It is suggested that as energies of 1, 2 and 4 MeV were used in this study there, there would have been increased damage both closer to the surface and deeper in the sample, resulting in a larger total volume of damage in comparison to the Armstrong experiments. The damage region in Armstrong *et al.*'s experiment extends across ~300 nm, in comparison to ~500 nm in this paper, which could explain the larger hardness increase observed. Another factor contributing to the greater hardness increase observed in the study in this paper could be due to the fact multiple ion energies were used. Whereas, Armstrong *et al.* used a single energy of 2MeV [12]. It would be beneficial to carry out further investigations in the use of multiple energies to create similar doses as a single energy beam.

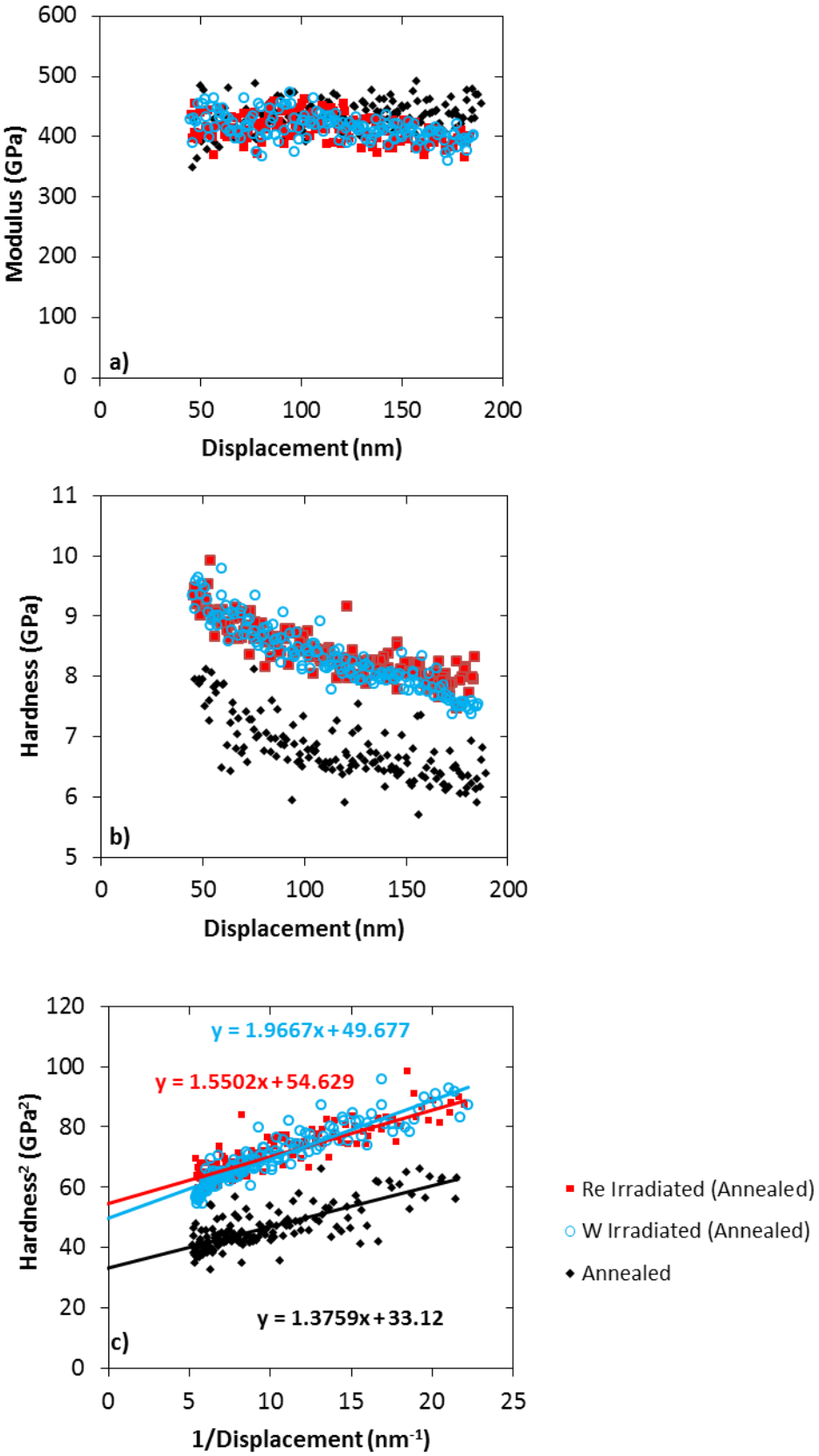

Fig. 6.13: Measurement of a) actual modulus against displacement, b) hardness against displacement and c) demonstration of the Nix Gao relationship – Hardness^2 against reciprocal of displacement sample for non-irradiated and W and Re irradiated annealed samples.

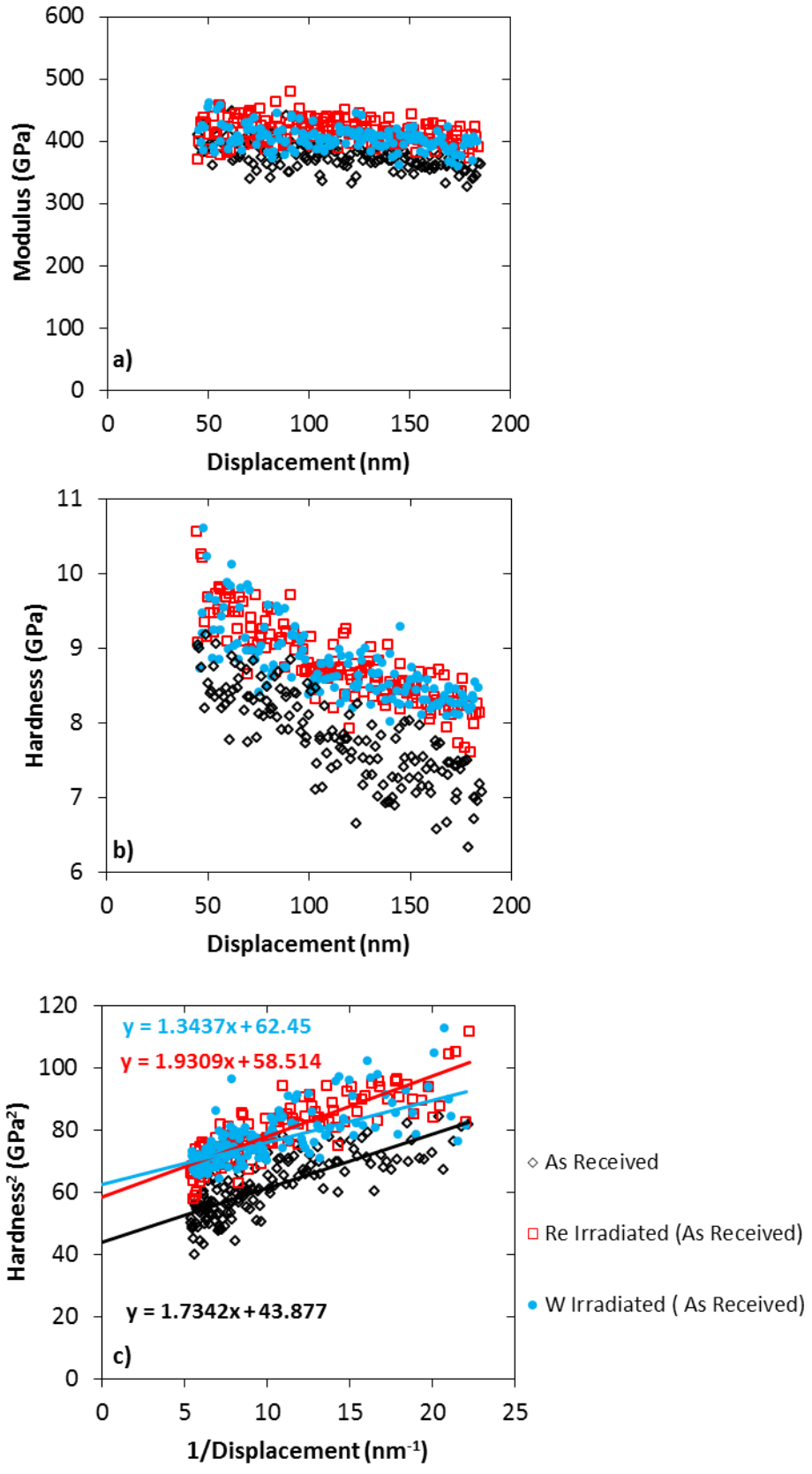

Fig. 6.14: Measurement of a) actual modulus against displacement, b) hardness against displacement and c) demonstration of the Nix Gao relationship – Hardness^2 against reciprocal of displacement sample for non-irradiated and W and Re irradiated as received samples.

6.4 Conclusions

The effect of radiation damage and implanted rhenium on the hardness and modulus of as received and annealed tungsten samples was investigated by irradiating them with both tungsten ions and rhenium ions at a temperature of 400°C. It was found that at peak damage levels of around 40 dpa the originally annealed samples underwent a 23% increase in hardness, while as received samples showed a 13% increase. The effect of rhenium irradiation was found to be indistinguishable from that of tungsten irradiation for peak rhenium concentrations up to 1600 appm. For annealed samples, it was further observed that both kinds of ion irradiation caused significant surface damage to the samples. This was confirmed by the EBSD pole figure degradation with decreasing electron accelerating voltage, which corresponds to a decreasing penetration depth as calculated using CASINO software. Initial qualitative analysis of the EBSD images suggested that there was an orientation dependence of irradiation damage, however following a quantitative study it was seen that this was not the case.

Acknowledgements

We acknowledge access to NCRIS facilities (ANFF and the Heavy Ion Accelerator Capability) at the Australian National University. This work was supported by the Engineering and Physical Sciences Research Council [EP/K504178/1]. Thanks are also given to Andy Wallwork for his help with the annealing of the samples and to Marc Schmidt for his help with EBSD. The author also gratefully acknowledges the useful conversations with Michael Faulkner.

References

[1] R. A. Pitts, S. Carpentier, F. Escourbiac, T. Hirai, V. Komarov, S. Lisgo, A. S. Kukushkin, A. Loarte, M. Merola, A. Sashala Naik, R. Mitteau, M. Sugihara, B. Bazylev, and P. C. Stangeby, "A full tungsten divertor for ITER: Physics issues and design status," *J. Nucl. Mater.*, vol. 438, pp. S48–S56, Jul. 2013.

[2] PLANSEE, "Materials: Tungsten," 2013. [Online]. Available: http://www.plansee.com/en/Materials-Tungsten-403.htm. [Accessed: 02-Jul-2013].

[3] Y. Ueda, H. T. Lee, N. Ohno, S. Kajita, A. Kimura, R. Kasada, T. Nagasaka, Y. Hatano, A. Hasegawa, H. Kurishita, and Y. Oya, "Recent progress of tungsten R&D for fusion application in Japan," *Phys. Scr.*, vol. 2011, no. T145, pp. 1–6, Dec. 2011.

[4] M. Rieth, J. L. Boutard, S. L. Dudarev, T. Ahlgren, S. Antusch, N. Baluc, M.-F. Barthe, C. S. Becquart, L. Ciupinski, J. B. Correia, C. Domain, J. Fikar, E. Fortuna, C.-C. Fu, E. Gaganidze, T. L. Galán, C. García-Rosales, B. Gludovatz, H. Greuner, K. Heinola, N. Holstein, N. Juslin, F. Koch, W. Krauss, K. J. Kurzydlowski, J. Linke, C. Linsmeier, N. Luzginova, H. Maier, M. S. Martínez, J. M. Missiaen, M. Muhammed, A. Muñoz, M. Muzyk, K. Nordlund, D. Nguyen-Manh, P. Norajitra, J. Opschoor, G. Pintsuk, R. Pippan, G. Ritz, L. Romaner, D. Rupp, R. Schäublin, J. Schlosser, I. Uytdenhouwen, J. G. van der Laan, L. Veleva, L. Ventelon, S. Wahlberg, F. Willaime, S. Wurster, and M. A. Yar, "Review on the EFDA programme on tungsten materials technology and science," *J. Nucl. Mater.*, vol. 417, no. 1–3, pp. 463–467, Oct. 2011.

[5] M. R. Gilbert and J.-C. Sublet, "Neutron-induced transmutation effects in W and W-

alloys in a fusion environment," *Nucl. Fusion*, vol. 51, no. 4, p. 43005, Apr. 2011.

[6] M. R. Gilbert, S. L. Dudarev, D. Nguyen-Manh, S. Zheng, L. W. Packer, and J.-C. Sublet, "Neutron-induced dpa, transmutations, gas production, and helium embrittlement of fusion materials," *J. Nucl. Mater.*, pp. 1–6, Apr. 2013.

[7] T. Tanno, A. Hasegawa, J.-C. He, M. Fujiwara, S. Nogami, M. Satou, T. Shishido, and K. Abe, "Effects of Transmutation Elements on Neutron Irradiation Hardening of Tungsten," *Mater. Trans.*, vol. 48, no. 9, pp. 2399–2402, 2007.

[8] A. Hasegawa, T. Tanno, S. Nogami, and M. Satou, "Property change mechanism in tungsten under neutron irradiation in various reactors," *J. Nucl. Mater.*, vol. 417, no. 1–3, pp. 491–494, 2011.

[9] M. Fukuda, K. Yabuuchi, S. Nogami, A. Hasegawa, and T. Tanaka, "Microstructural development of tungsten and tungsten–rhenium alloys due to neutron irradiation in HFIR," *J. Nucl. Mater.*, vol. 455, no. 1–3, pp. 460–463, 2014.

[10] D. E. J. Armstrong, A. J. Wilkinson, and S. G. Roberts, "Mechanical properties of ion-implanted tungsten–5 wt% tantalum," *Phys. Scr.*, vol. 2011, no. T145, p. 14076, Dec. 2011.

[11] J. Gibson, D. Armstrong, and S. Roberts, "The micro-mechanical properties of ion irradiated tungsten," *Phys. Scr.*, vol. 2014, no. T159, pp. 1–3, Apr. 2014.

[12] D. E. J. Armstrong, X. Yi, E. A. Marquis, and S. G. Roberts, "Hardening of self ion implanted tungsten and tungsten 5-wt% rhenium," *J. Nucl. Mater.*, vol. 432, no. 1–3, pp. 428–436, Jan. 2013.

[13] C. D. Hardie, C. A. Williams, S. Xu, and S. G. Roberts, "Effects of irradiation temperature and dose rate on the mechanical properties of self-ion implanted Fe and Fe-Cr alloys," *J. Nucl. Mater.*, vol. 439, no. 1–3, pp. 33–40, 2013.

[14] J. F. Ziegler, J. P. Biersack, and U. Littmark, "The Stopping and Range of Ions in Solids." Pergamon, New York, 1985.

[15] D. Drouin, a. R. Couture, D. Joly, X. Tastet, V. Aimez, and R. Gauvin, "CASINO V2.42 - A fast and easy-to-use modeling tool for scanning electron microscopy and microanalysis users," *Scanning*, vol. 29, no. 3, pp. 92–101, 2007.

[16] Université de Sherbrooke, "CASINO," 2007. [Online]. Available: http://www.gel.usherbrooke.ca/casino/download2.html. [Accessed: 14-Jan-2016].

[17] G. M. Pharr, W. C. Oliver, and F. R. Brotzen, "On the generality of the relationship among contact stiffness, contact area, and elastic modulus during indentation," *J. Mater. Res.*, vol. 7, no. 03, pp. 613–617, Jan. 2011.

[18] G. Simmons and H. Wang, *Single Crystal Elastic Constants and Calculated Eleastic Properties: A Handbook*. MIT Press, Cambridge, MA, 1971.

[19] A. Al-Ajlony, J. K. Tripathi, and A. Hassanein, "Role of carbon impurities on the surface morphology evolution of tungsten under high dose helium ion irradiation," *J. Nucl. Mater.*, vol. 466, pp. 569–575, 2015.

[20] E. R. Anderson and E. A. Marquis, “A snapshot of the microstructural evolution of Alloy 800H under heavy ion irradiation,” Poster, SMINS4 2016 conference, 2016.

[21] W. D. Nix and H. J. Gao, “Indentation size effects in crystalline materials: A law for strain gradient plasticity,” *J. Mech. Phys. Solids*, vol. 46, no. 3, pp. 411–425, 1998.

[22] M. Ekman, K. Persson, and G. Grimvall, “Phase diagram and lattice instability in tungsten–rhenium alloys,” *J. Nucl. Mater.*, vol. 278, no. 2–3, pp. 273–276, Apr. 2000.

[23] Z. X. Zhang, D. S. Chen, W. T. Han, and A. Kimura, “Irradiation hardening in pure tungsten before and after recrystallization,” *Fusion Eng. Des.*, vol. 98–99, pp. 2103–2107, 2015.

7 Effect of Proton Irradiations at 400 °C and 800 °C on the Mechanical Properties of Tungsten for Nuclear Fusion Applications

A paper submitted to the peer reviewed journal: Journal of Nuclear Materials

Presented as an adaptation of the submitted form.

Authors
Aneeqa Khan, Daniel Robertson , Joven J. H. Lim, Andrew Forrest, Llion M. Evans, Paul Mummery

Effect of Proton Irradiations at 400 °C and 800 °C on the Mechanical Properties of Tungsten for Nuclear Fusion Applications

Aneeqa Khan[a], Daniel Robertson[b] , Joven J. H. Lim[c], Andrew Forrest[c], Llion Evans[d], Paul Mummery[a]

[a] *School of Mechanical, Aerospace and Civil Engineering, The University of Manchester, M13 9PL, UK*
[b] *ISNAP, University of Notre Dame*
[c] *School of Materials, The University of Manchester, M13 9PL, UK*
[d] *Culham Centre for Fusion Energy, Culham Science Centre, Abingdon, Oxon, OX14 3DB, UK*

Abstract

The effect of temperature and microstructure on irradiation damage on as-received and annealed tungsten was investigated using 1 MeV proton irradiations, resulting in a damage level of ~2 dpa in the first 2 μm, at 400 °C and 800 °C. Continuous Stiffness Measurement nanoindentation was used in order to investigate mechanical properties. The hardness increase was greater in the annealed material, compared to the as-received.

The hardness increases measured at 400 °C in the as-received material were similar to previous proton irradiation experiments to lower does, and the annealed material showed a slightly higher hardness increase. In all cases the hardness increases measured were greater than heavy ion experiments to higher doses.

SEM showed limited surface damage in the samples irradiated at 400 °C. At 800 °C, the annealed sample displayed grain specific tungsten carbides and the as-received sample showed surface roughening, indicating sputtering. Cracking was observed in and around the indents carried out in the as-received material irradiated at 800 °C.

EBSD carried out on the non-irradiated and irradiated annealed samples, showed negligible change in microstructure.

7.1 Introduction

Tungsten is a candidate material for the divertor within a future fusion reactor [1]. This is because of its high melting point of 3420 °C [2], low sputtering rate (for the case of deuterium, E_{th} is ~200 eV [3]) and its strength at high temperatures (stress relieved has a yield strength of ~604 MPa at 800 °C [4]). However it has some weak characteristics. It has a high ductile to brittle transition temperature (embrittlement is predicted to occur below 800-1000 °C in neutron irradiated W[5]), low fracture toughness (longitudinal three point bend specimens (L-R) of polycrystalline tungsten from a rolled rod have K_Q between 5.4 and 9.1 $MPam^{0.5}$ [4]) and poor resistance to oxidation at elevated temperatures (a linear oxidation rate of 1.4×10^{-2} mg $cm^{-2}s^{-1}$ is observed in pure tungsten at a temperature of 1000 °C [6]). In the D-T operation of ITER and DEMO, 14 MeV neutrons will result in irradiation damage, including displacement cascades and transmutation of the tungsten. The 14 MeV neutron damage that occurs in a tokamak results in transmutation of the tungsten to rhenium and

osmium, alterations to its microstructure, formation of point defects and dislocation loops, and may result in the formation of σ and χ phase precipitates which are known be the cause of hardening and embrittlement due to irradiation [7], [8].

Heavy ion irradiations have previously been used as a proxy for neutrons to create fusion relevant damage within tungsten and tungsten alloys [9], [10]. Heavy ions produce damage cascades very similar to neutron damage cascades, however these typically result in extremely thin damage layers, normally between a few hundred nanometres to 10 μm [11]. Additionally multiple energies need to be used in order to get a more uniform damage profile. The depth of penetration is dependent on the energies of the ions used and irradiation temperature. This means that when doing nanoindentation tests in order to measure hardness changes of the sample there can be interaction between the irradiated layer and the non-irradiated bulk [11]. This issue also arises when indenting thin coatings on substrates of dissimilar materials. The damage cascades from protons are less dense than that of neutrons or heavy ions. Proton irradiations result in the formation of either isolated or small clusters of Frenkel pairs, whereas neutron and heavy ion irradiations result in much larger clusters of damage [12]. The damage profile resulting from proton irradiations varies gradually close to the surface, followed by a Bragg peak close to the final depth of penetration of the protons. The region close to the surface provides a fairly uniform region to analyse, and hence an irradiation at a single energy can be used. Protons also penetrate much further into the sample in comparison to heavy ions[13], meaning that when nanohardness measurements in the surface are carried out they are less likely to be affected by the bulk non-irradiated properties. It is for this reason that the effect of proton damage on microstructure and mechanical properties of tungsten will be investigated in this study.

Furthermore proton irradiations carried out by He *et al.* [14], show that the hardness increases measured in tungsten irradiated to 0.15 dpa is only 10% lower than neutron irradiated W to the same dose. This is in contrast to heavy ion irradiations, where the hardness increase following a dose of 0.4dpa is ~60% less than that seen in neutron irradiated tungsten [15], [16]. Although the data is limited, there is a small indication that proton irradiation may induce hardness responses closer to those induced by neutron irradiation, in comparison to heavy ion irradiation. This provides further motivation for investigating the hardness response of proton irradiated tungsten.

7.2 Materials

99.95 % commercial purity tungsten sheet that was 2 mm in thickness, was purchased from Goodfellow. The as-received sheet had a {100} fibre texture with respect to the common sheet plane. 1 cm^2 squares were cut from the sheet. To achieve a uniform microstructure, half of the squares were annealed under vacuum for 18 hours at 1400 °C. A slightly stronger {100} fibre texture was observed in the annealed material. All specimens were polished to a mirror finish and were then cleaned ultrasonically in acetone, ethanol and deionised water. Figure 7.1 shows the microstructures of the as-received sheet and annealed sheet.

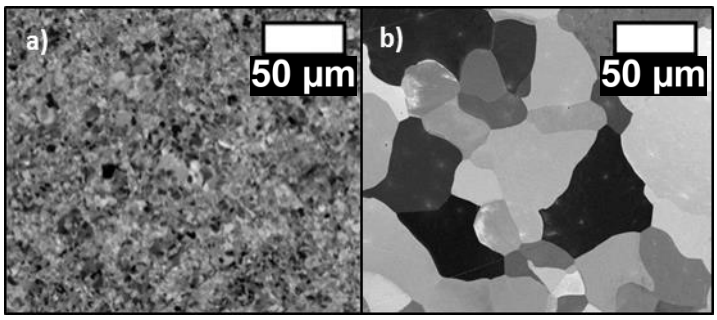

Figure 7.1: SEM Back Scatter Images for a) as-received and b) annealed tungsten sheet.

The average grain size of the as-received sheet is ~1 µm and ~21 µm for the annealed sheet. The grain sizes were estimated using Channel 5 software.

7.3 Experimental

All irradiations were completed at the 5 MV pelletron accelerator, located in the Nuclear Science Laboratory (NSL) of the University of Notre Dame. Samples were loaded and held at the zero degree target location, mounted on the high-temperature irradiation station shown in Figure 7.2 and Figure 7.3.

Low-energy protons were focused to the end of the activation line through collimation systems prior to the target station. The beam uses the following systems;

1. Tantalum collimator 0.25 inch. Used for tuning of beam parameters and constraining beam.
2. Tantalum suppressor set to -300 V. The suppressor is used to prevent secondary electrons being emitted from the sample and giving false beam current readings. It also prevents possible scattered electrons from reaching the sample.
3. Tantalum mask 0.25 inch. This both holds the sample in place through compression, and prevents stray beam hitting sample.
4. PBN plate heater. This provides possible heating up to 1200 °C, used to stabilize sample temperature adding to beam heating.

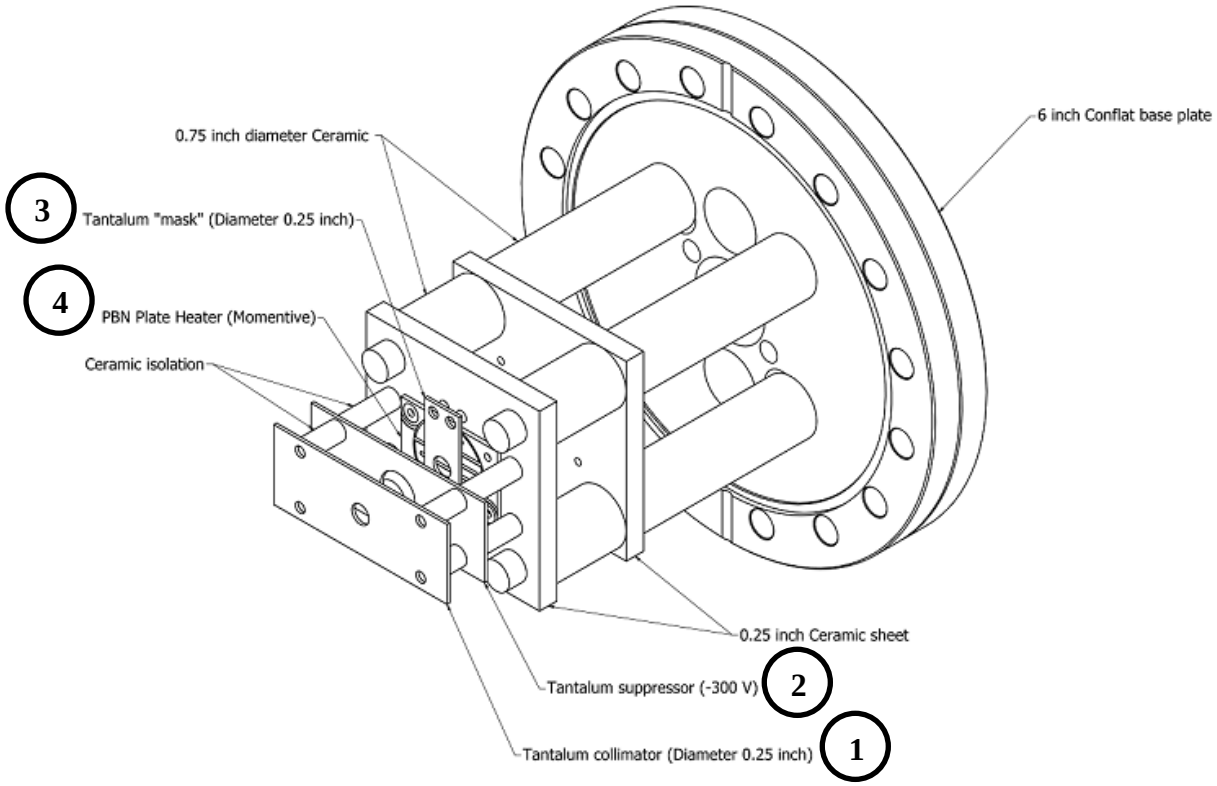

Figure 7.2: High-temperature irradiation station designed and constructed at NSL. No sample shown.

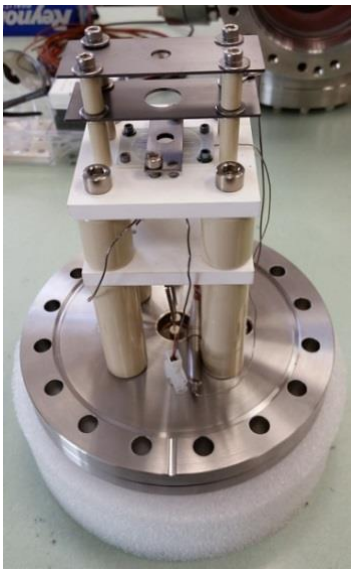

Figure 7.3: Constructed heating target station.

Two as-received samples (hereafter called R400 and R800) and two annealed tungsten samples (hereafter referred to A400 and A800) were irradiated during this set of experiments. The initial properties of the sample are indicated in Table 7.1.

Table 7.1: Initial sample conditions as-received at the NSL.

Sample	Mass (g)	Width 1 (mm)	Width 2 (mm)	Thickness (mm)
R400	3.5516	9.89	9.93	1.91
R800	3.7352	9.86	9.94	1.99
A400	3.5222	9.83	9.91	1.91
A800	3.4944	9.81	9.91	1.88

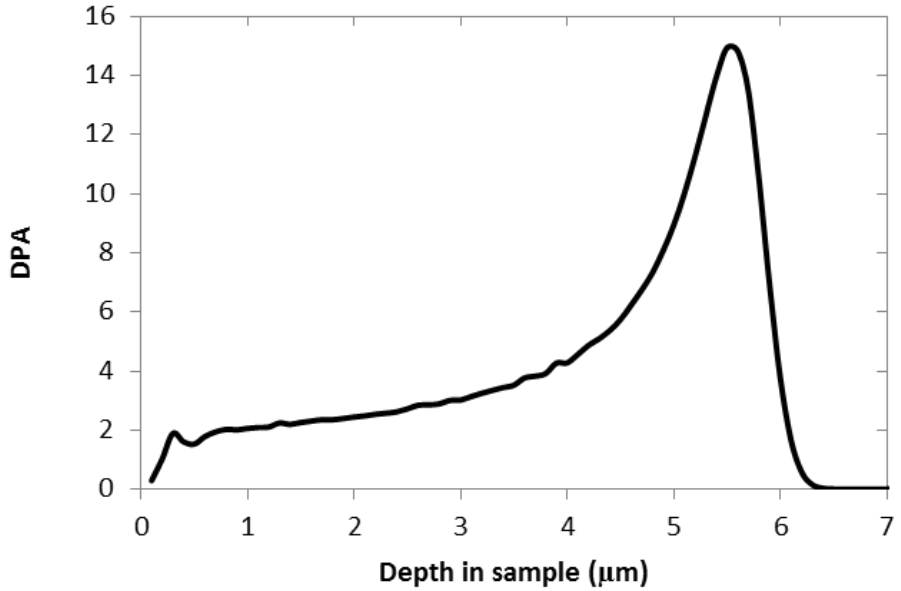

Figure 7.4: Stopping range of ions in matter (SRIM) calculated profile of displacements per atom for hydrogen implanted in tungsten at 1 MeV using a 68 eV displacement value.

All samples were irradiated with a defocussed beam of protons at an energy of 1 MeV, in order to achieve the damage profile shown in Figure 7.4. The damage profile was calculated using the Kinchin Pease Model in SRIM (Stopping range of ions in matter, a Monte Carlo code) (Annapolis, MD) [17]. If the full damage calculations were used with high energy protons, anomalous peaks and dips would be observed [17]. It is for this reason that the Kinchin-Pease model was utilised. A displacement value (the energy required to produce a vacancy and interstitial) of 68 eV was assumed for tungsten [18]. This resulted in a Bragg peak of 14.9 dpa at a depth of 5.5 µm into the sample, and a fairly uniform damage profile of approximately 2 dpa between 0.5 and 2 µm into the sample.

In order to investigate the effect of temperature, samples R400 and A400 were irradiated at 400 °C and samples R800 and A800 at 800 °C. A summary of the samples used is shown in Table 7.2.

Figure 7.5 and Figure 7.6 show the irradiation set up.

Table 7.2: Summary of Sample Nomenclature.

Temperature (°C)	As-received (R)	Annealed (A)
400	R400	A400
800	R800	A800

Incident beam intensities had to be limited due to induced heating caused by deposited power from ion beam bombardment. To prevent temperatures increasing above those required of 400 °C and 800 °C, beam intensities were deliberately restricted to 14 μA and 35 μA respectively. The heater placed under the target sample was then used to maintain a steady temperature and to compensate for beam fluctuations.

Samples at 400 °C took 18 hours of continuous irradiation each, and 800 °C samples took 8 hours each. Due to heat input considerations the fluxes used at 400 °C were lower than those used at 800 °C. Minor temperature fluctuations during irradiation occurred due to beam current oscillations and were continuously corrected. To insure similar irradiation conditions at each temperature, maximum temperature fluctuations were maintained at comparable levels for both samples (±10 °C long term fluctuation and ±2 °C short term fluctuation). The irradiation conditions are summarized in Table 7.3**.** The mass of the samples before and after irradiation is summarized in Table 7.4.

Table 7.3: Irradiation conditions and final sample state.

Sample	Ion	Energy (MeV)	Temp (°C)	Cross sec (cm^2)	Charge (Col)	Total ions	Flux ($ions/cm^2s$)	Fluence ($ions/cm^2$)
R400	H	1.00	400	0.196	0.944	5.891×10^{18}	4.63×10^{14}	3.00×10^{19}
A400	H	1.00	400	0.196	0.944	5.891×10^{18}	4.63×10^{14}	3.00×10^{19}
R800	H	1.00	800	0.196	0.944	5.891×10^{18}	1.04×10^{15}	3.00×10^{19}
A800	H	1.00	800	0.196	0.944	5.891×10^{18}	1.04×10^{15}	3.00×10^{19}

Table 7.4: Mass change of samples after irradiation.

Sample	Mass before (g)	Mass after (g)	Mass Difference (g)
R400	3.5516	3.5516	0
R800	3.7352	3.7320	-0.0032
A400	3.5222	3.5224	0.0002
A800	3.4944	3.4947	0.0003

During irradiation, samples were checked visually to insure sample stability. Beam current was integrated and monitored on a 10 second integration time, with temperature variations monitored on a 1 second time variation.

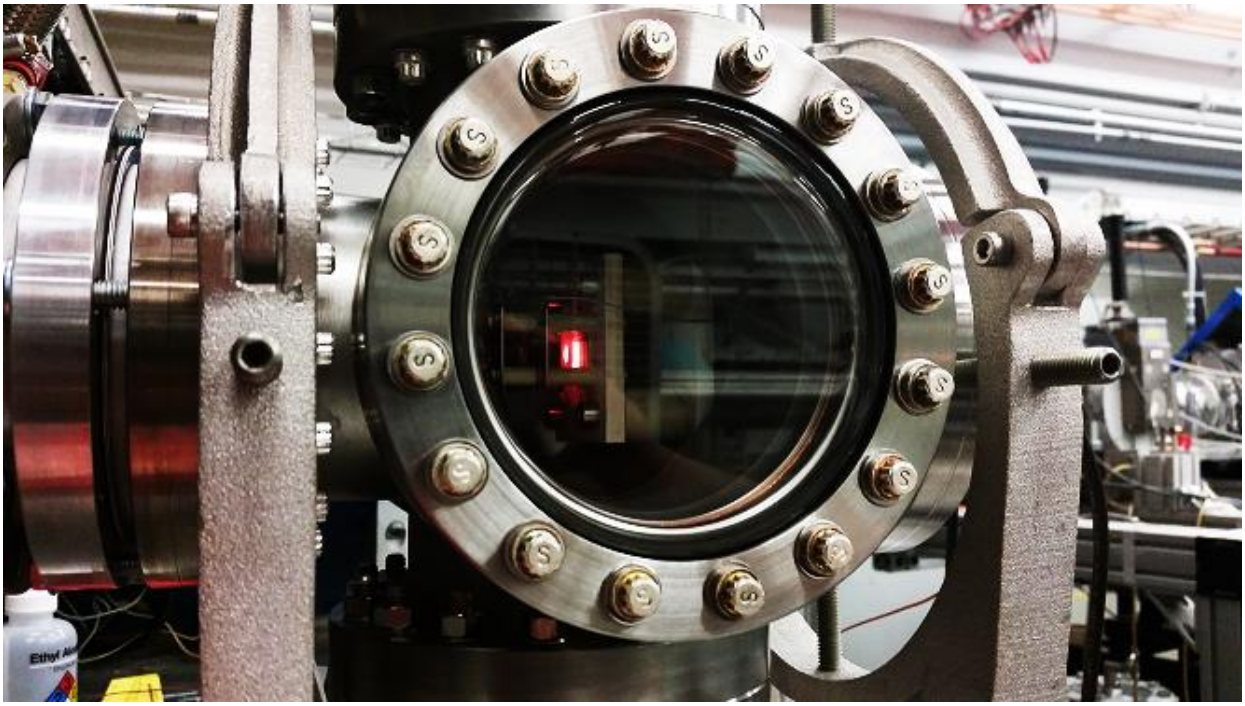

Figure 7.5: Set-up of target sample irradiation. Beam on target, temperature at 800 °C.

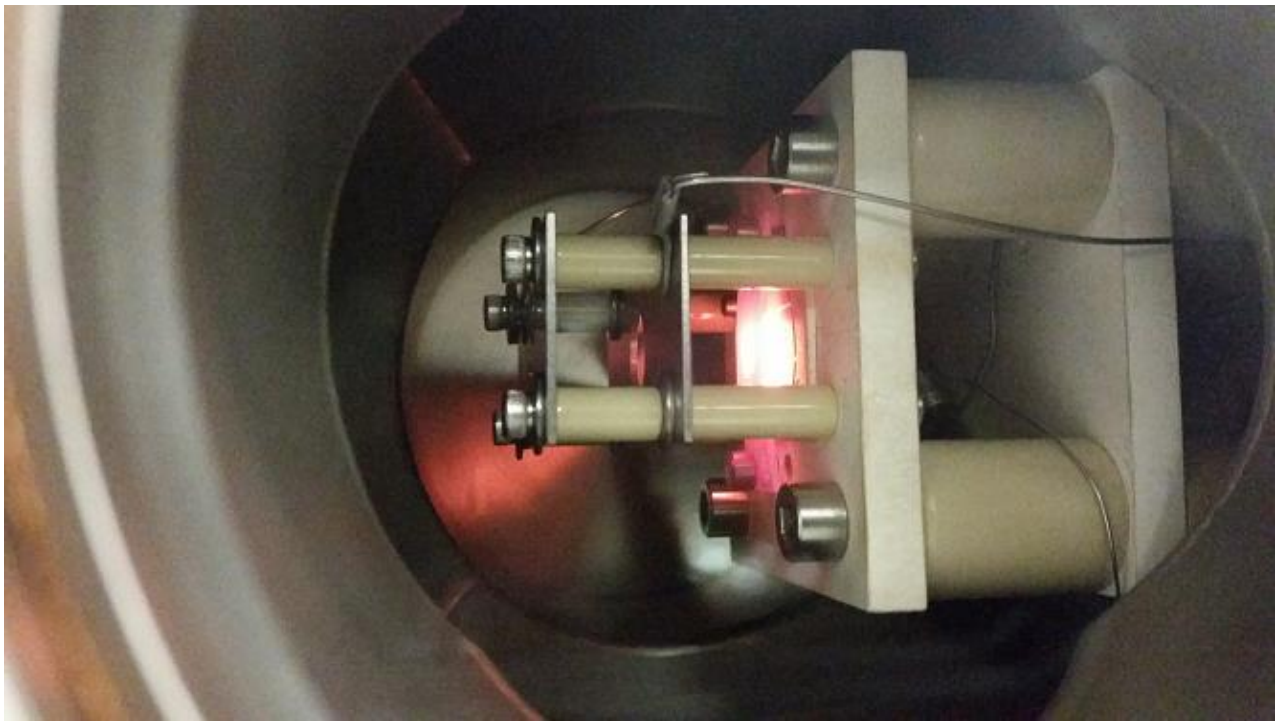

Figure 7.6: Zoomed version of target sample irradiation. Beam on target, temperature at 800 °C.

7.4 Results and Discussion

Following the irradiations, nanoindentation using a Berkovich tip was carried out in order to determine changes in mechanical properties. The irradiated samples were compared to non-irradiated as-received and annealed samples in order to determine the change in hardness.

For all irradiated samples, an array of 25 ~2000 nm deep Continuous Stiffness Measurement (CSM) indents, with 50 µm spacing were performed in order to cover a variety of grains within the irradiation damage spot and also to obtain data throughout the sample from the surface, up to a depth of 2000 nm. In all samples the arrays were two rows of ten, with a single row of 5 indents, with the exception of ND400 where a five by five array was used. The indents were performed in the centre of the sample each time, so as to analyse damage from the same region of the ion beam, and hence damage profile. SEM was then utilised to look at the indents within the irradiated samples. Some indents were within grains, and some crossed grain boundaries in the annealed material. In the as-received samples, each indent covered multiple grains.

In the as-received samples (Figure 7.7 a)), at 400 °C we see a 1.9 GPa (29 %) average increase (averaged across all indents at depths between 500 and 1800 nm) in hardness. For the 800 °C irradiated as-received sample (Figure 7.7 c)), the increase between these displacements is 4.1 GPa (63 %). However in this sample there is a substantial hardness increase close to the sample surface, which indicates some kind of surface layer or modification. This is confirmed when we look at SEM images shown later in the results section, which show significant surface roughening. If we then look at the indents, cracking was observed around all the indents in the as-received sample irradiated at 800 °C, something that was not observed in any of the other samples. Not only does this suggest that the data collected from the nanoindentation in this sample is not directly comparable to the other samples, but also indicates that the region has been significantly embrittled from the irradiation process, which is one of the main concerns with using tungsten for fusion structural materials. Cracking around indents has not been previously observed at lower temperature irradiations using heavy ions [19]or in heavy ion irradiations at 800 °C by Gibson et al. [10].

If we then consider the annealed samples, from Figure 7.7 b) and d) we can see that there is an average increase in hardness of 2.6 GPa between a depth of 500 and 1800 nm for the sample irradiated at 400 °C, compared to a 3.5 GPa increase for the 800 °C sample. This corresponds to 48 and 64 % average increases in hardness in comparison to non-irradiated tungsten, which is significantly greater than hardness increases experienced in self-ion irradiated material even at much higher dpa levels(~23% hardness increase in self-ion irradiated annealed W to peak dose of 40 dpa at 400 °C) [19]. Although typically at increased temperatures, there should be increased annealing of defects and consequently a reduced hardness increase, this is not what is observed. It is most likely that due to temperature considerations, as increased dose rates were used in the 800 °C irradiations, and consequently the irradiation times were shorter in comparison to the 400 °C irradiations; there was reduced time for annealing of defects. This explains the increased hardness increase for the higher

temperature irradiations. Additionally as will be subsequently discussed, carbide formation on the surface could also explain the increased hardness.

Consistent with previous ion irradiation experiments, the hardness increase observed in the annealed samples is greater than in comparison to the as-received material [19], [20]. This is most likely due to the fact there is an increased grain boundary area in the as-received material, which will act as a sink for defects.

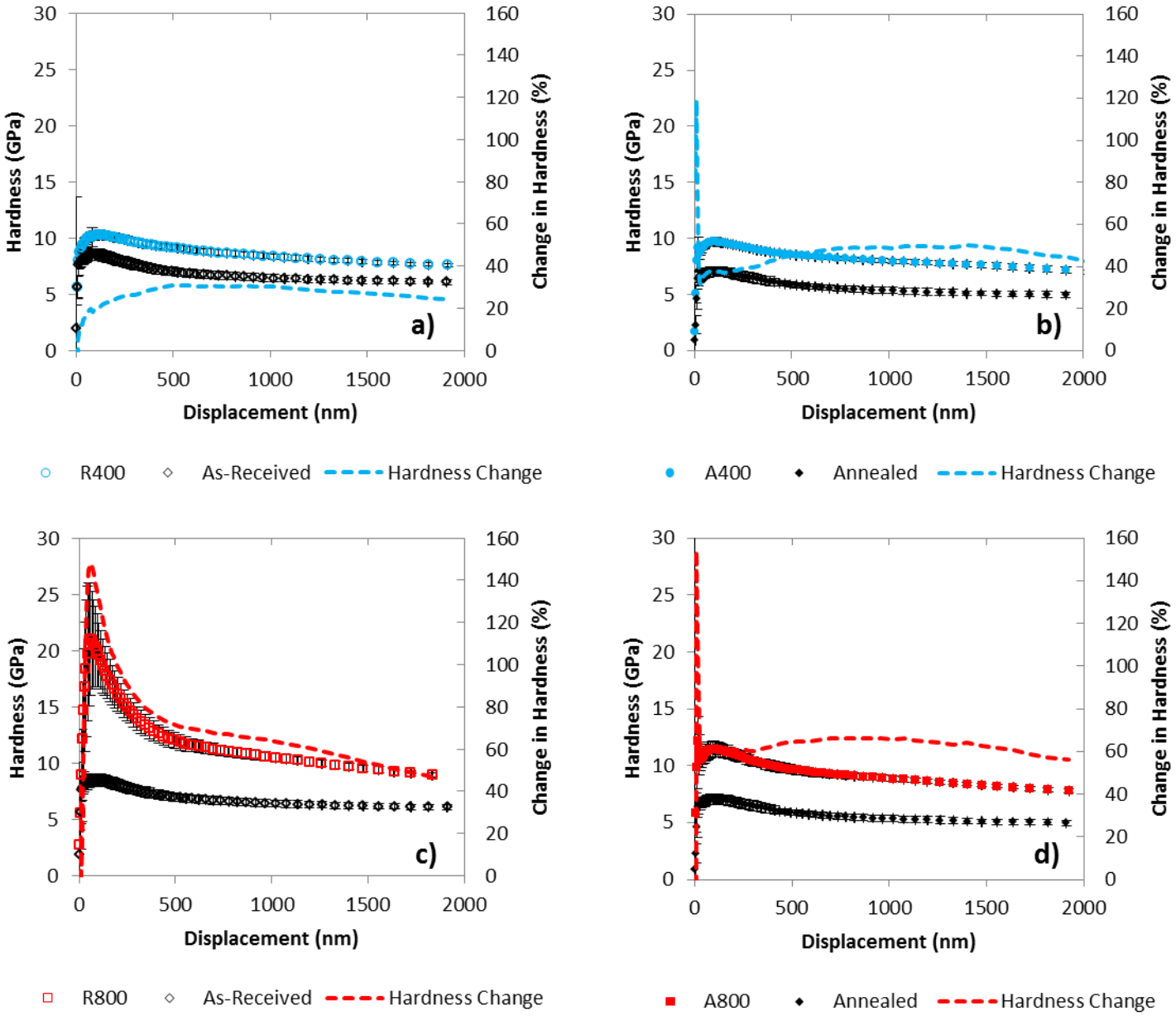

Figure 7.7: Raw hardness and % hardness change for a) R400, b) A400, c) R800 and d) A800.

The irradiations carried out at 400 °C can be compared to previous proton irradiations in the literature by He. *et al.* [14]. He *et al.* carried out 1 MeV proton irradiations at 500 °C, resulting in a dose of ~0.15 dpa at a depth of 2µm into the surface. Despite the lower doses used by He *et al.*, the shape of the damage profile was similar to that achieved in the experiments in this chapter, with a Bragg peak at ~5.5 µm. There is no information provided by He *et al.* on the initial microstructure of the irradiated material, which combined with the fact that Vickers hardness testing was used by He *et al.*, makes direct comparison difficult. Nevertheless, as this is the only relevant data in the literature that the results from the experiments in this chapter can be compared to, the Vickers hardness measurements by He *et al.* have been converted to GPa, and compared to the hardness increases in the as-received and annealed materials at 400 °C (Figure 7.8).

As can be seen in Figure 7.8, the data from the literature is very similar to the hardness increase seen in the as-received material irradiated to 400 °C. The annealed material shows a hardness increase that is ~0.6 GPa than the two other samples. This provides a reminder that, while dose is an important parameter, the initial microstructure of a material is crucial when looking at irradiation damage. It would be beneficial to conduct irradiations on the same starting microstructure, at a range of doses in order to see if there was a saturation in irradiation hardening as has been seen in some heavy ion and neutron irradiated W [21], [22].

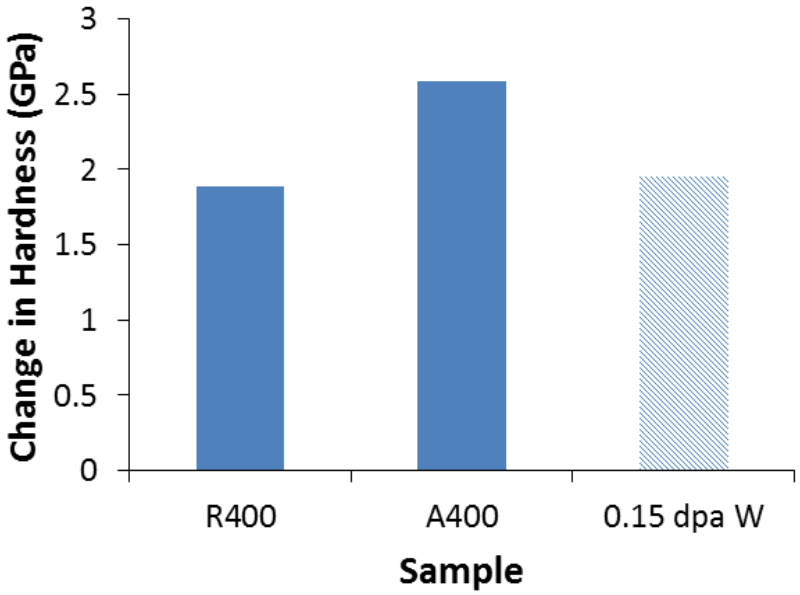

Figure 7.8: Comparison of the change in hardness observed in proton irradiated as-received and annealed W at 400 °C to 2 dpa (R400, R800) with 500 °C irradiations to 0.15 dpa by He et al.[14].

The hardness increase for both the as-received and annealed material is greater than hardness increases observed in heavy ion irradiated material [19], [21] at similar temperatures to higher doses. For example, Armstong *et al.* observed a hardness increase of 0.92 GPa in self-ion irradiated ultra high purity tungsten irradiated to 33 dpa at a temperature of 300 °C [21]. Khan *et al.* only saw hardness increases of ~1.6 GPa in the same annealed material used in

this proton irradiation study, following W irradiations to a peak dose of ~40 dpa at 400 °C. An as-received material, similar to that used in this proton irradiation study was also self ion irradiated to a peak dose of ~40 dpa at 400 °C, where only a 0.8 GPa hardness increase was observed [19]. It is suggested that this is most likely due to the fact the penetration depth is much greater in proton irradiated material, in comparison to the heavy ion experiments. This means the nano-hardness measurements are not influenced by the non-irradiated bulk material properties, but by the hardness increase caused by the increased dose deeper in the sample. Additionally, dpa does not take into account recombination of defects[23], and due to the fact that the cascades induced by proton irradiations are much less dense than those created in heavy ion irradiations, during the cooling phase there is less recombination of defects [12]. This could also contribute to the higher hardness increase observed in comparison to heavy ion irradiations.

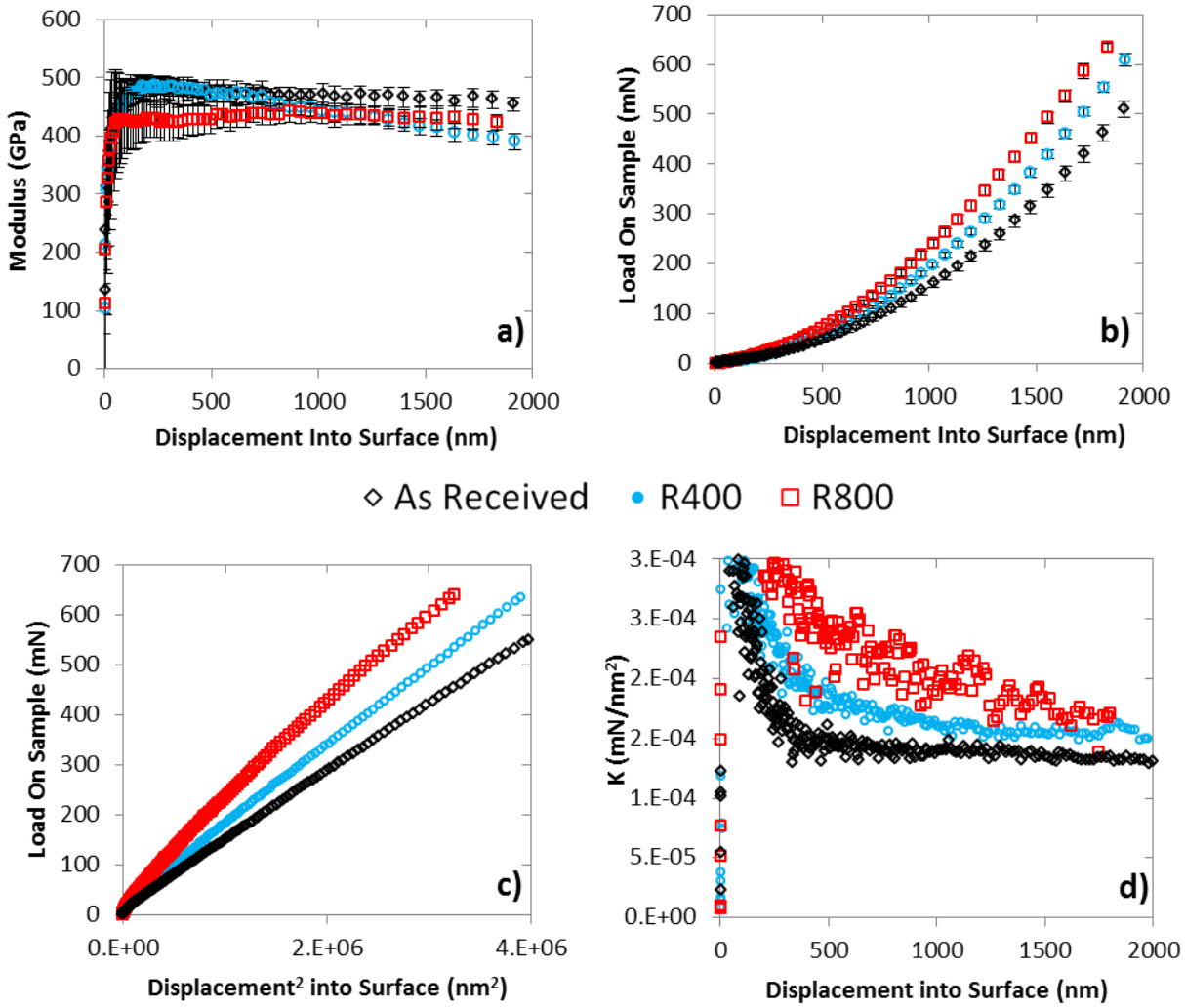

Figure 7.9: Variation of a) modulus with displacement, b) load with displacement, c) load with displacement^2 and d) gradient of load displacement^2 graph for non-irradiated as-received tungsten and proton irradiated as-received tungsten at 400 and 800 °C. All data points are for 'as-received' samples, the black diamonds are non-irradiated.

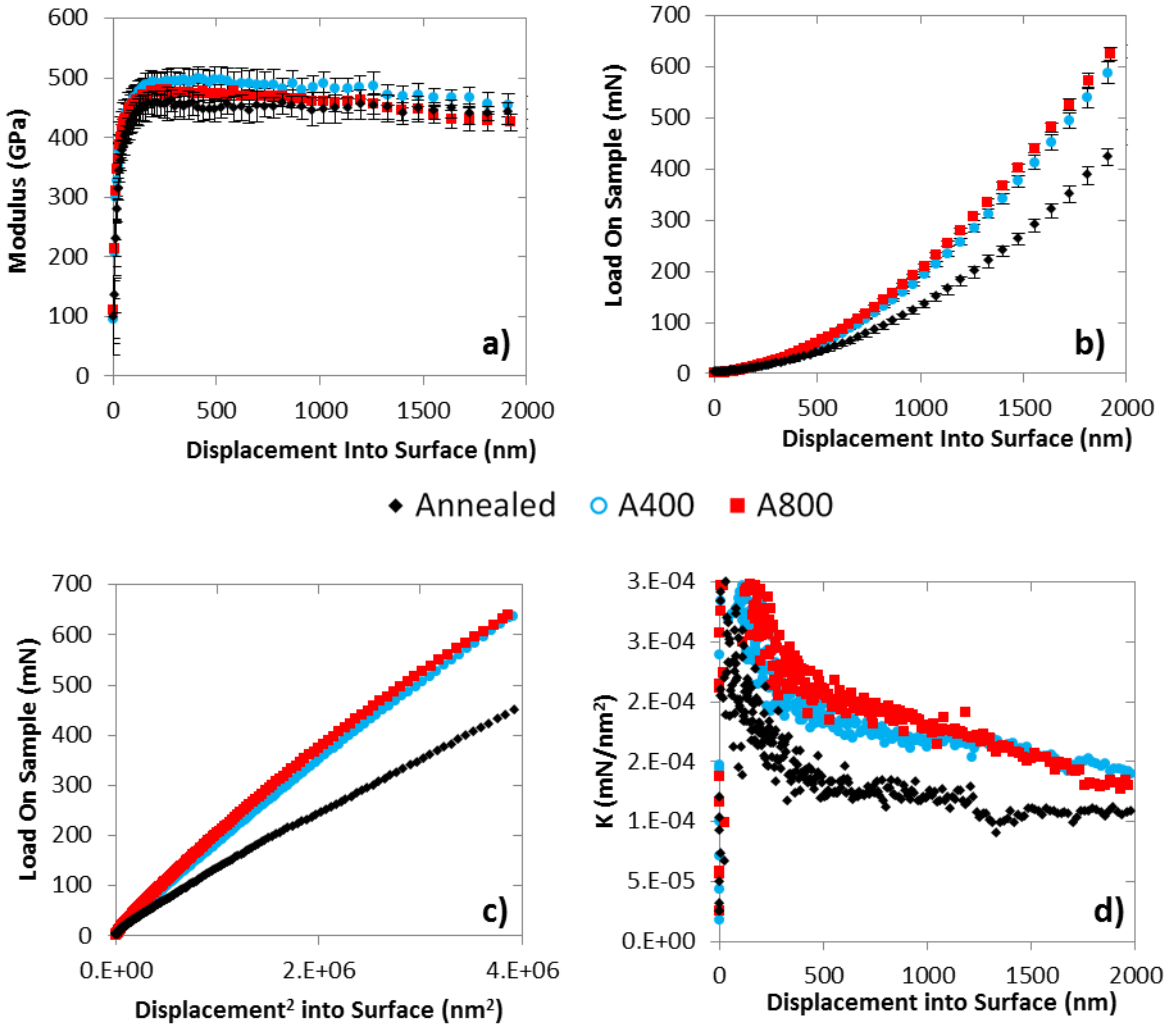

Figure 7.10: Variation of a) modulus with displacement, b) load with displacement, c) load with displacement^2 and d) gradient of load displacement^2 graph for non-irradiated non-irradiated annealed tungsten and proton irradiated annealed tungsten at 400 and 800 °C. All data points are for 'annealed' samples, the black diamonds are non-irradiated.

Figure 7.9 and Figure 7.10 a) illustrate the variation of modulus with displacement into the sample. There is a clear decrease in modulus in sample R800, which can be explained by the extensive surface roughening and cracking in that sample. There is also a slight decrease in modulus for sample R400 at higher depths; however this could just be due to sample mounting (super glue could result in an apparent reduction in contact stiffness at higher loads due to compliance which would result in an apparent reduction in modulus). There is a negligible change in modulus in both the annealed samples. Figure 7.9 and Figure 7.10 b) show average load/displacement graphs for the as-received and annealed samples. In order for the indenter to penetrate further into the sample, the load required increases and is proportional to the square of the displacement into the sample. We can see that in all cases that there is an increase in the gradient following irradiation, which corresponds to the increase in hardness, meaning that a higher load is required to get the indenter tip to achieve

the same displacement into the sample. In order to see the interaction between a coating and a substrate often the gradient of load/displacement^2 (shown in Figure 7.9 and Figure 7.10 c)), K, is plotted against displacement [24], as shown in Figure 7.9 and Figure 7.10 d) [24]. These plots are for a typical indent. We can observe in the case of both the as-received and annealed samples that the influence of the bulk non-irradiated material properties on the measured properties of the irradiated layer is limited (i.e. the K values of the irradiated samples remain separate to the line from the non-irradiated materials). In the case of the annealed samples there is a small difference between the 400 °C and 800 °C irradiations, however with the as-received samples there is a much bigger difference between the irradiations at different temperatures. This is most likely due to the embrittled layer on the surface of the sample which affects the data.

From Figure 7.11 it can be seen that there is a clear variation in greyscale values between the irradiation spot and the non-irradiated region of the sample, with the irradiated region appearing much darker than the non-irradiated area. This is something that is observed in all the irradiated samples.

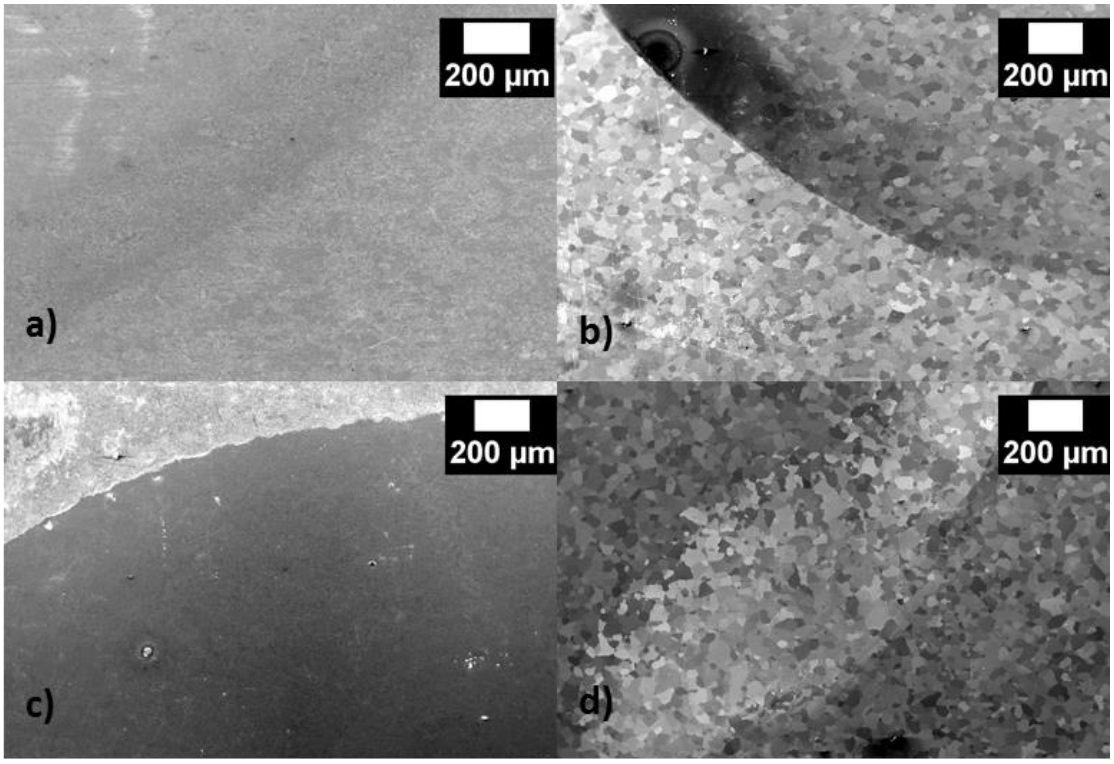

Figure 7.11: SEM secondary electron images showing difference between irradiated (dark) and non-irradiated (light) regions in a) R400, b) A400, c) R800 and d) A800.

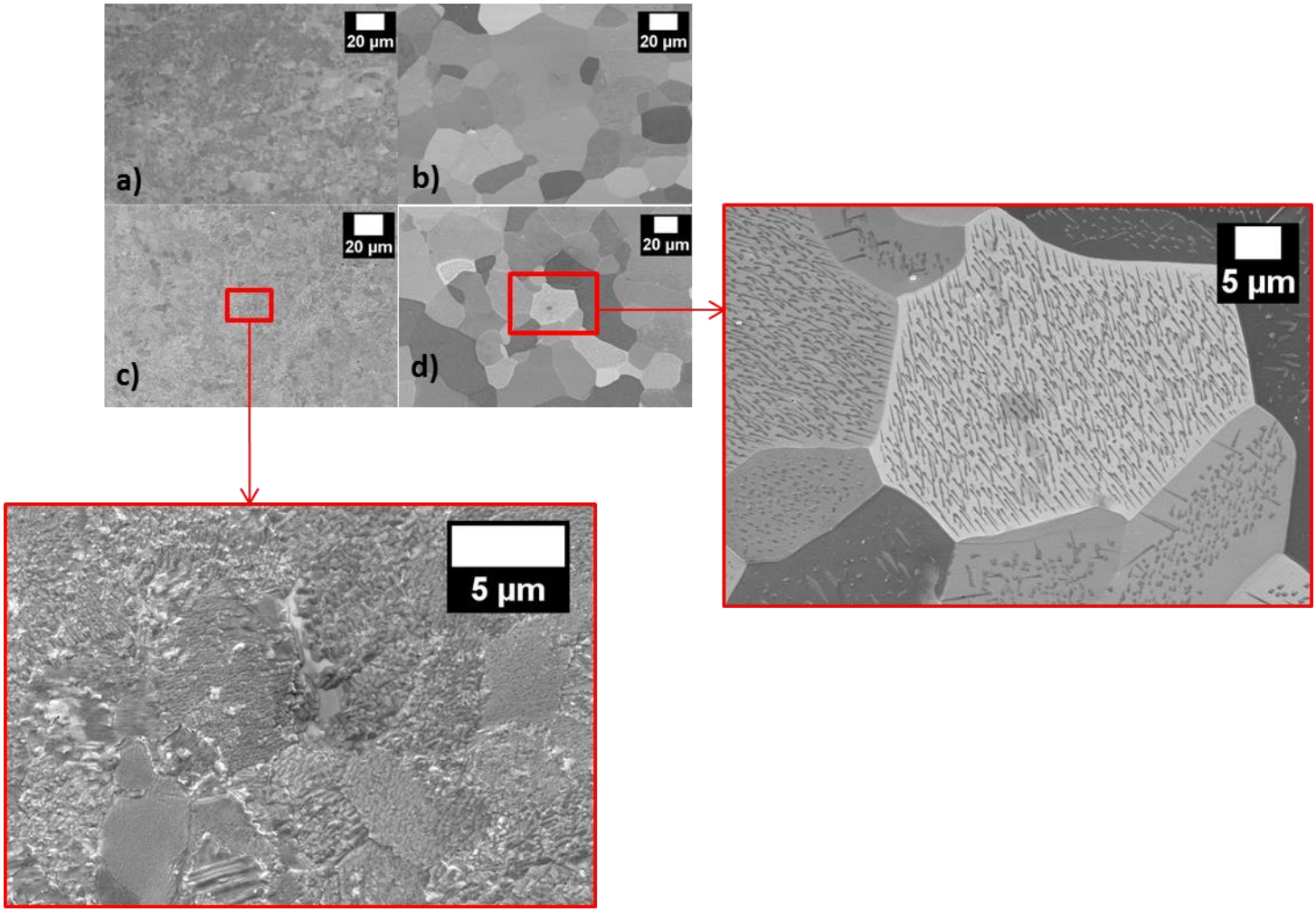

Figure 7.12: SEM secondary electron images within irradiated spot in regions in a) R400, b) A400, c) R800 and d) A800.

If we then consider the surface damage on all the irradiated samples, in Figure 7.12 a) and b) we can see that in both as-received and annealed samples irradiated at 400 °C there is no significant surface damage and indeed the samples appear similar to the non-irradiated samples. However, this is clearly not the case for the samples irradiated at 800 °C, as seen in Figure 7.12 c) and d). From Figure 7.12 d) we can see that surface features or precipitates have developed in the annealed samples. These differ between each grain orientation and are not visible close to grain boundaries. Using EDX, these have been identified as tungsten carbides (Figure 7.13). No carbides were observed at 400 °C in the annealed sample. The carbides were only observed in the irradiated region of the annealed sample irradiated at 800 °C, and not in the region outside of irradiation, confirming that they were introduced during the irradiation.

Although ion irradiations are carried out in a vacuum environment, carbide formation is something that has recently been observed and also discussed at the SMINS4 2016 conference [25], [26]. There is uncertainty as to why carbide formation occurs. For the specific case of the 800 °C irradiations in this experiment, from the W-C phase diagram

(Figure 7.14), it is not clear from the temperature alone that carbide formation should occur [27]. Therefore the energy deposited from irradiation is also contributing to carbide formation. There are three main theories as to why carbide formation could occur. Firstly, there could have been contamination of the source, secondly contamination of the chamber and finally redistribution of carbon in the material could have occurred [28]. In the specific case of this experiment, it is unlikely that contamination of the source could have occurred. Pure hydrogen gas was used and the ions were selected to high precision based on their momentum/charge ratio, hence no carbon containing compounds should be present in the beam. It is possible that redistribution of carbon in the sample could have occurred. In terms of contamination from the chamber, in this experiment, the pumping system was oil-free and the vacuum systems were o-ring free. Nevertheless, it is still possible that organic material could have been released from components in the beam line, and the beam could have deposited the carbon on the tungsten surface. The influence of the irradiation, as well as the higher temperatures reached in the irradiated spot may help to explain why carbides are only observed in the irradiated region.

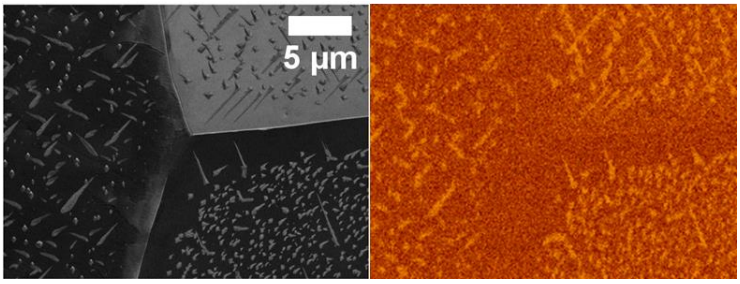

Figure 7.13: Micrograph and corresponding EDX of precipitates identified as carbides in annealed proton irradiated tungsten at 800 °C. Red represents the W M series, yellow the C K series, and hence orange represents the simultaneous presence of W and C (i.e. tungsten carbides).

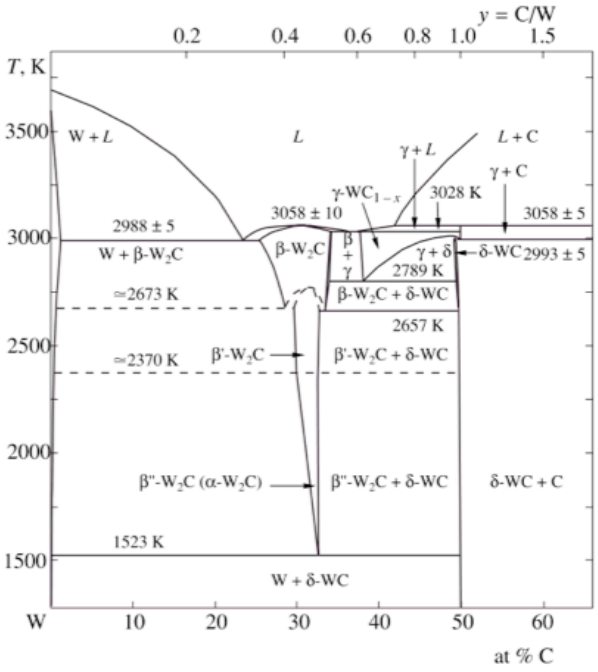

Figure 7.14: W-C phase diagram, taken from [27].

From Figure 7.12 c) we can see there is extensive surface roughening in the as-received sample. EDX does not reveal any carbides or oxides. However smaller carbides, could have formed that are beyond the limit of resolution in the SEM. A mass loss of 0.0032 g observed in the as-received sample indicates some sputtering.

SEM analysis of the nanoindents in the non-irradiated samples is shown in Figure 7.15**.** We can see that no obvious cracks visible around the indents. Figure 7.16 gives examples of indents in the irradiated samples. In Figure 7.16 c) we see extensive cracking in and propagating from the indent itself, indicating that the surface has been significantly damaged and embrittled in the as-received irradiated sample at 800 °C. This can explain why the nanoindentation hardness is so much harder compared to the 400 °C irradiation, especially in comparison between the different temperature irradiations in the annealed samples. This casts doubt on the reliability of the nanoindentation data in this sample to give hardness measurements that are comparable to the other samples, but it does prove that the surface of this sample is more brittle and prone to fracture, which is a problem envisaged in tungsten for nuclear fusion applications. Sputtering is responsible for the surface roughening observed, resulting in an extremely brittle surface. Additionally, in the 800 °C irradiations, an increased flux was utilised in comparison to the 400 °C irradiations. Therefore as the irradiation time was reduced, there was less time for annealing of defects to occur, which could explain the increased hardness.

The nanoindentation data from the 800 °C irradiated annealed material could be influenced by the presence of the carbides. However, the carbides have nucleated and grown at the surface (Figure 7.17 shows there are no carbides below the surface). Therefore, although the carbides could have affected the initial measurements close to the surface, in the region of interest (500-1800 nm), they may not have as significant an effect.

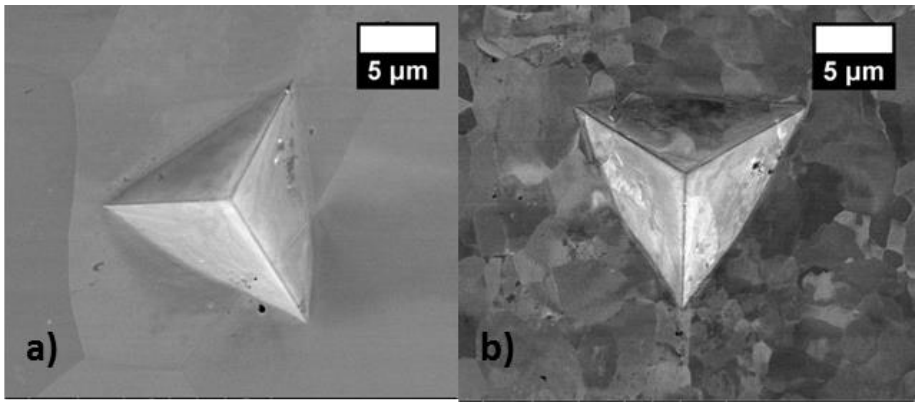

Figure 7.15: Example of 2000 CSM Berkovich nanoindents in a) annealed and b) as-received tungsten.

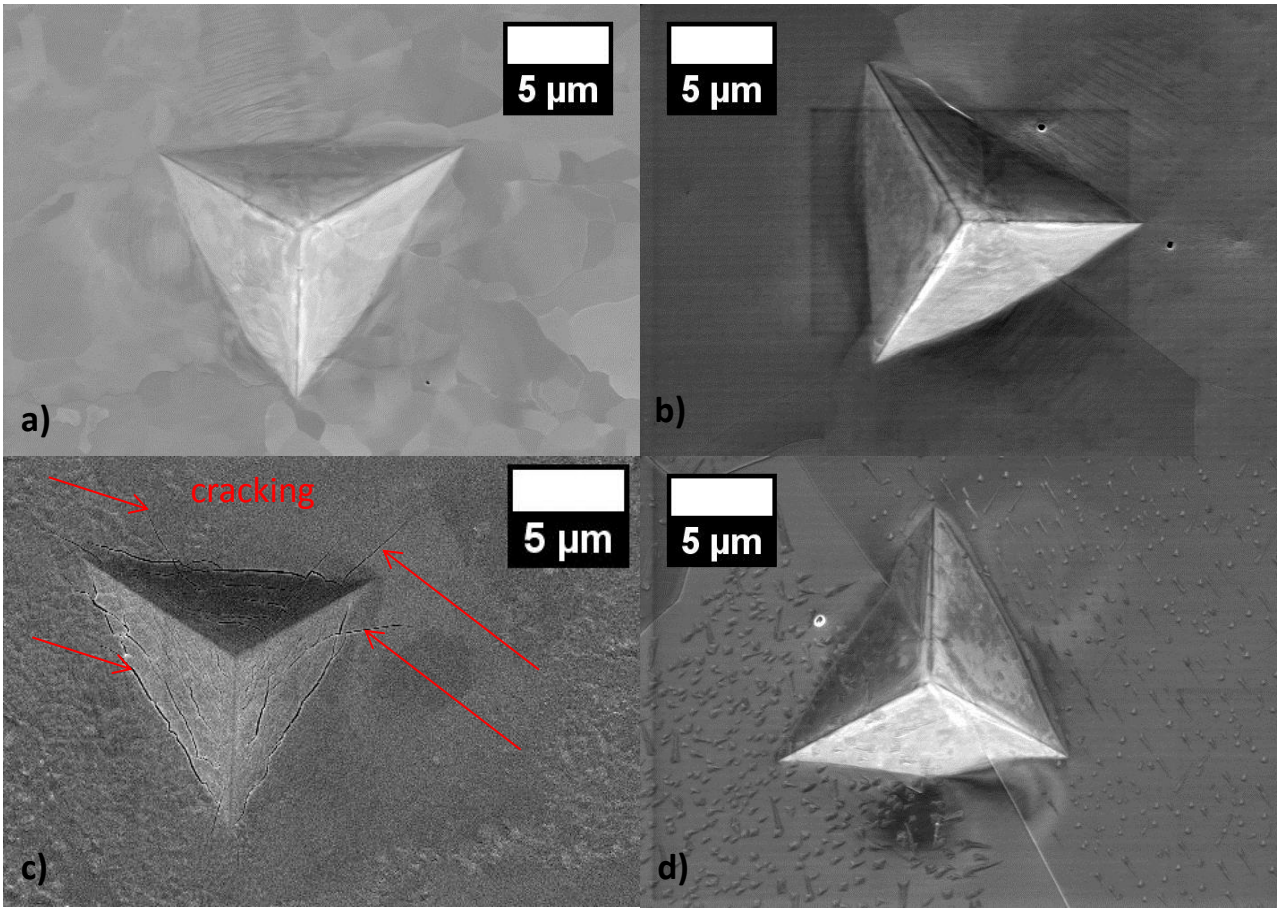

Figure 7.16: Example of 2000 CSM Berkovich nanoindents in a) R400, b) A400, c) R800 and d) A800.

Figure 7.17: FIB cross section of A800 sample. Image is taken at 45 °, and the tilt corrected scale bar is provided in the y direction. The darker contrast at the bottom is due to shadowing from redeposited material at the side of the trench. Carbides were observed in plan view, as shown in Figure 7.13, but not in cross section.

EBSD was carried out at a step size of 1 µm in the annealed samples. The focus was on the annealed samples due to the larger grain size. There was no apparent change in microstructure, when compared to EBSD in the non-irradiated sample. EBSD was conducted at 15 kV as shown in Figure 7.18, where there was a greater than 97 % hit rates in both cases. This indicates that close to the surface of the samples (75 % of the signal comes from within the first 40 nm as calculated by CASINO version 2.48 (monte CArlo Simulation of electron trajectory in sOlids)(Québec, Canada) [29]) there is limited surface damage. This is in stark contrast to previous work in heavy ion irradiated samples (up to levels of 40 dpa [19]where extensive surface damage that impacted the indexing of EBSD pole figures was observed.

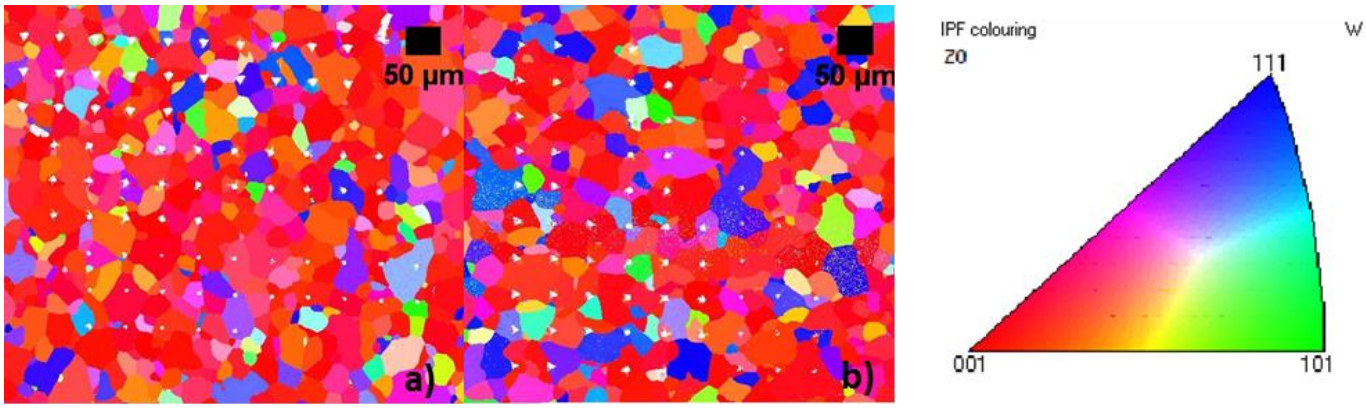

Figure 7.18: Inverse Pole Figures of proton irradiated annealed tungsten at a) 400 °C and b) 800 °C over nanoindented region at electron voltage of 15 kV.

7.5 Conclusions

Proton irradiations result in a significant increase in hardness in both as-received and annealed tungsten samples. The hardness increase observed was greater in the annealed samples in comparison to the as-received material. This is consistent with previous heavy ion irradiation experiments [19], [20].

The hardness increase measured in the as-received material following 400 °C irradiations were of a similar level to those observed in previous proton irradiations to 0.15 dpa, with the annealed material showing a ~0.6 GPa greater hardness increase. The hardness increases observed for both as-received and annealed W at 400 °C were greater than those seen in self-ion and Re ion irradiations in W to higher doses at the same temperature. It is suggested that one of the reasons for this could be due to the fact in the proton irradiations, the hardness measurements are not influenced by non-irradiated bulk material, as is the case in the heavy ion irradiated material, where the implantation depth is shallower [19], [21]. Instead in the case of proton irradiations, the irradiation damage at the Bragg peak could influence hardness. Additionally, it is suggested that the fact there is less recombination in the cooling phase, following irradiation by protons in comparison to heavy ions could also contribute to the higher hardness increases observed [12].

The formation of tungsten carbide precipitates within the grains of annealed tungsten irradiated at 800 °C has been observed, the source of which is not confirmed. It is possible that carbide formation arises from contamination from organics in the chamber. Investigation into the exact structure of the carbides as well as their formation mechanism should be investigated. The average hardness increase observed in the annealed material at 800 °C is 64 %, compared to 48 % at 400 °C. Typically at higher temperatures, there should be increased annealing of defects and the hardness increase is expected to be reduced. There are two reasons suggested as to why this is not the case in this experiment. The carbides observed on the surface may influence the hardness measurements, but the effect may not be as significant at the depths of 500-1800 nm from where the hardness measurements are taken. Additionally, in the 800 °C irradiations, an increased flux was utilised in comparison to the 400 °C irradiations. Therefore as the irradiation time was reduced, there was less time for annealing of defects to occur, which could explain the increased hardness.

Extreme surface roughening was seen on the surface of the as-received material irradiated to 800 °C, which could have been due to a sputtering effect. This resulted in an extremely brittle surface, and cracking was seen in the nanoindents, and meant that the nano-hardness data obtained was not accurate.

Acknowledgements

The author gratefully acknowledges access to the ISNAP facilities. Thanks are also given to Andy Wallwork for his help with the heat treatment of the samples and to Mike Gorley for his useful comments. This work was supported by the Engineering and Physical Sciences Research Council [EP/K504178/1].

References

[1] R. A. Pitts, S. Carpentier, F. Escourbiac, T. Hirai, V. Komarov, S. Lisgo, A. S. Kukushkin, A. Loarte, M. Merola, A. Sashala Naik, R. Mitteau, M. Sugihara, B. Bazylev, and P. C. Stangeby, “A full tungsten divertor for ITER: Physics issues and design status,” *J. Nucl. Mater.*, vol. 438, pp. S48–S56, Jul. 2013.

[2] PLANSEE, “Materials: Tungsten,” 2013. [Online]. Available: http://www.plansee.com/en/Materials-Tungsten-403.htm. [Accessed: 02-Jul-2013].

[3] J. W. Davis, V. R. Barabash, A. Makhankov, L. Plöchl, and K. T. Slattery, “Assessment of tungsten for use in the ITER plasma facing components,” *J. Nucl. Mater.*, vol. 258–263, pp. 308–312, 1998.

[4] B. Gludovatz, S. Wurster, A. Hoffmann, and R. Pippan, “Fracture toughness of polycrystalline tungsten alloys,” *Int. J. Refract. Met. Hard Mater.*, vol. 28, no. 6, pp. 674–678, 2010.

[5] H. Bolt, V. Barabash, G. Federici, J. Linke, A. Loarte, J. Roth, and K. Sato, “Plasma facing and high heat flux materials - Needs for ITER and beyond,” *J. Nucl. Mater.*, vol. 307–311, no. 1, Supplement, pp. 43–52, 2002.

[6] F. Koch and H. Bolt, “Self passivating W-based alloys as plasma facing material for nuclear fusion,” *Phys. Scr.*, vol. 2007, no. T128, pp. 100–105, 2007.

[7] M. R. Gilbert, S. L. Dudarev, D. Nguyen-Manh, S. Zheng, L. W. Packer, and J.-C. Sublet, “Neutron-induced dpa, transmutations, gas production, and helium embrittlement of fusion materials,” *J. Nucl. Mater.*, pp. 1–6, Apr. 2013.

[8] M. Fukuda, K. Yabuuchi, S. Nogami, A. Hasegawa, and T. Tanaka, “Microstructural development of tungsten and tungsten–rhenium alloys due to neutron irradiation in HFIR,” *J. Nucl. Mater.*, vol. 455, no. 1–3, pp. 460–463, 2014.

[9] D. E. J. Armstrong, A. J. Wilkinson, and S. G. Roberts, “Mechanical properties of ion-implanted tungsten–5 wt% tantalum,” *Phys. Scr.*, vol. 2011, no. T145, p. 14076, Dec. 2011.

[10] J. Gibson, D. Armstrong, and S. Roberts, “The micro-mechanical properties of ion irradiated tungsten,” *Phys. Scr.*, vol. 2014, no. T159, pp. 1–3, Apr. 2014.

[11] D. E. J. Armstrong, X. Yi, E. A. Marquis, and S. G. Roberts, “Hardening of self ion implanted tungsten and tungsten 5-wt% rhenium,” *J. Nucl. Mater.*, vol. 432, no. 1–3, pp. 428–436, Jan. 2013.

[12] G. S. Was, *Fundamentals of radiation materials science: metals and alloys*. New York: Springer, 2007.

[13] G. S. Was and T. R. Allen, *Radiation Damage From Differeant Particle Types*. Springer, 2007.

[14] J. C. He, A. Hasegawa, and K. Abe, “Effects of transmutation elements on the defect structure development of W irradiated by protons and neutrons,” *J. Nucl. Mater.*, vol. 377, no. 2, pp. 348–351, 2008.

[15] T. Tanno, A. Hasegawa, J.-C. He, M. Fujiwara, S. Nogami, M. Satou, T. Shishido, and K. Abe, “Effects of Transmutation Elements on Neutron Irradiation Hardening of Tungsten,” *Mater. Trans.*, vol. 48, no. 9, pp. 2399–2402, 2007.

[16] D. E. J. Armstrong, X. Yi, E. A. Marquis, and S. G. Roberts, “Hardening of self ion implanted tungsten and tungsten 5-wt% rhenium,” *J. Nucl. Mater.*, vol. 432, no. 1–3, pp. 428–436, Jan. 2013.

[17] J. F. Ziegler, J. P. Biersack, and U. Littmark, “The Stopping and Range of Ions in Solids.” Pergamon, New York, 1985.

[18] Q. Xu, T. Yoshiie, and H. C. Huang, “Molecular dynamics simulation of vacancy diffusion in tungsten induced by irradiation,” *Nucl. Instruments Methods Phys. Res. Sect. B Beam Interact. with Mater. Atoms*, vol. 206, pp. 123–126, May 2003.

[19] A. Khan, R. Elliman, C. Corr, J. J. H. Lim, A. Forrest, P. Mummery, and L. Evans, “Effect of Rhenium Irradiations on the Mechanical Properties of Tungsten for Nuclear Fusion Applications,” *J. Nucl. Mater.*, vol. 477, pp. 42–49, 2016.

[20] D. E. J. Armstrong and T. B. Britton, “Effect of dislocation density on improved radiation hardening resistance of nano-structured tungsten-rhenium,” *Mater. Sci. Eng. A*, vol. 611, pp. 388–393, 2014.

[21] D. E. J. Armstrong, X. Yi, E. A. Marquis, and S. G. Roberts, “Hardening of self ion implanted tungsten and tungsten 5-wt% rhenium,” *J. Nucl. Mater.*, vol. 432, no. 1–3,

pp. 428–436, Jan. 2013.

[22] T. Tanno, M. Fukuda, S. Nogami, and A. Hasegawa, “Microstructure Development in Neutron Irradiated Tungsten Alloys,” *Mater. Trans.*, vol. 52, no. 7, pp. 1447–1451, 2011.

[23] J. Knaster, A. Moeslang, and T. Muroga, “Materials research for fusion,” *Nat. Phys.*, vol. 5, no. 2, pp. 77–80, 2016.

[24] M. R. McGurk and T. F. Page, “Using the P-δ2 analysis to deconvolute the nanoindentation response of hard-coated systems,” *J. Mater. Res.*, vol. 14, no. 06, pp. 2283–2295, 1999.

[25] E. R. Anderson and E. A. Marquis, “A snapshot of the microstructural evolution of Alloy 800H under heavy ion irradiation,” Poster, SMINS4 2016 conference, 2016.

[26] A. Al-Ajlony, J. K. Tripathi, and A. Hassanein, “Role of carbon impurities on the surface morphology evolution of tungsten under high dose helium ion irradiation,” *J. Nucl. Mater.*, vol. 466, pp. 569–575, 2015.

[27] A. S. Kurlov and A. I. Gusev, “Tungsten carbides and W-C phase diagram,” *Inorg. Mater.*, vol. 42, no. 2, pp. 121–127, 2006.

[28] E. R. Anderson, “Private Conversation.” 2016.

[29] Université de Sherbrooke, “CASINO,” 2007. [Online]. Available: http://www.gel.usherbrooke.ca/casino/download2.html. [Accessed: 14-Jan-2016].

8 Discussions and Conclusions

The original aim of the project as discussed in Chapter 2 is given below and Figure 8.1 is a re-presentation of Figure 2.56 from Chapter 2, giving an overview of the project.

The aim of this project is to study aspects of degradation of W arising from the products of the D-T reaction.

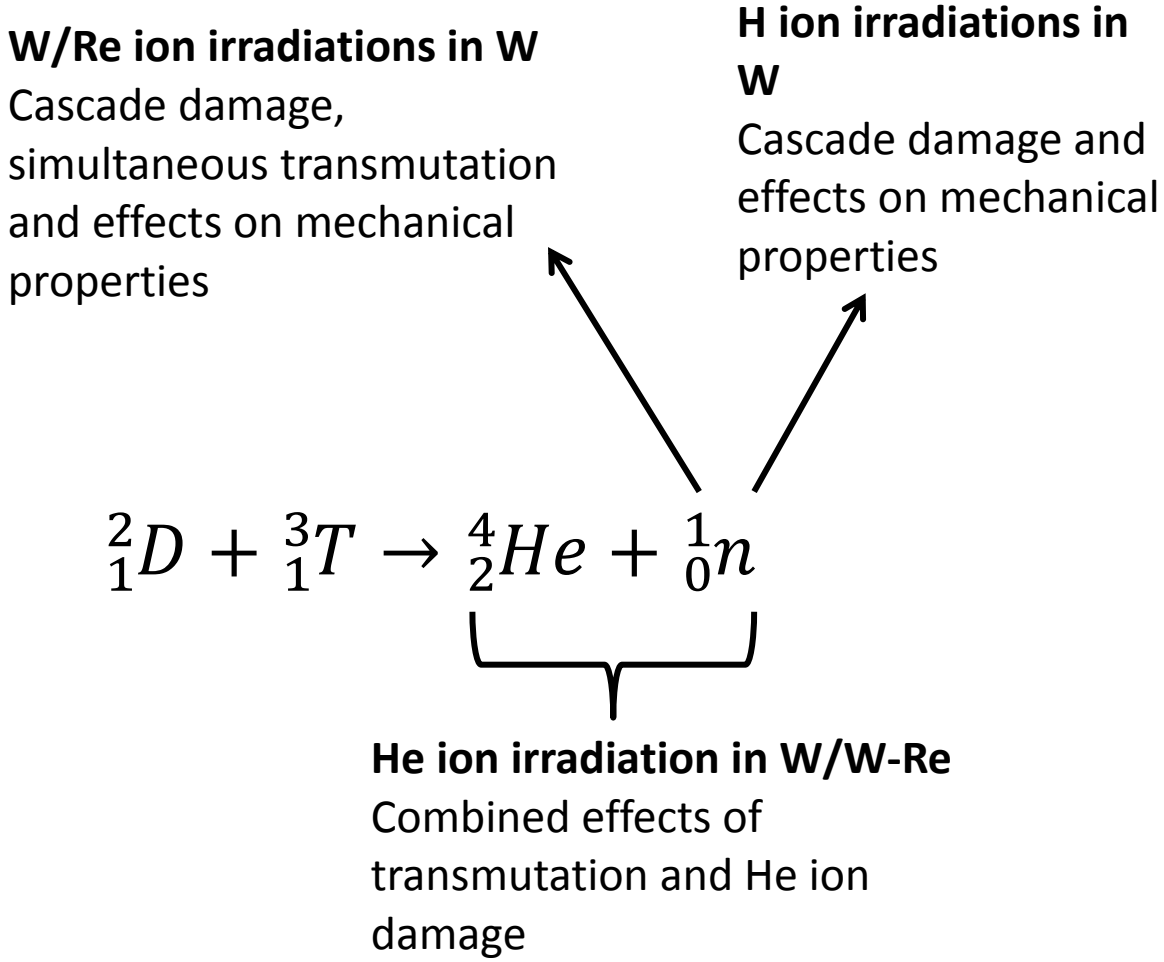

Figure 8.1: Overview of project

This thesis focussed on investigating different techniques for mimicking the degradation in W expected from the D-T fusion reaction, including neutron displacement cascade damage, transmutation effects and impinging helium ions. Magnum and Pilot-PSI linear plasma devices were used to study the effect of

impinging helium ions on tungsten-rhenium alloys, which acted as a proxy for the transmutation caused by 14 MeV fusion neutrons. Displacement damage and transmutation to low levels (1600 appm) was mimicked simultaneously by utilising the tandem accelerator at ANU to irradiate tungsten samples with rhenium ions, using tungsten ion irradiation as a comparison. Displacement damage was also mimicked by using the tandem accelerator at Notre Dame University to conduct proton irradiation at temperatures of 400 and 800 °C.

In this chapter the results from the experiments conducted in order to study degradation in W relevant to fusion will be discussed and compared to previous findings in the literature that have been covered in detail in Chapter 2.

8.1 Discussions

Firstly the results from Chapters 4 and 5 are considered, which investigated the effect of Re addition on the growth of fuzz in W. In these chapters, W-3%Re and W-5%Re alloys were used to simulate transmutation that would occur in W due to the 14 MeV neutrons generated in the D-T reaction. According to Gilbert and Sublet, after five years of DEMO operation, the concentration of Re could reach 3.8%Re [133]. Therefore concentrations of 3 and 5%Re provided a good simulation of transmutation effects. As discussed in Chapter 2, there was a hint in the literature that Re had been seen to inhibit fuzz growth in W. However, the W-Re alloys in the literature had a different manufacturing history to the pure W they were compared to [221]. Therefore due to the fact Re is a transmutation product, and additionally fuzz growth had also been observed on pure Re samples [263], it was important to determine if Re really was inhibiting fuzz growth.

Two experiments were carried out in Chapter 4, using both the Magnum and Pilot-PSI LPDs. In Magnum PSI exposures were carried out for durations of 40-200 s at

temperatures of ~970 °C. In Pilot-PSI, 400 s exposures were carried out at ~ 1400 °C. In both cases pulsed exposures were carried out due to limitations of cooling in the LPDs. In the Magnum-PSI experiments the pulses were 10 s in duration, and in Pilot-PSI, they were 100 s in duration.

In the shorter exposures, qualitative surface analysis revealed an orientation dependence of fuzz growth. Fuzz grew in different direction and the shape of the tendrils varied in different grains. As mentioned in Chapter 4, orientation dependence is something that has been extensively observed [270], [271], particularly during the early stages of fuzz growth [239]. Yamagiwa *et al.* [270] suggested that orientation dependence observed during early stages of fuzz growth was due to differences in the diffusion of He in different orientations. Ohno *et al.* [271] suggested the importance of the angle between the {101} slip face and the plane of the grain under exposure effected the formation of a wavy structure seen as a precursor to fuzz formation. Ideally EBSD should have been carried out in order to determine which grains were more likely to grow fuzz, and this is something that could be carried out as further work. EBSD could be carried out on cross sections across several grains in order to determine which grains are more likely to grow fuzz.

In the 400 s exposures, there was an indication that the addition of Re was indeed having an inhibiting effect on fuzz growth. Typically fluences of ~ 1×10^{27} m^{-2} were achieved in the 400 s of exposure. The fuzz thicknesses observed were between ~0.5-2.3 μm. Using the thickness of the pure W sample, the growth equation developed by Petty *et al.* ($x(\Phi) = (C(\Phi - \Phi_0))^{\alpha}$) was solved for C [207]. The C value determined was an order of magnitude lower than that determined by Petty for temperatures of 1047 °C. The temperatures used in this experiment were ~1400 °C.

This indicated that at these temperatures annealing processes were having an impact. Annealing has been observed at lower temperatures than those used in this experiment, and therefore it is likely that this had an impact on the fuzz growth [230]. Additionally, though not considered here, recrystallization could have had an impact on the results [231]. There no longer appeared to be a visible orientation dependence by just analysing the surface of the samples, which is in agreement with the literature, where it is suggested that orientation dependence of fuzz growth is only significant during early stages [239]. In the FIB cross sections that were carried out in the samples, the fuzz layer thickness was fairly uniform, however it would have been beneficial to make cross sections across several orientations within the same region in order to confirm the fact that orientation no longer had an impact.

In Chapter 5, in order to remove the effect of annealing and perhaps recrystallization, further He plasma exposures were carried out in Pilot-PSI, this time at temperatures of ~1025 °C. Exposures were carried out for continuous durations of 800, 1600 and 3200 s. As has been observed in the literature, there can be a difference between fuzz growth following a pulsed exposure or a continuous one [253], but this is mostly noticeable if there is an extended period of time of the order of hours between pulses. In the case of the experiments in Chapter 4, the time between pulses was of the order of minutes, so it is assumed that the effect is negligible. In this study mass loss measurements were also conducted, which revealed that low levels of erosion can occur even below the sputtering threshold of W to He. It is suggested that this is due to impurity species in the plasma, where there is a lower sputtering threshold. This is in agreement with previous work by Petty *et al.* [207], where sputtering from impurities had been discussed.

In this study, the fluences achieved were between 0.5-6.2×10^{26} m^{-2}. Generally Re was seen to inhibit fuzz growth. It is extremely difficult to elucidate a mechanism by which Re is inhibiting fuzz growth, particularly as discussed in Chapter 2, there are so many mechanisms that have been suggested to explain fuzz growth. The one thing that was found to be in common in the majority of the mechanisms discussed in Chapter 2, whether experimental or physics based, was that bubbles are a necessary prerequisite for fuzz growth [203], [220], [260], [262], [263], [267], [268]. Several possible reasons why Re may be inhibiting fuzz growth were discussed. It was suggested that reasons for the inhibitory effect of Re on fuzz growth could be due to inhibition of **b**=1/2⟨111⟩ loop motion [143]. This is something that has been observed by Yi *et al.* [143] in self-ion irradiated W-5%Re. Many models explain bubble growth in the fuzz formation mechanism to occur via loop punching, with Kobayashi *et al.* specifically mention that the edge dislocation making up the loop has **b**=1/2⟨111⟩ [305]. Therefore it was suggested that the slower **b**=1/2⟨111⟩ loop motion in the Re alloys could result in a reduced rate of bubble growth, and therefore an increased time before the bubbles can burst, and consequently form fuzz (bubble bursting has been suggested as part of the mechanism of fuzz formation by Takamura *et al*. [263]). Additionally it was suggested that as Re has been shown to ductilise W [117], and bubble growth occurs via a plastic deformation process, that the bubbles could grow more before bursting. As the bursting of bubbles has been suggested to be the part of the experimentally observed mechansim where tendrils of fuzz are formed [263], if the bubbles are slower to burst, fuzz may be slower to form.

As mentioned, these are just suggestions and to fully elucidate a mechansim of Re inhibition, TEM would be required to find the microstructural explanations for reduced fuzz growth.

In addition to looking at the effect of Re addition on fuzz growth, Chapter 5 also considered the variation of fuzz growth with flux and fluence, and comapred this to several previous experiments in other LPDs and a magnetron device ([207], [219], [221], [222], [232], [233]). It was very interesting to see that all the fuzz thicknesses measured during the Pilot-PSI experiments lay below those achieved in the other devices at similar fluences and temperatures, as well as below the expected values predicted by the growth equation developed by Petty *et al.* [207]. Petty *et al* had suggested that there is an incubation fluence before fuzz growth can occur, however the data from the experiment in Pilot-PSI gave further evidence for an incubation time; something that had been previously suggested by Baldwin *et al.* [249]. The fluxes used in Pilot-PSI were typically higher than those used in the rest of the literature and therefore the same fluences were achieved in a shorter time. Therefore, especially for the shorter exposures, the incubation time would not have been exceeded by a sufficient amount, in order to achieve the higher levels of fuzz growth that had been achieved at the same fluences in other devices. This is in agreement with the data from the magnetron, which seem to follow a $\Phi^{1/2}$ relationship, rather than the incubation fluence fit that the other literature data from LPDs seems to follow [253]. The data from the magnetron is achieved using fluxes at least an order of magnitude lower than the lowest fluxes used in LPDs. This means that even to achieve fluences less than the incubation fluence, exposure times of hours are required, rather than minutes as typically the case in LPDs. Therefore, any incubation time is significantly exceeded even at lower fluences in a magnetron, resulting in thicker fuzz layers than could be achieved at higher fluxes. The magnetron and Pilot-PSI data are essentially at the two extremes of flux in the data, and both of these suggest there is an incubation time.

In Chapter 6, methods of predicting the effects arising from the 14 MeV neutron product of the D-T reaction were investigated. Previous neutron irradiation experiments in the JOYO fast reactor [67], [134], [162] had revealed that the mechanism of hardening differed, whether the starting material was pure W, as opposed to a W-Re alloy, with a void formation mechanism being dominant in the original pure W material. The addition of Re prior to irradiation supressed the formation of voids and a precipitation mechanism was dominant, with the formation of σ and χ phases [67], [134], [162]. In order to mimic the transmutation and displacement damage expected from the 14 MeV neutrons, Armstrong *et al.* carried out W ion irradiations in W-5%Re, up to doses of 33 dpa and at temperatures of 300 °C [145]. At high doses above 13 dpa, clustering of Re was observed via atom probe, which it was suggested could be a precursor to σ phase tungsten that had been observed during the neutron irradiations. The results from these ion irradiations appear to match up with findings from neutron irradiations, in that the apparent precursors to precipitate formation are seen when W-Re is the starting material. In neutron irradiation experiments carried out by Tanno *et al.* [67], [134], [162], irradiation hardening in pure W, driven by a void formation mechanism was observed to saturate above doses of ~1 dpa. In the W-Re samples, where the precipitation formation mechanism is dominant there is no apparent saturation in irradiation hardening. Similar trends are seen in the W ion irradiations carried out by Armstrong *et al.* [145]. In the W ion irradiations carried out by Armstrong *et al.*, a saturation of irradiation hardening was also observed in pure W, this time at ~0.4 dpa. In W-5%Re with a low dislocation density there was no saturation in irradiation hardening, and the hardness continued to increase with dose. It should be noted that

microstructure is extremely important, and that Armstrong and Briton observed saturation of irradiation hardening in W-5%Re with a high dislocation density [180].

In order to see whether the addition of Re during ion irradiation, as opposed to self-ion irradiation in W had an impact on hardening, samples of as-received and annealed W were irradiated with either W or Re ions to doses of ~40 dpa and ~1600 appm. This allowed for two different microstructures to be analysed. Despite the fact that the concentration of Re added to the materials is relevant to end of ITER operation, and also to some regions of a DEMO reactor, there is a difference in the appm/dpa ratio. Although there is no specific data for the dose in specific regions of the divertor, there is for region A of the first wall armor in a DEMO model (refer to Figure 2.10), as well as transmutation information [33]. This predicts an appm/dpa ratio of 460 appm/dpa [33]. This is higher than what was achieved in the experiment in Chapter 6 of ~40 appm/dpa. However, it was not feasible to achieve a higher ratio, as in order to implant Re, by default displacements will occur as the Re acts a PKA. This means that this technique may not be suitable for implanting larger quantities of Re, as by default displacements will be created.

The data comparing the hardness increase in the W and Re irradiated material, showed that the difference between the two types of implanted ion were negligible at the doses employed. It was suggested that due to the fact the mass of W and Re is similar; the two implanted ions will cause similar damage cascades.

The difference in hardness increase observed in the as-received and annealed samples was in agreement with the work by Armstrong and Britton [180]. The % hardness increase observed in the annealed samples was much greater than that observed in the as-received samples. As had previously been suggested by

Armstrong and Britton, areas of high dislocation density can act as sinks, where point defects can recombine, resulting in a reduced rate of hardening. It is also consistent with other findings in the literature where both as-received and recrystallized W was irradiated with Fe ions [306]. The hardness increase was greater in the recrystallized material, in comparison to the as-received material; which it was suggested due to the grain boundary area being higher in the as-received material. The grain boundaries acted as sinks, resulting in increased recombination of defects and therefore a less significant hardness increase in the as-received material in comparison to the annealed.

Through quantitative analysis of EBSD pole figures, it had initially appeared that there may be some kind of orientation dependence of the irradiation damage due to a degradation of image quality with reduced accelerating voltage. However, quantitative analysis of the samples revealed that this was not the case, and as the sample was textured it would be beneficial to repeat the experiments with a fully recrystallized texture or to conduct EBSD analysis in the cross section of the material to get a greater variety of orientations to study.

Chapter 7 then focused on the use of proton irradiations as a proxy for fusion neutron damage. As discussed in Chapter 2, there is a suggestion from the literature, that despite the fact that proton damage cascades are much more widely spaced out and smaller than those of neutrons, that the hardness increase observed in proton irradiations is only ~10% lower than that observed in neutron irradiations at similar conditions [185]. This is in contrast to heavy ion irradiations, such as those conducted in Chapter 6. In heavy ion irradiations, it has been observed in the literature that at doses of 0.4 dpa, there is a 60% decrease in the hardness increase observed in ion irradiated material in comparison to neutron irradiated material [25],

[67], [68], [145]. The displacement cascade induced by heavy ions is more similar to neutron irradiation cascades, as the heavy ions act as a PKA and cause dense cascades. Whereas the cascades induced by protons are smaller and more spaced out. This means that during the cooling phase there is more recombination in the denser cascades induced by heavy ions in comparison to the smaller and less dense proton cascades [130]. Additionally the penetration depth of proton irradiations is typically higher than heavy ion irradiations [130]. The increased recombination in the heavy ion irradiations and the smaller damage volume could be contributing to the hardness increase being so much lower than equivalent neutron irradiation experiments.

The results in Chapter 7 give further evidence for an increased hardness induced by proton irradiations in comparison to heavy ion irradiations. The hardness increases for the irradiations carried out at 400 °C at ~ 2 dpa are significantly greater than those observed at the same temperature at ~40 dpa in the W an Re irradiated material in Chapter 6. The method to calculate the dpa for the protons was via Kinchin Pease, whereas for the heavy ions the full damage calculations method was utilised in SRIM [121]. Nevertheless, even if the full damage calculations are used for the proton irradiations, the dose in terms of dpa is still higher in the heavy ion irradiated material, in comparison to the proton irradiated material. It should be noted that the beam for the heavy ion irradiations was raster scanned across the sample, whereas for the proton irradiations a defocussed beam was used, which also makes direct comparison difficult. Localised fluxes in raster scanning can influence the mechanism of damage, and annealing of damage can occur while the sample is not under irradiation [130]. This means that the rate of defect production is typically higher in a defocused beam in comparison to a raster-scanned beam [130]. However, this was not investigated in this thesis. In the W and Re ion irradiated as-received

material there was ~13% increase in hardness and in the annealed material there was ~23% increase in hardness. This is in comparison to a 29% and 48% increase in hardness in the as-received and annealed proton irradiated material at the same temperature. There were significantly different damage profiles in both sets of irradiations. In the heavy ion irradiations there was an ~150 nm wide damage peak caused by the multiple energies used, and the peak penetration depth was ~ 500 nm. In the proton irradiated material, a single energy was utilised and the damage profile was fairly uniform between 0.5-3 μm and a large Bragg peak of ~15 dpa was observed at ~5.5 μm. Additionally, the hardness measurements were taken from different regions of the samples. For the heavy ion irradiated material, the hardness was measured in the first 50-200 nm, compared to 500-1800 nm in the proton irradiated material. Nanoindentation data is influenced by the substrate material [145], [307], and therefore as there is a significantly larger volume of irradiated material in the proton sample this could also contribute to the higher hardness increases observed. Another factor that could contribute to the greater hardness increase observed in the proton irradiations, is the fact that in proton irradiations there is less recombination of defects in comparison to heavy ion irradiations [130].

In terms of the irradiation response of the as-received and annealed material, a similar response is seen in the proton irradiated material, as to that observed in the heavy ion irradiated material. There is a greater hardness increase observed in the annealed material in comparison to the as-received. In the proton irradiated material the ratio between the raw hardness increase in the annealed and as-received and annealed material at 400 °C is ~1.4, which is similar to both the W and Re irradiated materials, where the ratio is ~ 1.7.

If the irradiations at 400 °C are specifically considered, they can be compared to the previous proton irradiations in the literature by He. *et al.* [185]. He *et al.* carried out 1 MeV proton irradiations at 500 °C, resulting in a dose of ~0.15 dpa at a depth of 2μm into the surface. The shape of the damage profile was similar to that achieved in the experiments in Chapter 7, with a Bragg peak at ~5.5 μm. However, the doses achieved by He *et al.* were much lower. It is difficult to directly compare the data, as no information about the starting microstructure of the W used for the 0.15 dpa irradiations carried out by He *et al.* is given. Additionally, Vickers hardness testing was used by He *et al.* in order to obtain the hardness measurements, which has been converted to GPa for comparison. The hardness increase in the as-received sample is very similar to that observed in the 0.15 dpa irradiations, with the increase in the annealed material ~0.6 GPa greater than the other two samples. Therefore it is again shown that while dose is an important parameter, the initial microstructure of a material is crucial when looking at irradiation damage.

In the 800 °C proton irradiations, tungsten carbide formation was observed in the annealed material and extensive surface roughening, suggested to be due to sputtering was seen in the as received material. It is interesting that the carbide formation has only been observed in the irradiations at 800 °C. Recently carbon contamination is something that has been observed to be a problem in ion irradiation experiments, despite the vacuum environment [237], [308], [309] and this something that was discussed in detail at the SMINS4 2016 conference. Several avenues are being considered as to the source of contamination, which include contamination of the source, contamination of the chamber and also redistribution of carbon in the material [310]. It is suggested that in the case of the proton irradiation experiment carried, it is unlikely that there is carbon contamination from the source, due to the

fact pure hydrogen gas was utilised, and additionally the momentum/charge ratio of the ions was analysed. Redistribution of carbon in the material is a possibility. Despite the fact an oil free pumping system and o-ring free vacuum systems were used, it is also possible that organics were released from surrounding material in the beamline, and the beam deposited the carbon onto the sample. Considering the low amount of C likely to be present as an impurity and the 800 °C temperature used; from the W-C phase diagram it is not clear that tungsten carbide should form from the temperature alone [311]. The energy deposited from the irradiation itself could contribute to the carbide formation. This would explain why the carbides were only observed in the irradiated region and not in the region of the sample that was not exposed to the proton beam. Furthermore, the temperature would be higher in the irradiated area. The carbide formation varied from grain to grain. Carbon contamination is an important issue that is only recently being discussed and requires significant investigation.

In the as-received material irradiated at 800 °C, in addition to the surface roughening observed, there was also cracking seen on the nanoindents. This suggests that the surface of the sample is brittle. Although carbides are not observed on the SEM, it could be that there are some present that may only be observable through TEM techniques.

8.2 Conclusions

The original aim of this thesis as highlighted in Figure 8.1 was to study the degradation of W from the products of the D-T reaction. The three areas of specific investigation identified were:

- The effect of Re on the growth of fuzz in W exposed to He plasmas.

- Investigating the use of Re as an implanted species in ion irradiations as opposed to an alloying element.
- Further investigation of the response of W to proton irradiations.

This has been attempted through various irradiation techniques:

- Low energy, high flux He ion irradiations in LPDs
- W and Re ion irradiations in a tandem accelerator.
- Proton irradiation in a tandem accelerator.

In the study of Re addition on the fuzz formation mechanism, it was found that at exposure lengths greater than 400 s (corresponding to fluences between ~0.5-10×10^{26} m^{-2}), Re addition was observed to generally inhibit fuzz formation. This was in agreement with previous findings in the literature [221]. It was suggested that this could be due to the increased ductility of W-Re over W. Additionally, inhibition of $\mathbf{b}=1/2\langle111\rangle$ loop motion by Re could slow loop punching which may result in a reduction in the speed of bubble growth. Additionally a key new finding was that the incubation fluence theory suggested in the literature [207], may not hold at all fluxes, and the importance of the incubation time theory was confirmed via the analysis of the high flux exposures. The theory of incubation time was in agreement with fuzz growth in a magnetron in the literature [222], [253].

The comparison of Re and W ion irradiations in as-received and annealed W showed a negligible difference between the two types of irradiation. A higher hardness increase was observed in annealed W, in comparison to as-received W. It was suggested that this was due to the fact that grain boundaries act as sinks, and as there is a smaller grain boundary area in the annealed material, there is an increased hardness increase.

The proton irradiations in as-received and annealed W showed the same relationship, in that the hardness increase was greater in the annealed material. The hardness increase observed in the proton irradiated material was greater than that seen in the heavy ion irradiated material. It was suggested this could be due to the larger volume of irradiated material in the proton irradiated material influencing the hardness measurements. Carbide formation was seen as an issue in irradiations at 800 °C, and it was suggested they could form as a result of carbon contamination from components in the beamline.

The damage mechanism in all three processes used are quite different, however there are some common conclusions that can be drawn from the combined data, in addition to the individual conclusions made at the end of each chapter.

Firstly, regardless of the irradiation damage mechanism, starting microstructure and defect densities have been of vital importance when investigating irradiation damage. Ideally, this thesis should have conducted more detailed microstructure studies before and after irradiations in all chapters in order to quantitatively determine the impact of grain orientation, size and defect density concentrations on the damage mechanisms. Specifically, it would have been beneficial to conduct EBSD before and after the low energy He ion irradiations to determine which grains were more prone to fuzz growth.

Impurity contamination is also something that has been observed in both the low energy He ion irradiations, as well as the high energy irradiations. In the case of the LPDs, sputtering due to impurities in the plasma was observed. For the proton irradiations, carbide formation was observed at 800 °C. In the heavy irradiations, although no impurities were measured, there was degradation in EBSD pole figure

image quality with reduced accelerating voltage. This could be due to impurities during the irradiation resulting in the formation of some kind of surface layer, although this has not been specifically measured. This is in agreement with recent findings and discussion of carbon contamination and sputtering from impurities in ion irradiation experiments and LPDs [207], [237], [308], [309].

In summary, all three methods have been used effectively to look at the degradation of W that could be possible in a fusion environment. This has gone towards addressing the aims of the project. The low energy irradiations were used to successfully confirm the inhibitory effect of Re on fuzz growth and additionally provide evidence for the incubation time theory. The heavy ion irradiations revealed that at the low concentration of 1600 appm, the addition of Re had a negligible effect on the mechanical properties of W. Although the concentration of Re implanted was relevant to ITER or DEMO, it should be noted that the appm/dpa ratios used were lower than those expected in ITER or DEMO. The proton irradiations showed a higher hardness increase in comparison to heavy ion irradiations, although there are some problems with direct comparison as previously discussed. The importance of starting microstructure was also shown in both ion irradiation experiments. Impurity contamination was seen as an issue in all three methods. All three methods are valid techniques to predict the performance of W in a fusion reactor. In the absence of a designated fusion materials testing facility it is vital that a combination of such techniques continue to be used.

8.3 Further Work

It has been noted in the literature, and additionally observed in the shorter duration plasma exposures in Magnum-PSI in Chapter 4 that during the initial stages, fuzz growth is orientation dependent. This is not something that was investigated in detail

within this thesis, and therefore analysis of orientation dependence of fuzz growth is important, in order to determine which orientations are more prone to fuzz formation. This can be achieved by conducting EBSD over irradiated areas prior to exposure, or additionally by making a cross section and doing EBSD in the cross section below the region of fuzz growth.

Furthermore, as displayed in Chapter 2, there is still much debate about the mechanism of fuzz growth. Carrying out TEM analysis of different stages of fuzz growth could help towards elucidating the mechanism. In-situ TEM analysis of low energy He ion irradiated material could also help to confirm the mechanism of growth. Additionally if carried out in W-Re samples, it could confirm the method by which Re was inhibiting fuzz growth.

One of the proposed mechanisms as to why Re inhibited fuzz growth was due to its increased ductility over W. However, as had been extensively reported in the literature, this increased ductility only holds in material irradiated up to ~0.4 dpa [25], [67]–[69]. Therefore, if ductility is a property that affects the fuzz growth mechanism, then it is important to also investigate fuzz growth in neutron irradiated W and W-Re, to see if Re has an inhibiting effect. Additionally, generally depending on the dose in the neutron irradiated sample, the mechanism of fuzz formation may vary in comparison to non-irradiated material.

Chapter 5 also provided some evidence for the incubation time theory for fuzz growth, as opposed to an incubation fluence. In order confirm this, further high flux plasma exposures should be carried out across a wider range of fluences. It would also be important to carry out fuzz growth experiments across a wider range of fluences in W-Re alloys, to see if the inhibitory effect was still visible.

In terms of the heavy ion irradiations, it would be beneficial to conduct detailed analysis via TEM in order to elucidate whether any coating has formed on the surface. Additionally the proton irradiation experiments at 800 °C should be repeated. This could provide improved data about the effect of higher temperatures on the response of W to proton irradiation hardening. Also, if contamination was to occur again, this could help to confirm the source.

It would also be important to conduct heavy ion and proton irradiations to the same dose, and then take hardness measurements in the cross section, so that indentations to the same depth can be carried out, and the effect of the irradiated bulk beneath the indent will be the same. In order to do this, higher energy heavy ion irradiations would be required, so as to achieve a wider damage profile that could be indented in a cross section. It should be attempted to achieve doses and temperatures in both cases that are close to those used in recent neutron irradiation experiments in the literature [67], [68], [119], [134], [158]–[164]. This would allow a direct comparison to be made and it can be determined whether ion or proton irradiations can provide data closer to that seen in neutron irradiation experiments. It is important to note that in both the heavy ion and proton irradiation cases, a raster scanned beam should be utilised, so as to allow direct comparison between the results. It would be important to also use similar stating microstructures to those used in the neutron irradiation experiments.

As has been observed in the literature, and confirmed in the experiments in Chapters 6 and 7, the starting microstructure is very important when conducting irradiation experiments. Armstrong and Britton [180] observed in the literature a difference in the response to W ion irradiation in an as-received and annealed W-5%Re sample. The hardness increase saturated with dose in the as-received sample, but continued

to increase with the annealed one. These are two quite different responses, and therefore to truly predict the degradation of tungsten for fusion applications, it is extremely important that future studies are also conducted on the exact microstructure that will be used in ITER and beyond.

References

[1] R. A. Pitts, S. Carpentier, F. Escourbiac, T. Hirai, V. Komarov, S. Lisgo, A. S. Kukushkin, A. Loarte, M. Merola, A. Sashala Naik, R. Mitteau, M. Sugihara, B. Bazylev, and P. C. Stangeby, "A full tungsten divertor for ITER: Physics issues and design status," *J. Nucl. Mater.*, vol. 438, pp. S48–S56, Jul. 2013.

[2] ITER Organization, "ITER- Science - ITER Goals," 2016. [Online]. Available: https://www.iter.org/sci/Goals. [Accessed: 17-Mar-2016].

[3] ITER Organization, "ITER-For The Press-Facts and Figures," 2016. [Online]. Available: https://www.iter.org/factsfigures. [Accessed: 20-Apr-2016].

[4] EFDA, "Fusion Electricity A roadmap to the realisation of fusion energy," 2012.

[5] BP, "Energy Economics," 2016. [Online]. Available: http://www.bp.com/en/global/corporate/energy-economics/energy-outlook-2035/carbon-emissions.html. [Accessed: 14-Oct-2016].

[6] J. E. Bistline and V. Rai, "The role of carbon capture technologies in greenhouse gas emissions-reduction models: A parametric study for the U.S. power sector," *Energy Policy*, vol. 38, no. 2, pp. 1177–1191, 2010.

[7] World Energy Council, "Energy Trilemma Index," 2015. [Online]. Available: https://www.worldenergy.org/data/trilemma-index/. [Accessed: 16-Mar-2016].

[8] C. L. Smith and S. Cowley, "The path to fusion power.," *Philos. Trans. A. Math. Phys. Eng. Sci.*, vol. 368, no. 1914, pp. 1091–1108, Mar. 2010.

[9] Nuclear Energy Institute, "Why Nuclear Energy," 2016. [Online]. Available:

http://www.nei.org/Why-Nuclear-Energy/Value-of-Electricity-Diversity. [Accessed: 14-Oct-2016].

[10] D. Fasel and M. Q. Tran, “Availability of lithium in the context of future D-T fusion reactors,” *Fusion Eng. Des.*, vol. 75–79, pp. 1163–1168, 2005.

[11] C. Llewellyn Smith and D. Ward, “Fusion,” *Energy Policy*, vol. 36, no. 12, pp. 4331–4334, Dec. 2008.

[12] T. Abram, “Reactor Physics MACE 21132,” University of Manchester, 2011.

[13] HyperPhysics, “Nuclear Binding Energy,” 2016. [Online]. Available: http://hyperphysics.phy-astr.gsu.edu/hbase/nucene/nucbin.html. [Accessed: 10-Aug-2016].

[14] ITER Organization, “What is Fusion?,” *2016*. [Online]. Available: https://www.iter.org/sci/whatisfusion. [Accessed: 11-Jul-2016].

[15] ITER Organization, “Fuelling the Fusion Reaction,” 2016. [Online]. Available: https://www.iter.org/sci/fusionfuels. [Accessed: 11-Jul-2016].

[16] EUROfusion, “JET’s main features,” 2016. [Online]. Available: https://www.euro-fusion.org/jet/jets-main-features/. [Accessed: 15-Jul-2016].

[17] M. Shimada, D. J. Campbell, V. Mukhovatov, M. Fujiwara, N. Kirneva, K. Lackner, M. Nagami, V. D. Pustovitov, N. Uckan, J. Wesley, N. Asakura, A. E. Costley, A. J. . Donné, E. . Doyle, A. Fasoli, C. Gormezano, Y. Gribov, O. Gruber, T. C. Hender, W. Houlberg, S. Ide, Y. Kamada, A. Leonard, B. Lipschultz, A. Loarte, K. Miyamoto, V. Mukhovatov, T. H. Osborne, A. Polevoi, and A. C. C. Sips, “Chapter 1: Overview and summary,” *Nucl.*

Fusion, vol. 47, no. 6, pp. S1–S17, 2007.

[18] EFDA, "A conceptual study for commercial fusion power plants. Final Report of the European Fusion Power Plant Conceptual Study (PPCS)," 2005.

[19] N. Balshaw, "All-the-World's Tokamaks," 2015. [Online]. Available: http://www.tokamak.info/. [Accessed: 19-May-2016].

[20] Culham Centre for Fusion Energy, "CCFE- Fusion Energy- The Tokamak," 2016. [Online]. Available: http://www.ccfe.ac.uk/tokamak.aspx. [Accessed: 17-Mar-2016].

[21] ITER Organization, "The ITER Tokamak/Cryostat," 2016. [Online]. Available: https://www.iter.org/mach/cryostat. [Accessed: 14-Jul-2016].

[22] ITER Organization, "The ITER Tokamak/Magnets," 2016. [Online]. Available: https://www.iter.org/mach/magnets. [Accessed: 14-Jul-2016].

[23] ITER Organization, "The ITER Tokamak/Vacuum Vessel," 2016. [Online]. Available: https://www.iter.org/mach/vacuumvessel. [Accessed: 14-Jul-2016].

[24] ITER Organization, "The ITER Tokamak/Blanket," 2016. [Online]. Available: https://www.iter.org/mach/blanket. [Accessed: 14-Jul-2016].

[25] R. G. Abernethy, "Predicting the performance of tungsten in a fusion environment: a literature review," *Mater. Sci. Technol.*, pp. 1–12, 2016.

[26] ITER Organization, "The ITER Tokamak/Divertor," 2016. [Online]. Available: https://www.iter.org/mach/divertor. [Accessed: 14-Jul-2016].

[27] M. Merola, F. Escourbiac, A. R. Raffray, P. Chappuis, T. Hirai, and S. Gicquel, "Engineering challenges and development of the ITER Blanket

System and Divertor," *Fusion Eng. Des.*, vol. 96–97, pp. 34–41, 2015.

[28] M. Rieth, S. L. Dudarev, S. M. Gonzalez de Vicente, J. Aktaa, T. Ahlgren, S. Antusch, D. E. J. Armstrong, M. Balden, N. Baluc, M.-F. Barthe, W. W. Basuki, M. Battabyal, C. S. Becquart, D. Blagoeva, H. Boldyryeva, J. Brinkmann, M. Celino, L. Ciupinski, J. B. Correia, A. De Backer, C. Domain, E. Gaganidze, C. García-Rosales, J. Gibson, M. R. Gilbert, S. Giusepponi, B. Gludovatz, H. Greuner, K. Heinola, T. Höschen, A. Hoffmann, N. Holstein, F. Koch, W. Krauss, H. Li, S. Lindig, J. Linke, C. Linsmeier, P. López-Ruiz, H. Maier, J. Matejicek, T. P. Mishra, M. Muhammed, A. Muñoz, M. Muzyk, K. Nordlund, D. Nguyen-Manh, J. Opschoor, N. Ordás, T. Palacios, G. Pintsuk, R. Pippan, J. Reiser, J. Riesch, S. G. Roberts, L. Romaner, M. Rosiński, M. Sanchez, W. Schulmeyer, H. Traxler, A. Ureña, J. G. van der Laan, L. Veleva, S. Wahlberg, M. Walter, T. Weber, T. Weitkamp, S. Wurster, M. A. Yar, J. H. You, and A. Zivelonghi, "Recent progress in research on tungsten materials for nuclear fusion applications in Europe," *J. Nucl. Mater.*, vol. 432, no. 1–3, pp. 482–500, Jan. 2013.

[29] ITER Organization, "The ITER Tokamak," 2016. [Online]. Available: https://www.iter.org/mach. [Accessed: 14-Jul-2016].

[30] S. J. Zinkle, "Advanced materials for fusion technology," *Fusion Eng. Des.*, vol. 74, no. 1–4, pp. 31–40, 2005.

[31] J. Knaster, A. Moeslang, and T. Muroga, "Materials research for fusion," *Nat. Phys.*, vol. 5, no. 2, pp. 77–80, 2016.

[32] L. Giancarli, V. Chuyanov, M. Abdou, M. Akiba, B. G. Hong, R. Lässer, C.

Pan, and Y. Strebkov, “Test blanket modules in ITER: An overview on proposed designs and required DEMO-relevant materials,” *J. Nucl. Mater.*, vol. 367–370, pp. 1271–1280, 2007.

[33] M. R. Gilbert, S. L. Dudarev, D. Nguyen-Manh, S. Zheng, L. W. Packer, and J.-C. Sublet, “Neutron-induced dpa, transmutations, gas production, and helium embrittlement of fusion materials,” *J. Nucl. Mater.*, pp. 1–6, Apr. 2013.

[34] M. Li, F. Maviglia, G. Federici, and J. H. You, “Sweeping heat flux loads on divertor targets: Thermal benefits and structural impacts,” *Fusion Eng. Des.*, vol. 102, pp. 50–58, 2016.

[35] V. Barabash, M. Akiba, A. Cardella, I. Mazul, B. C. Odegard Jr, L. Plöchl, R. Tivey, and G. Vieider, “Armor and heat sink materials joining technologies development for ITER plasma facing components,” *J. Nucl. Mater.*, vol. 283–287, pp. 1248–1252, 2000.

[36] J. H. You, E. Visca, C. Bachmann, T. Barrett, F. Crescenzi, M. Fursdon, H. Greuner, D. Guilhem, P. Languille, M. Li, S. McIntosh, A. V. Müller, J. Reiser, M. Richou, and M. Rieth, “European DEMO divertor target: Operational requirements and material-design interface,” *Nucl. Mater. Energy*, vol. 0, pp. 1–6, 2015.

[37] M. Rieth, S. L. Dudarev, S. M. Gonzalez de Vicente, J. Aktaa, T. Ahlgren, S. Antusch, D. E. J. Armstrong, M. Balden, N. Baluc, M.-F. Barthe, W. W. Basuki, M. Battabyal, C. S. Becquart, D. Blagoeva, H. Boldyryeva, J. Brinkmann, M. Celino, L. Ciupinski, J. B. Correia, A. De Backer, C. Domain,

E. Gaganidze, C. Garcia-Rosales, J. Gibson, M. R. Gilbert, S. Giusepponi, B. Gludovatz, H. Greuner, K. Heinola, T. Höschen, A. Hoffmann, N. Holstein, F. Koch, W. Krauss, H. Li, S. Lindig, J. Linke, C. Linsmeier, P. Lopez-Ruiz, H. Maier, J. Matejicek, T. P. Mishra, M. Muhammed, A. Munoz, M. Muzyk, K. Nordlund, D. Nguyen-Manh, J. Opschoor, N. Ordas, T. Palacios, G. Pintsuk, R. Pippan, J. Reiser, J. Riesch, S. G. Roberts, L. Romaner, M. Rosiński, M. Sanchez, W. Schulmeyer, H. Traxler, A. Urena, J. G. van der Laan, L. Veleva, S. Wahlberg, M. Walter, T. Weber, T. Weitkamp, S. Wurster, M. A. Yar, J. H. You, and A. Zivelonghi, "A brief summary of the progress on the EFDA tungsten materials program," *J. Nucl. Mater.*, vol. 442, no. 1–3, Supplement 1, pp. S173–S180, Mar. 2013.

[38] T. Muroga, J. M. Chen, V. M. Chernov, R. J. Kurtz, and M. Le Flem, "Present status of vanadium alloys for fusion applications," *J. Nucl. Mater.*, vol. 455, no. 1–3, pp. 263–268, 2014.

[39] T. Muroga, T. Nagasaka, K. Abe, V. M. Chernov, H. Matsui, D. L. Smith, Z. Y. Xu, and S. J. Zinkle, "Vanadium alloys - Overview and recent results," *J. Nucl. Mater.*, vol. 307–311, pp. 547–554, 2002.

[40] F. Najmabadi, C. G. Bathke, M. C. Billone, J. P. Blanchard, L. Bromberg, E. Chin, F. R. Cole, J. A. Crowell, D. A. Ehst, L. A. El-Guebaly, J. S. Herring, T. Q. Hua, S. C. Jardin, C. E. Kessel, H. Khater, V. D. Lee, S. Malang, T.-K. Mau, R. L. Miller, E. A. Mogahed, T. W. Petrie, E. E. Reis, J. Schultz, M. Sidorov, D. Steiner, I. N. Sviatoslavsky, D.-K. Sze, R. Thayer, M. S. Tillack, P. Titus, L. M. Wagner, X. Wang, and C. P. C. Wong, "Overview of the ARIES-RS reversed-shear tokamak power plant study," *Fusion Eng. Des.*,

vol. 38, no. 1–2, pp. 3–25, 1997.

[41] R. J. Kurtz, K. Abe, V. M. Chernov, V. A. Kazakov, G. E. Lucas, H. Matsui, T. Muroga, G. R. Odette, D. L. Smith, and S. J. Zinkle, "Critical issues and current status of vanadium alloys for fusion energy applications," *J. Nucl. Mater.*, vol. 283–287, pp. 70–78, 2000.

[42] S. J. Zinkle, H. Matsui, D. L. Smith, A. F. Rowcliffe, E. V. van Osch, K. Abe, and V. A. Kazakov, "Research and development on vanadium alloys for fusion applications," *J. Nucl. Mater.*, vol. 258–263, pp. 205–214, 1998.

[43] A. Möslang, E. Diegele, M. Klimiankou, R. Lässer, R. Lindau, E. Lucon, E. Materna-Morris, C. Petersen, R. Pippan, J. W. Rensman, M. Rieth, B. Van Der Schaaf, H.-C. Schneider, and F. Tavassoli, "Towards reduced activation structural materials data for fusion DEMO reactors," *Nucl. Fusion*, vol. 45, no. 7, pp. 649–655, Jul. 2005.

[44] A. Iveković, S. Novak, G. Dražić, D. Blagoeva, and S. G. de Vicente, "Current status and prospects of SiCf/SiC for fusion structural applications," *J. Eur. Ceram. Soc.*, vol. 33, no. 10, pp. 1577–1589, 2013.

[45] L. L. Snead, T. Nozawa, Y. Katoh, T. S. Byun, S. Kondo, and D. A. Petti, "Handbook of SiC properties for fuel performance modeling," *J. Nucl. Mater.*, vol. 371, no. 1–3, pp. 329–377, 2007.

[46] S. J. Zinkle, "Fusion materials science: Overview of challenges and recent progress," *Phys. Plasmas*, vol. 12, no. 5, pp. 1–8, 2005.

[47] C. H. Carter Jr, R. F. Davis, and J. Bentley, "Kinetics and Mechanisms of High-Temperature Creep in Silicon Carbide: II, Chemically Vapor

Deposited," *J. Am. Ceram. Soc.*, vol. 67, no. 11, pp. 732–740, 1984.

[48] D. A. Petti, K. A. McCarthy, N. P. Taylor, C. B. A. Forty, and R. A. Forrest, "Re-evaluation of the use of low activation materials in waste management strategies for fusion," *Fusion Eng. Des.*, vol. 51–52, pp. 435–444, 2000.

[49] A. Hasegawa, "Helium implantation effects on mechanical properties of SiCf/SiC composites,", *J. Nucl. Mater.,* vol. 253, pp. 31–35, 2000.

[50] R. J. Kurtz, A. Alamo, E. Lucon, Q. Huang, S. Jitsukawa, A. Kimura, R. L. Klueh, G. R. Odette, C. Petersen, M. a. Sokolov, P. Spätig, and J. W. Rensman, "Recent progress toward development of reduced activation ferritic/martensitic steels for fusion structural applications," *J. Nucl. Mater.*, vol. 386–388, no. C, pp. 411–417, 2009.

[51] G. R. Odette, "On the ductile to brittle transition in martensitic stainless steels — Mechanisms, models and structural implications," *J. Nucl. Mater.*, vol. 212–215, pp. 45–51, 1994.

[52] T. Muroga, M. Gasparotto, and S. J. Zinkle, "Overview of materials research for fusion reactors," *Fusion Eng. Des.*, vol. 61–62, pp. 13–25, 2002.

[53] G. R. Odette, M. J. Alinger, and B. D. Wirth, "Recent Developments in Irradiation-Resistant Steels," *Annu. Rev. Mater. Res.*, vol. 38, no. 1, pp. 471–503, Aug. 2008.

[54] PLANSEE, "Materials: Tungsten," 2013. [Online]. Available: http://www.plansee.com/en/Materials-Tungsten-403.htm. [Accessed: 02-Jul-2013].

[55] E. Lassner and W. D. Schubert, *Tungsten: Properties, Chemistry, Tecnology of the Element, Alloys, and Chemical Compounds*. Springer, 1999.

[56] L. Briant, F. Zaverl, and E. L. Hall, "Warm rolling of sintered tungsten ingots," *Mater. Sci. Technol.*, vol. 7, no. October, pp. 923–936, 1991.

[57] Q. Wei and L. J. Kecskes, "Effect of low-temperature rolling on the tensile behavior of commercially pure tungsten," *Mater. Sci. Eng. A*, vol. 491, no. 1–2, pp. 62–69, 2008.

[58] K. Farrell, A. C. Schaffhauser, and J. O. Stiegler, "Recrystallization, grain growth and the ductile-brittle transition in tungsten sheet," *J. Less Common Met.*, vol. 13, no. 2, pp. 141–155, 1967.

[59] J. Reiser, M. Rieth, B. Dafferner, and A. Hoffmann, "Tungsten foil laminate for structural divertor applications–Analyses and characterisation of tungsten foil," *J. Nucl. Mater.*, vol. 424, no. 1–3, pp. 197–203, 2012.

[60] A. A. F. Tavassoli, "Present limits and improvements of structural materials for fusion reactors - A review," *J. Nucl. Mater.*, vol. 302, no. 2–3, pp. 73–88, 2002.

[61] A. Giannattasio, Z. Yao, E. Tarleton, and S. G. Roberts, "Brittle–ductile transitions in polycrystalline tungsten," *Philos. Mag.*, vol. 90, no. 30, pp. 3947–3959, Oct. 2010.

[62] J. W. Davis, V. R. Barabash, A. Makhankov, L. Plöchl, and K. T. Slattery, "Assessment of tungsten for use in the ITER plasma facing components," *J. Nucl. Mater.*, vol. 258–263, pp. 308–312, 1998.

[63] P. L. Raffo, “Yielding and fracture in tungsten and tungsten-rhenium alloys,” *J. Less-Common Met.*, vol. 17, pp. 133–149, 1969.

[64] H. Bolt, V. Barabash, G. Federici, J. Linke, A. Loarte, J. Roth, and K. Sato, “Plasma facing and high heat flux materials - Needs for ITER and beyond,” *J. Nucl. Mater.*, vol. 307–311, no. 1, Supplement, pp. 43–52, 2002.

[65] S. J. Zinkle and N. M. Ghoniem, “Operating temperature windows for fusion reactor structural materials,” *Fusion Eng. Des.*, vol. 52, pp. 55–71, 2000.

[66] V. Philipps, “Tungsten as material for plasma-facing components in fusion devices,” *J. Nucl. Mater.*, vol. 415, no. 1, Supplement, pp. S2–S9, 2011.

[67] T. Tanno, A. Hasegawa, J.-C. He, M. Fujiwara, S. Nogami, M. Satou, T. Shishido, and K. Abe, “Effects of Transmutation Elements on Neutron Irradiation Hardening of Tungsten,” *Mater. Trans.*, vol. 48, no. 9, pp. 2399–2402, 2007.

[68] J. C. He, G. Y. Tang, A. Hasegawa, and K. Abe, “Microstructural development and irradiation hardening of W and W–(3–26) wt%Re alloys after high-temperature neutron irradiation to 0.15 dpa,” *Nucl. Fusion*, vol. 46, no. 11, pp. 877–883, 2006.

[69] V. Barabash, G. Federici, and M. Rödig, “Neutron irradiation effects on plasma facing materials,” *J. Nucl. Mater.*, vol. 283–287, pp. 138–146, 2000.

[70] N. J. Petch, “The Cleavage Strength of Polycrystals,” *J. Iron Steel Inst.*, vol. 174, pp. 25–28, 1953.

[71] L. Veleva, “Contribution to the Production and Characterization of W-Y , W-

Y2O3 and W-TiC Materials for Fusion Reactors," École Polytechnique Fédérale de Lausanne Thesis, 2011.

[72] M. Battabyal, R. Schäublin, P. Spätig, M. Walter, M. Rieth, and N. Baluc, "Microstructure and mechanical properties of a W-2wt.%Y2O 3 composite produced by sintering and hot forging," *J. Nucl. Mater.*, vol. 442, pp. S225–S228, 2013.

[73] M. A. Yar, S. Wahlberg, H. Bergqvist, H. G. Salem, M. Johnsson, and M. Muhammed, "Chemically produced nanostructured ODS–lanthanum oxide–tungsten composites sintered by spark plasma," *J. Nucl. Mater.*, vol. 408, no. 2, pp. 129–135, Jan. 2011.

[74] V. Livramento, D. Nunes, J. B. Correia, P. A. Carvalho, R. Mateus, K. Hanada, N. Shohoji, H. Fernandes, C. Silva, and E. Alves, "Tungsten-tantalum composites for plasma facing components V. Livramento," in *Materials for Energy, ENMAT*, 2010.

[75] J. Reiser, M. Rieth, B. Dafferner, and A. Hoffmann, "Tungsten foil laminate for structural divertor applications – Basics and outlook," *J. Nucl. Mater.*, vol. 423, no. 1–3, pp. 1–8, Apr. 2012.

[76] J.-H. You, A. Brendel, S. Nawka, T. Schubert, and B. Kieback, "Thermal and mechanical properties of infiltrated W/CuCrZr composite materials for functionally graded heat sink application," *J. Nucl. Mater.*, vol. 438, no. 1–3, pp. 1–6, Jul. 2013.

[77] ITER Organization, "Divertor," 2016. [Online]. Available: https://www.iter.org/mach/divertor. [Accessed: 11-Jul-2016].

[78] T. Loarer, S. Brezinsek, V. Philipps, J. Bucalossi, D. Douai, H. G. Esser, S. Grunhagen, J. Hobirk, S. Jachmich, E. Joffrin, U. Kruezi, C. Lowry, G. Matthews, R. Smith, E. Tsitrone, and S. Vartanian, "Comparison of long term fuel retention in JET between carbon and the ITER-Like Wall," *J. Nucl. Mater.*, vol. 438, pp. S108–S113, 2013.

[79] G. Federici, C. H. Skinner, J. N. Brooks, J. P. Coad, C. Grisolia, A. A. Hassz, A. Hassanein, V. Philipps, C. S. Pitcher, J. Roth, W. R. Wampler, and D. G. Whyte, "Plasma-material interactions in current tokamaks and their implications for next step fusion reactors," *Nucl. Fusion*, vol. 1967, no. 12R, p. 1967, 2001.

[80] J. Roth and K. Schmid, "Hydrogen in tungsten as plasma-facing material," *Phys. Scr.*, vol. 2011, no. T145, pp. 1–9, Dec. 2011.

[81] R. A. Pitts, S. Carpentier, F. Escourbiac, T. Hirai, V. Komarov, a. S. Kukushkin, S. Lisgo, A. Loarte, M. Merola, R. Mitteau, a. R. Raffray, M. Shimada, and P. C. Stangeby, "Physics basis and design of the ITER plasma-facing components," *J. Nucl. Mater.*, vol. 415, no. 1, Supplement, pp. S957–S964, 2011.

[82] G. M. McCracken and P. E. Stott, "Plasma-surface interactions in tokamaks," *Nucl. Fusion*, vol. 19, pp. 889–981, 1979.

[83] S. J. Zinkle and L. L. Snead, "Designing Radiation Resistance in Materials for Fusion Energy*," *Annu. Rev. Mater. Res.*, vol. 44, no. 1, pp. 241–267, 2014.

[84] N. Baluc, K. Abe, J. L. Boutard, V. M. Chernov, E. Diegele, S. Jitsukawa, A. Kimura, R. L. Klueh, A. Kohyama, R. J. Kurtz, R. Lässer, H. Matsui, A.

Möslang, T. Muroga, G. R. Odette, M. Q. Tran, B. van der Schaaf, Y. Wu, J. Yu, and S. J. Zinkle, “Status of R&D activities on materials for fusion power reactors,” *Nucl. Fusion*, vol. 47, no. 10, pp. S696–S717, 2007.

[85] R. J. Hawryluk, K. Bol, N. Bretz, D. Dimock, D. Eames, E. Hinnov, J. Hosea, H. Hsuan, F. C. Jobes, D. Johnson, E. Meservey, N. Sauthoff, G. L. Schmidt, S. Suckewer, M. Ulrickson, and S. Von Goeler, “The effect of current profile evolution on plasma-limiter interaction and the energy confinement time,” *Nucl. Fusion*, vol. 19, no. 10, pp. 1307–1317, 1979.

[86] H. Nakamura, T. Ando, H. Yoshida, S. Niikura, T. Nishitani, and K. Nagashima, “Divertor experiment on particle and energy control in neutral beam heated JT-60 discharges,” *Nucl. Fusion*, vol. 28, no. 1, pp. 43–52, 1988.

[87] TFR Group, “TFR , the tokamak of Fontenay-aux-Roses,” *Nucl. Fusion*, vol. 25, no. 9, pp. 1025–1032, 1985.

[88] J. W. M. Paul, “The DITE experiment,” *Nucl. Fusion*, vol. 25, no. 9, pp. 1097–1100, 1985.

[89] F. Alladio, “Results from the Frascati tokamak FT,” *Nucl. Fusion*, vol. 25, no. 9, pp. 1069–1072, 1985.

[90] B. Lipschultz, D. A. Pappas, B. LaBombard, J. E. Rice, D. Smith, and S. J. Wukitch, “A study of molybdenum influxes and transport in Alcator C-Mod,” *Nucl. Fusion*, vol. 41, no. 5, p. 585, 2001.

[91] G. F. Matthews, “Plasma operation with an all metal first-wall: Comparison of an ITER-like wall with a carbon wall in JET,” *J. Nucl. Mater.*, vol. 438, pp. S2–S10, 2013.

[92] R. Neu, A. Kallenbach, M. Balden, V. Bobkov, J. W. Coenen, R. Drube, R. Dux, H. Greuner, A. Herrmann, J. Hobirk, H. Höhnle, K. Krieger, M. Kočan, P. Lang, T. Lunt, H. Maier, M. Mayer, H. W. Müller, S. Potzel, T. Pütterich, J. Rapp, V. Rohde, F. Ryter, P. A. Schneider, J. Schweinzer, M. Sertoli, J. Stober, W. Suttrop, K. Sugiyama, G. Van Rooij, and M. Wischmeier, "Overview on plasma operation with a full tungsten wall in ASDEX Upgrade," *J. Nucl. Mater.*, vol. 438, pp. 34–41, 2013.

[93] G. Federici, P. Andrew, P. Barabaschi, J. Brooks, R. Doerner, A. Geier, A. Herrmann, G. Janeschitz, K. Krieger, A. Kukushkin, A. Loarte, R. Neu, G. Saibene, M. Shimada, G. Strohmayer, and M. Sugihara, "Key ITER plasma edge and plasma-material interaction issues," *J. Nucl. Mater.*, vol. 313–316, pp. 11–22, 2003.

[94] CCFE, "EURATOM/CCFE Fusion Association Annual Report 2014/15," 2014.

[95] J. Roth, E. Tsitrone, T. Loarer, V. Philipps, S. Brezinsek, A. Loarte, G. F. Counsell, R. P. Doerner, K. Schmid, O. V. Ogorodnikova, and R. A. Causey, "Tritium inventory in ITER plasma-facing materials and tritium removal procedures," *Plasma Phys. Control. Fusion*, vol. 50, pp. 1–20, 2008.

[96] W. Eckstein and J. Lhszxi, "Sputtering of tungsten and molybdenum," *J. Nucl. Mater.*, vol. 183, pp. 19–24, 1991.

[97] V. Philipps, T. Tanabe, Y. Ueda, A. Pospieszczyk, M. Z. Tokar, B. Unterberg, L. Konen, B. Schweer, U. Samm, P. Wienhold, J. Winter, M. Rubel, B. Emmoth, and N. C. Hawkes, "Molybdenum Test Limiter Experiments in

Textor," *Nucl. Fusion*, vol. 34, no. 11, pp. 1417–1429, 1994.

[98] PLANSEE, "Molybdenum," 2016. [Online]. Available: https://www.plansee.com/en/materials/molybdenum.html. [Accessed: 17-Oct-2016].

[99] E. Hotston, "Threshold energies for sputtering," *Nucl. Fusion*, vol. 15, no. 3, pp. 544–547, 1975.

[100] W. Eckstein, "Calculated Sputtering, Reflection and Range Values," IPP Report, Max-Planck-Institut für Plasmaphysik, 2002.

[101] D. Maisonnier, D. Campbell, I. Cook, L. Di Pace, L. Giancarli, J. Hayward, a. Li Puma, M. Medrano, P. Norajitra, M. Roccella, P. Sardain, M. Q. Tran, and D. Ward, "Power plant conceptual studies in Europe," *Nucl. Fusion*, vol. 47, no. 11, pp. 1524–1532, 2007.

[102] J. Roth, "Chemical erosion of carbon based materials in fusion devices," *J. Nucl. Mater.*, vol. 266, pp. 51–57, 1999.

[103] R. Neu, C. Hopf, A. Kallenbach, T. Pütterich, R. Dux, H. Greuner, O. Gruber, A. Herrmann, K. Krieger, H. Maier, and V. Rohde, "Operational conditions in a W-clad tokamak," *J. Nucl. Mater.*, vol. 367–370, no. Special Issue, pp. 1497–1502, 2007.

[104] R. J. Hawryluk, D. J. Campbell, G. Janeschitz, P. R. Thomas, R. Albanese, R. Ambrosino, C. Bachmann, L. Baylor, M. Becoulet, I. Benfatto, J. Bialek, A. Boozer, A. Brooks, R. Budny, T. Casper, M. Cavinato, J.-J. Cordier, V. Chuyanov, E. Doyle, T. Evans, G. Federici, M. Fenstermacher, H. Fujieda, K. G'al, A. Garofalo, L. Garzotti, D. Gates, Y. Gribov, P. Heitzenroeder, T. C.

Hender, N. Holtkamp, D. Humphreys, I. Hutchinson, K. Ioki, J. Johner, G. Johnson, Y. Kamada, A. Kavin, C. Kessel, R. Khayrutdinov, G. Kramer, A. Kukushkin, K. Lackner, I. Landman, P. Lang, Y. Liang, J. Linke, B. Lipschultz, A. Loarte, G. D. Loesser, C. Lowry, T. Luce, V. Lukash, S. Maruyama, M. Mattei, J. Menard, M. Merola, A. Mineev, N. Mitchell, E. Nardon, R. Nazikian, B. Nelson, C. Neumeyer, J.-K. Park, R. Pearce, R. A. Pitts, A. Polevoi, A. Portone, M. Okabayashi, P. H. Rebut, V. Riccardo, J. Roth, S. Sabbagh, G. Saibene, G. Sannazzaro, M. Schaffer, M. Shimada, A. Sen, A. Sips, C. H. Skinner, P. Snyder, R. Stambaugh, E. Strait, M. Sugihara, E. Tsitrone, J. Urano, M. Valovic, M. Wade, J. Wesley, R. White, D. G. Whyte, S. Wu, M. Wykes, and L. Zakharov, "Principal physics developments evaluated in the ITER design review," *Nucl. Fusion*, vol. 49, no. 6, pp. 1–15, 2009.

[105] G. F. Matthews, M. Beurskens, S. Brezinsek, M. Groth, E. Joffrin, A. Loving, M. Kear, M.-L. Mayoral, R. Neu, P. Prior, V. Riccardo, F. Rimini, M. Rubel, G. Sips, E. Villedieu, P. de Vries, and M. L. Watkins, "JET ITER-like wall—overview and experimental programme," *Phys. Scr.*, vol. 2011, no. T145, pp. 1–6, 2011.

[106] S. Krat, Y. Gasparyan, A. Pisarev, I. Bykov, M. Mayer, G. De Saint Aubin, M. Balden, C. P. Lungu, and A. Widdowson, "Erosion at the inner wall of JET during the discharge campaign 2011-2012 in comparison with previous campaigns," *J. Nucl. Mater.*, vol. 456, pp. 106–110, 2015.

[107] H. Bolt, V. Barabash, W. Krauss, J. Linke, R. Neu, S. Suzuki, and N. Yoshida, "Materials for the plasma-facing components of fusion reactors," *J.*

Nucl. Mater., vol. 329–333, pp. 66–73, Aug. 2004.

[108] B. Gludovatz, S. Wurster, A. Hoffmann, and R. Pippan, "Fracture toughness of polycrystalline tungsten alloys," *Int. J. Refract. Met. Hard Mater.*, vol. 28, no. 6, pp. 674–678, 2010.

[109] S.-H. Wei, H. Krakauer, and M. Weinert, "Linearized augmented-plane-wave calculation of the electronic structure and total energy of tungsten," *Phys. Rev. B*, vol. 32, no. 12, pp. 7792–7797, 1985.

[110] A. Zunger and M. L. Cohen, "Self-consistent pseudopotential calculation of the bulk properties of Mo and W," *Phys. Rev. B*, vol. 19, no. 2, pp. 568–582, 1979.

[111] T. Troev, N. Nankov, and T. Yoshiie, "Simulation of displacement cascades in tungsten irradiated by fusion neutrons," *Nucl. Instruments Methods Phys. Res. Sect. B Beam Interact. with Mater. Atoms*, vol. 269, no. 6, pp. 566–571, Mar. 2011.

[112] F. Koch and H. Bolt, "Self passivating W-based alloys as plasma facing material for nuclear fusion," *Phys. Scr.*, vol. 2007, no. T128, pp. 100–105, 2007.

[113] E. Tarleton and S. G. Roberts, "Dislocation dynamic modelling of the brittle–ductile transition in tungsten," *Philos. Mag.*, vol. 89, no. 31, pp. 2759–2769, 2009.

[114] J. Gibson, D. Armstrong, and S. Roberts, "The micro-mechanical properties of ion irradiated tungsten," *Phys. Scr.*, vol. 2014, no. T159, pp. 1–3, Apr. 2014.

[115] M. Roedig, W. Kuehnlein, J. Linke, M. Merola, E. Rigal, B. Schedler, and E. Visca, “Investigation of tungsten alloys as plasma facing materials for the ITER divertor,” *Fusion Eng. Des.*, vol. 61–62, pp. 135–140, 2002.

[116] J.-C. Carlen and B. D. Bryskin, “Rhenium - A Unique Rare Metal,” *Mater. Manuf. Process.*, vol. 9, no. 6, pp. 1087–1104, 1994.

[117] L. Romaner, C. Ambrosch-Draxl, and R. Pippan, “Effect of Rhenium on the Dislocation Core Structure in Tungsten,” *Phys. Rev. Lett.*, vol. 104, no. 19, p. 195503, May 2010.

[118] H. Li, S. Wurster, C. Motz, L. Romaner, C. Ambrosch-Draxl, and R. Pippan, “Dislocation-core symmetry and slip planes in tungsten alloys: Ab initio calculations and microcantilever bending experiments,” *Acta Mater.*, vol. 60, no. 2, pp. 748–758, Jan. 2012.

[119] S. Wurster, N. Baluc, M. Battabyal, T. Crosby, J. Du, C. García-Rosales, A. Hasegawa, A. Hoffmann, A. Kimura, H. Kurishita, R. J. Kurtz, H. Li, S. Noh, J. Reiser, J. Riesch, M. Rieth, W. Setyawan, M. Walter, J.-H. You, and R. Pippan, “Recent progress in R&D on tungsten alloys for divertor structural and plasma facing materials,” *J. Nucl. Mater.*, vol. 442, pp. S181–S189, Mar. 2013.

[120] P. M. Derlet, D. Nguyen-Manh, and S. L. Dudarev, “Multiscale modeling of crowdion and vacancy defects in body-centered-cubic transition metals,” *Phys. Rev. B - Condens. Matter Mater. Phys.*, vol. 76, no. 5, pp. 1–22, 2007.

[121] J. F. Ziegler, J. P. Biersack, and U. Littmark, “The Stopping and Range of Ions in Solids.” Pergamon, New York, 1985.

[122] J. F. Ziegler, M. D. Ziegler, and J. P. Biersack, “SRIM - The stopping and range of ions in matter (2010),” *Nucl. Instruments Methods Phys. Res. Sect. B Beam Interact. with Mater. Atoms*, vol. 268, no. 11–12, pp. 1818–1823, 2010.

[123] M. T. Robinson, “Basic physics of radiation damage production,” *J. Nucl. Mater.*, vol. 216, no. C, pp. 1–28, 1994.

[124] S. J. Zinkle, “Radiation-induced effects on microstructure,” *Compr. Nucl. Mater.*, vol. 1, no. February 2012, pp. 65–98, 2012.

[125] G. S. Was and T. R. Allen, *Radiation Damage From Differeant Particle Types*. Springer, 2007.

[126] L. R. Greenwood, “Neutron interactions and atomic recoil spectra,” *J. Nucl. Mater.*, vol. 216, pp. 29–44, Oct. 1994.

[127] L. K. Mansur and M. L. Grossbeck, “Mechanical property changes induced in structural alloys by neutron irradiations with different helium to displacement ratios,” *J. Nucl. Mater.*, vol. 155–157, pp. 130–147, 1988.

[128] G. H. Kinchin and R. S. Pease, “The Displacement of Atoms in Solids by Radiation,” *Reports Prog. Phys.*, vol. 18, pp. 1–51, 1955.

[129] K. . Russell, “Phase stability under irradiation,” *Prog. Mater. Sci.*, vol. 28, pp. 229–434, 1984.

[130] G. S. Was, *Fundamentals of radiation materials science: metals and alloys*. New York: Springer, 2007.

[131] M. J. Norgett, M. T. Robinson, and I. M. Torrens, “A proposed method of calculating displacement dose rates,” *Nucl. Eng. Des.*, vol. 33, pp. 50–54,

1975.

[132] R. Pampin, “Tungsten transmutation and resonance self-shielding in PPCS models for the study of sigma-phase formation,” EURATOM/UKAEA Fusion Association, 2005.

[133] M. R. Gilbert and J.-C. Sublet, “Neutron-induced transmutation effects in W and W-alloys in a fusion environment,” *Nucl. Fusion*, vol. 51, no. 4, pp. 1–13, Apr. 2011.

[134] T. Tanno, A. Hasegawa, M. Fujiwara, J.-C. He, S. Nogami, M. Satou, T. Shishido, and K. Abe, “Precipitation of Solid Transmutation Elements in Irradiated Tungsten Alloys,” *Mater. Trans.*, vol. 49, no. 10, pp. 2259–2264, 2008.

[135] M. Ekman, K. Persson, and G. Grimvall, “Phase diagram and lattice instability in tungsten–rhenium alloys,” *J. Nucl. Mater.*, vol. 278, no. 2–3, pp. 273–276, Apr. 2000.

[136] A. Möslang, “IFMIF: the intense neutron source to qualify materials for fusion reactors,” *Comptes Rendus Phys.*, vol. 9, no. 3–4, pp. 457–468, Apr. 2008.

[137] E. Surrey, M. Porton, A. Caballero, T. Davenne, D. Findlay, A. Letchford, J. Thomason, J. Marrow, S. Roberts, A. Seryi, B. Connolly, P. Mummery, and H. Owen, “FAFNIR: Strategy and risk reduction in accelerator driven neutron sources for fusion materials irradiation data,” *Fusion Eng. Des.*, vol. 89, no. 9–10, pp. 2108–2113, 2014.

[138] G. Was and T. Allen, *Radiation Effects in Solids*, vol. 235. Berlin: Springer,

2007.

[139] A. M. Stoneham, J. R. Matthews, I. J. Ford, H. Search, C. Journals, A. Contact, M. Iopscience, and I. P. Address, “Innovative materials for fusion power plant structures: separating functions,” *J. Phys. Condens. Matter*, vol. 16, pp. S2597–S2621, 2004.

[140] A. E. Sand, K. Nordlund, and S. L. Dudarev, “Radiation damage production in massive cascades initiated by fusion neutrons in tungsten,” *J. Nucl. Mater.*, vol. 455, pp. 207–211, 2014.

[141] R. Dierckx, “The Importance of the PKA Energy Spectrum for Radiation Damage Simulation,” *J. Nucl. Mater.*, vol. 144, pp. 214–227, 1987.

[142] M. J. Caturla, T. Diaz de la Rubia, M. Victoria, R. K. Corzine, M. R. James, and G. A. Greene, “Multiscale modeling of radiation damage: Applications to damage production by GeV proton irradiation of Cu and W, and pulsed irradiation effects in Cu and Fe,” *J. Nucl. Mater.*, vol. 296, pp. 90–100, 2001.

[143] X. Yi, M. L. Jenkins, M. Briceno, S. G. Roberts, Z. Zhou, and M. A. Kirk, “In situ study of self-ion irradiation damage in W and W-5Re at 500oC,” *Philos. Mag.*, vol. 93, no. 14, pp. 1715–1738, May 2013.

[144] R. S. Nelson, D. J. Mazey, and J. A. Hudson, “The use of ion accelerators to simulate fast neutron-induced voidage in metals,” *J. Nucl. Mater.*, vol. 37, no. 1, pp. 1–12, 1970.

[145] D. E. J. Armstrong, X. Yi, E. a. Marquis, and S. G. Roberts, “Hardening of self ion implanted tungsten and tungsten 5-wt% rhenium,” *J. Nucl. Mater.*, vol. 432, no. 1–3, pp. 428–436, Jan. 2013.

[146] A. Xu, C. Beck, D. E. J. Armstrong, K. Rajan, G. D. W. Smith, P. A. J. Bagot, and S. G. Roberts, “Ion-irradiation-induced clustering in W-Re and W-Re-Os alloys: A comparative study using atom probe tomography and nanoindentation measurements,” *Acta Mater.*, vol. 87, pp. 121–127, 2015.

[147] L. K. Mansur, “Correlation of neutron and heavy-ion damage: II. The predicted temperature shift if swelling with changes in radiation dose rate,” *J. Nucl. Mater.*, vol. 78, no. 1, pp. 156–160, 1978.

[148] M. Thompson, “The damage and recovery of neutron irradiated tungsten,” *Philos. Mag.*, vol. 5, no. 51, pp. 278–296, 1960.

[149] L. K. Keys and J. Moteff, “Neutron irradiation and defect recovery of tungsten,” *J. Nucl. Mater.*, vol. 34, no. 3, pp. 260–280, 1970.

[150] L. K. Keys, J. P. Smith, and J. Moteff, “High-temperature recovery of tungsten after neutron irradiation,” *Phys. Rev.*, vol. 176, no. 3, pp. 851–856, 1968.

[151] J. M. Steichen, “Tensile properties of neutron irradiated TZM and tungsten,” *J. Nucl. Mater.*, vol. 60, no. 1, pp. 13–19, 1976.

[152] R. Herschitz and D. N. Seidman, “An atomic resolution study of homogeneous radiation-induced precipitation in a neutron irradiated W-10at.% Re alloy,” *Acta Metall.*, vol. 32, no. 8, pp. 1141–1154, 1984.

[153] R. Herschitz and D. N. Seidman, “An atomic resolution study of homogeneous radiation-induced precipitation and solute segregation effects in a neutron irradiated W-25at.% Re alloy,” *Acta Metall.*, vol. 32, no. 8, pp. 1155–1171, 1984.

[154] R. Cauvin and G. Martin, “Solid-Solutions Under Irradiation .1. a Model for Radiation-Induced Metastability,” *Phys. Rev. B*, vol. 23, no. 7, pp. 3322–3332, 1981.

[155] C. H. Wu and U. Mszanowski, “A comparison of lifetimes of beryllium, carbon, molybdenum and tungsten as divertor armour materials,” *J. Nucl. Mater.*, vol. 218, no. 3, pp. 293–301, 1995.

[156] D. Naujoks, K. Asmussen, M. Bessenrodt-Weberpals, S. Deschka, R. Dux, W. Engelhardt, A. R. Field, G. Fussmann, J. C. Fuchs, C. Garcia-Rosales, S. Hirsch, P. Ignacz, G. Lieder, K. F. Mast, R. Neu, R. Radtke, J. Roth, and U. Wenzel, “Tungsten as target material in fusion devices,” *Nucl. Fusion*, vol. 36, no. 6, pp. 671–687, 1996.

[157] G. Janeschitz, K. Borrass, G. Federici, Y. Igitkhanov, Kukushkin, A., H. D. Pacher, G. W. Pacher, and M. Sugihara, “The ITER divertor concept,” *J. Nucl. Mater.*, vol. 220–220, pp. 73–88, 1995.

[158] A. Hasegawa, T. Tanno, S. Nogami, and M. Satou, “Property change mechanism in tungsten under neutron irradiation in various reactors,” *J. Nucl. Mater.*, vol. 417, no. 1–3, pp. 491–494, 2011.

[159] A. Hasegawa, M. Fukuda, S. Nogami, and K. Yabuuchi, “Neutron irradiation effects on tungsten materials,” *Fusion Eng. Des.*, vol. 89, no. 7–8, pp. 1568–1572, 2014.

[160] T. Tanno, A. Hasegawa, J. C. He, M. Fujiwara, M. Satou, S. Nogami, K. Abe, and T. Shishido, “Effects of transmutation elements on the microstructural evolution and electrical resistivity of neutron-irradiated tungsten,” *J. Nucl.*

Mater., vol. 386–388, no. C, pp. 218–221, 2009.

[161] Y. Ueda, H. T. Lee, N. Ohno, S. Kajita, A. Kimura, R. Kasada, T. Nagasaka, Y. Hatano, A. Hasegawa, H. Kurishita, and Y. Oya, "Recent progress of tungsten R&D for fusion application in Japan," *Phys. Scr.*, vol. 2011, no. T145, pp. 1–6, Dec. 2011.

[162] T. Tanno, M. Fukuda, S. Nogami, and A. Hasegawa, "Microstructure Development in Neutron Irradiated Tungsten Alloys," *Mater. Trans.*, vol. 52, no. 7, pp. 1447–1451, 2011.

[163] S. N. and A. H. Makoto Fukuda, Takashi Tanno, "Effects of Re Content and Fabrication Process on Microstructural Changes and Hardening in Neutron Irradiated Tungsten," *Mater. Trans.*, vol. 53, no. 12, pp. 2145–2150, 2012.

[164] Y. Nemoto, A. Hasegawa, M. Satou, and K. Abe, "Microstructural development of neutron irradiated W–Re alloys," *J. Nucl. Mater.*, vol. 283–287, pp. 1144–1147, Dec. 2000.

[165] Y. Ueda, J. W. Coenen, G. De Temmerman, R. P. Doerner, J. Linke, V. Philipps, and E. Tsitrone, "Research status and issues of tungsten plasma facing materials for ITER and beyond," *Fusion Eng. Des.*, vol. 89, no. 7–8, pp. 901–906, 2014.

[166] A. V Karasiov, D. V Efremov, and L. R. Greenwood, "Neutron flux spectra and radiation damage paraeters for the Russian BOR-60 and SM-2 reactors," Efremov Scientific Research Institute of Electrophysical Apparatus, St. Petersburg, Russia, 1994.

[167] J.-C. He, A. Hasegawa, M. Fujiwara, M. Satou, T. Shishido, and K. Abe,

"Fabrication and Characterization of W-Re-Os Alloys for Studying Transmutation Effects of W in Fusion Reactors," *Mater. Trans.*, vol. 45, no. 8, pp. 2657–2660, 2004.

[168] L. R. Greenwood and F. A. Garner, "Impact of transmutation issues on interpretation of data obtained from fast reactor irradiation experiments," *J. Nucl. Mater.*, vol. 329–333, pp. 1147–1150, 2004.

[169] L. R. Greenwood and F. A. Garner, "Transmutation of Mo, Re, W, Hf, and V in various irradiation test facilities and STARFIRE," *J. Nucl. Mater.*, vol. 212–215, pp. 635–639, 1994.

[170] J. Bentley and J. O. Stiegler, "Irradiation Induced Precipitation in Tungsten Based, W-Re Alloys," *Metall. Trans. A*, vol. 14A, pp. 655–666, 1983.

[171] V. K. Sikka and J. Moteff, "Superlattice of voids in neutron-irradiated tungsten," *J. Appl. Phys.*, vol. 43, no. 12, pp. 4942–4944, 1972.

[172] Y. Mutoh, K. Ichikawa, K. Nagata, and M. Takeuchi, "Effect of rhenium addition on fracture toughness of tungsten at elevated temperatures," *J. Mater. Sci.*, vol. 30, no. 3, pp. 770–775, 1995.

[173] M. Fukuda, K. Yabuuchi, S. Nogami, A. Hasegawa, and T. Tanaka, "Microstructural development of tungsten and tungsten–rhenium alloys due to neutron irradiation in HFIR," *J. Nucl. Mater.*, vol. 455, no. 1–3, pp. 460–463, 2014.

[174] J. T. Buswell, "Vacancy damage in heavy ion and neutron-irradiated tungsten," *Philos. Mag.*, vol. 22, no. 178, pp. 787–802, 1970.

[175] V. F. Häussermann, “Eine elektronenmikroskopische analyse von versetzungsringen in wolfram nach bestrahlung mit 60 keV-goldionen,” *Philos. Mag.*, vol. 25, no. 3, pp. 561–581, 1972.

[176] V. F. Häussermann, “Elektronenmikroskopische Untersuchung der Strahlenschädigung durch hochenergetische Goldionen in den kubisch-raumzentrierten Metallen Molybdan und Wolfram,” *Philos. Mag.*, vol. 25, no. 3, pp. 583–598, 1972.

[177] W. Jäger and M. Wilkens, “Formation of vacancy-type dislocation loops in tungsten bombarded by 60 keV Au ions,” *Phys. Status Solidi*, vol. 32, no. 1, pp. 89–100, 1975.

[178] B. L. Eyre and R. Bullough, “On the formation of interstitial loops in b.c.c. metals,” *Philos. Mag.*, vol. 12, no. 115, pp. 31–39, 1965.

[179] D. E. J. Armstrong, A. J. Wilkinson, and S. G. Roberts, “Mechanical properties of ion-implanted tungsten–5 wt% tantalum,” *Phys. Scr.*, vol. 2011, no. T145, pp. 1–4, Dec. 2011.

[180] D. E. J. Armstrong and T. B. Britton, “Effect of dislocation density on improved radiation hardening resistance of nano-structured tungsten-rhenium,” *Mater. Sci. Eng. A*, vol. 611, pp. 388–393, 2014.

[181] Ciupiński, O. V. Ogorodnikova, T. Płociński, M. Andrzejczuk, M. Rasiński, M. Mayer, and K. J. Kurzydłowski, “TEM observations of radiation damage in tungsten irradiated by 20 MeV W ions,” *Nucl. Instruments Methods Phys. Res. Sect. B Beam Interact. with Mater. Atoms*, vol. 317, pp. 159–164, 2013.

[182] C. D. Hardie, C. A. Williams, S. Xu, and S. G. Roberts, “Effects of irradiation

temperature and dose rate on the mechanical properties of self-ion implanted Fe and Fe-Cr alloys," *J. Nucl. Mater.*, vol. 439, no. 1–3, pp. 33–40, 2013.

[183] S. A. Maloy, M. R. James, W. Sommer, G. J. Willcutt, M. Lopez, and T. J. Romero, "The Effect of 800 MeV Proton Irradiation on the Mechanical Properties of Tungsten," *Mater. Trans.*, vol. 43, no. 4, pp. 633–637, 2002.

[184] R. Sakamoto, T. Muroga, and N. Yoshida, "Microstructural evolution induced by low energy hydrogen ion irradiation in tungsten," *J. Nucl. Mater.*, vol. 222, pp. 819–822, 1995.

[185] J. C. He, A. Hasegawa, and K. Abe, "Effects of transmutation elements on the defect structure development of W irradiated by protons and neutrons," *J. Nucl. Mater.*, vol. 377, no. 2, pp. 348–351, 2008.

[186] C. Abromeit, "Aspects of simulation of neutron damage by ion irradiation," *J. Nucl. Mater.*, vol. 216, pp. 78–96, Oct. 1994.

[187] S. L. Dudarev, M. R. Gilbert, K. Arakawa, H. Mori, Z. Yao, M. L. Jenkins, and P. M. Derlet, "Langevin model for real-time Brownian dynamics of interacting nanodefects in irradiated metals," *Phys. Rev. B - Condens. Matter Mater. Phys.*, vol. 81, no. 22, pp. 1–15, 2010.

[188] L. K. Mansur, "Theory and experimental background on dimensional changes in irradiated alloys," *J. Nucl. Mater.*, vol. 216, pp. 97–123, 1994.

[189] W. Wang, J. Roth, S. Lindig, and C. H. Wu, "Blister formation of tungsten due to ion bombardment," *J. Nucl. Mater.*, vol. 299, no. 2, pp. 124–131, 2001.

[190] M. Y. Ye, H. Kanehara, S. Fukuta, N. Ohno, and S. Takamura, "Blister

formation on tungsten surface under low energy and high flux hydrogen plasma irradiation in NAGDIS-I," *J. Nucl. Mater.*, vol. 313–316, no. SUPPL., pp. 72–76, 2003.

[191] T. Venhaus, R. Causey, R. Doerner, and T. Abeln, "Behavior of tungsten exposed to high fluences of low energy hydrogen isotopes," *J. Nucl. Mater.*, vol. 290–293, pp. 505–508, 2001.

[192] Y. Ueda, M. Fukumoto, J. Yoshida, Y. Ohtsuka, R. Akiyoshi, H. Iwakiri, and N. Yoshida, "Simultaneous irradiation effects of hydrogen and helium ions on tungsten," *J. Nucl. Mater.*, vol. 386–388, pp. 725–728, Apr. 2009.

[193] M. Miyamoto, D. Nishijima, Y. Ueda, R. P. Doerner, H. Kurishita, M. J. Baldwin, S. Morito, K. Ono, and J. Hanna, "Observations of suppressed retention and blistering for tungsten exposed to deuterium–helium mixture plasmas," *Nucl. Fusion*, vol. 49, no. 6, p. 065035, 2009.

[194] V. K. Alimov, W. M. Shu, J. Roth, K. Sugiyama, S. Lindig, M. Balden, K. Isobe, and T. Yamanishi, "Surface morphology and deuterium retention in tungsten exposed to low-energy, high flux pure and helium-seeded deuterium plasmas," *Phys. Scr.*, vol. T138, p. 014048, 2009.

[195] R. P. Doerner, M. J. Baldwin, D. Nishijima, J. Roth, and K. Schmid, "Impact of beryllium surface layers on deuterium retention in tungsten," *J. Nucl. Mater.*, vol. 415, no. 1 SUPPL, pp. S717–S720, 2011.

[196] M. Miyamoto, D. Nishijima, M. Baldwin, R. Doerner, Y. Ueda, and A. Sagara, "Influence of Be seeding on microstructures of tungsten exposed to D-He mixture plasmas in PISCES and its impacts on retention properties," *J.*

Nucl. Mater., vol. 438, no. SUPPL, pp. S216–S219, 2013.

[197] D. Nishijima, H. Iwakiri, K. Amano, M. . Ye, N. Ohno, K. Tokunaga, N. Yoshida, and S. Takamura, "Suppression of blister formation and deuterium retention on tungsten surface due to mechanical polishing and helium pre-exposure," *Nucl. Fusion*, vol. 45, no. 7, pp. 669–674, 2005.

[198] K. O. E. Henriksson, K. Nordlund, A. Krasheninnikov, and J. Keinonen, "Difference in formation of hydrogen and helium clusters in tungsten," *Appl. Phys. Lett.*, vol. 87, no. 16, pp. 1–3, 2005.

[199] N. Yoshida, H. Iwakiri, K. Tokunaga, and T. Baba, "Impact of low energy helium irradiation on plasma facing metals," *J. Nucl. Mater.*, vol. 337–339, pp. 946–950, Mar. 2005.

[200] H. Iwakiri, K. Yasunaga, K. Morishita, and N. Yoshida, "Microstructure evolution in tungsten during low-energy helium ion irradiation," *J. Nucl. Mater.*, vol. 283–287, pp. 1134–1138, Dec. 2000.

[201] M. R. Gilbert, S. L. Dudarev, S. Zheng, L. W. Packer, and J.-C. Sublet, "An integrated model for materials in a fusion power plant: transmutation, gas production, and helium embrittlement under neutron irradiation," *Nucl. Fusion*, vol. 52, no. 8, pp. 1–12, Aug. 2012.

[202] M. Miyamoto, D. Nishijima, M. J. Baldwin, R. P. Doerner, Y. Ueda, K. Yasunaga, N. Yoshida, and K. Ono, "Microscopic damage of tungsten exposed to deuterium-helium mixture plasma in PISCES and its impacts on retention property," *J. Nucl. Mater.*, vol. 415, pp. S657–S660, 2011.

[203] S. Kajita, W. Sakaguchi, N. Ohno, N. Yoshida, and T. Saeki, "Formation

process of tungsten nanostructure by the exposure to helium plasma under fusion relevant plasma conditions," *Nucl. Fusion*, vol. 49, no. 9, pp. 1–6, Sep. 2009.

[204] D. Nishijima, M. Y. Ye, N. Ohno, and S. Takamura, "Formation mechanism of bubbles and holes on tungsten surface with low-energy and high-flux helium plasma irradiation in NAGDIS-II," *J. Nucl. Mater.*, vol. 329–333, pp. 1029–1033, 2004.

[205] D. E. J. Armstrong, P. D. Edmondson, and S. G. Roberts, "Effects of sequential tungsten and helium ion implantation on nano-indentation hardness of tungsten," *Appl. Phys. Lett.*, vol. 102, no. 251901, pp. 1–5, 2013.

[206] J. S. K. L. Gibson, S. G. Roberts, and D. E. J. Armstrong, "High temperature indentation of helium-implanted tungsten," *Mater. Sci. Eng. A*, vol. 625, pp. 380–384, 2015.

[207] T. J. Petty, M. J. Baldwin, M. Hasan, R. P. Doerner, and J. W. Bradley, "Tungsten 'fuzz' growth re-eaxmined: The dependence on ion fluence in erosive and non-erosive helium plasma," *Nucl. Fusion*, vol. 55, no. 9, pp. 1–11, 2015.

[208] G. M. Wright, D. Brunner, M. J. Baldwin, R. P. Doerner, B. Labombard, B. Lipschultz, J. L. Terry, and D. G. Whyte, "Tungsten nano-tendril growth in the Alcator C-Mod divertor," *Nucl. Fusion*, vol. 52, no. 4, pp. 1–5, 2012.

[209] A. M. Ito, A. Takayama, Y. Oda, T. Tamura, R. Kobayashi, T. Hattori, S. Ogata, N. Ohno, S. Kajita, M. Yajima, Y. Noiri, Y. Yoshimoto, S. Saito, S. Takamura, T. Murashima, M. Miyamoto, and H. Nakamura, "Hybrid

simulation research on formation mechanism of tungsten nanostructure induced by helium plasma irradiation," *J. Nucl. Mater.*, vol. 463, pp. 109–115, 2015.

[210] C. E. Beck, S. G. Roberts, P. D. Edmondson, and D. E. J. Armstrong, "Effect of Alloy Composition & Helium ion-irradiation on the Mechanical Properties of Tungsten, Tungsten-Tantalum & Tungsten-Rhenium for Fusion Power Applications," *MRS Proc.*, vol. 1514, pp. 99–104, 2013.

[211] C. S. Becquart and C. Domain, "A density functional theory assessment of the clustering behaviour of He and H in tungsten," *J. Nucl. Mater.*, vol. 386–388, no. C, pp. 109–111, 2009.

[212] J. Gong and A. J. Wilkinson, "Anisotropy in the plastic flow properties of single-crystal α titanium determined from micro-cantilever beams," *Acta Mater.*, vol. 57, no. 19, pp. 5693–5705, 2009.

[213] D. E. J. Armstrong, C. D. Hardie, J. S. K. L. Gibson, A. J. Bushby, P. D. Edmondson, and S. G. Roberts, "Small-scale characterisation of irradiated nuclear materials: Part II nanoindentation and micro-cantilever testing of ion irradiated nuclear materials," *J. Nucl. Mater.*, vol. 462, pp. 374–381, 2015.

[214] A. J. Bushby, S. G. Roberts, and C. D. Hardie, "Nanoindentation investigation of ion-irradiated Fe-Cr alloys using spherical indenters," *J. Mater. Res.*, vol. 27, no. 1, pp. 85–90, 2012.

[215] D. Di Maio and S. G. Roberts, "Measuring fracture toughness of coatings using focused-ion-beam-machined microbeams," *J. Mater. Res.*, vol. 20, no. 02, pp. 299–302, Mar. 2011.

[216] P. E. Lhuillier, A. Debelle, T. Belhabib, A. L. Thomann, P. Desgardin, T. Sauvage, M. F. Barthe, P. Brault, and Y. Tessier, “Helium desorption in 3He implanted tungsten at low energy,” *J. Nucl. Mater.*, vol. 417, no. 1–3, pp. 504–507, 2011.

[217] S. Saito, A. Takayama, A. M. Ito, and H. Nakamura, “Binary-collision-approximation-based simulation of noble gas irradiation to tungsten materials,” *J. Nucl. Mater.*, vol. 438, pp. S895–S898, 2013.

[218] G. De Temmerman, K. Bystrov, R. P. Doerner, L. Marot, G. M. Wright, K. B. Woller, D. G. Whyte, and J. J. Zielinski, “Helium effects on tungsten under fusion-relevant plasma loading conditions,” *J. Nucl. Mater.*, vol. 438, pp. S78–S83, Jul. 2013.

[219] M. J. Baldwin and R. P. Doerner, “Helium induced nanoscopic morphology on tungsten under fusion relevant plasma conditions,” *Nucl. Fusion*, vol. 48, pp. 1–5, Mar. 2008.

[220] S. Kajita, N. Yoshida, R. Yoshihara, N. Ohno, and M. Yamagiwa, “TEM observation of the growth process of helium nanobubbles on tungsten: Nanostructure formation mechanism,” *J. Nucl. Mater.*, vol. 418, no. 1–3, pp. 152–158, Nov. 2011.

[221] M. J. Baldwin and R. P. Doerner, “Formation of helium induced nanostructure ‘fuzz’ on various tungsten grades,” *J. Nucl. Mater.*, vol. 404, no. 3, pp. 165–173, Sep. 2010.

[222] T. J. Petty, “Tungsten nanostructure formation in a magnetron sputtering device,” University of Liverpool Thesis, 2015.

[223] G. Federici, J. N. Brooks, D. P. Coster, G. Janeschitz, A. Ukuskhin, A. Loarte, H. D. Pacher, J. Stober, and C. H. Wu, “Assessment of erosion and tritium codeposition in ITER-FEAT,” *J. Nucl. Mater.*, vol. 290–293, pp. 260–265, 2001.

[224] D. Nishijima, R. P. Doerner, D. Iwamoto, Y. Kikuchi, M. Miyamoto, M. Nagata, I. Sakuma, K. Shoda, and Y. Ueda, “Response of fuzzy tungsten surfaces to pulsed plasma bombardment,” *J. Nucl. Mater.*, vol. 434, no. 1–3, pp. 230–234, 2013.

[225] S. Kajita, G. De Temmerman, T. Morgan, S. van Eden, T. de Kruif, and N. Ohno, “Thermal response of nanostructured tungsten,” *Nucl. Fusion*, vol. 54, no. 3, p. 033005, 2014.

[226] M. Ye, S. Fukuta, N. Ohno, S. Takamura, K. Tokunaga, and N. Yoshida, “Modifications of Tungsten Irradiated by Low Energy and High Flux Helium Plasma,” *J. Plasma Fusion Res.*, vol. 3, pp. 265–269, 2000.

[227] K. Tokunaga, R. P. Doerner, R. Seraydarian, N. Noda, Y. Kubota, N. Yoshida, T. Sogabe, T. Kato, and B. Schedler, “Surface morphology and helium retention on tungsten exposed to low energy and high flux helium plasma,” *J. Nucl. Mater.*, vol. 313–316, pp. 92–96, 2003.

[228] S. Takamura, N. Ohno, D. Nishijima, and S. Kajita, “Formation of Nanostructured Tungsten with Arborescent Shape due to Helium Plasma Irradiation,” *Plasma Fusion Res.*, vol. 1, no. 051, pp. 1–2, 2006.

[229] S. Kajita, S. Takamura, N. Ohno, D. Nishijima, H. Iwakiri, and N. Yoshida, “Sub-ms laser pulse irradiation on tungsten target damaged by exposure to

helium plasma," *Nucl. Fusion*, vol. 47, no. 9, pp. 1358–1366, Sep. 2007.

[230] S. Kajita, N. Ohno, M. Yajima, and J. Kato, "Growth annealing equilibrium of tungsten nanostructures by helium plasma irradiation in non-eroding regimes," *J. Nucl. Mater.*, vol. 440, no. 1–3, pp. 55–62, 2013.

[231] W. Sakaguchi, S. Kajita, N. Ohno, M. Takagi, and H. Kurishita, "Formation Condition of Fiberform Nanostructured Tungsten by Helium Plasma Exposure," *Plasma Fusion Res.*, vol. 5, pp. S1023–S1023, 2010.

[232] Y. Ueda, K. Miyata, Y. Ohtsuka, H. T. Lee, M. Fukumoto, S. Brezinsek, J. W. Coenen, A. Kreter, A. Litnovsky, V. Philipps, B. Schweer, G. Sergienko, T. Hirai, A. Taguchi, Y. Torikai, K. Sugiyama, T. Tanabe, S. Kajita, and N. Ohno, "Exposure of tungsten nano-structure to TEXTOR edge plasma," *J. Nucl. Mater.*, vol. 415, no. 1, pp. S92–S95, Aug. 2011.

[233] S. Kajita, N. Yoshida, R. Yoshihara, N. Ohno, T. Yokochi, M. Tokitani, and S. Takamura, "TEM analysis of high temperature annealed W nanostructure surfaces," *J. Nucl. Mater.*, vol. 421, no. 1–3, pp. 22–27, 2012.

[234] R. P. Doerner, M. J. Baldwin, and P. C. Stangeby, "An equilibrium model for tungsten fuzz in an eroding plasma environment," *Nucl. Fusion*, vol. 51, no. 4, p. 043001, Apr. 2011.

[235] Y. Noiri, S. Kajita, and N. Ohno, "Nanostructure growth by helium plasma irradiation to tungsten in sputtering regime," *J. Nucl. Mater.*, vol. 463, pp. 285–288, 2015.

[236] R. M. Corless, G. H. Gonnet, D. E. G. Hare, D. J. Jeffrey, and D. E. Knuth, "On the Lambert W function," *Adv. Comput. Math.*, vol. 5, no. 1, pp. 329–

359, 1996.

[237] F. W. Meyer, H. Hijazi, M. E. Bannister, K. A. Unocic, L. M. Garrison, and C. M. Parish, “Flux threshold measurements of He-ion beam induced nano-fuzz formation on hot tungsten surfaces,” *Phys. Scr.*, vol. 2016, no. T167, pp. 1–7, 2016.

[238] G. De Temmerman, T. W. Morgan, G. G. van Eden, T. de Kruif, M. Wirtz, J. Matejicek, T. Chraska, R. A. Pitts, and G. M. Wright, “Effect of high-flux H/He plasma exposure on tungsten damage due to transient heat loads,” *J. Nucl. Mater.*, vol. 463, pp. 198–201, 2015.

[239] G. De Temmerman, K. Bystrov, J. J. Zielinski, M. Balden, G. Matern, C. Arnas, and L. Marot, “Nanostructuring of molybdenum and tungsten surfaces by low-energy helium ions,” *J. Vac. Sci. Technol. A Vacuum, Surfaces, Film.*, vol. 30, no. 4, p. 041306, 2012.

[240] I. Tanyeli, L. Marot, M. C. M. Van De Sanden, and G. De Temmerman, “Nanostructuring of iron surfaces by low-energy helium ions,” *ACS Appl. Mater. Interfaces*, vol. 6, no. 5, pp. 3462–3468, 2014.

[241] T. J. Petty and J. W. Bradley, “Tungsten nanostructure formation in a magnetron sputtering device,” *J. Nucl. Mater.*, vol. 453, no. 1–3, pp. 320–322, 2014.

[242] H. Hijazi and F. W. Meyer, “A large-acceptance beam-deceleration module for retrofitting into ion-source beam lines,” *Rev. Sci. Instrum.*, vol. 84, no. 3, p. 033305, 2013.

[243] K. Tokunaga, S. Tamura, N. Yoshida, K. Ezato, M. Taniguchi, K. Sato, S.

Suzuki, and M. Akiba, “Synergistic effects of high heat loading and helium irradiation of tungsten,” *J. Nucl. Mater.*, vol. 329–333, pp. 757–760, 2004.

[244] M. Akiba and S. Suzuki, “Overview of the Japanese mock-up tests for ITER high heat flux components,” *Fusion Eng. Des.*, vol. 39–40, pp. 219–225, 1998.

[245] M. Seki, M. Akiba, M. Araki, K. Yokoyama, M. Dairaku, T. Horie, K. Fukaya, M. Ogawa, and H. Ise, “Thermal shock tests on various materials of plasma facing components for FER/ITER,” *Fusion Eng. Des.*, vol. 15, pp. 59–74, 1991.

[246] M. Tokitani, N. Yoshida, K. Tokunaga, H. Sakakita, S. Kiyama, H. Koguchi, Y. Hirano, and S. Masuzaki, “Microscopic Deformation of Tungsten Surfaces by High Energy and High Flux Helium/Hydrogen Particle Bombardment with Short Pulses,” *Plasma Fusion Res.*, vol. 5, no. 012, pp. 1–4, 2010.

[247] J. Zielinski, H. van der Meiden, T. Morgan, D. Schram, and G. De Temmerman, “Characterization of a high-power/current pulsed magnetized arc discharge,” *Plasma Sources Sci. Technol.*, vol. 21, p. 065003, 2012.

[248] G. De Temmerman, M. A. van den Berg, J. Scholten, A. Lof, H. J. van der Meiden, H. J. N. van Eck, T. W. Morgan, T. M. de Kruijf, P. A. Zeijlmans van Emmichoven, and J. J. Zielinski, “High heat flux capabilities of the Magnum-PSI linear plasma device,” *Fusion Eng. Des.*, vol. 88, no. 6–8, pp. 483–487, Oct. 2013.

[249] M. J. Baldwin, R. P. Doerner, D. Nishijima, K. Tokunaga, and Y. Ueda, “The effects of high fluence mixed-species (deuterium, helium, beryllium) plasma

interactions with tungsten," *J. Nucl. Mater.*, vol. 390–391, pp. 886–890, Jun. 2009.

[250] Y. Ueda, H. Y. Peng, H. T. Lee, N. Ohno, S. Kajita, N. Yoshida, R. Doerner, G. De Temmerman, V. Alimov, and G. Wright, "Helium effects on tungsten surface morphology and deuterium retention," *J. Nucl. Mater.*, vol. 442, no. 1–3, pp. S267–S272, Nov. 2013.

[251] M. J. Baldwin, T. C. Lynch, R. P. Doerner, and J. H. Yu, "Nanostructure formation on tungsten exposed to low-pressure rf helium plasmas: A study of ion energy threshold and early stage growth," *J. Nucl. Mater.*, vol. 415, no. 1 SUPPL, pp. 104–107, 2011.

[252] D. Nishijima, M. Y. Ye, N. Ohno, and S. Takamura, "Incident ion energy dependence of bubble formation on tungsten surface with low energy and high flux helium plasma irradiation," *J. Nucl. Mater.*, vol. 313–316, pp. 97–101, 2003.

[253] T. J. Petty, A. Khan, T. Heil, and J. W. Bradley, "Fuzzy tungsten in a magnetron sputtering device," *J. Nucl. Mater.*, vol. 480, pp. 374–385, 2016.

[254] G. M. Wright, D. Brunner, M. J. Baldwin, K. Bystrov, R. P. Doerner, B. Labombard, B. Lipschultz, G. De Temmerman, J. L. Terry, D. G. Whyte, and K. B. Woller, "Comparison of tungsten nano-tendrils grown in Alcator C-Mod and linear plasma devices," *J. Nucl. Mater.*, vol. 438, pp. S84–S89, 2013.

[255] Y. Ueda, M. Fukumoto, A. Yamawaki, Y. Soga, Y. Ohtsuka, S. Brezinsek, T. Hirai, A. Kirschner, A. Kreter, A. Litnovsky, V. Philipps, A. Pospieszczyk, B. Schweer, G. Sergienko, T. Tanabe, K. Sugiyama, K. Ohya, N. Ohno, and T.

Textor, “Effects of tungsten surface conditions on carbon deposition,” *J. Nucl. Mater.*, vol. 390–391, pp. 44–48, 2009.

[256] D. L. Rudakov, C. P. C. Wong, R. P. Doerner, G. M. Wright, T. Abrams, M. J. Baldwin, J. A. Boedo, A. R. Briesemeister, C. P. Chrobak, H. Y. Guo, E. M. Hollmann, A. G. McLean, M. E. Fenstermacher, C. J. Lasnier, A. W. Leonard, R. A. Moyer, D. C. Pace, D. M. Thomas, and J. G. Watkins, “Exposures of tungsten nanostructures to divertor plasmas in DIII-D,” *Phys. Scr.*, vol. 2016, no. T167, pp. 1–5, 2016.

[257] S. Kajita, N. Ohno, N. Yoshida, R. Yoshihara, and S. Takamura, “Arcing on tungsten subjected to helium and transients: ignition conditions and erosion rates,” *Plasma Phys. Control. Fusion*, vol. 54, no. 3, p. 035009, 2012.

[258] W. R. Wampler, D. G. Whyte, C. P. C. Wong, and W. P. West, “Suppression of net erosion in the DIII-D divertor with detached plasmas,” *J. Nucl. Mater.*, vol. 290–293, pp. 346–351, 2001.

[259] J. N. Brooks, R. Causey, G. Federici, and D. N. Ruzic, “Assessment of erosion and surface tritium inventory issues for the ITER divertor,” *J. Nucl. Mater.*, vol. 241–243, pp. 294–298, 1997.

[260] S. I. Krasheninnikov, “Viscoelastic model of tungsten ‘fuzz’ growth,” *Phys. Scr.*, vol. 2011, no. T145, pp. 1–4, Dec. 2011.

[261] Y. V. Martynenko and M. Y. Nagel, “Model of fuzz formation on a tungsten surface,” *Plasma-Surface Interact.*, vol. 38, no. 12, pp. 996–999, 2012.

[262] A. Lasa, S. K. Tähtinen, and K. Nordlund, “Loop punching and bubble rupture causing surface roughening —A model for W fuzz growth,” *EPL*

(Europhysics Lett., vol. 105, p. 25002, 2014.

[263] S. Takamura and Y. Uesugi, “Experimental identification for physical mechanism of fiber-form nanostructure growth on metal surfaces with helium plasma irradiation,” *Appl. Surf. Sci.*, vol. 356, pp. 888–897, 2015.

[264] S. Sharafat, A. Takahashi, Q. Hu, and N. M. Ghoniem, “A description of bubble growth and gas release of helium implanted tungsten,” *J. Nucl. Mater.*, vol. 386–388, no. C, pp. 900–903, 2009.

[265] P. Fiflis, N. Connolly, and D. N. Ruzic, “Experimental mechanistic investigation of the nanostructuring of tungsten with low energy helium plasmas,” *J. Nucl. Mater.*, vol. 482, pp. 201–209, 2016.

[266] F. Sefta, K. D. Hammond, N. Juslin, and B. D. Wirth, “Tungsten surface evolution by helium bubble nucleation, growth and rupture,” *Nucl. Fusion*, vol. 53, no. 7, p. 073015, Jul. 2013.

[267] R. D. Smirnov, S. I. Krasheninnikov, and J. Guterl, “Atomistic modeling of growth and coalescence of helium nano-bubbles in tungsten,” *J. Nucl. Mater.*, vol. 463, pp. 359–362, 2015.

[268] S. I. Krasheninnikov and R. D. Smirnov, “He cluster dynamics in fusion related plasma facing materials,” *Nucl. Fusion*, vol. 55, p. 073005, 2015.

[269] A. Lasa, K. O. E. Henriksson, and K. Nordlund, “MD simulations of onset of tungsten fuzz formation under helium irradiation,” *Nucl. Instruments Methods Phys. Res. Sect. B Beam Interact. with Mater. Atoms*, vol. 303, pp. 156–161, 2013.

[270] M. Yamagiwa, S. Kajita, N. Ohno, M. Takagi, N. Yoshida, R. Yoshihara, W. Sakaguchi, and H. Kurishita, “Helium bubble formation on tungsten in dependence of fabrication method,” *J. Nucl. Mater.*, vol. 417, no. 1–3, pp. 499–503, Oct. 2011.

[271] N. Ohno, Y. Hirahata, M. Yamagiwa, S. Kajita, M. Takagi, N. Yoshida, R. Yoshihara, T. Tokunaga, and M. Tokitani, “Influence of crystal orientation on damages of tungsten exposed to helium plasma,” *J. Nucl. Mater.*, vol. 438, pp. S879–S882, 2013.

[272] K. D. Hammond and B. D. Wirth, “Crystal orientation effects on helium ion depth distributions and adatom formation processes in plasma-facing tungsten,” *J. Appl. Phys.*, vol. 116, no. 14, p. 143301, Oct. 2014.

[273] J. Amano and D. N. Seidman, “Diffusivity of 3He atoms in perfect tungsten crystals,” *J. Appl. Phys.*, vol. 56, no. 4, pp. 983–992, 1984.

[274] K. Tokunaga, M. J. Baldwin, R. P. Doerner, D. Nishijima, H. Kurishita, T. Fujiwara, K. Araki, Y. Miyamoto, N. Ohno, and Y. Ueda, “Nanoscale surface morphology of tungsten materials induced by Be-seeded D-He plasma exposure,” *J. Nucl. Mater.*, vol. 417, no. 1–3, pp. 528–532, 2011.

[275] S. Kajita, T. Yoshida, D. Kitaoka, R. Etoh, M. Yajima, N. Ohno, H. Yoshida, N. Yoshida, and Y. Terao, “Helium plasma implantation on metals: Nanostructure formation and visible-light photocatalytic response,” *J. Appl. Phys.*, vol. 113, no. 13, p. 134301, 2013.

[276] S. Takamura, “Temperature Range for Fiber-Form Nanostructure Growth on Molybdenum Surfaces due to Helium Plasma Irradiation,” vol. 9, pp. 1–4,

2014.

[277] X. Wu, X. S. Kong, Y. W. You, C. S. Liu, Q. F. Fang, J. L. Chen, G. N. Luo, and Z. Wang, “First principles study of helium trapping by solute elements in tungsten,” *J. Nucl. Mater.*, vol. 455, no. 1–3, pp. 151–156, 2014.

[278] S. Kajita, T. Saeki, N. Yoshida, N. Ohno, and A. Iwamae, “Nanostructured black metal: Novel fabrication method by use of self-growing helium bubbles,” *Appl. Phys. Express*, vol. 3, no. 8, pp. 8–11, 2010.

[279] S. Kajita, T. Yokochi, N. Ohno, and T. Kumano, “Near infrared radiation from heated nanostructured tungsten,” *Jpn. J. Appl. Phys.*, vol. 51, no. 01AJ03, pp. 1–5, 2012.

[280] D. Nishijima, M. J. Baldwin, R. P. Doerner, and J. H. Yu, “Sputtering properties of tungsten ‘fuzzy’ surfaces,” *J. Nucl. Mater.*, vol. 415, pp. S96–S99, 2011.

[281] S. Takamura, T. Miyamoto, and N. Ohno, “Effects of fibre-form nanostructures on particle emissions from a tungsten surface in plasmas,” *Nucl. Fusion*, vol. 52, no. 12, p. 123001, 2012.

[282] M. J. Baldwin, R. P. Doerner, W.R.Wampler, D. Nishijima, T. Lynch, and M. Miyamoto, “Effect of He on D retention in W exposed to low-energy, high-fluence (D, He, Ar) mixture plasmas,” *Nucl. Fusion*, vol. 51, pp. 1–9, 2011.

[283] D. Nishijima, Y. Kikuchi, M. Nakatsuka, M. J. Baldwin, R. P. Doerner, M. Nagata, and Y. Ueda, “Effects of Steady-State Plasma Exposure on Tungsten Surface Cracking due to Elm-Like Pulsed Plasma Bombardment,” *Fusion Sci. Technol.*, vol. 60, no. 4, pp. 1447–1450, 2011.

[284] S. Takamura, T. Miyamoto, and N. Ohno, “Deepening of Floating Potential for Tungsten Target Plate on the way to Nanostructure Formation,” *Plasma Fusion Res.*, vol. 5, pp. 039–039, 2010.

[285] S. Kajita, S. Takamura, and N. Ohno, “Prompt ignition of a unipolar arc on helium irradiated tungsten,” *Nucl. Fusion*, vol. 49, pp. 1–4, 2009.

[286] M. Tokitani, S. Kajita, S. Masuzaki, Y. Hirahata, N. Ohno, and T. Tanabe, “Exfoliation of the tungsten fibreform nanostructure by unipolar arcing in the LHD divertor plasma,” *Nucl. Fusion*, vol. 51, pp. 1–5, 2011.

[287] S. Kajita, N. Ohno, and S. Takamura, “Tungsten blow-off in response to the ignition of arcing: Revival of arcing issue in future fusion devices,” *J. Nucl. Mater.*, vol. 415, pp. S42–S45, 2011.

[288] D. U. B. Aussems, D. Nishijima, C. Brandt, H. J. van der Meiden, M. Vilémová, J. Matějíček, G. De Temmerman, R. P. Doerner, and N. J. Lopes Cardozo, “The occurrence and damage of unipolar arcing on fuzzy tungsten,” *J. Nucl. Mater.*, vol. 463, pp. 2–6, 2014.

[289] DIFFER, “Tungsten Polishing Procedure,” Lab Handbook, Nieuwegein, 2014.

[290] S. Reyntjens and R. Puers, “Focused ion beam induced deposition: fabrication of three-dimensional microstructures and Young’s modulus of the deposited material,” *J. Micromechanics Microengineering*, vol. 10, pp. 181–188, 2000.

[291] DIFFER, “Pilot-PSI,” 2014. [Online]. Available: http://www.differ.nl/research/fusion_physics/psi_experimental/pilot_psi.

[292] R. E. Stoller, M. B. Toloczko, G. S. Was, A. G. Certain, S. Dwaraknath, and

F. A. Garner, “On the use of SRIM for computing radiation damage exposure,” *Nucl. Instruments Methods Phys. Res. Sect. B Beam Interact. with Mater. Atoms*, vol. 310, pp. 75–80, 2013.

[293] ASTM International, “ASTM E521-96, Standard Practice for Neutron Radiation Damage Simulation by Charged-Particle Irradiation,” West Conshohocken, PA, 2009.

[294] NEC, “NEC Tutorials,” 2002. [Online]. Available: http://www.pelletron.com/tutor.htm. [Accessed: 01-Jan-2016].

[295] Notre Dame University, “Institute for Structure and Nuclear Physics,” 2016. [Online]. Available: http://isnap.nd.edu/html/research_FN.html. [Accessed: 23-Feb-2016].

[296] Keysight, “Keysight Nano Indenter G200 Data Sheet,” 2014. [Online]. Available: http://literature.cdn.keysight.com/litweb/pdf/5990-4172EN.pdf?id=1724253. [Accessed: 18-May-2016].

[297] W. C. Oliver and G. M. Pharr, “Measurement of hardness and elastic modulus by instrumented indentation: Advances in understanding and refinements to methodology,” *J. Mater. Res.*, vol. 19, no. 01, pp. 3–20, Mar. 2003.

[298] G. M. Pharr, J. H. Strader, and W. C. Oliver, “Critical issues in making small-depth mechanical property measurements by nanoindentation with continuous stiffness measurement,” *J. Mater. Res.*, vol. 24, no. 03, pp. 653–666, 2009.

[299] C. D. Hardie, “Micro-Mechanics of Irradiated Fe-Cr Alloys for Fusion Reactors,” University of Oxford Thesis, 2013.

[300] C. Wilkins, “Component Parts of a Scanning Electron Microscope: School of Materials, SEM Training Guide,” University of Manchester, 2014.

[301] J. Goldstein, H. Yakowitz, D. E. Newbury, E. Lifshin, J. W. Colby, and J. R. Coleman, *Practical Scanning Electron Microscopy: Electron and Ion Microprobe Analysis*. New York: Plenum Press, 1975.

[302] M. Eastman, “Materials World Modules,” 2010. [Online]. Available: http://materialsworld.utep.edu/Background/SCANNING ELECTRON MICROSCOPY/SccaningElectronMicroscopy.htm. [Accessed: 21-Feb-2016].

[303] Oxford Instruments, “Introduction to EBSD,” 2016. [Online]. Available: http://www.ebsd.com/ebsd-explained/introduction-to-ebsd. [Accessed: 21-Feb-2016].

[304] Université de Sherbrooke, “CASINO,” 2007. [Online]. Available: http://www.gel.usherbrooke.ca/casino/download2.html. [Accessed: 14-Jan-2016].

[305] R. Kobayashi, T. Hattori, T. Tamura, and S. Ogata, “A molecular dynamics study on bubble growth in tungsten under helium irradiation,” *J. Nucl. Mater.*, vol. 463, pp. 1071–1074, 2015.

[306] Z. X. Zhang, D. S. Chen, W. T. Han, and A. Kimura, “Irradiation hardening in pure tungsten before and after recrystallization,” *Fusion Eng. Des.*, vol. 98–99, pp. 2103–2107, 2015.

[307] M. R. McGurk and T. F. Page, “Using the P-δ2 analysis to deconvolute the nanoindentation response of hard-coated systems,” *J. Mater. Res.*, vol. 14, no. 06, pp. 2283–2295, 1999.

[308] E. R. Anderson and E. A. Marquis, “A snapshot of the microstructural evolution of Alloy 800H under heavy ion irradiation,” Poster, SMINS4 2016 conference, 2016.

[309] A. Al-Ajlony, J. K. Tripathi, and A. Hassanein, “Role of carbon impurities on the surface morphology evolution of tungsten under high dose helium ion irradiation,” *J. Nucl. Mater.*, vol. 466, pp. 569–575, 2015.

[310] E. R. Anderson, “Private Conversation.” 2016.

[311] A. S. Kurlov and A. I. Gusev, “Tungsten carbides and W-C phase diagram,” *Inorg. Mater.*, vol. 42, no. 2, pp. 121–127, 2006.

[312] EUROfusion, “EUROfusion Glossary.” [Online]. Available: https://www.euro-fusion.org/glossary/vde-vertical-displacement-event/. [Accessed: 10-Aug-2016].